THE UNIVERSITY OF CHICAGO

TESTING A MODEL OF PLANCK-SCALE QUANTUM GEOMETRY WITH BROADBAND CORRELATION OF COLOCATED 40M INTERFEROMETERS

A DISSERTATION SUBMITTED TO
THE FACULTY OF THE DIVISION OF THE PHYSICAL SCIENCES
IN CANDIDACY FOR THE DEGREE OF
DOCTOR OF PHILOSOPHY

DEPARTMENT OF PHYSICS

BY
LEE PATRICK MCCULLER

CHICAGO, ILLINOIS
DECEMBER 2015

To Mom and Dad, who lovingly supported me without reservation nor insistence. You gave me the freedom to find a path that I enjoy and more importantly taught me the determination to follow it through. Thank you.

"All models are wrong, but some are useful."

George Box

Table of Contents

List of Figures

List of Symbols

q_{e}	Constant: The charge of a single electron, 1 coulomb $= 6.241 \cdot 10^{18} q_{\mathrm{e}}$.
λ	Constant: Wavelength of the interferometer laser light, 1064nm
E_λ	Constant: Energy of one photon at the given interferometer wavelength
h, H	Symbol: Transfer functions
T	Symbol: Transmission coefficient in power
t	Symbol: Transmission coefficient in field
R	Symbol: Reflection coefficient in power
r	Symbol: Reflection coefficient in field
K	Symbol: Template used for noise search
C	Symbol: Calibration coefficient
$\mathbf{C}$	Symbol: Calibration matrix
$\mathscr{F}\{\cdot; F\}$	Operation: The Fourier Transform to frequency variable F
$\mathscr{F}^{-1}\{\cdot; t\}$	Operation: The Inverse Fourier Transform to time variable t
$\mathscr{L}\{\cdot; s\}$	Operation: The Laplace Transform to variable s
$\{\cdot *_{\mathrm{T}} \cdot\}$	Operation: convolution in the time-domain
$\{\cdot *_{\mathrm{L}} \cdot\}$	Operation: convolution in the frequency-domain
$\delta[X]$	Operation: Dirac delta function
$\left\langle \hat{X} \right\rangle$	Notation: expectation value for the enclosed statistical variable moment
$\left\langle \check{X} \right\rangle_y$	Notation: quantum expectation value for the operator $\check{X}$ in the prepared state labeled by y: $\langle y \vert \check{X} \vert y \rangle$
$\check{X}$	Notation: Hat indicating the quantum mechanical operator for the coordinate X
$\hat{X}$	Notation: Hat indicating that $\hat{X}$ is a variable only observable by statistical expectations
$\overline{X}$	Notation: Bar indicating the expectation $\overline{X} = \langle \hat{X} \rangle$
$\lfloor \hat{X} \rceil$	Notation: Vector of statistical quantities

$\hat{N}, \hat{\vec{N}}$	Notation: Noise term or vector of noise modes adding to a statistic, subscripts indicate independent sources
$\lfloor \hat{x} \rceil$	Notation: box represent virtual estimate of physical parameter
$\lvert \text{HG}{:}ij \rangle$	Notation: For the transverse Hermite-Gauss wavefunction
$\lvert \text{HG}{:}ij,F{:}F_{\text{sb}} \rangle$	Notation: For the transverse Hermite-Gauss wavefunction for field at frequency F
$\lvert \text{HG}{:}\langle i_0 j_0 \rvert i_1 j_1 \rangle, F{:}F_{\text{sb}} \rangle$	Notation: For transverse function of beating transverse Hermite-Gauss modes
$\Xi_{\delta}^{(+)}(F)$	Variable: The one-sided power spectrum of the tested holographic-noise model
L_{Δ}	Variable: DC differential-arm fringe offset of an interferometer, [m]
L_{δ}	Variable: RMS modulation of interferometer differential-arm length, [m]
$\hat{L}_{\delta}$	Variable: Fluctuation timeseries of differential-arm motion in interferometer, [m]
$\lfloor \hat{L}_{\delta} \rceil$	Variable: Virtual representation of $\hat{L}_{\delta}$
ξ_{PD}	Symbol: Conversion efficiency of photodiode [A/W]
Υ_{FOLD}	Variable: Factor of 1 or 2 distinguishing between the two or one-sided power-spectrum estimators

ACKNOWLEDGMENTS

I feel that so many people have shaped me to create this document in culmination of a what seems a direct path but feels to me a grand tour of thoughts, ideas and ruminations.

I must supremely thank my advisor Stephan Meyer. He taught me the many things you can't learn in classes - physical intuition and a fair bit of wisdom about "how it all works" in lab and out. I think every time I've disagreed with Steve about something meaningful I've been wrong. Its always amazing that we'll end up agreeing eventually (after much chalk and discussion) with the same intuition, but different technical pictures. The work has been difficult at times but Steve has always provided just the right support and really the wisdom as to why science is difficult and why that's OK and why the passion requires a reasoned perseverance.

I would like to thank Aaron Chou for our many technical discussions. The ones not about the experiment were perhaps the most important. I feel that much of my broader relation to physics has come from us hashing out our respective crazy (but sometimes great) ideas. Those discussions occassionally felt distracting to my goals for the experiment, but as I move on I must state that hashing out those many ideas has made me a better physicist.

I must also thank Craig Hogan for out many great discussions about the experiment while driving out to the lab. The experiment is good and bold and really does look at something truly new. I must largely attribute my great appreciation for strong and novel *measurement* to a theorist.

I must thank the rest of the Holometer collaboration in their great efforts pushing the experiment foreward. I really saw the machine be *built* from nothing through strong collaboration a small team. Amongst all this effort I must thank my fellow graduate students, Bobby Lanza, Jonathan Richardson and Brittany Kamai, for braving through the tunnels with me, working with me during the small hours, and the full campaign of data-taking and analysis.

I must thank the University of Texas at Austin, their Dean's Scholars program, and their physics and math departments. I do not feel I could have had a better foundation from college. Across all of the undergraduate programs I met talented people and good friends. Among them I would like to acknowledge Ivo Popov. He was my counterpart in our coursework and in keeping up with Ivo I was infected with his relentles desire to understand deeply rather than learn our material. I also must thank my undergraduate advisor Sacha Kopp for his mentorship preparing me for individual research.

As I dedicated, I would like to thank my parents. I had many hobbies dabbling around science and they always supported me. It's no wonder I feel such reward in tinkering when they associated it so well with their own interest. I would like to thank my Uncle Dennis for instilling his own electronics hobbyist interests in me (and letting me talk his ear off). I finally understand all the little motors and LED's I tinkered with him to blink on and off.

Science requires personal strength along technical skill and I would like to thank my good friend ZZ Lazarine for his influence. He taught me to be an individual and to stand up for myself and do these things with a sense of integrity.

I must finally thank Kate, who along with her support, has given me wisdom and context through discussions of science as a career, endeavor, source of pride to keep the effort worthwhile and fulfilling amongst the many facets of life.

ABSTRACT

The Holometer is designed to test for a Planck diffractive-scaling uncertainty in long-baseline position measurements due to an underlying noncommutative geometry normalized to relate Black hole entropy bounds of the Holographic principle to the now-finite number of position states. The experiment overlaps two independent 40 meter optical Michelson interferometers to detect the proposed uncertainty as a common broadband length fluctuation. 150 hours of instrument cross-correlation data are analyzed to test the prediction of a correlated noise magnitude of $7{\cdot}10^{-21}\mathrm{m}/\sqrt{\mathrm{Hz}}$ with an effective bandwidth of 750kHz. The interferometers each have a quantum-limited sensitivity of $2.5{\cdot}10^{-18}\mathrm{m}/\sqrt{\mathrm{Hz}}$, but their correlation with a time-bandwidth product of $4{\cdot}10^{11}$ digs between the noise floors in search for the covarying geometric jitter. The data presents an exclusion of 5 standard deviations for the tested model. This exclusion is defended through analysis of the calibration methods for the instrument as well as further sub shot noise characterization of the optical systems to limit spurious background-correlations from undermining the signal.

Chapter 1

HOLOGRAPHIC NOISE PREDICTION

1.1 Introduction

The reach of any physical theory to describe the composition of time, matter and space in the universe is always limited by a scale of validity. This scale represents a limited region in whatever dimensions describe in the composition and arrangement of matter attempting description by the theory. The push for physics research in some sense is to expand and connect models or descriptions across many scales into a consistent and fundamental "core", and that through successive approximations that core is sufficient to bridge from scale-to-scale to describe the full complexity of the natural world. Expanding the domain of physical theories then requires not just the improvement of known models, but the definition and exploration of new scales to find the intersection of seemingly unrelated or incompatible models.

The Holometer is an experiment attempting to detect a novel effect at an unexplored-scale. The effect predicts physics relating the scales of quantum mechanics to those of General-Relativity. The unexplored-scale investigates the coherence of position-data imprinted on optical fields as they propagate laboratory-distance simultaneously in orthogonal directions.

Quantum Mechanics is a theory with remarkable predictive-power at very small scales of length, mass, and particle-number[1]. It has been pushed to extremes of these scales through the development of quantum field theories and the standard-model of particle physics. Despite its successes in these regimes, quantum-mechanics demands an number of assumptions on the nature of matter and its interaction with the spatial coordinates used to describe it.

1. The particle number scale is really a requirement to have coherent effects, which is otherwise assured for large systems at low tempurature.

1. All matter and interacting fields are composed of particles[2].

2. Particle-states are inherently *non-local* in their resolution to spatial coordinates.

3. The position-momentum space of particles is given limited resolution through the Heisenberg Uncertainty Principle and the canonical-quantization of classical theories into a quantized description.

4. Energy is a quantity locally and globally-conserved - no interaction changes the total energy integrated across all of space.

5. The universe can be describe as existing in a single coherent superposition of particle-states, advancing continuously into a new state in a way that preserves the *unitarity* of time-evolution.

On the opposite limits of models, the well-developed general theory of relativity describes extreme collections of matter, distributed across astronomical scales of space and cosmological scales of time. It requires a number of assumptions to the systems it describes.

1. All matter and interacting fields have a energy-momentum tensor, defined locally at every coordinate with definite values.

2. Energy is only a *locally conserved* quantity, only definable globally from the (unobservable) fields at asymptotic distances.

3. The interacting field is a change to geometry-itself and nonlinearities of the Einstein-equation prevent its expression as particle-states.

4. Extreme objects (e.g. black holes and horizons) of the theory appear to violate unitarity, recovering it through mechanisms currently escaping exact description.

2. More rigorously all matter and fields can be perturbatively linearized into *particle-states* of a functional-space describing them.

These theories, existing at two extremes on the scales of space and time contain in these lists a number of incongruities. A particular theme of which is inability of quantum-mechanics and general-relativity to simultaneously express the *delocalization* of matter in coordinate-parameters of one theory with the localized matter in the coordinates of the other. Assuming gravity as a stationary background geometry for particle physics circumvents these issues, but ignores any systems attempting to predict the interactions between the two.

The vast difference in scales of these two principle descriptions of spacetime and matter has prevented any current experiment from detecting new models that may interact at the intersection. The scales relevant for testing gravity using the direct techniques of particle theory are the Planck-length, Planck-time, and Planck-mass.

$$l_{\mathrm{p}} = \sqrt{\frac{\hbar G}{c^3}} \approx 1.616{\cdot}10^{-35}\mathrm{m} \tag{1.1}$$

$$t_{\mathrm{p}} = \sqrt{\frac{\hbar G}{c^5}} \approx 5.3912{\cdot}10^{-44}\mathrm{s} \tag{1.2}$$

$$M_{\mathrm{p}} = \sqrt{\frac{\hbar c}{G}} \approx 2.176{\cdot}10^{-8}\mathrm{kg} = 2.435{\cdot}10^{18}\mathrm{GeV} \tag{1.3}$$

The experimental divide from of these scales from the state of the art experimental tests with particles is from the Large Hadron Collider at 14TeV. There has been work investigating the intersection or unification of the two theories which attempts to assign quantum effects and entropy to the "particles" of the general-relativity world, black-holes. At the heart of this work are the theoretical action of the third-law of thermodynamics in Hawking-radiation and the assigning of entropy to Black-Holes through the Bekenstein-Hawking formula:

$$S_{\mathrm{BH}} = \frac{kA}{4l_{\mathrm{p}}^2} \tag{1.4}$$

Assigning an entropy to a purely gravitating system implies a number of possibilities about how to account for microstates providing that entropy. In the purely gravitating

system of a black-hole, the microstates are presumably held in some description of the *geometry* itself. It is otherwise also reasonable to assume that some expression of the as-yet-known or even possibly-unknown quantum-fields could express those microstates without an incompatibility to the extreme geometrical state of the black-hole. In either case, the finite-number of microstates must have the quantum-mechanical property of undefined localization in the classical coordinates of the black-hole space-time. Without the constraint of finite-states, the continuum of coordinates could carry any number of field states,classical point-like locality could be maintained and the entropy could not be defined as it has.

The delocalization of whatever states constitute the entropy of a black-hole do not constrain them in any way to being near or within the hole. Many avenues of research use field-theoretic correspondences to view the states from asymptotic infinities and, in that picture, the microstates of the black-hole are truly distributed across all coordinates. Simply defining the meaning of "near" or "within" becomes nebulous in the context of such undefined states. Such states are in contrast to physical particle states, which present wavefronts that localize their defined mass. Experiments can produce entangled states challenging the description that the mass is ever localized until measurement, but laboratory scales are ultimately finite in size.

Photons are an extreme yet typical example of the entangling of microstate degrees-of-freedom across coordinate space. Any single photon is emitted or detected as a localized wavepacket, but a continuous coherent beam of photons into a large, resonant laser-cavity exercises the wave-nature of the states, delocalizing any photon in time or location, but imprinting upon them some data describing their boundaries. Leakage or coupling out of such a cavity to measure the photon energy, then behaves as a barrier-tunnelling to the delocalized photon-state and phase or timing information can extract the data on the system's boundaries.

All of these concepts have come together to motivate (not prove) a notion known as the

holographic-principle. This principle attempts to assign to all space the maximum-entropy bound of a black-hole[3]. The maximum entropy described for space is extremely large and typically difficult to invoke as relevant for laboratory-scale measurements, but the bound is quite notable for the scaling-law associated to it, in which the entropy scales as the area bounded in a spacelike-surface, rather than the volume-enclosed.

Like the many analytical descriptions applicable to General-Relativity, the precise definition of the areas and states invoked by the holographic principle are difficult to pin-down. The review of the holographic-principle by Bousso [2] composes the various perspective. Of particular note in it is the emphasis for a *covariant* formulation, whereby the entropy must describe micro-states of fields imprinted on null-boundaries of the past/future causal-cones defining a spacelike volume or surrounding area.

Expressions of the holograph principle are incorporated on a number of theoretical fronts to extend field-theories into the realm of geometry and general relativity. Two commonly known such examples are string-theory and loop-quantum gravity. These theories dissolve the lab-frame coordinates to develop from abstract and higher-dimensional spaces meeting each theories' motivating constraints. The ultimate hope then is to condense from either the standard model as yet-another successive approximation at the GeV scale.

The alternative approach is to build effective or phenomenological theories incorporating the holograph-principle with the expectation that any fundamental theory would be constrained when expressed at the scales of a tested such phenomenological theory.

1.2 Transverse-uncertainty

The Holometer experiment is designed as a test of a particular phenomenological representation of the Holographic Principle. The theory it predicts a novel uncertainty-principle and related noise in measurements of transverse distance. This thesis distinguishes this model

3. Or more generally the same entropy-bound has been proven for any horizon arising in general relativity

to be tested as the Hogan-noise model, developed by Craig Hogan and compared against current length-sensitive experiments by Ohkyung Kwon[7]. Alternative models have been proposed which enforce minimum length-scales (or alternatively maximum energy-scales) and/or metric-fluctuations as way of tying $l_{\rm p}$ to laboratory physics and deriving the phenomenology. The general strategy of the Hogan-noise model and other such theories is to impose additional uncertainty or dispersion relations, limiting the resolution of particle states to coordinates and therefore enforcing some geometric constraint on the number of microstates available. These theories contrast to quantum-field theory which not only does not impose bounds on the total number of states, it performs most calculations in the momentum-space of an infinite volume, deriving (exceedingly accurate) results in the continuum approximation. Quantum field theories' implicit use of plane-waves excludes it from the regime described in the Hogan-noise model.

These theories are often testable by amplifying the Planck-scale modification through dispersion and diffraction into a type of long-baseline uncertainty relations with the scaling to the system following $\sqrt{l_{\rm p} R_{\rm sys}}$, where $R_{\rm sys}$ is some distance or displacement scale for the system.

The reduced microstates of the phenomenological theories can then be related to the scaling law of the Hawking-Bekenstein entropy and the holographic-principal. A review of constraints from current experiments covers that many theories with metric-fluctuations and longitudinal uncertainty of wavefronts are largely ruled-out by current experiments [7].

The theory behind the Holometer attempts to choose a measurement scale to enforce the holographic principle that typically escapes the description of General-Relativity and Quantum-field-theory by expressing a large effect only for measurements of small transverse wavefronts propagated over great distance. It too benefits from long-baseline Planckian-diffractive scaling, $\sqrt{l_{\rm p} R_{\rm sys}}$, although its notions of transverse diffraction are unconventional with the traditional sense of paraxial spreading along a linear propagation. The Hogan-noise

model enforces a limit to the total number of position-states through *transverse* uncertainty, which will be expressed in the units of area.

To describe the new physics I first detour into an analogous uncertainty-limit for standard wavefunction coordinates built from orbital spin-states. Here the operators, $\check{J}$ describe *orbital* wavefunctions, rather than the conventional, J, labelling total angular-momentum. This breach of convention is to distinguish from later operators using $\check{L}$ which are related to length. These $\check{\vec{J}}$ operators have the uncertainty relation:

$$[\check{J}_{\mathrm{i}}, \check{J}_{\mathrm{j}}] = \mathrm{i}\hbar\epsilon_{\mathrm{ijk}}\check{J}_{\mathrm{k}} \tag{1.5}$$

And this uncertainty relation falls out of the Poisson-bracket classical-commutator for any wavefunction with a rotationally-invariant interaction. The rotational invariance is a particular property, noticed classically, of the coordinates used to describe fields. The operators generated from rotation-invariance allow any wavefunction to be expressed in the basis of spherical-harmonics rather than Cartesian-location. In contrast, the generators of Cartesian translations, P_{i}, appear classically to have a zero commutator, which is preserved when lifting the classical observations into quantum mechanics. However, it is possible that the commutator for translation has simply *escaped experimental detection.* Were there a commutator of the translation operators, the Poincaré-group expression for the symmetries of physics could only represent an approximation, just as the Euclidean group of translations was assumed until special-relativity enforced a lift into the Poincaré group.

Returning to the angular-momentum operators, A system with a known total angular momentum $\check{\vec{J}}^2 = \hbar^2\bar{J}(\bar{J}+1)$ can be measured repeatedly in attempt to resolve the "location" of the wavefunction in spherical-coordinates $\check{J}_{\mathrm{x}}$ and $\check{J}_{\mathrm{y}}$. The angular-momentum algebra can be expressed in raising and lowering operators, here defined with their action on the QJx quantum-number. The existence of raising and lowering operators enables the expression of the repeated-measurement wavefunction as a coherent-state of $\check{J}_{\mathrm{x}}$, defined and labeled as

eigenstates $\check{J}_{\text{-x}}|j_{\text{x}}\rangle = j_{\text{x}}|j_{\text{x}}\rangle$[1]. The repeated measurement, assuming it has equal sensitivity to X and Y, will evolve the state into the minimum-uncertainty state, which is a coherent-state of $\check{J}_{\text{x}}$(or equivalently $\check{J}_{\text{y}}$)[5]. The measurements will ultimately pick up an irreducible variance from the minimum-uncertainty state.

$$\left\langle (\Delta\check{J}_{\text{x}})^2 \right\rangle_{j_{\text{x}}} = \left\langle (\Delta\check{J}_{\text{y}})^2 \right\rangle_{j_{\text{x}}} = \left\langle (\Delta\check{J}_{\text{z}})^2 \right\rangle_{j_{\text{x}}} = \frac{1}{2}\hbar^2\bar{J} \tag{1.6}$$

where the subscripted bra-ket notation takes the expectation through the prepared-state labeled in the subscript: $\left\langle \check{H} \right\rangle_{j_{\text{x}}} = \left\langle j_{\text{x}}|\check{H}|j_{\text{x}} \right\rangle$ for any observable operator, $\check{H}$.

This is an interesting result because the angular-momentum coordinates also enforce a limit to the number of available states $N_{\bar{J}} = \bar{J}(\bar{J}+1)$, which scales with the square the total angular momentum rather than the cube.

An important observation about the angular-momentum states discussed is to reiterate the nonlocal-nature of orbital spherical-harmonic states. A particle expressed purely in this basis can be localized arbitrarily-well in Cartesian coordinates, but to do so requires amplitude over a broad spectrum of total and azimuthal quantum-numbers, operating with a constraint on the total angular momentum precludes the ability to localize such a wave-function. This observation of nonlocality stresses that the state must be extended over a spacelike-surface of space-time. This leads to a natural question regarding measurements of the angular-momentum-state - can the measurement itself be localized? And if two localized measurements are made at different places and times of the spherical-harmonic, what is the causal-structure and 2-point correlation-functions for the separated-sequences of measurements as the notion of simultaneity is lost.

With the properties of this rotation-algebra emphasized as coordinates, they motivate an *ad-hoc* treatment of position-states. As, mentioned, the zero commutator for translations and standard usage of the Poincaré-group to develop quantum field theories is convention only out of the lack of any observation to the contrary and the usual insensitivity of standard theory

to the commutator of translations. The well-tested calculations arising from Quantum field theory are described through plane-waves localized in momentum-space and the basis of the Fourier-mode decomposition lacks any wavefront-curvature. This prevents such scattering calculations from detuning via terms arising from the proposed nonzero commutator.

The Hogan-noise model attempts to determine the effects of the following commutator[7]. The $\check{L}$ operators now describe position or displacement from any reference point or world-line.

$$[\check{L}_{\mathrm{i}}, \check{L}_{\mathrm{j}}] = \mathrm{i}\frac{1}{\sqrt{4\pi}} l_{\mathrm{p}} \varepsilon_{ijk} \check{L}_{\mathrm{k}} \tag{1.7}$$

Now the usual azimuthal angular-momentum operators become the means of determining the classical Cartesian location for wavefunctions $\check{J}_{\mathrm{x}} \rightarrow \check{L}_{\mathrm{x}}$. The total size of a wavefunction becomes expressed from $|\check{\vec{L}}|^2$. The normalization of the new commutator is set from the total number of position-states saturating the holographic entropy bound through the analogous formula as the angular-momentum algebra $N_{\bar{L}} = \bar{L}(\bar{L}+1)$. The length, $\bar{L}$ now is actually expressed as an integer-index in the reduced-Planck units of the commutator. Changing back to physical length and approximating to scales much larger than l_{p}, the number of states becomes $N_{\bar{L}} = 4\pi \frac{R_{\mathrm{sys}}^2}{l_{\mathrm{p}}^2}$. The correspondence of this number with eq. (1.4) follows from arguments in the theory of entropic gravity [7]. It is not expressed here, but the commutator may also be expressed in a manifestly covariant form.

This theory is noted as one of transverse-uncertainty. This follows from the relationship with the standard angular-momentum algebra. For measurement-noise to be seen for $\check{J}$, measurements must be made simultaneously sensitive to modes of spherical harmonics (at fixed $\bar{J}$). For the commutator on $\check{L}$, measurements must be made in at least two directions (at fixed $\bar{L}$) for the additional noise to be expressed.

The causal structure of the angular-momentum modes and their algebra should be reiterated for this new case. What exactly is the nature of "local" length measurements and what

is their causal structure? The $\check{L}$ commutator expressed represents position, but position as well as time are only ever measured through the evolution of phase and ultimate inference of phase into power on a detector. For laser-length measurements, distance measurements are made along the null surfaces traversed by light, but along those surfaces the light undergoes no phase-advance. The light propagating across multiple spatial locations then must all be directed to the location of a common world-line. Although the light along any given path undergoes no phase-advance, the many paths reach the common world-line at different, comparable moments and the measurement along the world-line consists of both the phase differences of the light originating and the phase differences of the relative phase-advance or delay from reaching the destination world-line at different times.

This commutator expresses an effect whereby any wavefront along a null-surface that has spatial extent in multiple Cartesian-coordinates will have *only approximately* zero phase-advance. Uncertainty-relations constructed from the proposed commutator express the statistics of the approximate-null of the phase advance depending on the transverse-extent of the multiple paths followed by the wavefront. This novel phase-uncertainty adds noise to any comparison at the destination world-line with a magnitude dependent on the amount of non-commuting distance travelled.

1.3 Predicted Magnitude in a Michelson Interferometer

The geometry of a Michelson interferometer involves three world-lines, the beamsplitter and two endmirrors. Light entering the device is split at the beamsplitter world-line, travels along two edges of a causal-cone to intersect each respective endmirror world-lines, then returns to the beamsplitter along a second causal-cone for a final phase-comparison and ejection from the instrument. This process is depicted in fig. 1.1 on page 15. For a perfectly-balanced device the two wavefronts classically return at the same-time with no-phase advance, as each traversal along the cone itself did not advance the phase.

The noncommutativity of the length measurement now enforces an uncertainty from the now approximately-null differential phase advance of the two arms of light. The standard prediction for the Holometer arises from invoking this uncertainty and applying it separately for each light-cone "from" and then "to" the beamsplitter. This picture requires the world-lines of all three optics to remain approximately inertial in the lab-frame. The differential phase of the light can then be compared simultaneously in that frame as it represents the beamsplitter world-line. Call the two traversed-paths x and y, then the differential phase is defined: $\check{\theta}_\delta = \check{\theta}_x - \check{\theta}_y$. The continuity of the length-measurement puts the arm-length state (analogous the azimuthal angular-momentum) into a coherent-state of length.

$$\Delta\check{\theta}_\delta = \check{\theta}_\delta - \left\langle \check{\theta}_\delta \right\rangle_{l_x} \tag{1.8}$$

$$\left\langle (\Delta\check{\theta}_\delta)^2 \right\rangle_{l_x} = \left\langle \left(\frac{2\pi}{\lambda}\Delta\check{L}_\mathrm{x} - \frac{2\pi}{\lambda}\Delta\check{L}_\mathrm{y} \right)^2 \right\rangle_{l_x} \tag{1.9}$$

$$= \left(\frac{2\pi}{\lambda}\right)^2 \left(\left\langle (\Delta\check{L}_\mathrm{x})^2 \right\rangle_{l_x} + \left\langle (\Delta\check{L}_\mathrm{y})^2 \right\rangle_{l_x} - \left\langle \Delta\check{L}_\mathrm{x}\Delta\check{L}_\mathrm{y} \right\rangle_{l_x} - \left\langle \Delta\check{L}_\mathrm{y}\Delta\check{L}_\mathrm{x} \right\rangle_{l_x} \right) \tag{1.10}$$

using eq. 1.6, and assuming zero cross-terms (no squeezing)

$$= \left(\frac{2\pi}{\lambda}\right)^2 \frac{l_\mathrm{p}^2}{4\pi}\bar{L} = \left(\frac{2\pi}{\lambda}\right)^2 \frac{l_\mathrm{p} R_\mathrm{sys}}{\sqrt{4\pi}}$$

This expression is for the differential phase advance along orthogonal sides of a single light-cone. An additional, independent uncertainty is added from the advance through the returning cone, for a total round-trip phase-uncertainty of

$$\left\langle \Delta\check{\theta}_\delta^2 \right\rangle_{l_x}^{\mathrm{RT}} = \left(\frac{2\pi}{\lambda}\right)^2 \frac{2 l_\mathrm{p} R_\mathrm{sys}}{\sqrt{4\pi}} \tag{1.11}$$

The doubling of the variance through two cones has the interesting property that the system may just as well be described with an effective length defined as the round-trip distance,

$2R_{\rm sys}$. The round-trip picture follows more closely to a start-to-end world-line description, rather than an out-to-in description, as it does not require any boundary-point or frame of reference to be defined at the endmirrors. The start-to-end description has the conceptual advantage on not requiring the source at the same world-line as the destination.

A question of note is why should dropping the cross-terms of eq. (1.10) on page 11 be acceptable? It's not clear what mechanism would prevent the continuous measurement from squeezing the geometry state and reducing the uncertainty, but there are two good arguments against the possibility.

1. The light-propagation does not have any known form of back-action on the geometric data which would press it into a squeezed quadrature.

2. The Michelson could just as well measure both returning beams relative to a local reference, providing separate $\left\langle(\Delta\check{L}_{\rm x})^2\right\rangle$ and $\left\langle(\Delta\check{L}_{\rm x})^2\right\rangle$ measurements which would not expose the cross-terms. This view of the Michelson is explored in section 2.1.2 on page 22 in the context of the standard-quantum-limit for optical measurement.

The phase-variance applies for any given measurement of a Michelson picked out of a continuous sample. The continuous sample pushes the geometric-uncertainty into the coherent-state with minimum uncertainty, and the single round trip constitutes a single round-trip measurement through the outward and inward cones. This begs the question of how should the measurements correlate in time. The description arises from the overlap of the light-cones. For measurements separated by τ, $\check{\theta}_\delta(t)$ and $\check{\theta}_\delta(t-\tau)$, The 2-point correlation $\langle\Delta\check{\theta}_\delta(t)\Delta\check{\theta}_\delta(t-\tau)\rangle$ compares arm-lengths of a subsystem that is at most $2R-c\tau$ in size. The causal diamond of the correlation measurement consists only of the overlap of the diamonds of each individual measurement. In the two-cone picture, the correlation measures uncertainty generated in the inward-cone of the earlier measurement up to the boundary of the intersection with the outward-cone of the latter measurement and vice-versa for the

outward cone. The intersection points occur at a distance $L - \frac{c\tau}{2}$ for both cones, and the two contributions to the correlation still combine to produce the auto-correlation function of

$$\left\langle \Delta\check{\theta}_\delta(t)\Delta\check{\theta}_\delta(t-\tau) \right\rangle = \left(\frac{2\pi}{\lambda}\right)^2 \frac{l_{\mathrm{p}}}{\sqrt{4\pi}} \begin{cases} 2R_{\mathrm{sys}} - c\,|\tau| \ : \ \text{where } c\,|\tau| < 2R_{\mathrm{sys}} \\ 0 \ : \ \text{else} \end{cases} \tag{1.12}$$

The correlation implied by the overlapping causal diamond argument leads to another principle property of the Hogan noise prediction. Co-located Michelson interferometers similarly overlap in their causal structure and will see correlated phase-uncertainty. Two separate instruments do not share the same beamsplitters, so the beamsplitter world-line is not the central geometric information that is affected by the novel commutator of this theory. Instead it is the world-line of the reference frame that both beamsplitters are inertial in. This is an interesting point of the theory, imprinting the notion that geometric information is inherently entangled. It explains that the steadfastness of reference-points in the classical world can be attributed to strong localized coherence. Even if the entire local lab-frame seen at great distance would appear to move quite far, the distant-frames occupants would be unable to tell with local measurements. The same matter that reduced noise for small-baseline measurements causes correlated apparent-motion for overlapping large-baselines. This large-scale coherence prevents the apparent-angular motion of distant objects from colliding or affecting the apparent separation of those objects, even for arbitrarily distant objects.

This notion can be expressed for the causal structure of the Michelson. It is depicted in fig. 1.2 on page 16. If a world-line is viewed from two instruments, one larger (Alice) and containing-causally the other (Bob), then the larger (Alice) Michelson should also detect more noise in its autocorrelation, but its cross-correlation function to the smaller (Bob) should then be identical to the autocorrelation that Bob has itself. For this to be true, the

world-lines representing the boundary of the smaller instrument must also have an apparent motion that the larger instrument detects, as its causal structure contains those world-lines. It is however not apparent to the smaller instrument that its boundaries have an apparent motion. Again, the larger of the two (Alice) has more total noise in its autocorrelation, which is consistent with her conclusion that the inner volume (Bob) has an apparent-motion in addition to the apparent motion that Bob concludes of his center world-line.

The overlapping cross-correlation can be wielded to aid the experiment. Two interferometers can be used to measure the world-line-noise within the same causal boundary rather than one. This comes as a great benefit to the experiment in the ability to correlate below the usual photon-counting limits of a single optical interferometer. Furthermore the cross-correlation aids in preventing spurious background noises in electronics and laser-equipment from imprinting correlations in the experiment. Most such background sources will not correlate between physically separate instruments.

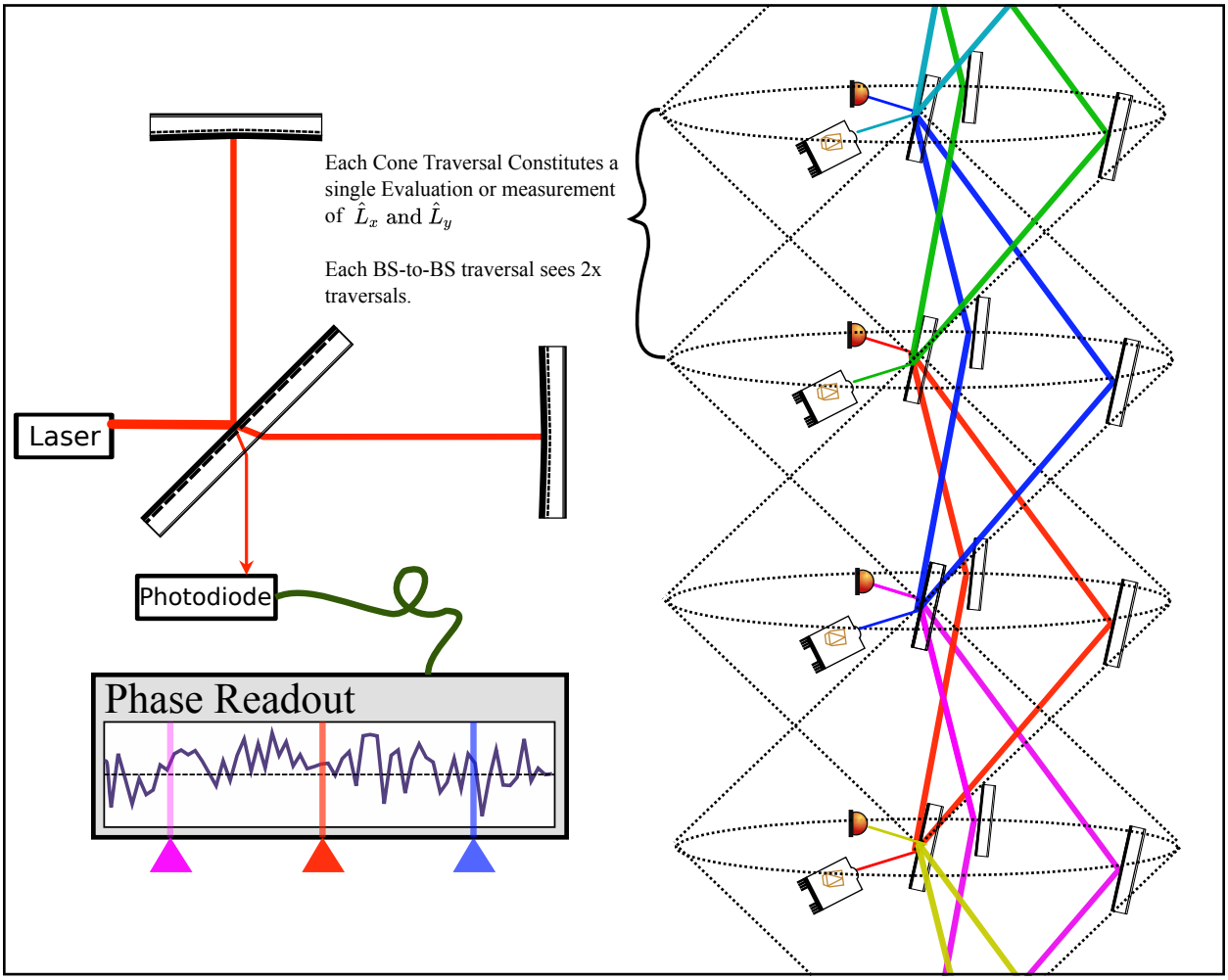

Figure 1.1: The space-time causal structure of a Michelson interferometer. The top-down view really reflects a sequence of measurements, each occurring through a traversal of the Michelson's causal-cone. The timeseries readout of the phase information is provided by the interference of the two arms fluctuating from geometric-noise imprinted on the phase.

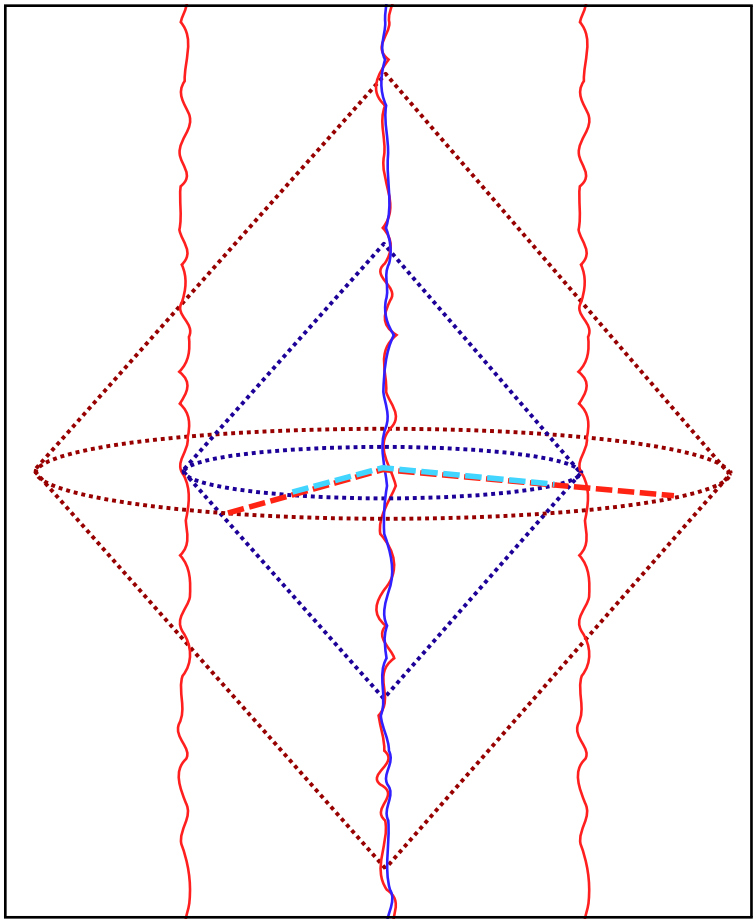

Figure 1.2: The pair systems making length measurements with one system overlapping the other is shown. The larger, purple system, Alice detects a larger noise given the predicted scaling. The additional noise also will not have coherence with the smaller system's measurement. This corresponds to the larger system concluding that the entire frame of the smaller system is not well-defined. In the limit of equal system-sizes, one cannot conclude that the reference-frames are inconsistent as the noise will correlate in both instruments. The opposite limit defines the noise in the measurement. The beamsplitter's action on the beam is perfectly coherent locally, but to the phase reference of both endmirrors, the reference frame that the beamsplitter recombination is occurring cannot be perfectly defined. This generates a noise which violates no local physical principles, but potentially violates energy-conservation in systems of large-spatial extent. Such apparent energy violation is a property shared by General Relativity.

1.4 Phase and Length conventions for the Hogan Model in a Michelson

The use of a Michelson interferometer will require a time-domain readout to estimate the cross-correlation function. Ground-noise and other frequency-dependent noise sources and correlations will be present and the model will ultimately be tested from a cross-spectrum rather than than cross-correlation. The next chapter will explain in detail how a single time-series allows both an integration in time and frequency to enhance the search for noise. For the sake of completion, the autocorrelation function will be presented in the power-spectrum language used for the remainder of this text.

First, the units and conventions should be made apparent. The sensitivity of a Michelson is typically referred to differential motion at the endmirrors, $L_\delta = L_1 - L_2$. Michelson instruments are typically used for sensitivity to real physical motion in the environment. The apparent motion of the beamsplitter world-line is indeed very different, and the use of the optical phase to generate the autocorrelation allows a direct conversion back to the units that the data systems and calibration-scheme were built to use.

The conversion is $\Delta\theta = \frac{2\pi}{\lambda} \cdot 2\Delta L_\delta$. The additional factor of two expresses that physical arm length in a Michelson requires two traversals of the optical beam. It is accounted fully in the following chapter. The phase autocorrelation function then is:

$$\Xi_\delta(\tau) = \left(\frac{\lambda}{4\pi}\right)^2 \langle \Delta\check{\theta}_\delta(t)\Delta\check{\theta}_\delta(t-\tau)\rangle \tag{1.13}$$

$$= \frac{l_{\mathrm{p}}}{4\sqrt{4\pi}} \begin{cases} 2R_{\mathrm{sys}} - c\,|\tau| & : \text{ where } c\,|\tau| < 2R_{\mathrm{sys}} \\ 0 & : \text{ else} \end{cases} \tag{1.14}$$

Finally this must be expressed as the *one-sided* power-spectral density to be commensurate with the calibrated data from the experimental analysis. The one-sided density is

denoted using a sub or superscript of $(+)$[4], and for the Holographic correlation function it generates the power-spectral-density:

$$\mathrm{PSD}_{(+)}\{\Xi_\delta(\tau);F\} = \begin{cases} 2\mathscr{F}\{\Xi_\delta(\tau);F\} & : \text{ where } F>0 \\ \mathscr{F}\{\Xi_\delta(\tau);F\} & : \text{ where } F=0 \\ 0 & : \text{ where } F<0 \end{cases} \tag{1.15}$$

$$\Xi_\delta^{(+)}(F) = \frac{t_\mathrm{p} R_\mathrm{sys}^2}{\sqrt{\pi}} \cdot \frac{\sin^2(\pi T_\mathrm{rt} F)}{(\pi T_\mathrm{rt} F)^2} \text{ where } F>0 \tag{1.16}$$

$$T_\mathrm{rt} = \frac{2R_\mathrm{sys}}{c} \tag{1.17}$$

Where $\mathscr{F}$ denotes the Fourier transform operation. The data analysis does not use the $F=0$ bin, so that special case is ignored. In the small F limit, the $\frac{\sin(x)}{x}$ term becomes one and the spectral density value becomes

$$\Xi_\delta^{(+)}(T_\mathrm{rt}F \ll 1) \approx \quad 4.86{\cdot}10^{-41}\frac{\mathrm{m}^2}{\mathrm{Hz}} \cdot \left(\frac{R_\mathrm{sys}}{40\mathrm{m}}\right)^2 \tag{1.18}$$

$$\approx \left(6.98{\cdot}10^{-21}\frac{\mathrm{m}}{\sqrt{\mathrm{Hz}}} \cdot \frac{R_\mathrm{sys}}{40\mathrm{m}}\right)^2 \tag{1.19}$$

4. The two sided power-spectral density uses the notation $(\pm)$

Chapter 2

BROADBAND-NOISE DETECTION BY OPTICAL INTERFEROMETRY

The optical interferometer converts geometric properties of the device - such as mirror locations - into modulations of light power. To do this, the geometry defines boundary conditions of the optical fields, imprinting into the phase of the light. The phase imprint then affects constructive or destructive interference, modulating the rate of photons incident on a detector. The Holometer uses this sensitivity to detect geometric-noise as fluctuations in the counting rate of photons.

This method of measurement for the experiment has two major difficulties. The first is that the signal to be detected is not a known modulation providing a reference template to weight the photon-counting at each moment in time. Instead the signal is itself a broadband noise. The second difficulty is that the counting-rate of photons itself fluctuates from Poisson statistics. Such counting-rate statistics are referred in this document as shot-noise. The experiment must have a particular design to detect one noise inside of another, and this chapter addresses how photon counting between separate instruments, each with shotnoise, can detect a much smaller underlying noise with a meaningful physical amplitude.

The apparent answer would seem to be "just multiply and average," to generate a statistic that mimics the two-point time-domain correlation function postulated by the theory. Averaging should generally "reduce the noise" that isn't shared between the instruments. The challenge in this concept comes in defining what an average means for continuous, white Poisson noise and in defining the scale for the number of measurements in that average.

The chapter answers these questions, relating them to the standard detection limit quoted for Michelson Interferometers, $\langle \Delta\theta^2 \rangle \langle \Delta N^2 \rangle \geq 1$, and determining how to precisely state the rate that measurement error is reduced for broadband detections. It starts discussing the meaning behind the standard limit then derives the Michelson length-to-phase conversion.

From there, statistics are built for the detection of signals within the photon shot noise limit. The standard quantum limit applies to detecting a background signal in a single interferometer against a *known* reference, unlike the 2 machine cross-correlation layout for this experiment. The Holometer case is treated rigorously at the end using the statistical machinery built through the chapter.

2.1 The Standard Quantum Limit For Michelson phase detection

The subject of sensitivity bounds in interferometers has been well-studied theoretically from both semiclassical and fully quantum mechanical perspectives. The subject of gravitational-wave astronomy has be a strong motivation for improvements to these limits, and new interferometry techniques attempt to circumvent the "Fundamental" bounds set by these papers. A select set of papers covering these limits includes

- A direct calculation for a multi-bounce Michelson, including the possibility of quantum-state squeezing and radiation-pressure noise on mirrors [3].
- A symmetry motivated calculation expressing interferometers by their Lie-group action transforming $|\text{in}\rangle$ photon states to $|\text{out}\rangle$ [14].
- A review of the phase-sensitivity of generic two-mode interferometers such as the optical Michelson [10]

The literature on experimental limits often expresses sensitivity bounds and terms without strictly defining the type of detection being made. The statistics of the rest of the chapter investigate what constitutes a template and what sets apart the detection of spectrally-incoherent noise predicted for the Holometer. In the context of templates provided later, the noise term referenced as this limit indicates the sensitivity of a *single, real* template test. For instance the matched-template searches for gravitational waves in LIGO are time-resolved

and therefore any "event" in LIGO's terms corresponds to a template match with statistical significance over the noise.

2.1.1 Phase sensitivity of a two-mode interferometer

A two mode interferometer is a system with two-inputs, two-intermediate states and two outputs. A Michelson as typically presented appears to have only a single input and output, however Faraday-rotators can allow light to be inserted into the "output" or "antisymmetric" ports or a detector placed at the "input" port. In fact, the second input port is essential for exceeding the coherent-state bounds. *Any* state prepared that injects only standard vacuum into the second port is destined to be constrained by the coherent-state limit [14].

The papers listed above are careful to consider the detector bounds for phase-sensitivity rather than as the "standard quantum limit" of phase sensitivity, which will be covered later in this section. The coherent-state limit (without squeezing or other preparation) of two-mode interferometers is:

$$\langle \Delta\theta^2 \rangle \langle \Delta N^2 \rangle \geq 1 \tag{2.1}$$

Where the N is the photon-number of the *total* input power. For the single-input Michelson this is the power incident on the beamsplitter from the input port. The θ term is the phase-difference accumulated in the light-modes of both arms $\theta = 2\pi \frac{2(L_1 - L_2)}{\lambda}$. The phase-difference conversion to length is derived in the following section. For a Michelson, the standard sensitivity limit can be expressed against the RMS differential length modulation,

L_δ as:

$$L_\delta = L_1 - L_2 = \frac{\lambda}{4\pi}\theta \tag{2.2}$$

$$\text{using } N = \frac{t_{\text{lock-in}} \cdot P_{\text{in}}}{E_\lambda} \text{ implies}$$

$$\sqrt{\langle \Delta L_\delta^2 \rangle} \geq \frac{\lambda}{4\pi}\sqrt{\frac{E_\lambda}{t_{\text{lock-in}} \cdot P_{\text{in}}}} \text{ in RMS distance [m]} \tag{2.3}$$

$$\text{whereas using } N = \frac{P_{\text{in}}}{E_\lambda} \text{implies}$$

$$\sqrt{\langle \Delta L_\delta^2 \rangle} \geq \frac{\lambda}{4\pi}\sqrt{\frac{E_\lambda}{P_{\text{in}}}} \text{ in RMS spectral-density } \left[\frac{\text{m}}{\sqrt{\text{Hz}}}\right] \tag{2.4}$$

And the limits in both sets of units are the same as the coherent and broadband examples will be examined in this chapter, and *only* reflect a single-template search, such as a single-photon, photons collected over an interval or photons collected with a weight defined at each moment in time.

2.1.2 Standard Quantum Limit

There are some difficulties in defining the phase operator for quantum states as phase is inherently time-dependent. The typical expression is from Dirac [13]. For a single-frequency optical state, the lowering operator $\check{a}$ can be decomposed into the phase and number operator using the form from Dirac.

$$\check{a} = e^{\mathrm{i}\check{\Phi}}\check{n}^{\frac{1}{2}} \tag{2.5}$$

Which leads the number-phase commutator and consequent uncertainty relation.

$$[\check{\Phi}, \check{n}] = -\mathrm{i} \tag{2.6}$$

$$\left\langle \check{\Phi}^2 \right\rangle^{\frac{1}{2}} \left\langle \check{n}^2 \right\rangle^{\frac{1}{2}} \geq \frac{1}{2} \tag{2.7}$$

There are multiple issues related to the phase operator and setting quantum limits using it, but the basic principles are sound and the issues are discussed in the following literature

- Comparisons amongst operator definitions: Dirac phase, Louisell phase, Susskind-Glogower phase, and the Pegg-Barnett phase [8].
- Uncertainty principles for time-resolved optical fields, where the DC average is the degenerate case of two sideband-modes collapsing into one [4][12].
- Decoherence and demolition of states through repeated measurement [5].
- Linear canonical transformation of phase-space, quadrature operators [6].

The standard quantum limit (SQL) as presented does not reflect the measurement limit in two-mode systems by an exact factor-of-two. The standard quantum limit suffers an even worse lack of a fundamental associated measurement defined for it. Figure 2.1 on the following page shows how two perfect phase sensors replicate the Michelson differential measurement. This setup actually requires two applications of the SQL, one for each detector. For a beamsplitter reflecting only a fraction x of light *power*, the limits work out to be (in spectral-density units):

$$\left\langle \Delta\check{\Phi}_1^2 \right\rangle \geq \frac{1}{4\left\langle \Delta\check{n}_1^2 \right\rangle} = \frac{E_\lambda}{4xP_{\text{in}}} \tag{2.8}$$

$$\left\langle \Delta\check{\Phi}_2^2 \right\rangle \geq \frac{1}{4\left\langle \Delta\check{n}_2^2 \right\rangle} = \frac{E_\lambda}{4(1-x)P_{\text{in}}} \tag{2.9}$$

$$\left\langle \check{\Phi}_\delta^2 \right\rangle = \left\langle \Delta\check{\Phi}_1^2 \right\rangle + \left\langle \Delta\check{\Phi}_2^2 \right\rangle \tag{2.10}$$

$$\geq \frac{E_\lambda}{4x(1-x)P_{\text{in}}} \geq \frac{E_\lambda}{P_{\text{in}}} \tag{2.11}$$

With the final limit saturated only for a 50-50 beamsplitter. This equality indicates that the Michelson isn't making a phase detection in the manner of the SQL, but is fundamentally unable to saturate that limit because a single phase detection is not useful at optical

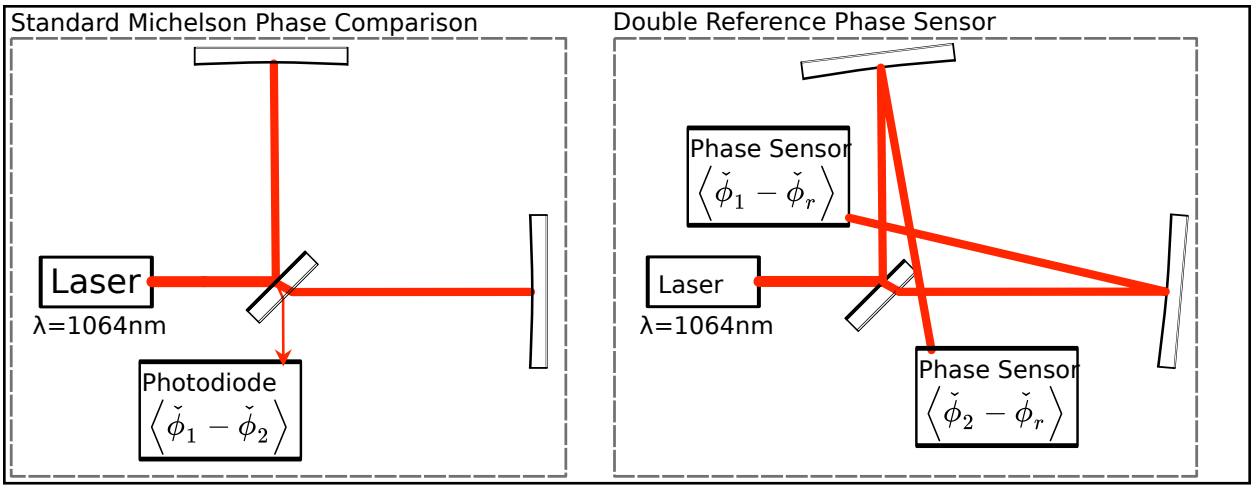

Figure 2.1: Fundamental phase measurement in the Michelson. The destructive interference refers one arm vs. another. Alternatively, the Michelson can be viewed as a pair of perfect phase measurements relative to an ideal reference phase (that adds no noise). In this case there are two separate measurements. The difference of the two referenced phase measurements restores the original Michelson sensor, but framed as ideal quantum phase measurements.

frequencies. Rather the Michelson makes two destructive measurements on a power-split beam.

All of these limits have held the caveat that they work for template searches. The picture is different for broadband source detection, where the signal can be resolved across many templates and the average improves the measurement up to saturating some limit on the number of independent templates. That limit is the time-bandwidth product, the definition of which is degenerate with many factors when the source noise or background noise are not spectrally-flat (white-noise). If the product is defined appropriately, the sensitivity bounds in the literature are again applicable with the N representing the total number of templates searched; however, the searches still only apply to interferometer measurements where the signal can be "locked-in" or made as a phase-sensitive homodyne detection.

The statistics developed in this chapter first model their detections from homodyne lock-in to related to the SQL, but the Holometer can not use those techniques. The detection of a

new fundamental source of noise must instead used techniques not perfectly reflective of the two-mode interferometer limits. The primary consequence of this is that the time-bandwidth scaling law to detect noise of a given spectral-density will scale as $\left(\Delta T_{\text{span}} \Delta F_{\text{span}}\right)^{-1/4}$ rather than the usual square-root. On one hand the scaling law is very unfavorable, on the other the large frequency-bandwidth provides many more measurements than single templates. The chapter culminates in developing the test-statistic used for the experiment and deriving the expected sensitivity to compare against the results of later chapters.

2.2 Light-field propagation, phase-modulation, and interference

The mechanics of interferometer length sensitivity starts at the phase-shifts associated with propagation in free-space. For this, plane-waves of light are assumed. Extensions into modes of the paraxial approximation can be treated later as perturbations of the plane-wave case. Given a steady-state wave passing first through point z_1 and to point z_2 over a distance $L = z_2 - z_1$. The light field can be written *at equal time* in the lab-frame as:

$$A(t, z) = Ae^{2\pi \mathrm{i} F(t - z/c) + \phi} \tag{2.12}$$

This is depicted in fig. 2.3 on page 27. Note the negative sign on the z-position argument. This negative sign is important later when solving for steady-state amplitudes of an interacting system. The sign is ultimately a matter of convention in defining a forward mode from the $\vec{E}$ and $\vec{H}$ fields with positive Poynting vector. The equation represents a steadily maintained wave at a given point advancing in phase with time. Along the null surface outward it is instead constant in phase, and for positive (forward) spacelike-separation, it lags in phase. Here the optical field is given in the units and conventions for port-amplitude in an optical scattering-network.

The units of the *optical field*, $A(t, z)$ in the port-amplitude description are in the un-

conventional units of $\sqrt{\text{Watts}}$. This is in contrast to the usual description for optical fields requiring phasors of the electric and magnetic fields, $E(t,z)$ and $\vec{H}(t,z)$. The usual complex phasors must have their imaginary-part dropped for the description of physical quantities as the physical field-observables are purely real. This causes difficulties for building scattering matrices between forward and reverse travelling waves, as the imaginary component represents different conventions for the forward and reverse waves in the phasor picture. The distinction between the conventions of field-port scattering units and electric-field phasors is explored in section A.1.1 on page 234. With the exception of the root-Watts vs. field-units, the concepts of phasors and port-amplitudes are usually safely conflated.

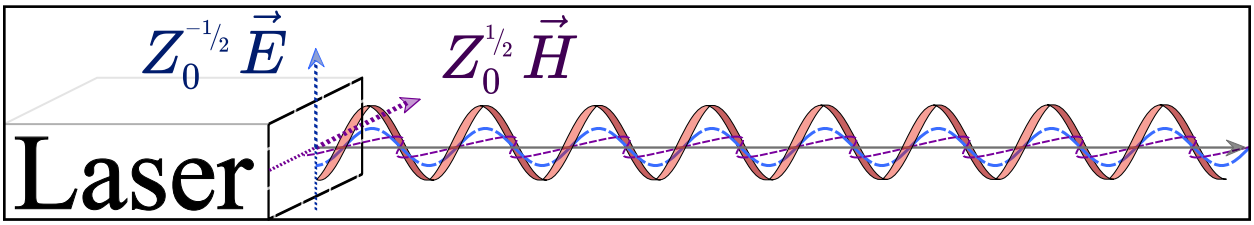

Figure 2.2: Diagram indicating the equal-time layout of a steady-state optical-field phasor. The spiral shape is actually not indicative of the physical $\vec{E}$ or $\vec{B}$ fields. Its physical significance can be attributed to the phase of the scattering amplitude or phasor, but it is really the phase of the two quadratures of the quantum-mechanical fields.

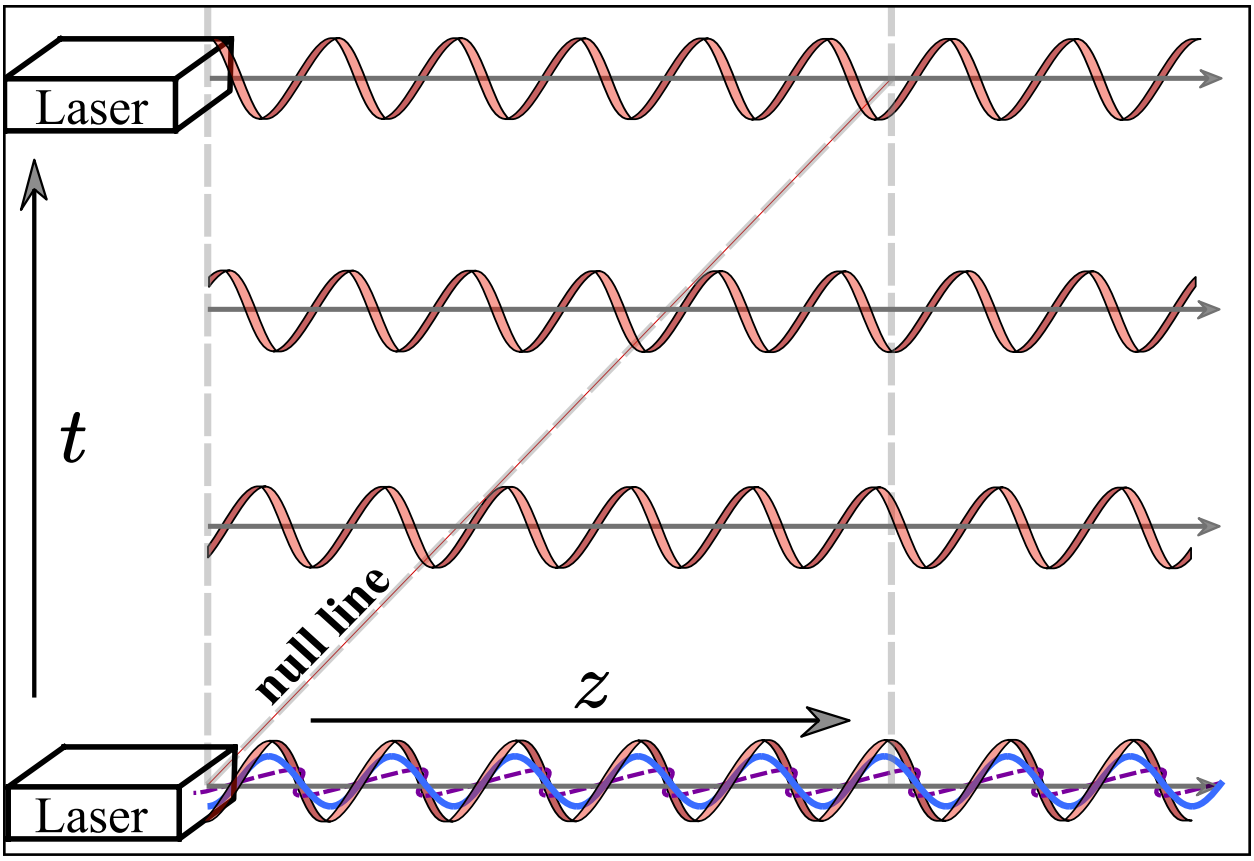

Figure 2.3: Space-time diagram indicating the propagation of an optical-field phasor. The propagation by the wave-equation carries equal-phase to points lying on the null-line. This advances phase with time, but retards phase for points in the direction of propagation.

2.3 Mirror displacement as phase-modulation

The relation of eq. (2.12) on page 25 provides a linear coupling coefficient between the amplitudes at the points z_1 and z_2. This coefficient can be placed in a scattering network shown such as the simple linear signal-flow-graph of fig. 2.4 on the following page. On top of the separation distance $L = z_2 - z_1$, a variation is applied, L_Δ. The coupling coefficients corresponding to propagation show the effect of this variation. The change to the output field with respect to the variation can be described as a phase shift with respect to the nominal output field. The fields of a Michelson interferometer wield this phase-shift to detect length. The second pass of light through the beamsplitter differences the fields

towards the asymmetric port (AS). The subtraction is influenced by the relative phase of the two returning beams. Propagating all of the terms in the signal-flow of fig. 2.5 on page 30 to the interferometer-output and setting the transmission and reflection field coefficients of the beamsplitter to $\frac{1}{\sqrt{2}}$ gives.

$$A_{\mathrm{AS}} = \frac{1}{2} e^{4\pi \mathrm{i} F \frac{L_C}{c}} \left(e^{2\pi \mathrm{i} F \frac{L_\Delta}{c}} - e^{-2\pi \mathrm{i} F \frac{L_\Delta}{c}} \right) A_{\mathrm{source}}(t) \tag{2.13}$$

$$P_{\mathrm{AS}} = |A_{\mathrm{AS}}|^2 = \sin^2 \left(2\pi F \frac{L_\Delta}{c} \right) P_{\mathrm{in}} \tag{2.14}$$

Now setting the operating point L_Δ for a nominal power (in fraction of the power on the

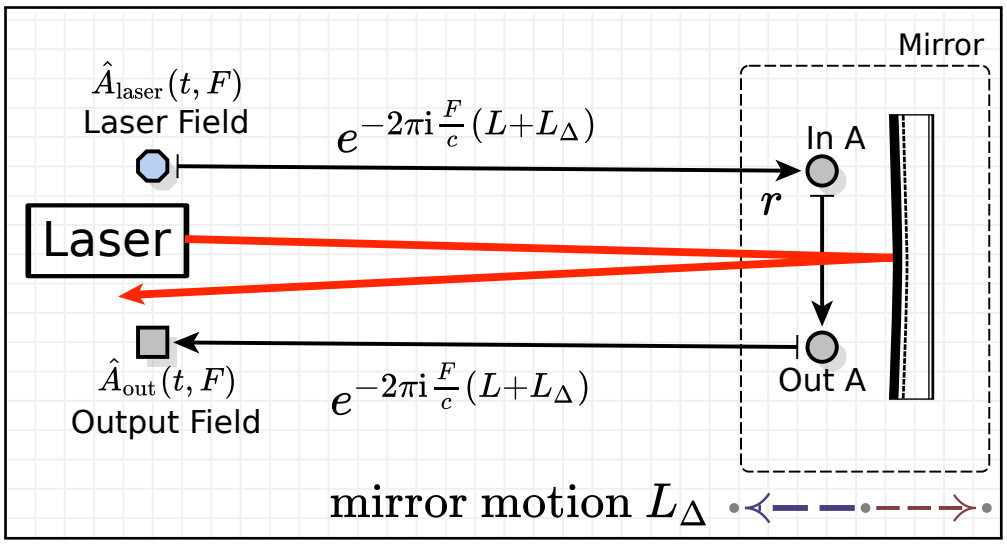

Figure 2.4: Signal flow for phase-effects of a moving mirror. The nodes represent the port-amplitude of the steady-state system. The incoming beam, $\hat{A}_{\mathrm{laser}}$, picks up the gain and phase along the flow-lines to each port. It starts with an advance term from path propagation, then picks up the reflection coefficient of the mirror (using little-r for the field coefficient, not the usual R coefficient for power transfer), then the reflected beam propagates back and gathers more advance. The phase advance is because nodes further along the beam are actually *earlier* in time compared to the beam that is propagating into them.

beamsplitter, xP_{in}, but without choosing a sign) and applying a modulation to move the

mirrors an amplitude of L_δ, the modulation term can be picked out of the power-detector.

$$x = \sin^2\left(2\pi F \frac{L_\Delta}{c}\right) \tag{2.15}$$

$$P_{\mathrm{AS}}\left(L_\Delta + L_\delta \cos(2\pi F_{\mathrm{mod}} t)\right) = \left(x \pm \sqrt{x(1-x)}\frac{4\pi F L_\delta}{c}\cos(2\pi F_{\mathrm{mod}} t)\right) P_{\mathrm{in}} \tag{2.16}$$

Taking the Fourier transform or using a mixer to pick out the modulation applies another factor of two to express the modulated photopower in units of RMS. This RMS photopower (convertible to photocurrent) locked into the modulation frequency is:

$$P_{\mathrm{AS@}F_{\mathrm{mod}}} = \sqrt{x(1-x)}\frac{2\pi F L_\delta}{c} P_{\mathrm{in}} \tag{2.17}$$

This photopower, compared against the Poisson-statistics of counting photons, sets the sensitivity of the Michelson to length variations. To relate to the standard limit of interferometers, it is still necessary to define a scale constituting a "single measurement" against Poisson statistics. Before diving further into those definitions, a peculiarity of this technique should be addressed. In the expression of eq. (2.16), the time-dependence of the power modulation carries no phase delay from the interferometer length. The calculation thus far indicates that the modulation does not have any dependence on the modulation frequency, yet any signal carried as a modulation must be delayed at least by the light-travel time. Note that the variation in the parameter of length is a manifestly non-local operation. The lack of simultaneity of separated points indicates that length variation is not well-defined. In effect the variation, as it is applied at the end of the analysis and expressed as power, can only rigorously refer to the *DC sensitivity* of the instrument. The largest arm-length sets the time-scale. The feedback-networks of the Holometer use resonant enhancement that adds additional scale-dependences to the response, so a more rigorous model of the interferometer signal model must be developed.

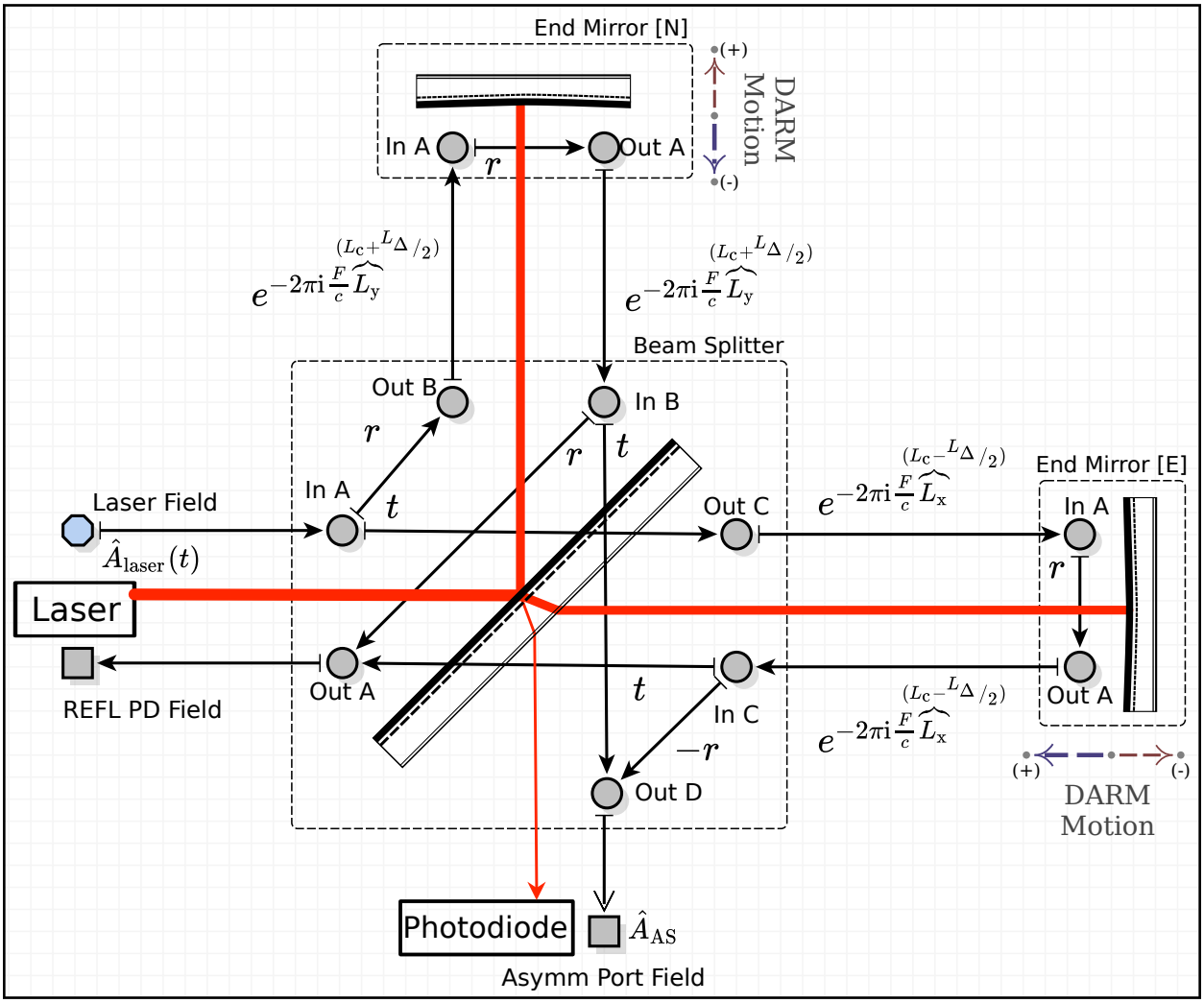

Figure 2.5: Signal flow for the basic length to phase sensitivity of a Michelson interferometer. The X and Y arm lengths may be decomposed into common and differential lengths. The beam is split at the In-A port to undergo the transmission and reflection through the beam-splitter. Each arm acts as in fig. 2.4 on page 28 and the beams are ejected from the two ports. The unitarity of the beamsplitter scattering matrix in this convention applies a negative sign to the In-C to Out-D element of the beamsplitter (reflection through the dashed-line). This sign makes the Out D port the asymmetric port and Out-A the symmetric port.

2.4 Phase sidebands

The absence of the physical delay is solved with a stronger, more "local" modeling effort. The issue arises because the length parameter is being modulated, but the motion is actually at the boundary defined by the mirror. Boundary motion on a reflecting wave causes a Doppler shift in the frequency. This frequency shift then applies the necessary phasing of the modulation signal to recover the expected phase interference of the Michelson. To emphasize, the description of the light in terms of modal field amplitudes (or phasors) is only a *representation* of the underlying wave-equations, and the scattering picture is an approximation that can only attempt to maintain consistency. Nevertheless, the Doppler shift informs the next iteration of the mirror-motion modelling. The light field of the outgoing wave from a mirror is treated as a function of the motion as well as the incoming beam. Assuming small displacements, this is a local operation of the incoming beam at time t affecting the conversion to the output beam at $t + dt$.

Let the beam field incoming to the mirror be $A_{\mathrm{in}}(t) = e^{2\pi \mathrm{i} F t} = e^{2\pi \mathrm{i} \int_{t_0}^{t} F dt}$. Let the mirror displacement be positive in the direction of the *incoming* beam and denoted as $z(t)$ and denote the unitless velocity $\beta = c^{-1} \frac{dz}{dt}$. The time-resolved field of the outgoing beam with Doppler-shift is

$$A_{\mathrm{out}}(t) = e^{2\pi \mathrm{i} \int_{t_0}^{t} F \frac{1+\beta}{1-\beta} dt'} \tag{2.18}$$

The numerator of the Doppler term contains the velocity of the wave receiver, and the denominator the source - each relative to the medium (in this case the mirror). More-rigorously the mirror isn't particularly representative of a medium. The Doppler term should be split into two separate applications, the wave field as seen by the surface of the mirror (only containing a nonzero β for the receiver term) and then the field as seen from an observer of the wave re-emitted from the surface (containing only the source β term). As

given, both effects are combined to indicates both source and receiver velocity with respect to the noninertial mirror frame. For the usual case of nonrelativistic modulation and a drive of $z(t) = L_\Delta \cos(2\pi F_{\text{mod}} t)$ the effects can be linearized and integrated.

$$A_{\text{out}}(t) \approx e^{2\pi \mathrm{i} \int_{t_0}^{t} F(1+2\frac{z'}{c})dt'} \tag{2.19}$$

$$= e^{2\pi \mathrm{i} F\left(t+\frac{2L_\Delta}{c}\cos(2\pi F_{\text{mod}} t)\right)} \tag{2.20}$$

Note that this form looks just like the variation fig. 2.4 on page 28 where $L_\Delta = L_\Delta \cos(2\pi F_{\text{mod}} t)$ and the propagation length, L is taken to zero. This confirms that the phase-shift is being handled correctly, having the same form in a length-changing picture as a moving boundary with Doppler-effect, although now the phase shift can be traced to a point. The resolution of the final phasing error then comes in the methodology for propagating the beam *after* the mirror/phase modulation. The description of section 2.2 on page 25 is only able propagate fields of constant frequency between points. The time-dependence is implicitly violating this requirement. To account for this, the expressions are simplified with the additional assumption that the phase-shift magnitudes ($2FL_\Delta \ll c$). Under this assumption the exponential can be linearized and modulation-term expanded into exponentials.

$$A_{\text{out}}(t) = e^{2\pi \mathrm{i} F t} + \frac{\mathrm{i}2\pi F L_\Delta}{c} e^{2\pi \mathrm{i}(F+F_{\text{mod}})t} + \frac{\mathrm{i}2\pi F L_\Delta}{c} e^{2\pi \mathrm{i}(F-F_{\text{mod}})t} \tag{2.21}$$

Superposition is again applicable to these additional frequencies, recovering the use of linear scattering techniques (signal-flow graphs). Figure 2.6 on the next page displays this linear-multifrequency formulation.

This approximation works very well for the typical case of small modulations, but will require always dropping factors of L_Δ^2 in power calculations as it does not account for the field strength that is extracted from the carrier. To include the terms for nonlinear large-modulation effects, the Jacobi-Anger expansion of the trig-exponential into Bessel-functions

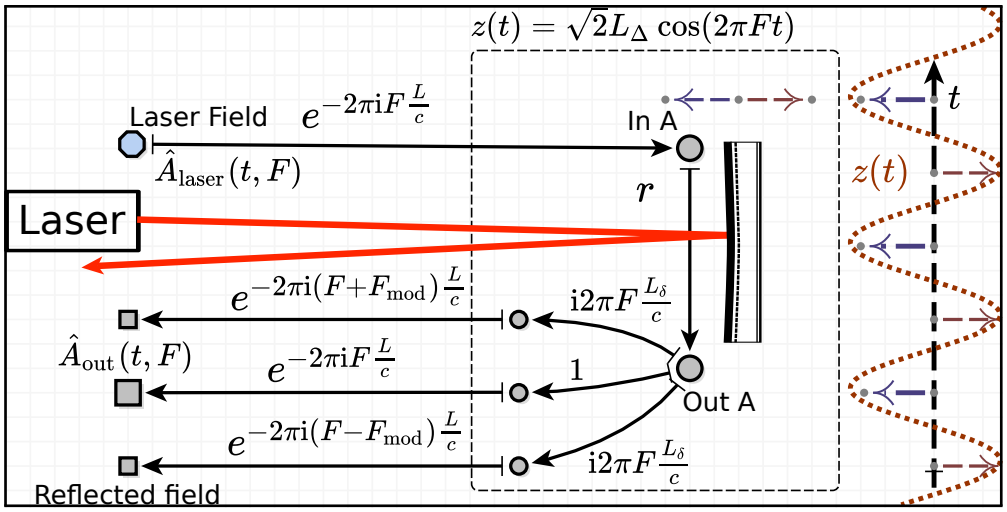

Figure 2.6: Full signal flow sideband effects of a modulated mirror motion. The oscillating mirror pushes carrier field into the sidebands, with a phase-modulation amplitude proportional to the modulation strength and carrier frequency. For optical beams the frequency term is extremely large and this term may be simplified: $\frac{F L_\Delta}{c} = \frac{L_\Delta}{\lambda}$.

must be used.

2.5 Frequency-dependence of the Michelson Transfer function

The original model of the Michelson phase sensitivity did not account for time-delay effects of the optical system propagating information about the endmirror position. This model was otherwise correct and predicted that aside from that delay, there is no frequency-dependence to the magnitude. The delay could be added to the model ad-hoc, but the full derivation of the Michelson is included here to show how the optical model must be extended with multiple-frequencies and sidebands to express its physics. While no new information is provided by this derivation compared to an ad-hoc extension, the methodology behind it is very important for the system modelled under the additional geometry of power-recycling.

Figure 2.7 on page 40 displays the scattering layout of a mirror-modulated Michelson accounting for phase-sidebands. The power detection for this system must be carried out including terms from all of the frequencies indicated from the fields at the AS port. The full time-domain calculation can be referenced at section A.1.2 on page 238, but the final result for the photodiode power is:

$$P_{\mathrm{AS}}(t) = |A_{\mathrm{AS}}|^2 \tag{2.22}$$

$$\begin{aligned} &\approx \overbrace{\sin\left(2\pi F\tfrac{L_\Delta}{c}\right)}^{\sqrt{x}}\left(\overbrace{\sin\left(2\pi F\tfrac{L_\Delta}{c}\right)}^{\sqrt{x}}\right. \\ &\quad \left. - \underbrace{\cos\left(2\pi F\tfrac{L_\Delta}{c}\right)}_{\sqrt{1-x}}\frac{4\pi F L_\delta}{c}\cos\left(2\pi F_{\mathrm{mod}}\tfrac{L_\Delta}{c}\right)\cos\left(2\pi F_{\mathrm{mod}}(\tfrac{L_C}{c}+t)\right)\right)P_{\mathrm{in}} \end{aligned} \tag{2.23}$$

A final approximation for the photopower in eq. (2.23) is to drop all L_δ^2 terms. They could be included, but only if fewer approximations are made earlier in the phase-sideband expansion (one must break out the books on Bessel-functions). The $\sin(2\pi F\frac{L_\Delta}{c})$ terms can be expressed in terms of the fractional power out of the asymmetric port as in the previous

section to become:

$$P_{\mathrm{AS}}(t) = P_{\mathrm{in}}\left(x - \sqrt{x(1-x)}\frac{4\pi F L_\delta}{c}\cos\left(2\pi F_{\mathrm{mod}}(t+\tfrac{L_C}{c})\right)\cos\left(2\pi F_{\mathrm{mod}}\tfrac{L_\Delta}{c}\right)\right) \quad (2.24)$$

This expression contains two correction terms to the DC-Michelson result. The first is that the time is shifted forward by the term $\frac{L_C}{c}$, which properly gives the delay of distant mirror signals carried to the center port. The second is the term $\cos(2\pi F_{\mathrm{mod}}\frac{L_\Delta}{c})$ which is the arm-imbalance term for mirror motion. For an interferometer with arm-lengths balanced to 10 cm, this term is within the cosine quadratic-maximum for mirror-modulation frequencies less than one GHz and the term has no effect on sensitivity. The arm imbalance is known as the Schnupp asymmetry. For the Holometer it does not affect sensitivity but is relevant to the parasitic laser-phase noise coupling to amplitude. Some experiments purposefully imbalance the arms to carry signals through that term.

2.6 Sensitivity of a Michelson Interferometer to coherent differential arm motion

As in eq. (2.17) on page 29 and elaborated in the previous section, the modulating power can be lockin-detected to give the power at the modulation-frequency. The lock-in picks up an additional coefficient of $\frac{1}{2}$on the time-dependent description by integrating a $\cos^2$ to represent result in the RMS-power units. Inserting the carrier frequency from the light wavelength $F = \frac{c}{\lambda}$, The conversion from RMS-length L_δ differential mirror modulation into coherent RMS-power on the photodiode is

$$C_{\frac{[\mathrm{W}]}{[\mathrm{m}]}\mathrm{AS}}(F_{\mathrm{mod}}) = \pm\frac{4\pi}{\lambda}\cdot\sqrt{x(1-x)}\cdot P_{\mathrm{in}}\cdot(e^{2\pi F_{\mathrm{mod}}\frac{L_C}{c}}) \quad (2.25)$$

$$\widetilde{P}_{\mathrm{AS}}(F_{\mathrm{mod}}) = C_{\frac{[\mathrm{W}]}{[\mathrm{m}]}\mathrm{AS}}L_\delta \quad (2.26)$$

Again, x here represents the fraction of power escaping the AS port vs. power on the beamsplitter. The $\pm$ sign is determined by which side of the interference fringe the machine is operating on. If the sin-terms are kept this sign is readily apparent, but in practice only x and its derivative are measurable and the arguments of the sin-term are not.

With the sensitivity of the interferometer from length to photon power well-developed, the comparison to counting rate statistics may finally be made. A set of *reference measurements* are established which meet the standard interferometer limit, $\langle \Delta\theta^2 \rangle \langle \Delta N^2 \rangle \geq 1$. Alternate measurements can then be described in terms of the reference. The setup is described in fig. 2.8 on page 41 is designed to determine the RMS drive magnitude, L_δ, into the interferometer. First, we can consider a known local-oscillator (LO) driving a coherent modulation into the endmirrors. The brackets given indicate an average over the statistical ensemble.

To account for averaging and the statistics of the measurement, all observables must be expressed inside of expectation operators, so the statistics of the inputs variables must be built before evaluating the expression of the outputs. All of these statistical random variables are indexed by time and have no cross-correlation with terms at non-equal time except for a non-zero mean. The hatted $\hat{F}$ and $\hat{\theta}$ do not have statistics given, as they represent the imperfect oscillator driving the measurement. They could have been made constants, however leaving them as random variables enforces that quality estimators should not assume that the oscillator parameters are perfectly known, consequently the estimators are derived from homodyne lock-in to the reference oscillator.

The system variables are all random in nature. The one and two-point correlation functions are given in order to generate statistics related to the physical system and calculated the variance on those statistics. The left column provides first moments as one-point correlation

functions, the right column second-moments or two-point correlation functions.

$$\langle \hat{S}_{\mathrm{LO}}(t)\rangle = \sqrt{2}\,\mathrm{U}\cos(2\pi\hat{F}t+\hat{\theta}) \qquad \langle \hat{S}_{\mathrm{LO}}(t)\hat{S}_{\mathrm{LO}}(t')\rangle = \langle \hat{S}_{\mathrm{LO}}(t)\rangle\langle \hat{S}_{\mathrm{LO}}(t')\rangle \overbrace{+0}^{\text{no excess noise over the power from the coherent mean}} \tag{2.27}$$

$$\langle \hat{N}_{\mathrm{SN}}(t)\rangle = P_{\mathrm{AS}} \qquad \langle \hat{N}_{\mathrm{SN}}(t)\hat{N}_{\mathrm{SN}}(t')\rangle = P_{\mathrm{AS}}E_{\lambda}\delta\big[t-t'\big] + \langle \hat{N}_{\mathrm{SN}}(t)\rangle\langle \hat{N}_{\mathrm{SN}}(t')\rangle \tag{2.28}$$

$$\hat{D}_{\mathrm{ifo}} = C_{[\frac{\mathrm{w}}{\mathrm{m}}]\mathrm{AS}}(F)\frac{L_{\delta}}{\mathrm{U}}\hat{S}_{\mathrm{LO}} + \hat{N}_{\mathrm{SN}} \qquad \langle \hat{N}_{\mathrm{SN}}\hat{S}_{\mathrm{LO}}\rangle = 0 \tag{2.29}$$

The data variable $\hat{D}_{\mathrm{ifo}}$ is assembled as shown in the associated signal flow diagram. The measurement is constructed by integrating the mixer output over time, normalizing by the oscillator strength and calibrating by the interferometer sensitivity. It is noted here that the calibration value is in units of frequency but the statistics so far are expressed in time. The Fourier transform will be related to measurements later and the frequency dependence will find its place in measurement estimators.

The units of these moment-statistics are important and fascinating. Equation (2.27) provides the coefficient U for the first and second moments of a coherent local oscillator, the second moment naturally being the square of the first. In the lab these would be something like volts in a cable, but such units have no physical relevance without further conversion. For this reason the units are marginalized with the coefficient U, which should cancel for any measurement of the Michelson but should remain between any characterization of the local oscillator (LO) coupling to the endmirrors. The factor of $\sqrt{2}$ represents that the local-oscillator has unit-RMS magnitude in the arbitrary coefficient of U.

Equation (2.28) detail the noise-terms. The first moment is zero, but actually carries the units of beam-power-variation-RMS in [Watts]. The second moment should be the square of the first, or [Watts^2] which is beam-power-variation-energy. At first glance however it appears to have the units $\left[\frac{\mathrm{Watts}^2}{\sqrt{\mathrm{Hz}}}\right]$. The role of the delta-function in an integral actually gives it units reciprocal to those of its argument. This restores the correct energy units and motivates how the delta function correlation naturally implies a broadband spectral-density.

The variable $\hat{D}_{\mathrm{ifo}}$ in eq. (2.29) ties these units together. It is in beam-power-variation-

RMS, converting the local oscillator from its arbitrary units to RMS differential arm-length, then converting to RMS-beam-power via the interferometer.

The measurement that we would like to make from these variables is how much RMS-length-variation is present in the instrument from the LO. Solving $\hat{D}_{\text{ifo}}$ into a length-units and normalizing by the LO strength provides an estimator which will given the requested expectation-value.

$$\hat{M} = \frac{\frac{1}{t}\int_0^t \frac{\hat{D}_{\text{ifo}}\hat{S}_{\text{LO}}}{C_{\left[\frac{\text{w}}{\text{m}}\right]\text{AS}}(F)}dt'}{\sqrt{\frac{1}{t}\int_0^t \langle \hat{S}_{\text{LO}}\hat{S}_{\text{LO}}\rangle dt'}} \tag{2.30}$$

Now the measurement implied can be determined from the expectation.

$$\text{E}[\hat{M}] = \langle \hat{M} \rangle = L_\delta \tag{2.31}$$

Again, units are RMS length variation because the lock-in providing the template was also in units of RMS magnitude. Evaluating the middle expectation requires using the linearity of both the integrals and the expectation operators to move the expectations fully inside of the integrals, expanding to terms that may be replaced with the system-statistics of equations (2.27 - 2.29). The integrals should alias the $\cos^2$ term in the integral, but the statistical uncertainty of $\hat{F}$ and $\hat{\phi}$ and the long-integration limit drop the edge-terms and base the expectation solely on the average of $\cos^2$.

The noise-terms begin to show in the higher-order statistics, where the variance of the

estimator has a grand cancellation of the signal terms, but the noise terms remain.

$$\textsc{Var}[\hat{M}] = \mathrm{E}\Big[(\hat{M} - \mathrm{E}[\hat{M}])^2\Big] = \langle \hat{M}^2 \rangle - \langle \hat{M} \rangle^2 \tag{2.32}$$

$$= t^{-1} \frac{P_{\mathrm{AS}} E_\lambda}{|C_{\frac{\mathrm{[w]}}{\mathrm{[m]}}\mathrm{AS}}(F)|} \tag{2.33}$$

$$\sigma[\hat{M}] = \frac{\lambda}{4\pi} \sqrt{\frac{E_\lambda}{t P_{\mathrm{BS}}(1-x)}} \tag{2.34}$$

This sensitivity calculation includes some features to note. First is that the operating point x denoting the AS-coupling factor drops out in the small-x limit. The second is that this representation appears to exactly recover the $\langle \Delta\theta^2 \rangle \langle \Delta N^2 \rangle \geq 1$ limit, where

$$N = t P_{\mathrm{in}} \tag{2.35}$$

$$\Delta N = \sqrt{\frac{1}{N}} \tag{2.36}$$

The caveat is that the L_δ must be in **RMS** power units. At least for the author, length variation is much more naturally expressed in amplitude rather than RMS. The following sections express the problem to search for more general broadband mirror motions. Under the reduced assumptions of broadband searches, RMS will the natural convention for analytical reasons to be explained.

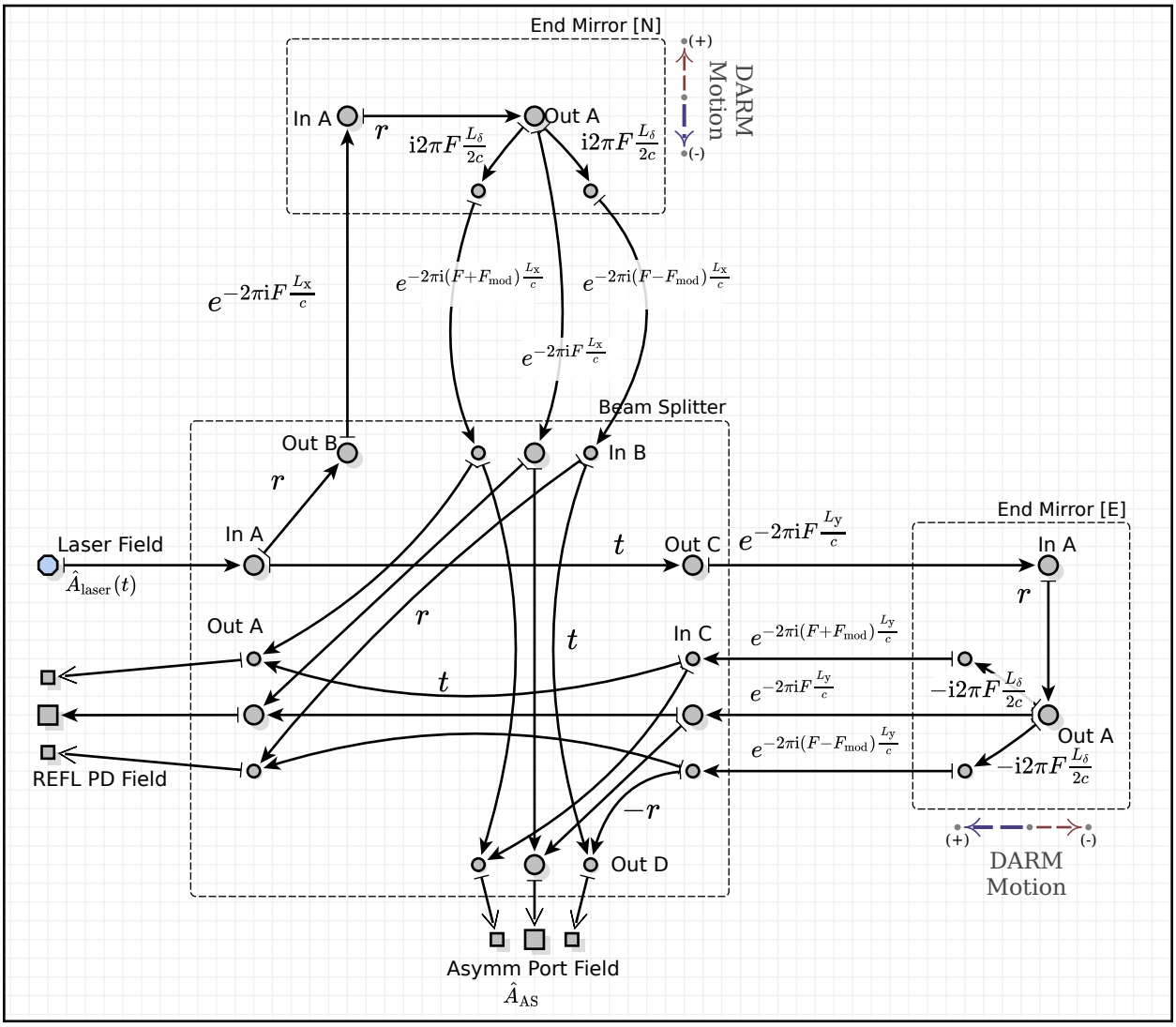

Figure 2.7: Full signal flow phase-effects of a modulated mirror motion. Note that the sideband generation does not depend on the DC length offset, L_Δ, but only the drive magnitude. In this setup the sidebands are immediately ejected and will beat with the carrier fields at the asymmetric and REFL (symmetric) ports.

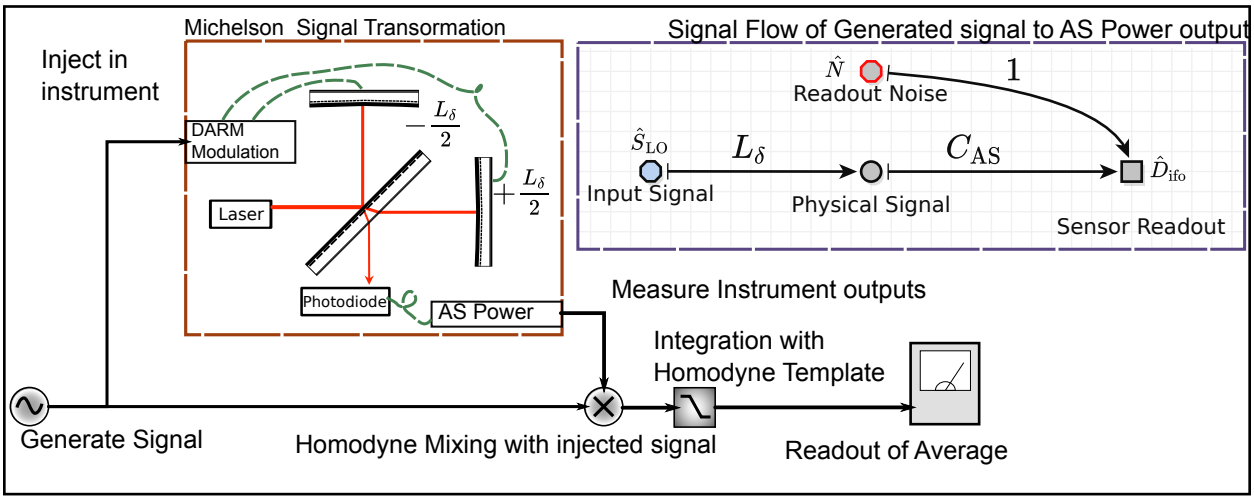

Figure 2.8: Reference measurement for a Michelson differential length sensor coherent detection of drive signal. The signal is measured in the instrument against a known source modulation by directly mixing with the modulation. The mixed signal is then integrated. The noise averages away when mixed with the source.

2.7 Broadband Motion Sensitivity of a Michelson Interferometer

This derivation is similar to the previous section, the difference is the statistics of the input signal. The "local oscillator" in this case is an incoherent signal. Instead of being derived from as oscillator, it can be thought of as a modulation with a noise-free reference channel providing a template. The layout in this section is yet to be representative of the Holometer, as the Holographic noise is not provided by any noise-free signal channel.

$$\langle \hat{S}_{\text{exc}}(t) \rangle = 0 \qquad \langle \hat{S}_{\text{exc}}(t) \hat{S}_{\text{exc}}(t') \rangle = \text{U}^2 A^2 \delta\big[t - t'\big] + \langle \hat{S}_{\text{exc}}(t) \rangle \langle \hat{S}_{\text{exc}}(t') \rangle \tag{2.37}$$

$$\langle \hat{N}_{\text{SN}}(t) \rangle = 0 \qquad \langle \hat{N}_{\text{SN}}(t) \hat{N}_{\text{SN}}(t') \rangle = P_{\text{AS}} E_\lambda \delta\big[t - t'\big] + \langle \hat{N}_{\text{SN}}(t) \hat{N}_{\text{SN}}(t') \rangle \tag{2.38}$$

$$\langle \hat{N}_{\text{SN}} \hat{S}_{\text{exc}} \rangle = 0 \tag{2.39}$$

$$\hat{D}_{\text{ifo}} = C_{\left[\frac{\text{W}}{\text{m}}\right]\text{AS}}(F) \frac{L_\delta}{\text{U}} \hat{S}_{\text{exc}} + \hat{N}_{\text{SN}} \tag{2.40}$$

The units of these altered noise terms are again important. The marginalized units expressed by "U" for the modulation are still present, but accompanied by an excitation amplitude A in $\frac{1}{\sqrt{\text{Hz}}}$. The excitation amplitude matches with the delta function to put the overall units of $\hat{S}_{\text{exc}}$ purely in U. The first estimator to investigate is equivalent to the previous section."

$$\hat{M}(\tau) = \frac{\frac{1}{t} \int_0^t \frac{\hat{D}_{\text{ifo}}(t') \hat{S}_{\text{exc}}(t' - \tau)}{C_{\left[\frac{\text{W}}{\text{m}}\right]\text{AS}}(F)} dt'}{\sqrt{\frac{1}{t} \int_0^t \langle \hat{S}_{\text{exc}} \hat{S}_{\text{exc}} \rangle dt'}} \tag{2.41}$$

But now it is challenging to express the convention of length-variation represented by this estimator. The length must be expressed in units of $\sqrt{\frac{1}{t} \int_0^t \langle \hat{S}_{\text{exc}} \hat{S}_{\text{exc}} \rangle dt'}$. Which for broadband excitations used in this example does represent RMS-length fluctuations, but the convention is inherently tied to the representation of the excitation itself. For non-white excitations this estimator is not related to the power-spectral-density and Fourier transform

usually defined. Furthermore, should the $\frac{1}{t}$ be present in the denominator expression? It must be for white-noise drive, but what about non-white excitations?

Furthermore, physical data does not arrive as a continuum. It is sampled and each sample represents averaging over some equipment bandwidth. The sampling and averaging process together represent each channel integrating through a series of convolution-kernels, $K_{i+1}(t) = K_i(t - \Delta T)$. The time shift represents the sequence of points from an Analog-to-digital converter.

$$\widehat{\mathrm{ADC}}[\hat{D}_{\mathrm{ifo}}; i] = \int_{-t}^{t} \hat{D}_{\mathrm{ifo}}(t') K_i(t') dt' \tag{2.42}$$

which is equivalently like convolution, using continuous time for the ADC rather than indices

$$\widehat{\mathrm{ADC}}[\hat{D}_{\mathrm{ifo}}; \tau] = \int_{-t}^{t} \hat{D}_{\mathrm{ifo}}(t') K_0(t' - \tau) dt' \tag{2.43}$$

A two-point correlation function takes a weighted collection of samples (the 0-delay correlation would use a single sample), sums each channel independently and then generates a statistic from those sums. Many ADC measurements are collected and apodized/weighted into perhaps an FFT. This is generically expressed through the weights on each sample w_i:

$$\widehat{\mathrm{FFT}}[\hat{D}_{\mathrm{ifo}}; F] = \sum_i w_i \widehat{\mathrm{ADC}}[\hat{D}_{\mathrm{ifo}}; i] \tag{2.44}$$

$$= \int_{-t}^{t} \hat{D}_{\mathrm{ifo}}(t') K_{\mathrm{FFT}}(t') dt' \tag{2.45}$$

$$K_{\mathrm{FFT}}(t) = \sum_i w_i K_i(t) \tag{2.46}$$

This shows that 2-point correlation functions even for sampled data can always be expressed as effective mode-selection kernels. Mode selection provides an avenue to rigorously define measurements involving broadband sources. Constraints of the real-world sampling-

rates, computation time and storage motivate upper and lower bandwidth limits on these mode-selection kernels. Otherwise the choice of mode-templates determines the domain the data or statistics are processed in. If the system noise sources have frequency dependence then Fourier-modes are a natural-choice, except that they are not practical to compute directly. The abstraction of this mode-template formalism allows us to relate Fourier-modes to the modes of a practical computation system. The use of integrals also allows the physical N-point correlation functions to be represented in the Fourier-domain, as long as the templates are integrated in that domain as well. Setting down definitions:

$$K(t) = \lim_{t\to\infty} \int_{-t}^{t} e^{2\pi i t' F} \widetilde{K}(F) dt' \tag{2.47}$$

$$\|K\|_2^2 = \lim_{t\to\infty} \int_{-t}^{t} K^2(t') dt' = \lim_{F\to\infty} \int_{-F}^{F} \widetilde{K}^2(F') dF' \tag{2.48}$$

Where the norm of K in eq. (2.48) holds for either time or frequency domain by Parseval's (or Plancherel's) theorem, and must be finite for a well-formed weight-kernel. The units of these expressions are also interesting. As a weight-function, K itself can be viewed as unitless or just to keep track it can be in "kernel units" [K], however the integral represented by $\|K\|_2^2$ always has the units of $[K^2 s]$ which *includes time*. Keeping these units arbitrary will force expressions later to cancel the K units.

A realizable experiment with bandwidth and computation limits enforces that any valid K have the following analytic properties for some Δt_K and some ΔF_K. The first of which enforces the finite computation requirements by localizing in time. This requirement then implies a finite frequency width. The second requirement enforces a maximum cutoff frequency of the template, allowing for a finite sampling rate or Nyquist-frequency. Both of

these requirements are phrased as analytical limits bounded by a fractional error ϵ.

$$\frac{\int_{-\Delta t_K}^{+\Delta t_K} K^2(t')dt'}{\|K\|_2^2} > 1-\epsilon \qquad (2.49)$$
$$\frac{\int_{-\Delta F_K}^{+\Delta F_K} \widetilde{K}^2(F')dF'}{\|K\|_2^2} > 1-\epsilon$$

The weight-kernel acting on a function inside an integral becomes a linear operator picking out mode K. Essential it transforms from the time or frequency basis, to the single basis vector defined by K. In this case a concise notation for the integration or linear action of K is helpful.

$$K\{\hat{x}\} \approx \int_{-\Delta t_K}^{+\Delta t_K} K(t')\hat{x}(t)dt' \qquad (2.50)$$
$$\approx \int_{-\Delta F_K}^{+\Delta F_K} \widetilde{K}(F')\hat{x}(F)dt' \qquad (2.51)$$

With this notation we can generate an estimator parameterized by the chosen weight function, K which picks out the RMS power in that mode. All of the divisions by the norm $\|K\|_2^2$ cancel all of the K units and represent the "unit length" mode $\frac{|K\rangle}{\|K\|}$.

$$\hat{M}_K = \frac{\|K\|_2^{-2}\, K\Big\{\hat{D}_{\text{ifo}}\Big\}\, K\Big\{\hat{S}_{\text{exc}}\Big\}}{|C_{[\frac{\text{W}}{\text{m}}]\text{AS}}|\sqrt{\|K\|_2^{-2}\left\langle K\Big\{\hat{S}_{\text{exc}}\Big\}\, K\Big\{\hat{S}_{\text{exc}}\Big\}\right\rangle}} \qquad (2.52)$$

This is in contrast to the less-abstract appearing estimator with explicit integrals over time. Each linear kernel-operator in this new estimator is an integral over time. With the normalization-terms, all factors scaling with the kernel-units [K] cancel, however all of the factors of time do not cancel. The numerator has two time-integrations for [s^2] units, but one factor of [s] cancels coming from the $\|K\|_2^2$. The denominator is the same but inside its root, so overall this estimator has the units of $\left([\hat{D}_{\text{ifo}}]\cdot[\frac{1}{\sqrt{\text{Hz}}}] = [\frac{\text{W}}{\sqrt{\text{Hz}}}]\right)$. The fascinating

thing about these units is that they represent the power in the unit-length mode $\frac{|K\rangle}{\|K\|}$, and unit-length for time-modes is $1/\sqrt{\text{Hz}}$.

This estimator acts much like the coherent-line estimator used with a Local Oscillator, but all of the projections include more integrals than the coherent lock-in. The two techniques should ultimately be equivalent, and in the case where the template K is chosen to be a cosine function exactly as long as the integration time, with the exact frequency and phasing as the coherent $\hat{S}_{\text{exc}}$ of eq. (2.27) on page 37 then ($\|K\|_2^{-2} K\Big\{\hat{S}_{\text{exc}}\Big\}|K\rangle = |\hat{S}_{\text{LO}}\rangle$) and the original (more simple) estimator is recovered.

Broadband noise has the concept of being distributed across all Fourier-modes. In this formalism, one can show that white noise actually pushes variance into any mode. The statistics of the estimator for the Michelson are:

$$\text{E}[\hat{M}] = L_\delta A \tag{2.53}$$

$$\text{VAR}[\hat{M}] = 2L_\delta^2 A^2 + \frac{P_{\text{AS}} E_\lambda}{|C_{[\frac{\text{W}}{\text{m}}]\text{AS}}|^2} \tag{2.54}$$

$$= 2L_\delta^2 A^2 + \left(\frac{\lambda}{4\pi}\right)^2 \frac{E_\lambda}{P_{\text{in}}} \tag{2.55}$$

The factor of two coming from the broadband excitation to be detected fall out the four-point correlation function.

$$\text{VAR}\Big[\|K\|_2^{-2} K\Big\{\hat{S}_{\text{exc}}\Big\} K\Big\{\hat{S}_{\text{exc}}\Big\}\Big] + \text{E}\Big[\|K\|_2^{-2} K\Big\{\hat{S}_{\text{exc}}\Big\} K\Big\{\hat{S}_{\text{exc}}\Big\}\Big]^2 = \tag{2.56}$$

$$= \|K\|_2^{-4} \iiiint K(t_1)K(t_2)K(t_2)K(t_3)\Big\langle \hat{S}_{\text{exc}}(t_1)\hat{S}_{\text{exc}}(t_2)\hat{S}_{\text{exc}}(t_3)\hat{S}_{\text{exc}}(t_4)\Big\rangle \text{d}\vec{t} \tag{2.57}$$

$$= \frac{4!}{2\cdot 2\cdot 2}\text{E}\Big[\|K\|_2^{-2} K\Big\{\hat{S}_{\text{exc}}\Big\} K\Big\{\hat{S}_{\text{exc}}\Big\}\Big]^2 \tag{2.58}$$

The combinatoric factors are similar to those required of N-point correlation functions for vertices of Feynman diagrams.

For an experiment operating at the shot noise limit, $L_\delta A \ll \frac{P_{\rm AS} E_\lambda}{|C_{\left[\frac{\rm w}{\rm m}\right]\rm AS}|^2}$, so the measurement limit over a single mode is consistent with the standard interferometer limit for N=1 of eq. (2.36) on page 39.

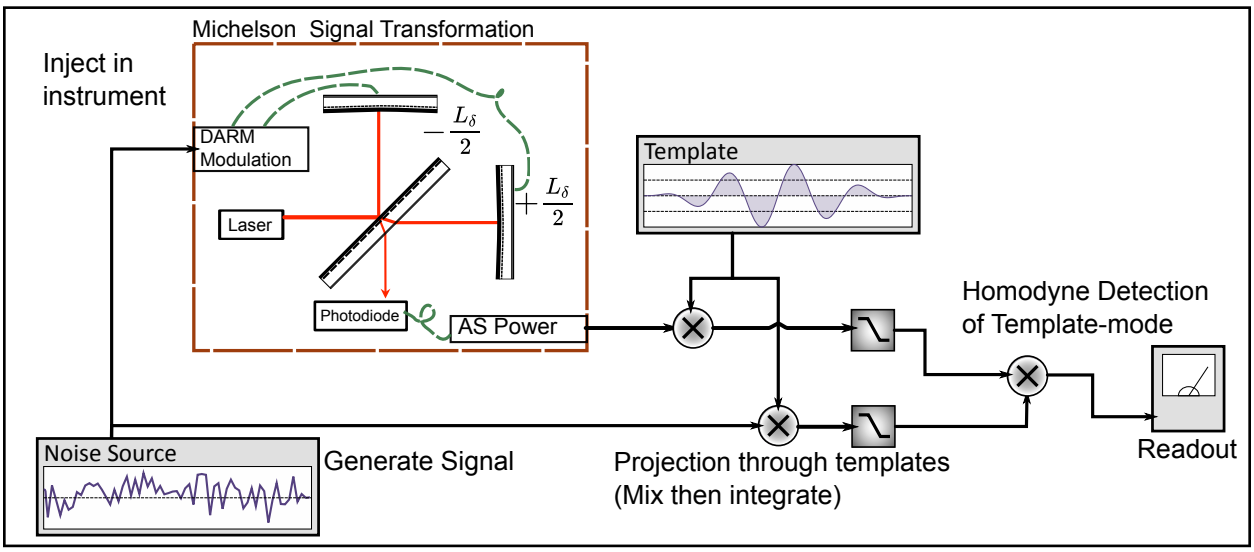

Figure 2.9: Reference measurement for a Michelson differential length sensor with a noise-drive and matched-template detection. Here the excitation modulation is still necessary, but the exact form of it may be random. The template serves to select from the instrument the piece of signal or mode (represented by the template) that the noise source also occupies. The instrument and noise are independently mixed with the template and integrated. The final multiplication detects common noise power in the template-mode within the instrument output. If the noise source has a large projection into the template compared to the instrument noise, then the detection will be significant.

2.8 The Time-Bandwidth Counting of Modes

A single template from the previous section gives effectively a single measurement, picking out a mode of the data where signal resides. The stationary white noise given is inherently multi-modal, so multiple measurements can and should be made. Multiple templates K_i, each provide a measurement from the dataset, $\hat{M}_{K_i}$. One can then perform a weighted average over the estimators two lower the noise further. The weights here are chosen optimally,

but the choice is arbitrary up the penalty of larger variance.

$$\hat{M}_\Sigma = \frac{\sum_i w_i \hat{M}_{K_i}}{\sum_i w_i} \tag{2.59}$$

$$w_i = \frac{1}{\textsc{Var}[\hat{M}_{K_i}]} \tag{2.60}$$

And the variance of this combined estimator is expressed:

$$\textsc{Var}[\hat{M}_\Sigma] = \frac{1}{(\sum_i w_i)^2}\left(\sum_i w_i^2 \textsc{Var}[\hat{M}_{K_i}] + \sum_i \sum_{j\neq i} w_j w_i \textsc{Cov}[\hat{M}_{K_i}, \hat{M}_{K_j}]\right) \tag{2.61}$$

And the inner covariance term is derived from the definition:

$$\textsc{Cov}[\hat{M}_{K_i}, \hat{M}_{K_j}] = \mathrm{E}\Big[(\hat{M}_{K_i} - \mathrm{E}[\hat{M}_{K_i}])(\hat{M}_{K_j} - \mathrm{E}[\hat{M}_{K_j}])\Big] \tag{2.62}$$

$$= \langle \hat{M}_{K_i} \hat{M}_{K_j} \rangle - \langle \hat{M}_{K_i} \rangle \langle \hat{M}_{K_j} \rangle \tag{2.63}$$

$$= \frac{1}{U_{K_i} U_{K_j}} \iint \left(2L_\delta^2 \langle \hat{S}_{\mathrm{exc}}(t_1) \hat{S}_{\mathrm{exc}}(t_2) \rangle + \frac{\langle \hat{N}_{\mathrm{SN}}(t_1) \hat{N}_{\mathrm{SN}}(t_2) \rangle}{|C_{[\mathrm{w}]\mathrm{AS}}(F)|^2} \right) K_i(t_1) K_j(t_2) dt_1 dt_2 \tag{2.64}$$

using the weights

$$U_{K_i} = \|K_i\|_2 \sqrt{\left\langle K_i\Big\{\hat{S}_{\mathrm{exc}}\Big\} K_i\Big\{\hat{S}_{\mathrm{exc}}\Big\} \right\rangle} \tag{2.65}$$

The integral term can be simplified into a dot-product notation, where the weight kernel is derived from the noise statistics

$$\langle K_i | \mathbf{w}_{\mathrm{sys}} | K_j \rangle = \iint K_i(t_1) K_j(t_2) \underbrace{\left(2L_\delta^2 \langle \hat{S}_{\mathrm{exc}}(t_1) \hat{S}_{\mathrm{exc}}(t_2) \rangle + \frac{\langle \hat{N}_{\mathrm{SN}}(t_1) \hat{N}_{\mathrm{SN}}(t_2) \rangle}{|C_{[\mathrm{w}]\mathrm{AS}}(F)|^2} \right)}_{\mathbf{w}_{\mathrm{sys}}(t_1, t_2)} dt_1 dt_2 \tag{2.66}$$

Now the covariance takes the form of an inner product and the correlation-coefficient

rives the inner product of norm-1 vectors in this space.

$$\textsc{Cor}[\hat{M}_{K_i}, \hat{M}_{K_j}] = \frac{\langle K_i|\mathbf{w}_{\text{sys}}|K_j\rangle}{\|K_i\|_{\mathbf{w}_{\text{sys}}} \left\|K_j\right\|_{\mathbf{w}_{\text{sys}}}} \tag{2.67}$$

$$\|K_i\|_{\mathbf{w}_{\text{sys}}} = \sqrt{\langle K_i|\mathbf{w}_{\text{sys}}|K_i\rangle} \tag{2.68}$$

This maps all questions about finding a complete set of measurements to finding a basis in the Hilbert space defined by this inner product. This basis is finite in size under the addition practical constraints on total bandwidth given by eq. (2.49) on page 45.

In practice a full orthonormal basis of templates is not needed, what is more useful is a basis which allows practical calculation of the multiple-measurement estimator and its variance terms. This is be ensured with the computation constraints on K, as well as if each template has only a small number of partners with nonzero covariance, rather than the stronger constraint (zero such partners) of an orthonormal set.

The expression given in eq. (2.66) is the full form for any statistics on a Michelson lock-in measurement. It works perfectly well to design templates for stationary and non-stationary noises with any frequency-spectrum. For sensor and shot noises which are typically stationary and white, along equally white excitations, the expression simplifies considerably due to the delta functions in the 2nd-order moments. White stationary noise statistics generates a statistical-vector space which is the "typical" unweighted L^2 Hilbert space. This space has translational invariance (a property only requiring of stationary noise) and such spaces are always spanned by the trigonometric function-modes. Furthermore, requiring the templates be finite in length and ultimately composed of bandwidth-limited samples suggests that a Discrete Fourier Transform provides a suitable set of basis templates.

The culmination of this (rough) analysis is to relate the "perfect" measurement (many-template estimator) which saturates the number of independent measurements in a finite measurement window against the apodized DFT, accumulated through the Welch-method.

The former describes the ideal expectation of the reference measurement, the latter to describe the practical method chosen for this thesis.

To demonstrate the saturated limit, select the integration time T_{span}, the L^2 space of stationary statistics now integrates over a compact set and has a discrete spectrum of Fourier-modes $K_{j:\text{real}}(t) = \cos(2\pi j \Delta F t)$ and $K_{j:\text{imag}}(t) = \sin(2\pi j \Delta F t)$ with $\Delta F = \frac{1}{T_{\text{span}}}$. The total number of independent measurements is $2F_{\text{span}}T_{\text{span}}$ as there is a separate real and imaginary template for each mode up to the frequency-cutoff. Since these modes are independent and white noise provides all template-estimators equal variance, the averaging-estimator has the variance:

$$\hat{M}_{\Sigma\mathscr{F}} = \frac{1}{2F_{\text{span}}T_{\text{span}}} \sum_j \hat{M}_{K_{j:\text{real}}} + \hat{M}_{K_{j:\text{imag}}} \tag{2.69}$$

$$\text{VAR}[\hat{M}_{\Sigma\mathscr{F}}] = \frac{1}{2F_{\text{span}}T_{\text{span}}} \text{VAR}[\hat{M}_{\text{single}}] \tag{2.70}$$

This works out for a discretely-sampled system as the sample rate of F_{sample} imposes a Nyquist-limited frequency of $F_{\text{nyquist}} = F_{\text{sample}}/2 = F_{\text{span}}$ and the number of samples is $F_{\text{sample}}T_{\text{span}}$, coinciding with the number of ADC sample-templates for a purely Nyquist-limited bandwidth.

The next section will go over complex templates useful in approximations to the Fourier-transform. Each complex template provides two measurements, so the variance of a complex-template estimator to white-noise is halved, giving the relation:

$$\text{VAR}[\hat{M}_{\Sigma\mathscr{F}}] = \frac{1}{F_{\text{span}}T_{\text{span}}} \text{VAR}[\hat{M}_{\text{complex}}] \tag{2.71}$$

This is the relation more commonly used.

2.9 The Fourier Transform as a complex-template search

A side result of the previous section for the cosine/sine pair of Fourier mode template, traditionally seen as the real and imaginary part of a single mode. The form of the statistical expressions can be adapted to have the complex template.

$$\mathcal{K}_j(t) = K_{j:\mathrm{real}}(t) + \mathrm{i}K_{j:\mathrm{imag}}(t) \tag{2.72}$$

$$= \cos(2\pi j \Delta F t) + \mathrm{i}\sin(2\pi j \Delta F t) \tag{2.73}$$

$$= e^{2\pi \mathrm{i} j \Delta F t} \tag{2.74}$$

$$\left\|\mathcal{K}_j\right\|_2^2 = \left\|K_{j:\mathrm{real}}\right\|_2^2 + \left\|K_{j:\mathrm{imag}}\right\|_2^2 \tag{2.75}$$

The form of the signal estimator using complex templates becomes.

$$\hat{M}_{\mathcal{K}_j} = \frac{1}{2} M_{K_{j:\mathrm{real}}} + \frac{1}{2} M_{K_{j:\mathrm{imag}}} \tag{2.76}$$

$$= \mathfrak{Re}\left\{ \frac{\|\mathcal{K}\|_2^{-2}\, \mathcal{K}\left\{\hat{D}_{\mathrm{ifo}}\right\} \mathcal{K}^*\left\{\hat{S}_{\mathrm{exc}}\right\}}{|C_{\left[\frac{\mathrm{W}}{\mathrm{m}}\right]\mathrm{AS}}| \sqrt{\|\mathcal{K}\|_2^{-2} \left\langle \mathcal{K}\left\{\hat{S}_{\mathrm{exc}}\right\} \mathcal{K}^*\left\{\hat{S}_{\mathrm{exc}}\right\}\right\rangle}} \right\} \tag{2.77}$$

$$\mathrm{E}[\hat{M}_{\mathcal{K}_j}] = L_\delta \tag{2.78}$$

$$\textsc{Var}[\hat{M}_{\mathcal{K}_j}] = L_\delta^2 A^2 + \frac{P_{\mathrm{AS}} E_\lambda}{2|C_{\left[\frac{\mathrm{W}}{\mathrm{m}}\right]\mathrm{AS}}|^2} \tag{2.79}$$

A subtle aspect of this template is that the variance shown from eq. (2.79) is exactly a factor of two below the single-template method. For future calculations accounting for the equivalent "number of measurements", this factor is important to relate the single-real-template variance vs. the complex template variance. Another subtle aspect is that application using the Fourier transform needs both the positive and negative frequencies, but the

estimator, coming from the real part, is actually the same for both:

$$\hat{M}_{\mathcal{K}_j} = \hat{M}_{\mathcal{K}_j^*} = \hat{M}_{\mathcal{K}_{-j}} \tag{2.80}$$

This is critically important when defining the total RMS motion, as both positive and negative frequencies are needed to provided RMS units. This is the distinction later between the one-sided PSDs and two-sided. Usually data is not plotted in the negative frequency as its estimators are degenerate, yet RMS requires both. The one-sided PSD attempts to avoid confusion by stating the power at negative frequencies is 0 and at positive it is doubled, but the choice of conventions is important to ensure the model is projected into the same spectrum-type as the data.

With the degeneracy in mind, complex templates allow future sensitivity calculations using the Fourier transform modeled off of this measurement estimator. The finite-time of any measurement forces the use of an apodization function to limit the Fourier-modes to a (soft) window $w(t)$. Let $\hat{X}(t)$ be any statistical time-series, and the approximate Fourier templates become.

$$\mathcal{K}_F = w(t) \cdot e^{2\pi \mathrm{i} F t} \tag{2.81}$$

$$\hat{X}(F) = \mathscr{F}\{\hat{X}; F\} \approx \mathcal{K}_F\Big\{\hat{X}\Big\} \tag{2.82}$$

$$\Delta F = \frac{1}{\|w(t)\|_2^2} \tag{2.83}$$

Now the window can be expressed as it Fourier transform $\widetilde{w}(F)$. The template and conjugate template from eq. (2.77) on page 51 are expressed in the Fourier domain and the inner product with them $\mathcal{K}\Big\{\hat{X}\Big\}$ becomes a convolution between the data and window that

is evaluated at the frequency selected.

$$\hat{M}(F) = \mathfrak{Re}\left\{ \frac{\Delta F\Big\{\widetilde{w} *_{\mathrm{F}} \hat{D}_{\mathrm{ifo}}\Big\}\Big\{\widetilde{w} *_{\mathrm{F}} \hat{S}^{*}_{\mathrm{exc}}\Big\}}{|C_{\left[\frac{\mathrm{w}}{\mathrm{m}}\right]\mathrm{AS}}|\sqrt{\Delta F\Big\langle\Big\{\widetilde{w} *_{\mathrm{F}} \hat{S}_{\mathrm{exc}}(F)\Big\}\Big\{\widetilde{w} *_{\mathrm{F}} \hat{S}^{*}_{\mathrm{exc}}\Big\}\Big\rangle}} \right\} \tag{2.84}$$

The key points from this expression are the bandwidth ΔF, the window-convolution $\{\widetilde{w}*_{\mathrm{F}}\}$ and the conjugate operation that acts on the Fourier-transform of the right-side argument.

2.10 The Cross-Spectral-Density

So far the collection of estimators has been built using templates or collections-of-templates and they have been designed to estimate the RMS power of an external excitation driving a Michelson Interferometer. The construction of these multiple-template-average estimators is cumbersome to express. This section presents relations to take desired measurements and build estimators from the practical time-resolved cross-spectral-density (CSD) matrix that naturally collect all of these templates and express them like the Fourier transform of the previous section. They will be implemented using the Welch-method explained in the next section.

An important new feature not present in the Fourier transform is that the Welch-method is time-resolved, so non-stationary noise can be resolved. This is useful for measurements like transfer-functions that drive modulations across frequencies. The weighting used to average within this time-resolution can optimize for certain measurements over others. The notation will reflect the time-resolution when it is important and otherwise assume a total time average with flat-weighting when it is not.

The CSD matrix fundamentally expresses the second-moments of a system of data-variables in the Fourier domain. For data variables $\hat{x}(t)$ and $\hat{y}(t)$, the cross-spectrum between

them should represent:

$$\langle \hat{x}(F_1)\hat{y}^*(F_2)\rangle \approx \overline{\mathrm{CSD}}_{(\pm)}[F_1;\hat{x},\hat{y}]\cdot\delta\left(F_1-F_2\right) \tag{2.85}$$

Note that this density, reflecting the Fourier transform, must use the conventions of a two-sided power-spectrum.

The units of this expectation value are quite strange since the Fourier transform, $\hat{x}(F)$, always adds a factor of $\frac{1}{\mathrm{Hz}}$ to the time-domain representation $\hat{x}(t)$. The pair of transforms indicate an overall $\frac{1}{\mathrm{Hz}^2}$. These units are a warning that an additional integral over frequency must be done and that *any* measurement to estimated the frequency distribution must be finite in time. They are related to the ΔF of the weight function in eq. (2.84) on page 53. The units of the expression confirm that any estimate of this ideal cross-spectrum must have come from some choice of templates, measurement-time, and accumulation method. The various ways the CSD is used will motivate different methods of assembling the CSD estimator to optimize for each science goal.

$$\widehat{\mathrm{CSD}}[\hat{X},\hat{Y}|\mathcal{K}] = \Upsilon_{\mathrm{FOLD}}\,\|\mathcal{K}\|_2^{-2}\,\mathcal{K}\Big\{\hat{X}\Big\}\,\mathcal{K}^*\Big\{\hat{Y}\Big\} \tag{2.86}$$

The Υ_{FOLD} factor represents that this CSD does not specify being a one or two sided. Many applications of the CSD take ratios of the form

$$\hat{M}_{\hat{X},\hat{Y},\hat{Z}} = \frac{\widehat{\mathrm{CSD}}[\hat{X},\hat{Y}|\mathcal{K}]}{\widehat{\mathrm{CSD}}[\hat{Z},\hat{Y}|\mathcal{K}]} \tag{2.87}$$

where the convention does not matter. It is super or sub scripted with $(+)$ or $(\pm)$ in this text to distinguish the one and two sided types respectively. The factor Υ_{FOLD} indicates that any model test must use a consistent convention to cancel all of the factors.

2.10.1 The CSD Frame

In general, the CSD-estimator will always be indexed with the items to take the expectation-of, but will have additional arguments to indicate the exact-scheme used. For CSDs built from the Welch-method, there can be indices for the Frequency-bin selected $F =$, the number of complex-template averages $N =$, and the time or time-index that the measurement was started, with the expectation that the averaging was contiguous. These parameters define a set of templates used $\mathbb{K}^{\text{welch}}_{F,N,t}$. The most fundamental measurement defined by these parameters is a **frame**.

$$\widehat{\text{CSD}}[\hat{X}, \hat{Y}|F, N, t] = \Upsilon_{\text{FOLD}} \frac{1}{N} \sum_{\mathcal{K} \in \mathbb{K}^{\text{welch}}_{F,N,t}} \|\mathcal{K}\|_2^{-2} \mathcal{K}\Big\{\hat{X}\Big\} \mathcal{K}^*\Big\{\hat{Y}\Big\} \tag{2.88}$$

2.10.2 Coadded Frames

Measurements can be composed of many CSD frames, where the weighting is chosen per-frame or even per frequency bin in order to generate an optimal CSD estimator for whatever the science is at-hand. The next sections will develop uses for the CSD and those will motivate optimal weightings for those uses. The data acquisition system provides a series of CSD-frames, which can be indexed $i = 1, 2, 3 \ldots$, and each provide start-times T_i and accumulation-numbers N_i. The scientist then decides the weighting scheme to combine those frames $w_i \in \mathbb{W}_{\text{scheme}}$:

(2.89)

$$\widehat{\text{CSD}}[\hat{X}, \hat{Y}|F, \mathbb{W}_{\text{scheme}}] = \frac{1}{\sum_{w_i \in \mathbb{W}} w_i} \sum_{w_i \in \mathbb{W}} w_i \widehat{\text{CSD}}[\hat{X}, \hat{Y}|F, N_i, t_i] \tag{2.90}$$

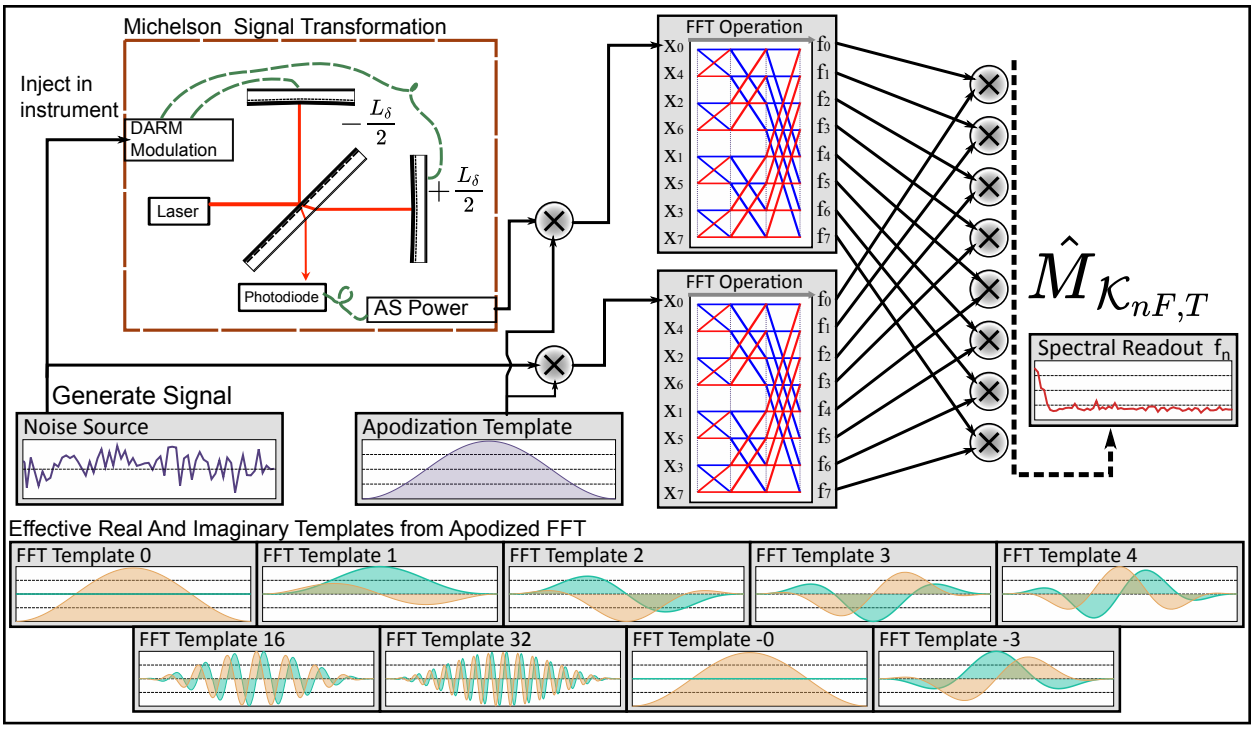

Figure 2.10: Reference measurement including many concurrent frequency-indexed templates through the fast-Fourier transform. The FFT efficiently performs the template multiplication and integration steps of fig. 2.9 on page 47 across a series of templates. The blue-red butterfly operations perform this computation. The final data are indexed by the time of the FFT start, as well as the index of the frequency-shifted apodization window. The final multiplication step uses the complex templates to generate a cross-spectrum between the instrument and the drive source.

2.10.3 CSD Matrix coordinate-independence

the CSD can also be represented as a matrix. Instead of having the single-variables like $\hat{x}$ and $\hat{y}$, all of the data variables can be collected into a data vector

$$\hat{\vec{D}} = \begin{bmatrix} \hat{x} \\ \hat{y} \\ \vdots \end{bmatrix} \tag{2.91}$$

And sub CSDs can be found by selecting for that matrix from the matrix-valued expectation. The transpose is used here with implicit vector operations to generate the exterior

product

$$\widehat{\mathrm{CSD}}\left[\hat{\vec{D}}, \hat{\vec{D}}^T\right] = \begin{bmatrix} \widehat{\mathrm{CSD}}[\hat{x}, \hat{x}] & \widehat{\mathrm{CSD}}[\hat{x}, \hat{y}] & \dots \\ \widehat{\mathrm{CSD}}[\hat{y}, \hat{x}] & \widehat{\mathrm{CSD}}[\hat{y}, \hat{y}] & \dots \\ \vdots & \vdots & \ddots \end{bmatrix} \tag{2.92}$$

The CSD-estimator is (sesqui)linear in its arguments due to the conjugation mentioned in eq. (2.84) on page 53 for Fourier-like templates

$$\widehat{\mathrm{CSD}}[\alpha\hat{x}, \beta\hat{y}] = \alpha\beta^* \widehat{\mathrm{CSD}}[\hat{x}, \hat{y}] \tag{2.93}$$

$$\widehat{\mathrm{CSD}}[\hat{x} + \hat{z}, \hat{y}] = \widehat{\mathrm{CSD}}[\hat{x}, \hat{y}] + \widehat{\mathrm{CSD}}[\hat{z}, \hat{y}] \tag{2.94}$$

$$\widehat{\mathrm{CSD}}[\hat{x}, \hat{y} + \hat{z}] = \widehat{\mathrm{CSD}}[\hat{x}, \hat{y}] + \widehat{\mathrm{CSD}}[\hat{x}, \hat{z}] \tag{2.95}$$

And these properties are sufficient to extend to full matrix operations. Using linear techniques, the CSD-matrix can be represented in a different basis for the data-vector without needing to develop a separate estimator.

$$\hat{\vec{D}}' = \mathbf{U}\hat{\vec{D}} \tag{2.96}$$

$$\widehat{\mathrm{CSD}}\left[\hat{\vec{D}}', \hat{\vec{D}}'^T\right] = \widehat{\mathrm{CSD}}\left[\mathbf{U}\hat{\vec{D}}, \hat{\vec{D}}^T\mathbf{U}^T\right] \tag{2.97}$$

$$= \mathbf{U}\widehat{\mathrm{CSD}}\left[\hat{\vec{D}}, \hat{\vec{D}}^T\right]\mathbf{U}^{*T} \tag{2.98}$$

This is important for the data analysis later. The CSD's collected were all in raw voltages at the ADC's, and calibrations, sensor combinations and what-have-you could be applied even after the data is collected. Only calibrations which must be applied before averaging CSDs requires some intervention into the linearity of all of the data analysis.

2.10.4 Example Basis Change - optimal combined sensor

Lets say there are four sensors such as the Holometer 2x/ifo length-sensing photodiodes. These four sensors ultimately represent only two independent measurements; However the four sensors need to be calibrated first and with with complex calibrations. Furthermore, the measurements will be combined with some chosen (hopefully optimal) weightings, but the CSD matrix is generated in the four-sensor basis. Call the measurement-CSD $\hat{\mathbf{M}}$ and call the desired measurement $\hat{M}_{\text{science}}$.

$$\hat{X}_c = \frac{w_{x_1}}{w_{x_1}+w_{x_2}} C_{x_1}\hat{X}_1 + \frac{w_{x_2}}{w_{x_1}+w_{x_2}} C_{x_2}\hat{X}_1 \tag{2.99}$$

$$\hat{Y}_c = \frac{w_{y_1}}{w_{y_1}+w_{y_2}} C_{y_1}\hat{Y}_1 + \frac{w_{y_2}}{w_{y_1}+w_{y_2}} C_{y_2}\hat{Y}_1 \tag{2.100}$$

$$\hat{\vec{D}}^T = \begin{bmatrix} \hat{X}_1 & \hat{X}_2 & \hat{Y}_1 & \hat{Y}_2 \end{bmatrix} \tag{2.101}$$

$$\hat{\mathbf{M}} = \widehat{\text{CSD}}[\hat{\vec{D}}, \hat{\vec{D}}^T] \tag{2.102}$$

$$\hat{\mathbf{M}}_{\text{science}} = \widehat{\text{CSD}}[\hat{X}_c, \hat{Y}_c] \tag{2.103}$$

Now with some definitions to simplify the coordinates, the true matrix can be determined

$$\mathbf{C} = \begin{bmatrix} C_{x_1} & & & \\ & C_{x_2} & & \\ & & C_{y_1} & \\ & & & C_{y_2} \end{bmatrix} \tag{2.104}$$

$$\mathbf{W} = \begin{bmatrix} \frac{w_{x_1}}{w_{x_1}+w_{x_2}} & \frac{w_{x_2}}{w_{x_1}+w_{x_2}} & & \\ & & \frac{w_{y_1}}{w_{y_1}+w_{y_2}} & \frac{w_{y_2}}{w_{y_1}+w_{y_2}} \end{bmatrix} \tag{2.105}$$

$$\hat{\vec{D}}_{\text{science}} = \mathbf{W}\mathbf{C}\hat{\vec{D}} \tag{2.106}$$

$$\hat{\mathbf{M}}_{\text{science}} = \begin{bmatrix} 1 & 0 \end{bmatrix} \mathbf{W}\mathbf{C}\hat{\mathbf{M}}\mathbf{C}^{*T}\mathbf{W}^{*T} \begin{bmatrix} 0 \\ 1 \end{bmatrix} \tag{2.107}$$

Here assume all weights are $\frac{1}{2}$ for simplicity

$$\hat{\mathbf{M}}_{\text{science}} = \begin{bmatrix} \frac{1}{2} & \frac{1}{2} & 0 & 0 \end{bmatrix} \mathbf{C}\hat{\mathbf{M}}\mathbf{C}^{*T} \begin{bmatrix} 0 & 0 & \frac{1}{2} & \frac{1}{2} \end{bmatrix}^T \tag{2.108}$$

$$= \begin{bmatrix} \frac{C_{x_1}}{2} & \frac{C_{x_2}}{2} & 0 & 0 \end{bmatrix} \hat{\mathbf{M}} \begin{bmatrix} 0 & 0 & \frac{C^*_{y_1}}{2} & \frac{C^*_{y_2}}{2} \end{bmatrix}^T \tag{2.109}$$

$$= \frac{1}{4}\Big(C_{x_1} C^*_{y_1} \widehat{\text{CSD}}[\hat{\vec{X}}_1, \hat{\vec{Y}}_1] + C_{x_1} C^*_{y_2} \widehat{\text{CSD}}[\hat{\vec{X}}_1, \hat{\vec{Y}}_2] \tag{2.110}$$

$$+ C_{x_2} C^*_{y_1} \widehat{\text{CSD}}[\hat{\vec{X}}_2, \hat{\vec{Y}}_1] + C_{x_2} C^*_{y_2} \widehat{\text{CSD}}[\hat{\vec{X}}_2, \hat{\vec{Y}}_2] \Big) \tag{2.111}$$

2.11 Practical Computation using the Welch Method

The Holometer experiment builds and averages estimators efficiently in time using the Welch-method for the discrete, apodized Fast-Fourier-Transform (FFT). The apodization chosen is the Hanning window, which prevents frequency-aliasing from the finite-time of the FFT. The FFT's collect N_{FFT} samples (chosen for efficiency to be a power-of-two). Each channel is apodized, then transformed. This creates an array of $\mathcal{K}_{\text{F,T}}\Big\{\hat{D}\Big\}$ samples for each channel's data $\hat{D}$. Now for each template, the various channels can be recomposed into all of the $\Big(\Delta F \mathcal{K}_{\text{F,T}}\Big\{\hat{D}_1\Big\}\mathcal{K}_{\text{F,T}}\Big\{\hat{D}_2\Big\}\Big)$ terms of interest for estimators. The machine generates this set not every N_{FFT} samples but at twice that rate. This prevents some data loss through the low-weight edges of the apodization-window, but shares data between templates of neighboring time-slices.

Even though every template measures in its own mode, the sharing of data prevents the modes from being independent. Ignoring this will over-count the effective number of measurements and underestimate the final estimator variance, unless corrected using the covariances of the templates. For a system with stationary-white statistics, every template has the same variance. This aids in the computation by only needing correlation coefficients with much more simple normalizations than the full variances.

Start by labeling all of the templates by their frame number and frequency-index. The sine/cosine pair of real templates are packed into a complex template with the understanding

that each template sum accounts for two measurements. The window length is defined to be $T_{\rm w}$ and each frame is separated by $\frac{1}{2}T_{\rm w}$. The i,j indices are used for the frame-number and count from 0 to $\frac{2T_{\rm span}}{T_{\rm w}}$. The u,v indices indicate frequency-index and count 0 to $T_{\rm w}F_{\rm span}$. The $\Pi(t,0,T_{\rm w})$ box-window function is defined to be 1 where $0<t<T_{\rm w}$ and otherwise 0.

$$K_{0,u}(t) = e^{2\pi {\rm i}\frac{ut}{T_{\rm w}}}\sin^2\left(\frac{\pi t}{T_{\rm w}}\right)\Pi(t,0,T_{\rm w}) \tag{2.112}$$

$$K_{i,u}(t) = K_{0,u}\left(t+\frac{iT_{\rm w}}{2}\right) \tag{2.113}$$

For measurements all with equal variance, there is an effective number of measurements $N_{\rm eff}$ associated with an overcomplete set of templates. This is the number to be compared against the time-bandwidth product and the overcounted modes $N_{\rm tot} = 2T_{\rm span}F_{\rm span}$ (counting from complex-templates). The simplifications to $N_{\rm eff}$ come from eq. (2.67) on page 49 with the assumptions of stationary-white noise. The factor of two entering at the second line comes from the norm of *complex* templates, which each contain two measurements must be modified by that factor from eq. (2.66) on page 48.

$$\frac{N_{\rm tot}}{N_{\rm eff}} = \frac{1}{N_{\rm tot}}\sum_{i,u}\sum_{j,v}{\rm Cor}[\hat{M}_{\mathcal{K}_{i,u}},\hat{M}_{\mathcal{K}_{j,v}}] \tag{2.114}$$

$$= \frac{2}{N_{\rm tot}}\sum_{i,u}\frac{\langle\mathcal{K}_{i,u}|}{\left\|\mathcal{K}_{i,u}\right\|_2}\sum_{j,v}\frac{|\mathcal{K}_{j,v}\rangle}{\left\|\mathcal{K}_{j,v}\right\|_2} \tag{2.115}$$

$$= \frac{2}{N_{\rm tot}\left\|\mathcal{K}_{0,0}\right\|_2^2}\sum_{i,u}\langle\mathcal{K}_{i,u}|\sum_{j,v}|\mathcal{K}_{j,v}\rangle \tag{2.116}$$

$$= \frac{2}{N_{\rm tot}\left\|\mathcal{K}_{0,0}\right\|_2^2}\sum_{u}\sum_{v}\int_0^{T_{\rm span}} e^{2\pi {\rm i}(u-v)\frac{t}{T_{\rm w}}}\left(\sin^2\left(\tfrac{\pi t}{T_{\rm w}}\right)+\cos^2\left(\tfrac{\pi t}{T_{\rm w}}\right)\right)^2 dt \tag{2.117}$$

$$= \frac{2T_{\rm span}F_{\rm span}}{N_{\rm tot}\left\|\mathcal{K}_{0,0}\right\|_2^2} = \frac{16T_{\rm span}F_{\rm span}}{3N_{\rm tot}} = \frac{8}{3} \tag{2.118}$$

$$N_{\rm eff} = \frac{3}{4}T_{\rm span}F_{\rm span} \tag{2.119}$$

Equation (2.114) is notable as the correlation coefficient of identical modes is always 1,

so for an orthonormal-mode set, the cross terms cancel and N_{eff} will be equal to N_{tot}.

2.12 Detecting Buried Noise in the Holometer

The measurements so far presented were chosen to produce results related to the standard quantum limit. This restricted the measurements to have units of RMS power, as well as to use homodyne techniques. This section details alternate estimators based off of the Michelson, primarily to demonstrate a means of avoiding the lock-in. The 2x interferometer method is used for the Holometer experiment, but also included is the Radiometer Method which could manage to use a single interferometer and has the same time-bandwidth scaling properties.

2.12.1 Radiometer method

Section 2.7 on page 42 provided the statistics of a shot-noise-limited Michelson, but assumed that the drive system could be independently measured. The Radiometer method drops that assumption, but at considerable cost. To generate an estimator, the excess noise must now be known very precisely. The CSD of the noise is used here, but it cannot, in general, be measured at the same time as $\hat{D}_{\text{ifo}}$. It may be possible to estimate it from other channels by modulating the excitation amplitude (or coupling) to see the noise without the signal. The Holometer can not affect its noise.

The CSD is created from complex Fourier-like templates. It is used here as a power-spectrum, $\widehat{\text{PSD}}[\hat{D}_{\text{ifo}}]$, so the signal is real. This would imply that purely-real templates could be used, and they could, but the variance would enlarge by a factor of two. The two factors of the standard quantum limit appearing here are due to the estimator being

constructed from complex templates.

$$\hat{M} = \frac{1}{\left|C_{\left[\frac{\mathrm{W}}{\mathrm{m}}\right]\mathrm{AS}}\right|^2}\left(\widehat{\mathrm{PSD}}\left[\hat{D}_{\mathrm{ifo}}\right] - \overline{\mathrm{PSD}}\left[\hat{N}_{\mathrm{SN}}\right]\right) \tag{2.120}$$

$$\mathrm{E}[\hat{M}_{\mathrm{single}}] = \Upsilon_{\mathrm{FOLD}} L_\delta^2 A^2 \tag{2.121}$$

$$\mathrm{VAR}[\hat{M}_{\mathrm{avg}}] = \Upsilon_{\mathrm{FOLD}}^2 \frac{1}{T_{\mathrm{span}} F_{\mathrm{span}}}\left(\underbrace{L_\delta^2 A^2 + \frac{P_{\mathrm{AS}} E_\lambda}{\left|C_{\left[\frac{\mathrm{W}}{\mathrm{m}}\right]\mathrm{AS}}\right|^2}}_{\overline{\mathrm{PSD}}[\hat{D}_{\mathrm{ifo}}]}\right)^2 \tag{2.122}$$

This estimator is in the units square of the desired result. For the result to be put into the physical units of RMS-power-density as shown in previous sections, the time-bandwidth scaling law is very unfortunate. To generate a test-statistic for this, the unitful statistic must be divided by its expectation.

$$\hat{\Theta} = \frac{\hat{M}}{\mathrm{E}\left[\hat{M}\right]}, \qquad \mathrm{E}[\hat{\Theta}] = 1, \qquad \mathrm{VAR}[\hat{\Theta}] = \frac{1}{T_{\mathrm{span}} F_{\mathrm{span}}}\left(\frac{(\lambda/4\pi)^4 \left(E_\lambda/P_{\mathrm{BS}}\right)^2}{L_\delta^2 A^2} + 1\right) \tag{2.123}$$

2.12.2 2x interferometer method used for the Holometer

If the underlying excitation cannot be measured except in an interferometer, then driving two interferometers from a common source provides a means of measuring the excitation coupling without requiring a perfect model of the background noise. The two interferometers then have the statistics.

$$\langle \hat{S}_{\mathrm{exc}}(t)\rangle = 0 \qquad \langle \hat{S}_{\mathrm{exc}}(t)\hat{S}_{\mathrm{exc}}(t')\rangle = \Xi_\delta(\tau) \tag{2.124}$$

$$\langle \hat{N}_{\mathrm{SN:A}}(t)\rangle = 0 \qquad \langle \hat{N}_{\mathrm{SN:A}}(t)\hat{N}_{\mathrm{SN:A}}(t')\rangle = P_{\mathrm{AS}} E_\lambda \delta\left[t - t'\right] \tag{2.125}$$

$$\langle \hat{N}_{\mathrm{SN:B}}(t)\rangle = 0 \qquad \langle \hat{N}_{\mathrm{SN:B}}(t)\hat{N}_{\mathrm{SN:B}}(t')\rangle = P_{\mathrm{AS}} E_\lambda \delta\left[t - t'\right] \tag{2.126}$$

$$\hat{D}_{\mathrm{ifo:A}} = C_{\left[\frac{\mathrm{W}}{\mathrm{m}}\right]\mathrm{AS}}(F)\hat{S}_{\mathrm{exc}} + \hat{N}_{\mathrm{SN:A}} \tag{2.127}$$

$$\hat{D}_{\mathrm{ifo:B}} = C_{\left[\frac{\mathrm{W}}{\mathrm{m}}\right]\mathrm{AS}}(F)\hat{S}_{\mathrm{exc}} + \hat{N}_{\mathrm{SN:B}} \tag{2.128}$$

The estimator uses the one-sided cross spectrum convention as that is what the data will eventually use.

$$\hat{M}(F) = \mathfrak{Re}\left\{ \frac{1}{C_{[\mathrm{w}]\mathrm{AS:A}} C^{*}_{[\mathrm{w}]\mathrm{AS:B}}} \widehat{\mathrm{CSD}}_{(+)} \left[\hat{D}_{\mathrm{ifo:A}}, \hat{D}_{\mathrm{ifo:B}}; F \right] \right\} \tag{2.129}$$

$$\mathrm{E}[\hat{M}(F)] = \overline{\mathrm{PSD}}_{(+)}[\hat{S}_{\mathrm{exc}}] = \Xi^{(+)}_{\delta}(F) \tag{2.130}$$

$$\mathrm{VAR}[\hat{M}(F)] = \frac{1}{2T_{\mathrm{span}}} \Big(\underbrace{2\Xi^{(+)}_{\delta}(F)}_{2\cdot\overline{\mathrm{PSD}}_{(+)}[\hat{N}_{\mathrm{SN:A}}]} + \frac{\overbrace{2P_{\mathrm{AS:A}}E_{\lambda}}^{\overline{\mathrm{PSD}}_{(+)}[\hat{N}_{\mathrm{SN:A}}]}}{|C_{[\mathrm{w}]\mathrm{AS:A}}|^2} \Big) \cdot \Big(\underbrace{2\Xi^{(+)}_{\delta}(F)}_{2\cdot\overline{\mathrm{PSD}}_{(+)}[\hat{N}_{\mathrm{SN:A}}]} + \frac{\overbrace{2P_{\mathrm{AS:B}}E_{\lambda}}^{\overline{\mathrm{PSD}}_{(+)}[\hat{N}_{\mathrm{SN:B}}]}}{|C_{[\mathrm{w}]\mathrm{AS:B}}|^2} \Big) \tag{2.131}$$

This expression provides the RMS noise power at each positive frequency, referred to Michelson DARM units. This is useful to relate the measurement to other noises seen in the instrument, but the model ultimately derives from a correlation-function which must be propagated consistently through all of the projections of the data-analysis. With all of the projections applied consistently, the observations of the data analysis can be directly compared with prediction. This is advantageous because the statistics of data-points are usually best described in the coordinates of the measurement. Any transformations of the data to put it into different model-coordinates (especially nonlinear ones) complicate the distributions of the data. For this reason, the statistical tests are done directly on cross-spectrum estimators in units of $\frac{m^2}{\mathrm{Hz}}$ rather than first converting to the RMS units $\frac{m}{\sqrt{\mathrm{Hz}}}$.

Note the variance! It is not quite the same as for the radiometer method. It carries two factors of the variance for *real* templates, but the coefficient on the left applies the scaling for the CSD estimator generated from *complex* templates. The 2x interferometer method gains a factor of 2 integration-time over the radiometer method, but otherwise has the same scaling.

2.12.3 Hypothesis-Test using a Prediction-Normalized estimator

For the final experiment, the average Holographic-noise into the interferometer is desired to relate estimates between frequencies, so all of the data will be normalized against the model to give a *model-spectral-density*. For these derivations, variance terms from the Holographic noise itself are dropped with the assumption that the noise-signal is very small and will not contribute largely to the likelihood-intervals. Dropping the term in this manner follows from the central-limit theorem and can be proven rigorously using strong versions of the central-limit theorem using the full χ^2_2 or Gaussian statistics that the power and cross spectral densities have [9].

$$\hat{\Theta}(F) = \frac{\hat{M}(F)}{\mathrm{E}[\hat{M}(F)]} \tag{2.132}$$

$$\mathrm{E}[\hat{\Theta}(F)] = 1 \tag{2.133}$$

$$\textsc{Var}[\hat{\Theta}(F)] = \frac{1}{2T_{\mathrm{span}}\left(\Xi^{(+)}_{\delta}(F)\right)^2}\left(\frac{2P_{\mathrm{AS:A}}E_{\lambda}}{|C_{[\mathrm{w}][\mathrm{m}]\mathrm{AS:A}}|^2}\right)\left(\frac{2P_{\mathrm{AS:B}}E_{\lambda}}{|C_{[\mathrm{w}][\mathrm{m}]\mathrm{AS:B}}|^2}\right) \tag{2.134}$$

The final significance can be estimated for an experiment with two perfect interferometers through a specific band of frequencies by including the time-bandwidth factors from the Welch-method (contributing the $\frac{4}{3}$ to the variance estimate) and performing a variance-weighted integral over the band. Note that although the expectation of $\hat{\Theta}(F)$ is 1 (unitless), its variance as shown in eq. (2.134) actually has units of Hz. This motivates its usage as the natural[1] weighting to form an estimator that is also unitless and has a unitless variance:

$$\hat{\Theta}_{\Sigma} = \mathrm{E}\left[\int_{\mathbb{F}} \frac{\hat{\Theta}(F)}{\textsc{Var}[\hat{\Theta}(F)]}\mathrm{d}F\right]^{-1} \cdot \int_{\mathbb{F}} \frac{\hat{\Theta}(F)}{\textsc{Var}[\hat{\Theta}(F)]}\mathrm{d}F \tag{2.135}$$

1. Assuming generic weighting function and minimizing the variance functional through the calculus of variations proves it to also be the optimal weighting.

$$\mathrm{VAR}[\hat{\Theta}_\Sigma] = \frac{4}{3}\int_{\mathbb{F}}\int_{\mathbb{F}} \frac{\mathrm{VAR}[\hat{\Theta}(F_0)]\delta[F_0-F_1]}{\mathrm{VAR}[\hat{\Theta}(F_0)]\mathrm{VAR}[\hat{\Theta}(F_1)]}\mathrm{d}F_0\,\mathrm{d}F_1 \cdot \left(\int_{\mathbb{F}} \frac{\overbrace{\mathrm{E}[\hat{\Theta}(F)]}^{1}}{\mathrm{VAR}[\hat{\Theta}(F)]}\mathrm{d}F\right)^{-2} \tag{2.136}$$

$$= \frac{4}{3}\left(\int_{\mathbb{F}} \frac{1}{\mathrm{VAR}[\hat{\Theta}(F)]}\mathrm{d}F\right)^{-1} \tag{2.137}$$

$$= \frac{4}{3}\cdot\frac{1}{\left(\Xi_\delta^{(+)}(0\mathrm{Hz})\right)^2}\cdot\left(\frac{\lambda}{4\pi}\right)^4\left(\frac{2E_\lambda}{P_{\mathrm{BS}}}\right)^2\cdot\left(2T_{\mathrm{span}}\underbrace{\int_{\mathbb{F}}\left(\frac{\Xi_\delta^{(+)}(F)}{\Xi_\delta^{(+)}(0\mathrm{Hz})}\right)^2\mathrm{d}F}_{F_{\mathrm{span}}}\right)^{-1} \tag{2.138}$$

This is evaluated for a pair of 1kW interferometers (or 2kW interferometers each with 50% "junk" light). The bottom 500kHz is removed due to background systematic correlations. The imperfect quantum-efficiency of the photodiodes is also accounted.

$$\left(\frac{\lambda}{4\pi}\right)^4\left(\frac{E_\lambda}{P_{\mathrm{BS}}}\right)^2 \approx \left(\frac{1.064{\cdot}10^{-6}\mathrm{m}}{4\pi}\right)^4\left(2\cdot 6.24{\cdot}10^{18}\frac{1}{\mathrm{s}\cdot\mathrm{A}}\cdot 0.7\frac{\mathrm{A}}{\mathrm{W}}\cdot 1{\cdot}10^3\mathrm{W}\right)^{-2} \tag{2.139}$$

$$\approx \Big(\underbrace{2.56{\cdot}10^{-18}\frac{\mathrm{m}}{\sqrt{\mathrm{Hz}}}}_{\text{appears as 1.28 in two-sided PSD or standard-quantum-limit calculation}}\Big)^4 \tag{2.140}$$

$$\left(\Xi_\delta^{(+)}(0\mathrm{Hz})\right)^2 \approx \left(6.98{\cdot}10^{-21}\frac{\mathrm{m}}{\sqrt{\mathrm{Hz}}}\right)^4 \tag{2.141}$$

$$T_{\mathrm{span}} = 150\,\mathrm{hours} = 5.4{\cdot}10^5\mathrm{s} \tag{2.142}$$

$$F_{\mathrm{span}} = \int_{500\mathrm{kHz}}^{\infty}\left(\frac{\Xi_\delta^{(+)}(F)}{\Xi_\delta^{(+)}(0\mathrm{Hz})}\right)^2\mathrm{d}F \approx 760\mathrm{kHz} \tag{2.143}$$

$$\mathrm{VAR}[\hat{\Theta}_\Sigma] = \frac{4}{3}\left(\underbrace{\frac{2.56{\cdot}10^{-18}\mathrm{m}/\sqrt{\mathrm{Hz}}}{6.98{\cdot}10^{-21}\mathrm{m}/\sqrt{\mathrm{Hz}}}}_{367}\right)^4\Big(2\cdot\underbrace{5.4{\cdot}10^5 s\cdot 760\mathrm{kHz}}_{410{\cdot}10^9}\Big)^{-1} \tag{2.144}$$

$$\mathrm{SNR}[\hat{\Theta}_\Sigma] = \frac{1}{\sqrt{\mathrm{VAR}[\hat{\Theta}_\Sigma]}} \approx 5.82\sigma \tag{2.145}$$

The final result will have a number of variations affecting this factor. The interferometers ran a bit better than 1kHz equivalents, however external noise reduced the effective bandwidth.

Chapter 3

EXPERIMENTAL LAYOUT

The realization of the Holometer experiment goes far beyond the simple description of two overlapping Michelson Interferometers. The implementation consists of a considerable list of details which could all be considered (sometimes large) perturbations of that ideal description. The goal of testing the Holographic-Noise prediction will describing as many of those details as necessary to project the instrument back to that ideal case for comparison with the model.

This chapter will go over the exact layout and emphasize the deviations from the ideal Michelson picture. In the process it will touch on some of the practical difficulties faced. Exposing these difficulties is useful both to provide intuition about how the machine operates, as well as to list potential pitfalls in relating the analysis back to the length-sensing measurement. Due to the complexity of the system, many of the in-depth descriptions of the instrument will be embedded later in this work as needed to describe the calibrations and analysis in context with the data. Often they will presented as approximations or phenomenological simplifications of the optical system processes' occurring in the cross-terms between many modes indexed by time, frequency, upper/lower modulation sideband, location, transverse-shape, and of course also which of the two interferometers. To start on these details, it is worthwhile to quickly hit on a number of the scales and trade-offs that were made in optimizing for signal-sensitivity.

The first such detail is the exact geometry of the instrument. The two interferometers are co-located with a translation of $\sim$ 3ft to practically fit them at-site and to keep both similarly-level to the ground for consistent mechanical stability. Despite their proximity, the two instruments are as isolated as possible. They used separate readout electronics, separate vacuum systems to contain the beams, separate power-lines to their electronics and most importantly separate lasers to power each interferometer. Of course ideally they

would share only space-time - practically they only additionally share a common electromagnetic RF-background. The physical separation of the vacuum-systems enclosing the two interferometers is indicated in fig. 3.1 on the following page.

Although physically separate, the organization of each machine is as similar as possible. Particularly the laser beam-sources conditioning table layouts preparing the beams for the interferometer. It is worth discussing the laser-sources in some detail. The experiment uses 1064nm Nd:YAG lasers. Although at the same wavelength, each laser operates at different frequencies, separated by many GHz and floating incoherently between the two. Using a shorter-wavelength would seem to linearly improve sensitivity, but also reduces the rate of photons. In the end the sensitivity improves only to the square-root of the wavelength. The Nd:YAG laser-technology for 1064nm, however, hits the best balance for the experiment between technical-noise impressed from the laser itself vs. emitting many photons to count. This last point is critical as technical-noise from the imperfect light sources is a major background analyzed later. The lasers provide 2W each, which after a series of transport, conditioning optics and quality-monitor pickoffs becomes $\sim$ 1W towards each interferometer.

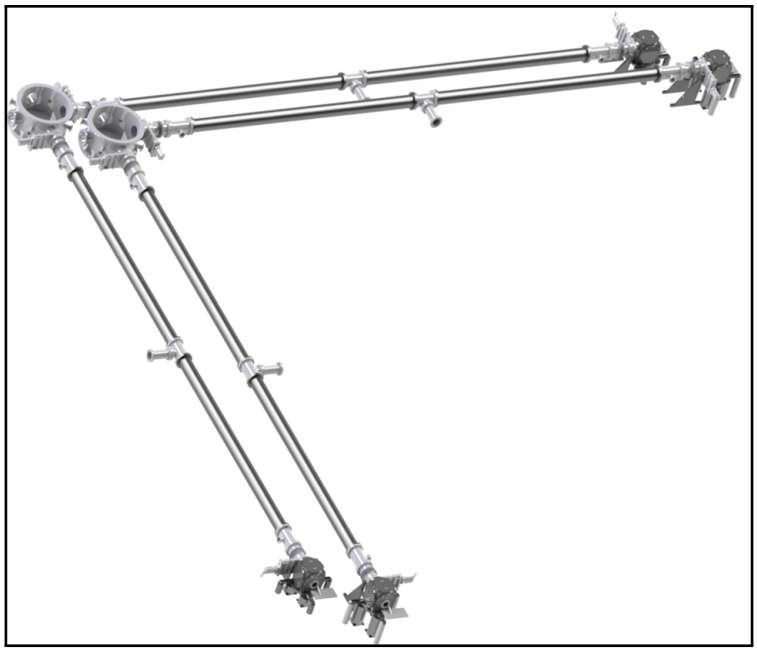

Figure 3.1: Layout of the vacuum enclosures of both interferometers. The vessels and tube-diameters are to scale, but the arm-lengths shortened to 7m rather than 40m for clarity. Beam travels downward from the top-left to enter the circular-vessels, crosses the Power-Recycling-Mirror immediately inside and then the beamsplitter at the vessel-center. It then travels each arm to the cubical end-stations, reflects and returns to the center. The Michelson asymmetric-port output exits the vessels to the left.

3.1 Power Recycling

Given the poor time-bandwidth scaling of a 2-interferometer buried-noise search. The advantage of higher beam power than 1W is essential. The integration time required for a given significance *scales linearly* with the power in *either interferometer*. This motivates the most major difference from the theoretical-descriptions - the experiment actually uses *power-recycled* Michelsons. The usual version, hereafter referred as the one-pass Michelson, conserves laser power between its two output ports. One of those ports being the typical output shown monitoring the destructively-interfered beam, the other is actually overlaid on the input laser, acting to reflect the constructive interference at the beamsplitter back to the input.

This reflected light allows a configuration whereby an additional mirror is inserted to

form a resonant Fabry-Perot cavity (etalon) between itself and the reflecting Michelson. This technique has many advantages, all deriving from consequences of the resonant enhancement in light amplitude incident on the beamsplitter. The additional power acts to raise the shot-noise scaling term, P_{in}, that sets the statistical limits of the previous chapter. Two factors affect the quality-factor of the cavity resonance, the transmissivity of the new Power-Recycling-Mirror (PRM) and the round-trip loss through the Michelson. Scattering and absorption add to the round-trip loss, but the light leaking out of the traditional destructive-interference output for measurement also adds to the loss. Fortunately, the shot-noise limited detection-rate derived in the previous chapter indicates saturation for *any* operating leakage that is in the quadratic-minimum of the output's sinusoidal interference. In practice, if the leakage is too-small then technical noise terms will dominate over shot-noise, so some balance must be made.

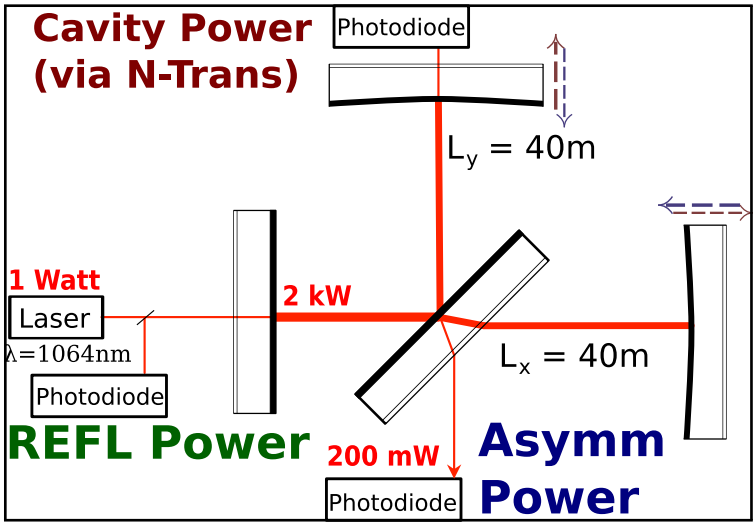

Figure 3.2: Basic layout of the Power-recycled interferometers with the major diagnostics-ports labelled. The Asymmetric port provides the broadband signal output, but all of the ports are useful at low-frequencies to determine the internal state of the resonant system. The reflection or REFL port is also used to derive a Pound-Drever-Hall laser/cavity resonance-condition frequency-offset discriminant.

All of the interferometer sensitivity is still derived from the destructive interference port - notated the asymmetric (AS) port of the instrument. The endmirrors have some trans-

missivity and are used to monitor the power-level of the cavity. Only the arm reflecting from the beamsplitter (the North arm) is used for this monitor and it is labelled NTrans. The light reflected at the input to the Fabry-Perot by the resonance boundary-conditions is monitored and its DC power-level is labeled REFL. These ports and the power-recycling layout are indicated in fig. 3.2 on page 69

3.1.1 Resonance Conditions

Power-recycling the interferometer imposes two main resonance conditions as requirements to operate.

The first condition is for the laser frequency must be at a multiple of the Free-Spectral-Range (FSR) of the interferometer cavity, defined by frequency-separation for the laser-wavenumber to be a multiple of the cavity-length. Alternatively, the common or average arm length (CARM) can be set to match the resonance with the laser. As the FSR boundary-conditions depends on the average length of the interferometer arms and can be actuated either by the laser frequency or the common endmirror position. The periodic condition of FSR-multiples sets range/units for the state-space of CARM, whereas the cavity-resonance bandwidth sets the scaling within this space that residual common-arm noise or laser-frequency-noise must be suppressed to. For the Holometer at nominal operation the FSR is 3.8MHz vs. and has a cavity-bandwidth of 600Hz FWHM optically, which generally translates to a 300Hz low-pass of any discriminant derived from it[1].

The second resonance condition maintains the interference at the beamsplitter to sit at a constant fringe-offset. This is the differential-arm (DARM) degree of freedom and is actuated by the endmirror differential position. The periodic fringe sets 1064nm of state-space. The residual noise scale depends on the operating point. For power storage of 1000x,

1. A laser frequency-detuned from the cavity can generate discriminants which violate this rule. The 300Hz low-pass is noted as the *cavity-pole*. Optical power-measurements fold the response through the detuning and can create resonant-discriminants. This is the principal behind signal-recycling in modern resonant interferometers

destructive interference must limit the ASymm port power coupling to $\sin^2(\frac{2\pi}{\lambda}L_\delta) < 1/1000$, or $L_\delta < 5\text{nm}$.

Together, these resonance conditions setup a state space that must be maintained to a part in one-millionth to maintain within linear output region. Although the predicted signal is so small to always act within a linear-region, the calibrations and interpretation of the photodiode-outputs requires maintaining the CARM and DARM parameters well-within that space.

3.2 Modeling the Resonant Interferometer

The complexity signal-flow diagrams for the Michelson in chapter 2 took a considerable jump with the introduction of phase-sideband frequencies. That complexity turns out to be essential to describe the signals that are output with power-recycling. The reason for this is the inherent nonlinearity of the Fabry-Perot resonance and its sensitivity to the loss out of every port. Figure 3.2 on page 69

These nonlinearities prevent the asymmetric-port from having a sinusoidal response at its DC operating point. The signal-flow of the PR-Michelson is given in fig. 3.3 on page 75. Its equivalent scattering-matrix calculation can be solved analytically to express the outputs of this machine as a function of the differential-arm, L_δ, offset. Also plotted are the responses of other ports. The Cavity-Power signal is measured by-proxy of the North-transmission photodiode (NTrans). The shape of these signals is indicated in fig. 3.4 on page 76. Note the square-Lorentzian shape of the cavity-power. This shape multiplies the Michelson sinusoidal coupling to create the PR Asymmetric-port output in blue. Dividing those two signals then recovers the Michelson. The REFL port sees nearly the inverse of the AS port by conservation of energy. It is plotted in fractions of the input-power as that is the easiest to calibrate through all of the transport-optics.

DARM length modulations through the endmirrors affect the loss coefficient of the AS-

port. This modulation interacts with the frequency-scales of the resonance. Far below the cavity-pole frequency, the slow change of the round-trip loss as a large effect on the power-gain of the cavity, which scales any photodiode measurement of that power times a coupling out of the cavity. Above that frequency the cavity cannot react to respond so the system behaves more like a traditional one-pass Michelson. Finally the complexity of endmirror sideband-generation must be applied to the power-recycled case. It is indicated in fig. 3.5 on page 77

This recovery of broadband response above the cavity-pole is good for the experiment, as that frequency is well below the expected "start frequency" where seismic and laser technical noises cross below the shot-noise sensitivity limit. Near the cavity pole there is a transition-region. This region encompasses the reliable bandwidth of the control-system piezoelectric endmirror actuators and must be considered to calibrate the instrument.

Two major examples of the unusual *frequency* response of the power-recycled systems will be given, first showing the not-fully broadband AS-port response described above, and later the frequency-response of the Pound-Drever-Hall phase discriminant.

3.2.1 Model of Asymmetric-Port Response

These sideband models are complicated, and analytic expressions derived from them are usually too complex to manipulate. Instead, software packages are used to explore the interferometer parameter-space and determine all of the effects on the signal sensitivities. This was done for the Holometer for general signals using the established LIGO tool *Optickle*. The signal-flow technique with perturbative sidebands was implemented symbolically in Python by the author, to fit against real-controls data. The figures (3.6) and (3.7) display the not-fully broadband response as modelled with local software. The models agree with the *optickle* software of LIGO.

This effect is analyzed in the calibration chapter in section 4.5 on page 103

3.2.2 Pound-Drever-Hall

The power recycled interferometer uses the Pound-Drever-Hall technique to determine the offset between the laser frequency and the nearest cavity Free-Spectral-Range. This signal is typically presented in units of laser Frequency-Modulation, but those units are equivalent to the phase-modulation times the frequency of interest.

For the Holometer the use is twofold. It allows the laser to lock at 0Hz detuning from the cavity, even though the reflected-power at that offset is always at an extremum and has no derivative for gain as a discriminant. The Pound-Drever-Hall signal uses an EOM to dither the laser frequency, then mixes with the drive to measure the derivative of the reflected power. Now the 0Hz-detuning extremum represents a null of the signal, and has a nice linear region between the inflection-points of the reflected signal that sit at the Lorenzian FWHM, or $\pm$ the cavity-pole frequency.

This dither-analysis can only describe the DC-steady-state signal generated by the PDH-mixer output. With the EOM dither, the technique requires upper/lower frequency-sidebands in its scattering-network to describe even the DC signal. That's three-times more than DC signals of usual carrier-referenced measurements. Modulations on top of that dither to derive the mixer-output frequency-response require yet another 3x sidebands to describe. Again modelling is helpful to characterize the response.

The DC and AC responses are plotted in fig. 3.8 on page 79. These are shown across multiple operating points of the instrument. Note the low-pass response of the FM discriminant signal that begins at the cavity-pole. These plots are normalized by the modulation-index of the EOM driving the discriminant generating sideband. Both instruments of the Holometer are setup to use a modulation-index of about 10 milliradians RMS amplitude.

The FM-signal on the right can be converted to phase, where it will instead look like a high-pass that flattens at the cavity pole. Using the models, the phase-sensitivity the PDH method in this broadband-region can be derived with only a few parameters of the

interferometer, the PRM transmissivity, the cavity-power, and the input-power.

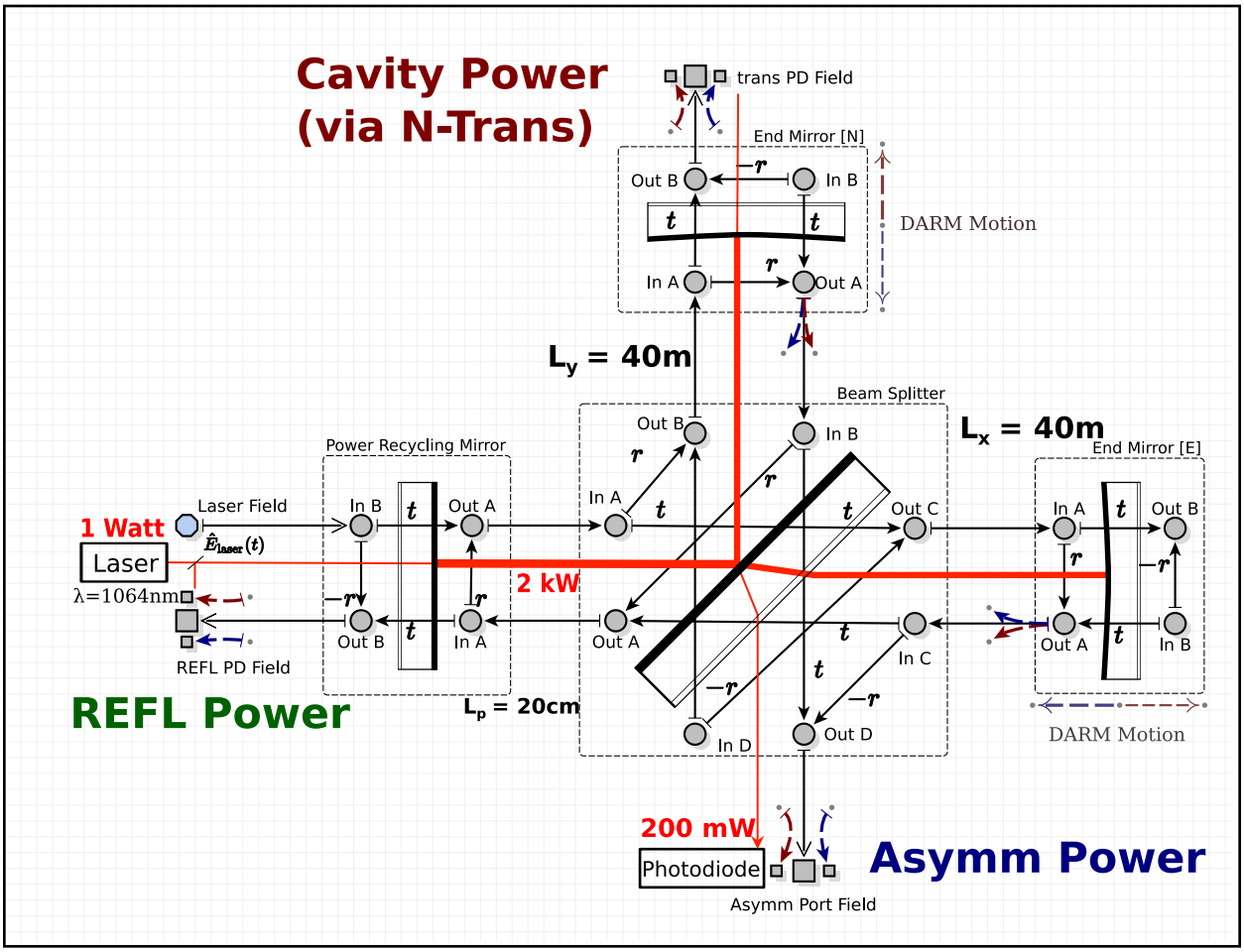

Figure 3.3: Signal flow for the resonant power-recycled interferometer. This diagram only represents the fields of single carrier frequency, but shows the blue and red-shifted sidebands that a DARM modulation would generate. This model also only represents a plane-wave mode, failing to capture misalignment and contrast-defect imperfections that require each state to be a vector of Hermite-Gauss modes.

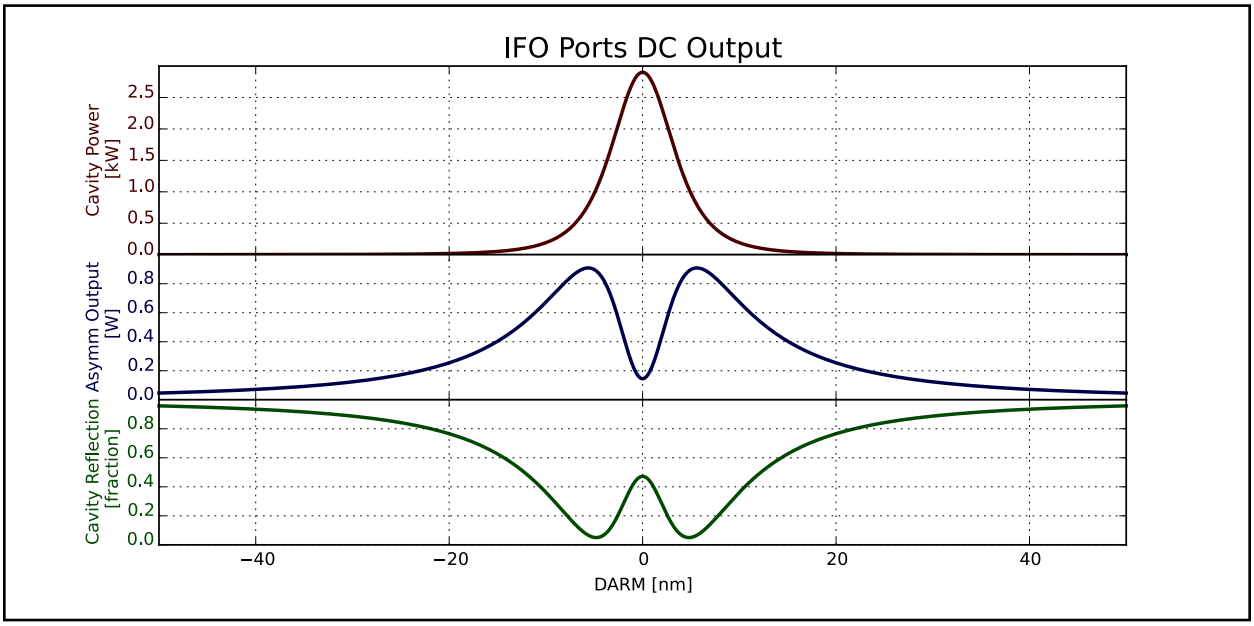

Figure 3.4: The simulated DC power measurements of the three major ports in a power-recycled interferometer.

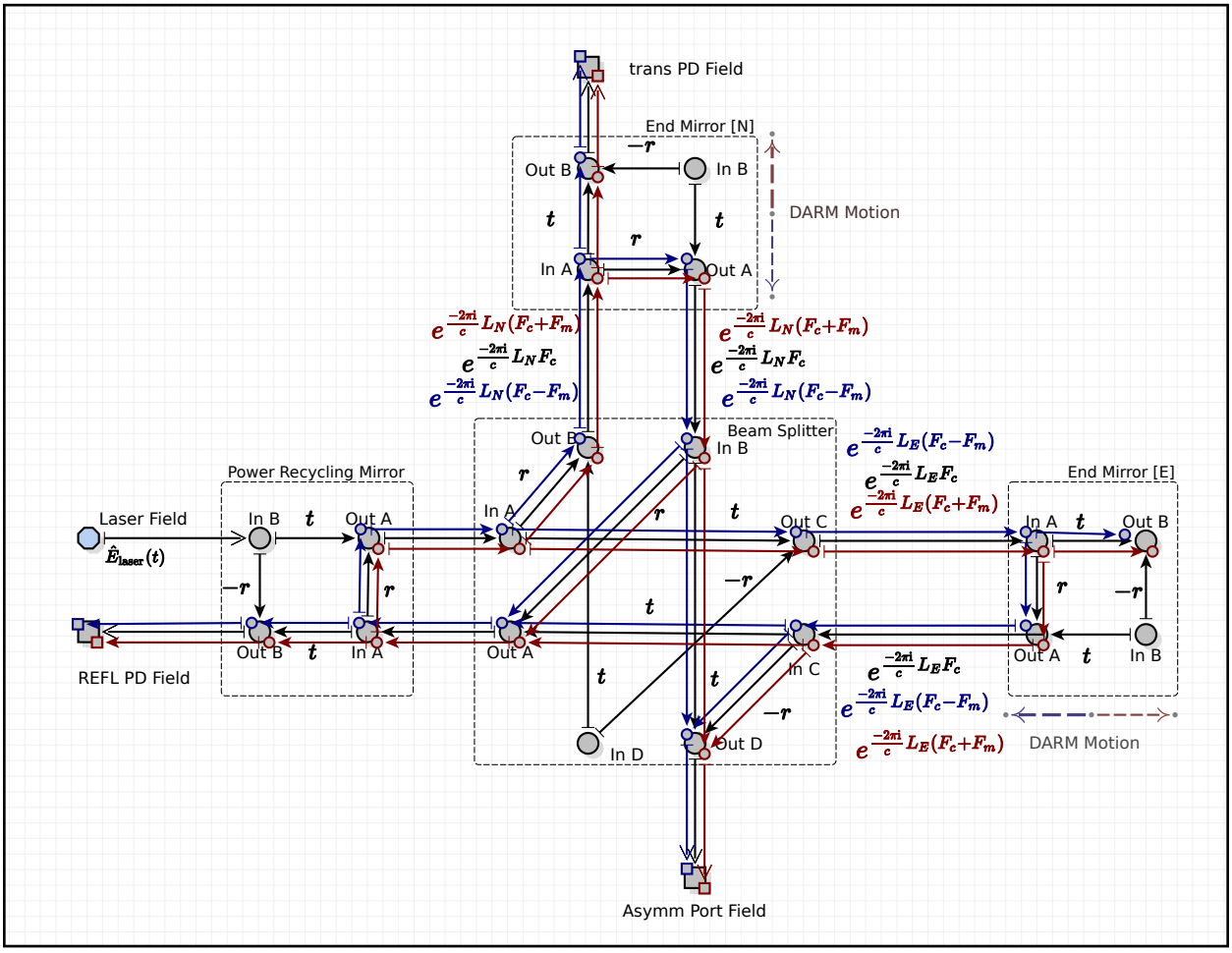

Figure 3.5: The signal-flow of the power-recycled Michelson with endmirror modulations. The edges showing the sideband-generation from the modulation are suppressed and only the first set of sidebands is shown. The sideband optical fields also experience resonant effects. They act to cancel against the carrier to ensure that the resonant stored-power decreases in-phase with increases of coupling out of the asymmetric-port. Above the resonant-frequency, the sidebands are ejected directly just as in the Michelson case and their effect on the stored-power is minimal. In the small-modulation limit, the sidebands can be treated as sources generated from a static steady-state carrier field. This graph can then be solved to generate the AC transfer functions of the interferometer.

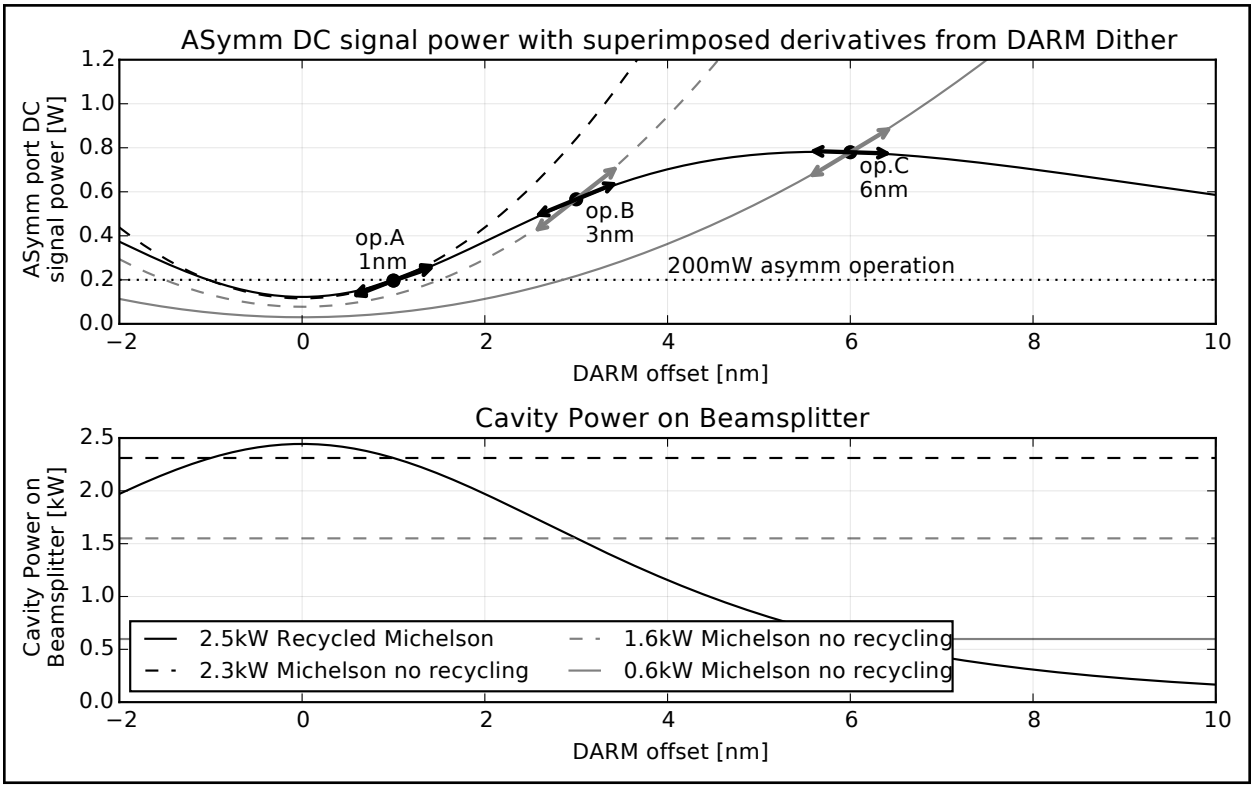

Figure 3.6: The two regimes of the AS-port response behave like derivatives in two extremes of the system. At low-frequencies, the response scales with the derivative of the "volcano" response first shown in fig. 3.4 on page 76. At high frequencies above the response-time of the effective Fabry-Perot, the system acts like a Michelson again and the sensitivity scales as the derivative of a sinusoid with large incident-power.

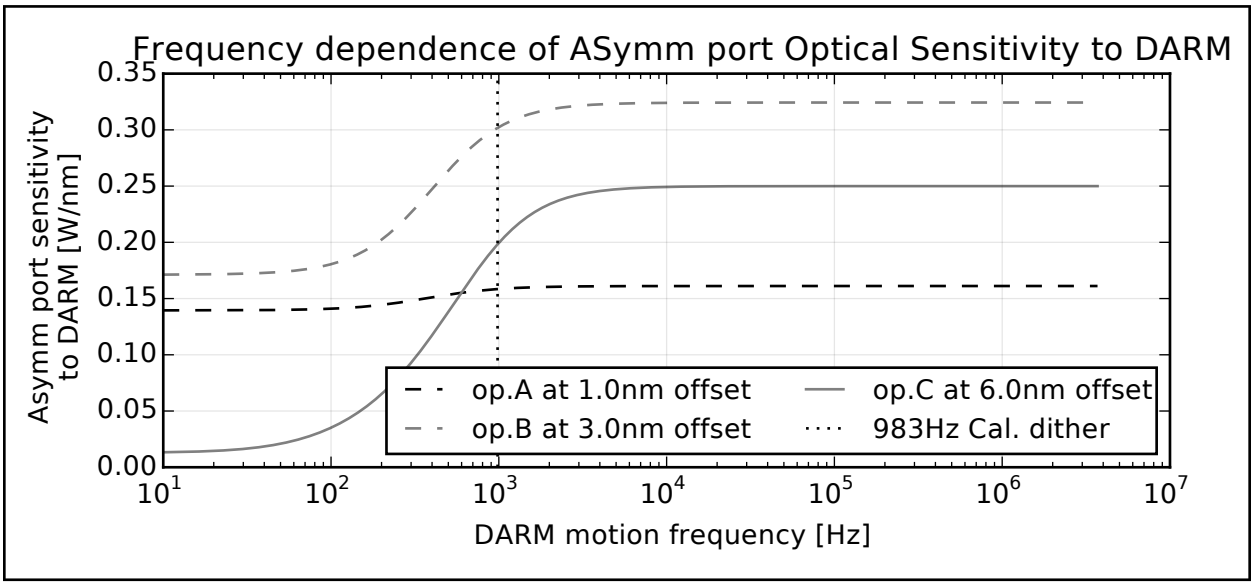

Figure 3.7: The frequency-dependence of the AS-port response across multiple operating-points. The transition region between AS-port regimes is apparent, and cuts off around 1kHz. This will require a relatively small adjustment when operating the instrument at 2.5kW, near the maximum of the cavity-power curve.

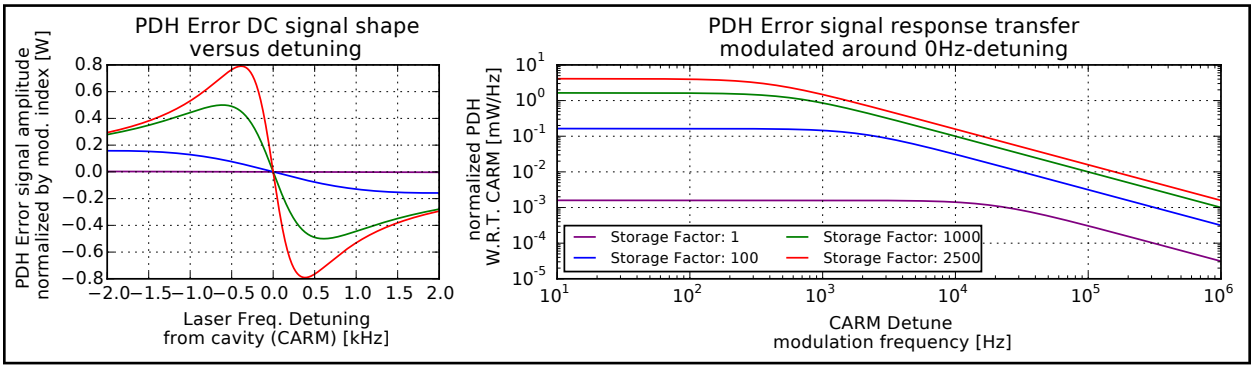

Figure 3.8: DC and AC signals for the frequency-sensitivity of the PDH discriminant of a power-recycled interferometer. The DC power level of the PDH mixer output on the left shows that the FM-offset measurement from the technique is nonlinear, but has a linear region within the full-width-half-max (FWHM) of the cavity resonance. As the cavity loss decreases, the resonance narrows, yet the sensitivity increases. The plot to the right shows the frequency response of the technique to FM modulations on the laser. The response shows that the cavity resonance applies a single pole low-passing the signal at the Half-width-half-max of the cavity resonance.

3.3 Beam Preparation

The laser beam must be prepared to match all of the resonance-conditions of the cavity. The PDH discriminants requires Faraday-isolators and EOMs, but in addition the polarization must be tuned for those Faraday-isolators, and the beam must be threaded through the EOMs. All of this requires a laser table to transport the beam, using powered optics the focus and defocus the beam as needed. Ultimately the PR-Michelsons are Fabry-Perot cavities tuned to a specific complex-beam-parameter, so the laser tables must arrange for that beam parameter to be match both in size and in alignment after transporting through a periscope from the table to the interferometer vacuum-system.

Figures (3.9) and (3.10) display the layouts used. These figures were prepared by Bobby Lanza, who was the primary operator physically mounting and aligning the optics on those tables.

The two interferometers have the names **L** and **T** from historical conventions of the experiment. The two tables and many measurements through the document will refer to the two machines by these names. The table layouts are not identical because of the differences in positioning some components can propagate and affect the idea alignment of later optics.

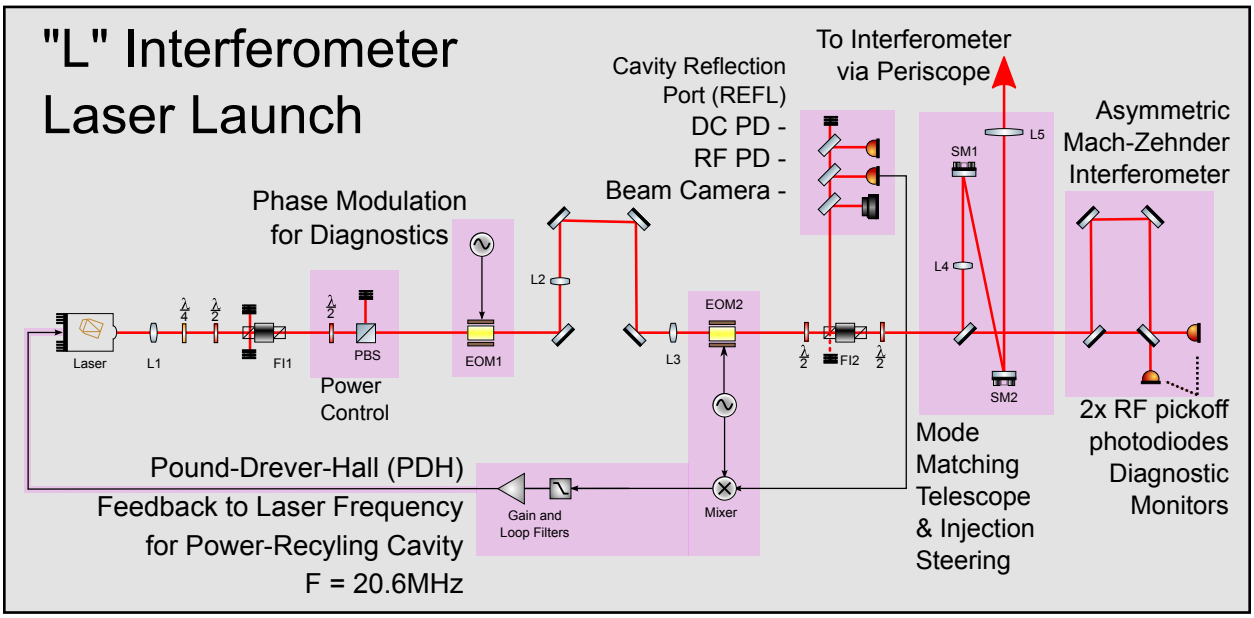

Figure 3.9: Laser launch table for the **L** interferometer.

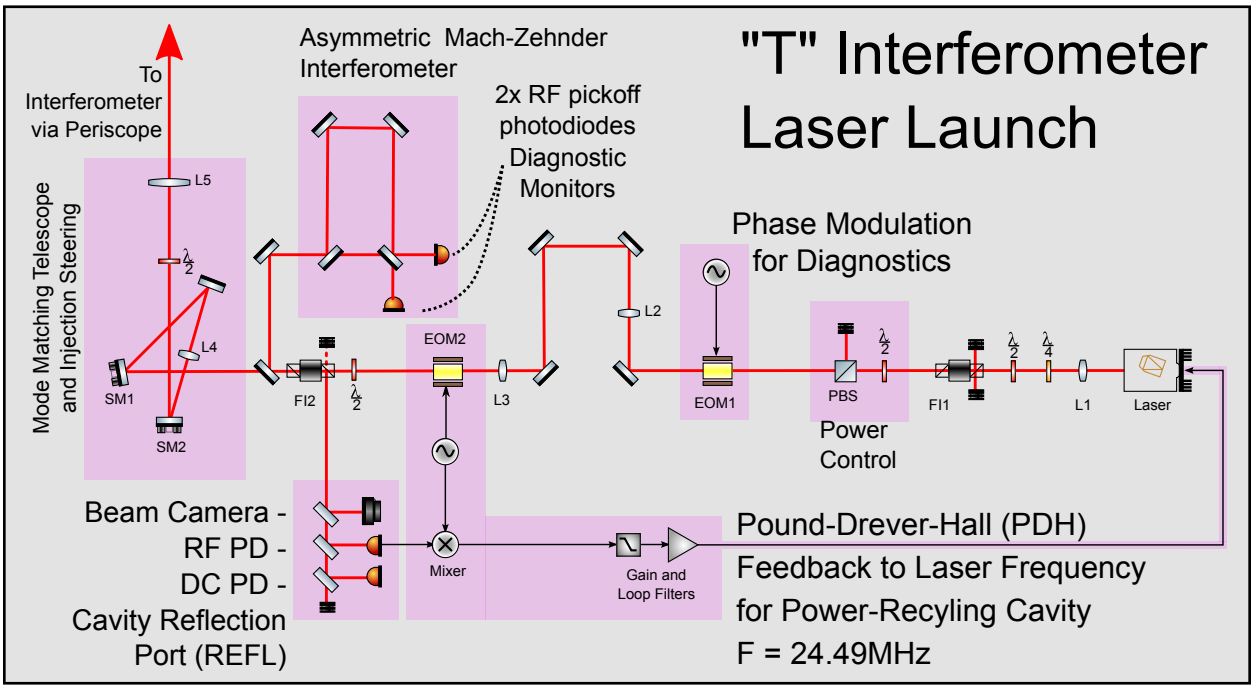

Figure 3.10: Laser launch table for the **T** interferometer

3.4 Asymmetric-Port Layout

The interferometer asymmetric port, located at the instrument vertex, splits the light to the two detectors, focuses, and splits pickoff light for cameras and quadrant photodiode for alignment/control. The imperfect optics prevent the beams returning to the beamsplitter from perfect destructive interference. This sets a nonzero limit to the minimum transmission of the incident power out of that port. This limitation is referred as "contrast-defect" and is around 50ppm in the Holometer-instruments. With 2.5kW of stored-power, this ensures that at least 125mW must be incident on signal-detectors. The defect-light does not carry any signal, so some additional transmission from the sinusoide-response offset of the Michelson is required, and in practice at least double the contrast-defect is necessary.

In total this calls for photodiodes which can absorb such a large incident power. The collaboration worked to modify stock diodes to have this capability. These are the 1811 diodes for the calibration of the vertex photodiodes.

These were only tested to handle 100mW, so the experiment splits the output of the interferometer to send equal parts two two separate detectors. It then measures both. CSD-matrix transformations can then synthesize a spectrum effectively representing single diodes.

Along the way to the signal diodes, the beam is picked-off to view in a camera as well as in a Quadrant-photodiode. This provides the control-system with data about the DARM operating point as well as alignment signals.

Chapter 4

LENGTH-SENSITIVITY CALIBRATION SCHEME

The RF data acquisition measures the photodiode output as a power spectrum in $\mathrm{Volts}^2/\mathrm{Hz}$, where volts indicates ADC volts at the end of signal cables through photodiode electronics measuring Watts out of a complicated optical instrument. The essential point of the Calibration scheme is to convert unreferenced units such as volts into physically relevant units.

Generating the physical units requires referencing multiple data-sources and components, so some notation must first be developed. Every photodiode (PD) calibration can have both a frequency dependence and time-dependence. The AS port photodiode calibrations convert volts into differential-arm length motion (DARM, L_δ). These diodes are labelled by their source interferometer, L or T, and which of two photodiodes each interferometer monitors at that port. For the 1st PD of the L, the calibration is labeled $\hat{C}_{[\frac{\mathrm{v}}{\mathrm{m}}]\mathrm{L1:ASPD:RF}}(t, F)$. This convention is wordy, displaying: the units - [m/v], the location - AS, the channel - RF, and the time and frequency as arguments. The auxiliary channels are not much discussed in this chapter, but their calibrations ultimately also all refer back to apparent motion of DARM as seen in AS port monitors due to the modes visible to that auxiliary channel. They are labelled similarly. For example the intensity monitor for the T is labelled $\hat{C}_{[\frac{\mathrm{v}}{\mathrm{m}}]\mathrm{T:IMon:RF}}(t, F)$.

These RF-calibration factors act to change the *basis* of the RF-DAQ CSD into physical units. This is done through the basis change method shown in section 2.10.3 on page 56 and 2.10.4. The calibration matrix is constructed and applied at an appropriate time-resolution to convert the voltage CSD matrix into AS port referred differential arm spectra. This matrix is diagonal, but the fusion of 2 PDs/interferometer requires non-square terms that could be considered non-diagonal if considered part of the calibration. The basis-converted CSD's are then averaged/integrated to generate science data.

4.1 Overview

The control system manages to hold the interferometer very precisely at a specific operating point defined by the optical system *outputs*. The values given for calibration factors all rely on knowledge of internal, independent states of the interferometer such as the differential-arm-length $\hat{L}_\delta$. Because only dependent variables are measured by photodiode voltages, the calibration factors are model dependent, first from solving the independent-states, then projecting those back through the model into calibrations. Furthermore, the power output at each interferometer port depends on a number of degenerate parameters which must be further calibrated to determine the system's response to physical motion. The primary model-output shown so far has been $C_{\frac{[\mathrm{W}]}{[\mathrm{m}]}\mathrm{AS}}$ from the Michelson chapter. This coefficient converts light fluctuations at the AS port into the equivalent DARM, $\hat{L}_\delta$, fluctuations. This factor, measured in-situ with a known length-modulation, provides a reference conversion that avoids all other model uncertainties. This is known as the end-to-end length calibration.

For a one-pass Michelson, the calibration is frequency-independent, but the storage time of a recycled Michelson imprints a dependence. The recycling cavity has frequency scales relevant through the reliable actuation frequencies of length-excitation, so some modelling is required to project calibrations from kHz frequencies into the MHz range of the tested model. The models are not highly sensitive to these external parameters at the nominal operating-point of the machines and do not propagate large errors from the additional parameters influencing the frequency-referencing model.

The end-to-end measurement must be done in-situ as RF science data is collected. The frequency scales and model-uncertainties pose additional unknown factors undermining a modelled calibration. A particular class of these unknowns are the cavity-couplings between Higher-Order-Modes (HOMs) which change over time as alignments drift, particularly the injection matching from the laser-tables into the resonant cavity, as well as the contrast-defect from beamsplitter/endmirror imperfections impacting the destructive interference along the

transverse face of the wavefronts combining at the beamsplitter.

A number of factors must be accounted for the calibration:

- All calibrations must be done "In-loop" of the control system and must account for loop response.
- The seismic and sensor noise in-loop requires optimization to see the physical injection of calibration lines, without excessively increasing DARM-loop residual RMS noise.
- The PZT drive voltage must be calibrated to motion.
- Assurance that this drive is purely longitudinal and does not drive angular modes corresponding to pure Hermite-Gauss Transverse Modes (TEM) $|\text{HG}{:}00\rangle$ with no cross-coupling into $|\text{HG}{:}10\rangle$).
- Calibration may only be done within 16kHz control Nyquist range and sufficiently below PZT resonances appearing around 1.5kHz.
- Data must be stored and later distilled into moment-by-moment calibration traces to merge with RF data as alignment and optical-mode couplings change.
- The AS port photodiodes also require calibration to cross-reference DC channels into the AC channels and voltages into photocurrent.

The final breakdown of these factors comes in eq. (4.12) on page 93 and eq. (4.14) on page 94, which reference sections of this chapter to detail the methods and sensitivities in determining calibration-factors for the Holometer. The sections leading to those equations explain the conventions and layouts motivating those factors, hopefully accounting for all known effects on the calibration.

4.1.1 Methods for in-situ Calibration

The end-to-end calibration operates by driving a known, physical motion and directly observing it in the instrument *while RF-data is being taken.* This actually implements either the coherent-line-oscillator the broadband-noise detection estimators discussed in chapter 2, but in a fashion to derive $C_{\frac{[\mathrm{W}]}{[\mathrm{m}]}\mathrm{AS}}(F)$ by detecting the magnitude of a known noise source into the photodiode power. The excitation is generated in software and injected into the endmirrors through calibrated piezoelectric actuators. With the excitation reference $\hat{S}_{\mathrm{exc}}$ available, the measurement follows from cross-spectrum estimators "locking-in" to that reference to detect the magnitude in photodiode power modulation, $\hat{D}_{\mathrm{ifo}}$, from the endmirror modulation.

In choosing the drive, either coherent single-frequency lines can be used, or a broadband noise. We chose to use multiple single-frequency sinusoidal drives at particular magnitudes tuned to provide sufficient statistical resolution without interfering with the control system. The power-spectrum of these lines injected is shown after further expository material in fig. 4.3 on page 95.

Although this method works essentially as described in 2, it does have some differences. At low frequencies the detectors are not photon-counting (shotnoise) limited. They have amplifier noise, and the ADC which reads them out generates bit-noise. This sets the noise-level for the continuous estimation of the $C_{\frac{[\mathrm{W}]}{[\mathrm{m}]}\mathrm{AS}}(F)$ value. The other complication is that the control-loop is acting to reduce ground-noise disturbances will also act on the reference magnitude of the excitation added. This chapter serves to detail how to account for these effects.

4.1.2 Units and labelling conventions

The units of signals in the FPGA-control-system are generally expressed as voltages, even though they often show on-screen in approximate physical units. In fact, require rigorous

analysis is needed to reference between FPGA values and physical units.

The indicator used for these unphysical reference point is the "boxing" of variables. The notation distinguishes true independent state of the physical system from the representation of that state inside of the control system. For example, DARM is physical state represented by $\hat{L}_\delta$, but in the actuation side of the controller, virtual-DARM is represented by $\lfloor\hat{L}_\delta\rceil$, which has units of voltage referenced through a chain of external voltage supplies applying further gain factors, to finally be converted by PZTs into physical motion. All of this chain can be drawn graphically to understand the layout, but as long as two endpoints are calibrated, the intermediate stages are collected and the details irrelevant. The distinction can be boiled-down to the property that in-situ $\lfloor\hat{L}_\delta\rceil$ can be recorded, $\hat{L}_\delta$ cannot, but only the latter is important. The control loop couples the chains of calibrations that are relevant, but linear model inversions can disentangle the relationships. The figures expressed in this chapter present these scattering calculations through signal-flow diagrams. The appendix B details the relationship between the CSD-estimators developed in chapter 2 and the scatter methods of signal-flow. CSDs are used with coherent reference channels to "select away" external noise sources. With the reduced nodes or state-variables in the scattering-network, it becomes easy to simplify and determine what measurement or chain of frequency-dependent coupling-constants are derived through the ratio of two cross-spectral-density measurements. For any three state-variables, the relative transfer of $\hat{z}$ into $\hat{x}$ vs. into $\hat{y}$ is computed with CSDs and denoted as:

$$\widehat{\textsc{Xfer}}[\hat{z}:\hat{x}\Rightarrow\hat{y}] = \frac{\widehat{\textsc{Csd}}[\hat{y},\hat{z}]}{\widehat{\textsc{Csd}}[\hat{x},\hat{z}]} \tag{4.1}$$

The result including the notion of boxing is that all in-situ measurements will be of the form $\overline{\textsc{Xfer}}\big[\lfloor\hat{z}\rceil:\lfloor\hat{x}\rceil\Rightarrow\lfloor\hat{y}\rceil\big]$, but the physical and model calibrations will have the non-virtual form $\overline{\textsc{Xfer}}[\hat{z}:\hat{x}\Rightarrow\hat{y}]$. This makes it readily apparent that ex-situ measurements of the signal-flow links (calibration coefficients) $\overline{\textsc{Xfer}}\big[\lfloor\hat{y}\rceil\Rightarrow\hat{y}\big]$, $\overline{\textsc{Xfer}}\big[\lfloor\hat{x}\rceil\Rightarrow\hat{x}\big]$ will be necessary.

In the end, the physical calibrations which express the physical relation between two unboxed states cannot take the form of eq. (4.1) on page 87 and instead the estimates must be built as:

$$\overline{\mathrm{XFER}}[\hat{z}:\hat{x}\Rightarrow\hat{y}] = \underbrace{\overline{\mathrm{XFER}}\big[\lfloor\hat{z}\rceil:\lfloor\hat{x}\rceil\Rightarrow\lfloor\hat{y}\rceil\big]}_{\text{in-situ}} \underbrace{\left(\frac{\overline{\mathrm{XFER}}\big[\lfloor\hat{z}\rceil:\lfloor\hat{y}\rceil\Rightarrow\hat{y}\big]}{\overline{\mathrm{XFER}}\big[\lfloor\hat{z}\rceil:\lfloor\hat{x}\rceil\Rightarrow\hat{x}\big]}\right)}_{\text{ex-situ}} \tag{4.2}$$

Which in this notation, naturally motivates a scheme for generating the measurement estimators

$$\widehat{\mathrm{XFER}}[\hat{z}:\hat{x}\Rightarrow\hat{y}] = \underbrace{\left(\frac{\widehat{\mathrm{CSD}}[\lfloor\hat{y}\rceil,\lfloor\hat{z}\rceil]}{\widehat{\mathrm{CSD}}[\lfloor\hat{x}\rceil,\lfloor\hat{z}\rceil]}\right)}_{\text{in-situ}} \underbrace{\left(\frac{\widehat{\mathrm{XFER}}\big[\lfloor\hat{z}\rceil:\lfloor\hat{y}\rceil\Rightarrow\hat{y}\big]}{\widehat{\mathrm{XFER}}\big[\lfloor\hat{z}\rceil:\lfloor\hat{x}\rceil\Rightarrow\hat{x}\big]}\right)}_{\text{ex-situ}} \tag{4.3}$$

The ex-situ measurements are not yet expressed as CSD ratios, but will eventually be. They will need additional cross referencing to create "natural" model conversions between virtual signals and physical signals. For example, the one-pass Michelson sweeps out a sine at its AS port as $\hat{L}_\delta$ sweeps a full wavelength, $\hat{P}_{\mathrm{AS}} = P_{\mathrm{in}}\sin^2(\frac{2\pi}{\lambda}\hat{L}_\delta)$. The sweep measures a natural scale for the virtual-photodiode $\lfloor\hat{P}_{\mathrm{AS}}\rceil$ to calibrate into physical units. The CSD-ratios of the measurement still only contain boxed-values, but a calibration from a time-domain measurement removes the box. This example is demonstrated and used in section 4.4 on page 98.

4.2 Layout between Acoustic-Control Loop and RF signal chain

As indicated in chapter 3, on layout, a control system must mediate to maintain the resonance conditions necessary for power-buildup and consistent operation. This control-system is also used as a readout of all of the "slow" < 32kHz channels. Included in this readout are the DC-channel outputs of all of the signal-photodiodes. Figure 4.1 on page 90 provides a reference.

At the top is a representative collection of all of the channels and conditioning processes of the interferometer in-loop. The full details inform some intuition about the machine.

This description flows clockwise from the top-left at the 6-signals entering the $\hat{L}_{\text{mirror}}$ testpoint. These represent the 6 piezoelectric-actuator degrees of freedom that compose the differential-arm-length actuation, with their couplings determined through geometry. This has a gain of 1 conversion into the true DARM-offset, $\hat{L}_{\delta}$, of the machine, but seismic noise along the baseline also superposes on that offset. The box represents a linearization of the optical interferences and boundary conditions impressing signals on many photodiodes. All of those diodes measure photocurrent-signals, but that representation is immediately obscured into voltages by readout electronics. Those voltages are transported, Nyquist-filtered and then read by ADCs.

The ADC moves the data into the digital controller, which records many of the values (circled in green). Other than data collection, some pickoff controls photodiodes are rough-calibrated and combined to form a linear discriminant of the DARM operating-point-error. This discriminant is filtered with a linear control-transfer optimized to reduce RMS distance from the nominal operating-point. The output of this is represented $\lfloor \hat{L}_{\text{ctrl}} \rceil$, and where the controller is highly effective, $\lfloor \hat{L}_{\text{ctrl}} \rceil \approx \hat{N}_{\text{seismic}}$. The calibration excitation-drive channel, $\lfloor \hat{L}_{\text{exc}} \rceil$ is then coadded to form the virtual-representation of the mirror-offset $\lfloor \hat{L}_{\delta} \rceil$. That representation is then filtered to compensate for piezo-mirror resonances and converted into the 6 voltages corresponding to linear motion across the 6 actuators. Those voltages enter HV-*de*whitening filters that high-pass, then are rendered into voltages by the DACs, are buffered, then enter the high-voltage supplies which invert the aforementioned HV-dewhitening filters. DAC bit-noise is added between the dewhiten-rewhiten step, so is effectively reduced at the cost of dynamic-range at high-frequencies. Finally these 6 PZT-drive signals are transported to the mirrors to complete the control-loop.

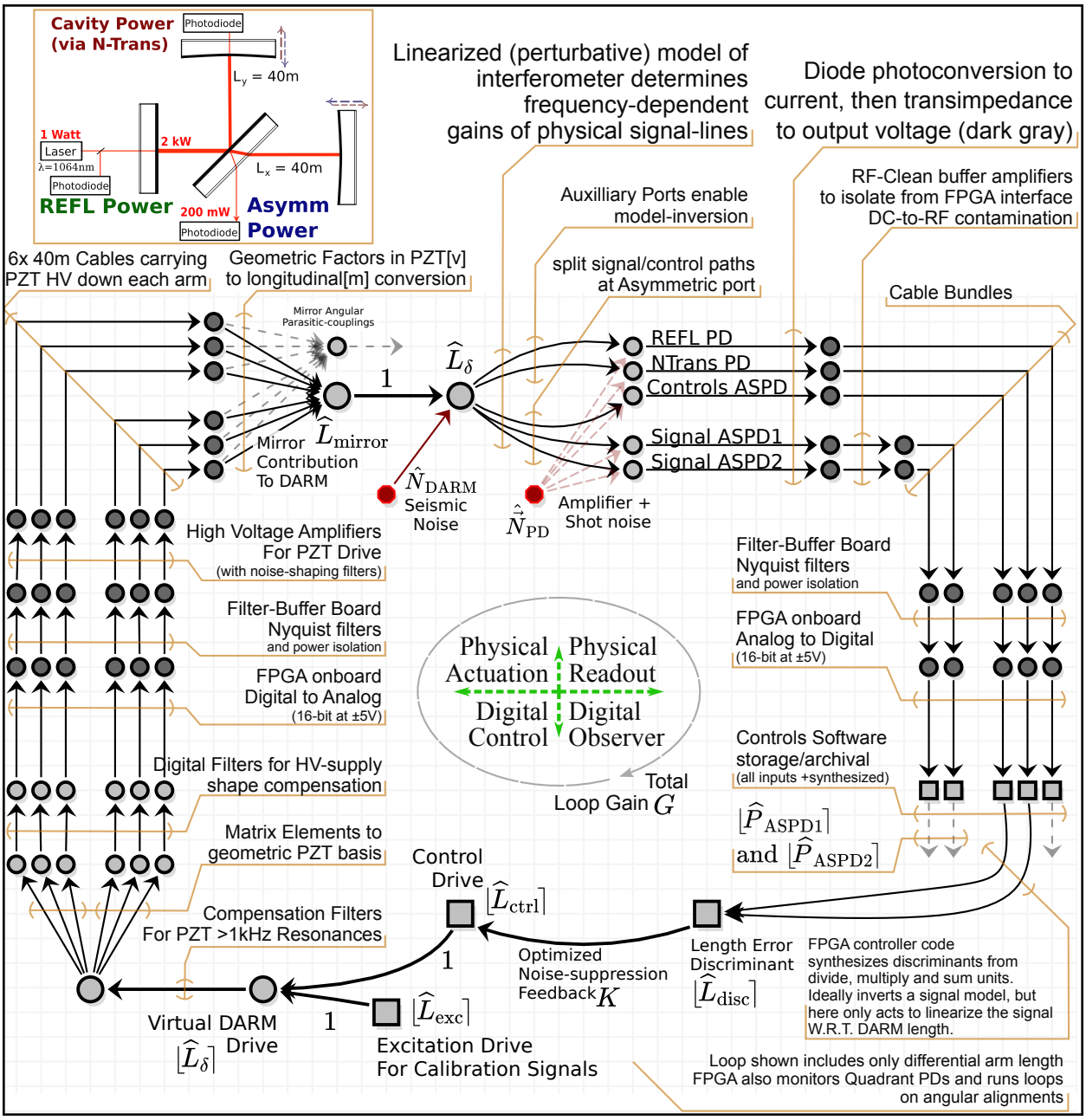

Figure 4.1: Diagram of the DARM Control and diagnostics loop. Each point represents a statistical state-variable of the system and orange lines annotate the transfer-coefficients from source state superimposing into destination states. Section 4.2 on page 88 fully details the contents. The lighter nodes represent true physical state, wheras dark nodes represent intermediate voltage signals. The square boxes are channels archived at 32kHz by the control system. This diagram showcases the many factors needed to run an optimized control loop, but can be highly simplified to collect the many intermediate terms.

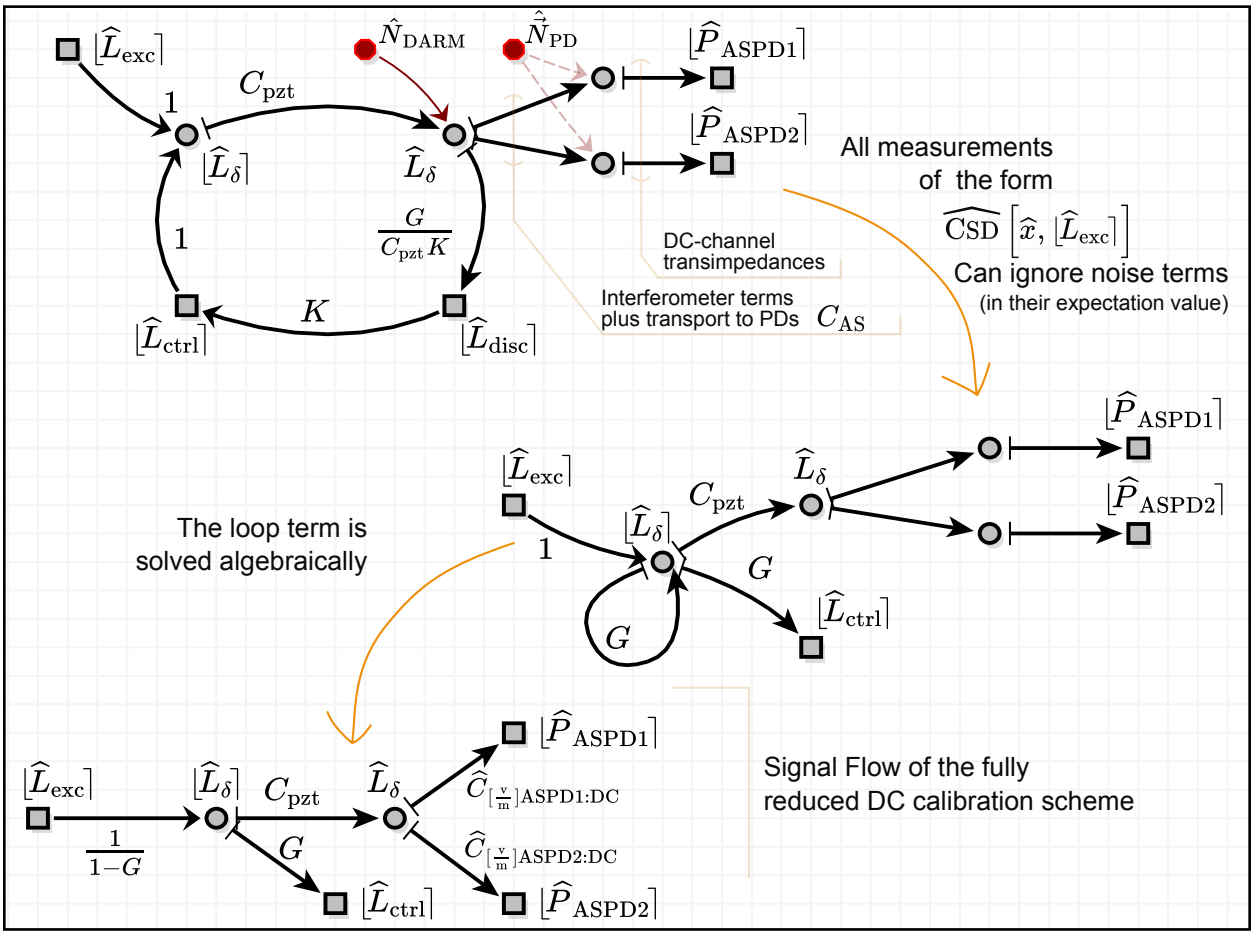

Figure 4.2: Reduction of the Fig. 4.1 graph into a reduced form suitable for describing the calibration. Measurements coherent with the excitation can ignore the noise terms. Note that the virtual DARM node is not recorded (is not a square), but the collection of terms allows every node to be reconstructed from the set of recorded terms. The $\hat{C}$ calibration terms are time-varying unknowns that are constructed from the recorded channels.

The coherent excitations injected through DARM-modulation lines are the central feature of the calibrations. CSD and transfer measurements "locked-in" to the excitation channel manage to ignore the external seismic and sensor noise in the DARM feedback loop. In particular, measurements with 2 other testpoints variables (boxed or unboxed) $\hat{x}$, $\hat{y}$ and taking the form:

$$\widehat{\mathrm{XFER}}\Big[\lfloor\hat{L}_{\mathrm{exc}}\rceil : \hat{x} \Rightarrow \hat{y}\Big] = \frac{\widehat{\mathrm{CSD}}[\hat{y}, \lfloor\hat{L}_{\mathrm{exc}}\rceil]}{\widehat{\mathrm{CSD}}[\hat{x}, \lfloor\hat{L}_{\mathrm{exc}}\rceil]} \tag{4.4}$$

Allow the first main simplification of fig. 4.2 on page 91 to ignore external noise. The series of reductions depicted resolves finally with a very direct flow of signals, without the complex loop process being apparent. Of all of the signals and effects depicted, one in particular is missing. That effect is the parasitic calibration biases from an imperfect conversion of the 6 PZT voltages into a DARM-modulation. Any residual will affect the interferometer output in complex ways and the output will not represent the signals as they would appear from the Holographic-noise. This issue of drive-purity is discussed in section 4.6 on page 107.

The essential measurement requires determining the recycled Michelson length-to-PD-power calibration, converting physical motion into a photocurrent or measurable voltage. ξ_{PD} is the conversion efficiency of the detector, in [A/W], and Z_{PD} is the transimpedance of the detector [V/A].

$$\hat{C}_{[\frac{\mathrm{V}}{\mathrm{m}}]\mathrm{ASPD:DC}}(t, F_{\mathrm{cal}}) = C_{[\frac{\mathrm{W}}{\mathrm{m}}]\mathrm{AS}}(F_{\mathrm{cal}}) \cdot \xi_{\mathrm{PD}} \cdot Z_{\mathrm{ASPD:DC}}(F_{\mathrm{cal}}) \tag{4.5}$$

$$= \overline{\mathrm{XFER}}\Big[\lfloor\hat{L}_{\mathrm{exc}}\rceil : \hat{L}_{\delta} \Rightarrow \lfloor\hat{V}_{\mathrm{PD}}\rceil\Big]_{F=F_{\mathrm{cal}}} \tag{4.6}$$

The in-situ transfer function reference $\hat{C}_{\mathrm{ASPD:DC}}(t, F_{\mathrm{cal}})$ shown in eq. (4.6) will be built from a series of measurements that complete the linkages between the points $\hat{L}_{\delta}$ and $\lfloor\hat{V}_{\mathrm{PD}}\rceil$. One of these points, $\hat{L}_{\delta}$, is physical which cannot be directly measured so additional ex-situ calibrations will cross-reference to measurable points (such as $\lfloor\hat{L}_{\delta}\rceil$) to generate estimates of

those couplings. These additional calibrations are derived from signal-flow, and they include terms for piezo-equivalent-motion $\left(\hat{C}_{[\frac{\mathrm{m}}{\mathrm{v}}]\mathrm{PZT}}\right)$ and the loop-suppression $\left(\frac{1}{1-G}\right)$.

$$\begin{aligned}\overline{\mathrm{XFER}}\Big[\lfloor\hat{L}_{\mathrm{exc}}\rceil \Rightarrow \lfloor\hat{V}_{\mathrm{PD}}\rceil\Big] &= \\ &= \overline{\mathrm{XFER}}\Big[\lfloor\hat{L}_{\mathrm{exc}}\rceil \Rightarrow \lfloor\hat{L}_{\delta}\rceil\Big] \cdot \overline{\mathrm{XFER}}\Big[\lfloor\hat{L}_{\mathrm{exc}}\rceil : \lfloor\hat{L}_{\delta}\rceil \Rightarrow \hat{L}_{\delta}\Big] \cdot \overline{\mathrm{XFER}}\Big[\lfloor\hat{L}_{\mathrm{exc}}\rceil : \hat{L}_{\delta} \Rightarrow \lfloor\hat{V}_{\mathrm{PD}}\rceil\Big]\end{aligned} \tag{4.7}$$

$$\overline{\mathrm{XFER}}\Big[\lfloor\hat{L}_{\mathrm{exc}}\rceil \Rightarrow \lfloor\hat{L}_{\mathrm{ctrl}}\rceil\Big] = \frac{\hat{G}_{\mathrm{loop}}}{1-\hat{G}_{\mathrm{loop}}} \tag{4.8}$$

$$\overline{\mathrm{XFER}}\Big[\lfloor\hat{L}_{\mathrm{exc}}\rceil \Rightarrow \lfloor\hat{L}_{\delta}\rceil\Big] = \frac{\hat{G}_{\mathrm{loop}}}{1-\hat{G}_{\mathrm{loop}}} + \underbrace{\overline{\mathrm{XFER}}\Big[\lfloor\hat{L}_{\mathrm{exc}}\rceil : \lfloor\hat{L}_{\mathrm{ctrl}}\rceil \Rightarrow \lfloor\hat{L}_{\delta}\rceil\Big]}_{=1 \text{ by signal-flow}} = \frac{1}{1-\hat{G}_{\mathrm{loop}}} \tag{4.9}$$

$$\overline{\mathrm{XFER}}\Big[\lfloor\hat{L}_{\mathrm{exc}}\rceil : \lfloor\hat{L}_{\delta}\rceil \Rightarrow \hat{L}_{\delta}\Big] = \hat{C}_{[\frac{\mathrm{m}}{\mathrm{v}}]\mathrm{PZT}}(F) \tag{4.10}$$

Solving eq. (4.5) on page 92 through these additional measurements presents a realizable moment-to-moment photodiode calibration:

$$\hat{C}_{[\frac{\mathrm{v}}{\mathrm{m}}]\mathrm{ASPD:DC}}(t, F_{\mathrm{cal}}) = C_{[\frac{\mathrm{w}}{\mathrm{m}}]\mathrm{AS}}(F_{\mathrm{cal}}) \cdot \xi_{\mathrm{PD}} \cdot Z_{\mathrm{ASPD:DC}}(F_{\mathrm{cal}}) \tag{4.11}$$

$$= \underbrace{\hat{C}^{-1}_{[\frac{\mathrm{m}}{\mathrm{v}}]\mathrm{PZT}}}_{\substack{\text{ex-situ}\\ \text{Michelson}\\ \text{sec. 4.4}}} \cdot \underbrace{\overline{\mathrm{XFER}}\Big[\lfloor\hat{L}_{\mathrm{exc}}\rceil \Rightarrow \lfloor\hat{V}_{\mathrm{PD}}\rceil\Big]}_{\substack{\text{live in-situ}\\ \text{sec. 4.7}}} \cdot \underbrace{\overline{\mathrm{XFER}}\Big[\lfloor\hat{L}_{\mathrm{exc}}\rceil \Rightarrow \lfloor\hat{L}_{\mathrm{ctrl}}\rceil\Big]^{-1}}_{\substack{\text{live in-situ}\\ \text{sec. 4.3}\\ \text{sec. 4.7}}} \tag{4.12}$$

All of the measurements contributing to eq. (4.5) on page 92 are made at low frequencies in the control system, where ($F_{\mathrm{cal}} \approx 1\mathrm{kHz}$) and the estimator $\hat{C}_{\mathrm{ASPD:DC}}(t, F_{\mathrm{cal}})$ is seen through the DC channel of the AS-port modified-NF1811 photodiodes. To calibrate higher

frequencies, the measurement must be referenced between DC-acoustic and RF frequencies.

$$\hat{C}_{[\frac{\mathrm{v}}{\mathrm{m}}]\mathrm{ASPD:RF}}(t,F) = C_{[\frac{\mathrm{W}}{\mathrm{m}}]\mathrm{AS}}(F)\cdot\xi_{\mathrm{PD}}\cdot Z_{\mathrm{ASPD:RF}}(F) \tag{4.13}$$

$$= \underbrace{\left(\frac{C_{[\frac{\mathrm{W}}{\mathrm{m}}]\mathrm{AS}}(F)}{C_{[\frac{\mathrm{W}}{\mathrm{m}}]\mathrm{AS}}(F_{\mathrm{cal}})}\right)}_{\substack{\text{ex-situ}\\ \text{modelling}\\ \text{sec. 4.5}}} \cdot \underbrace{\left(\frac{Z_{\mathrm{ASPD:RF}}(F)}{Z_{\mathrm{ASPD:DC}}(F_{\mathrm{cal}})}\right)}_{\substack{\text{ex-situ PD}\\ \text{characterization}\\ \text{chapter 5}}} \cdot \underbrace{\hat{C}_{\mathrm{ASPD:DC}}(t,F_{\mathrm{cal}})}_{\substack{\text{loop, control, PZT}\\ \text{eq. 4.12}}} \tag{4.14}$$

These different components are covered in the sections of this chapter as labelled in the equation. All of them must be applied, or accounted in error budgets. Figure 4.3 on the following page shows the power spectrum of the DARM calibration drive line-excitations. Four frequencies are included, but for this analysis only the highest frequency is used. The excitation amplitudes are given approximately. Tn the interferometer DARM-loop, the amplitudes are referenced to the point $\lfloor\hat{L}_{\delta}\rceil$ rather than $\lfloor\hat{L}_{\mathrm{exc}}\rceil$ and these amplitudes are detuned by the closed-loop-gain and not yet fully calibrated.

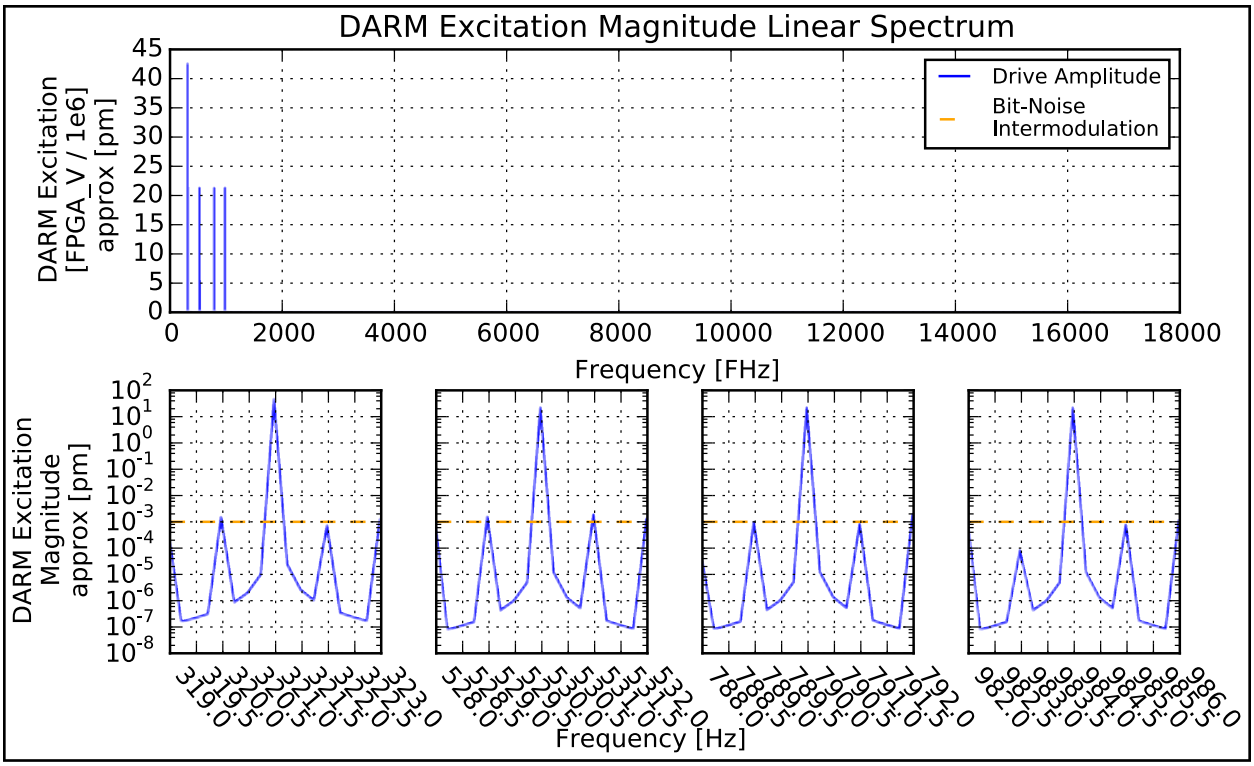

Figure 4.3: The drive represented as $\lfloor \hat{L}_{\text{exc}} \rceil$ approximately (∼30%) converted to picometer-amplitude of drive at four excitation frequencies. The bare graph on top shows their distribution and delta-function nature up to the 16384Hz Nyquist frequency. These frequencies represent the sources injected into the **T** interferometer. The lines of the **L** are shifted down in frequency by 1Hz.

4.3 Control Loop Corrections (in-situ)

The transfer notation used easily generates estimators as ratios of CSD's provided that the state-timeseries is available. For implementation limitations, only a subset of points are actually recorded from the digital control system. In particular, only the points $\lfloor \hat{L}_{\text{exc}} \rceil$, and $\lfloor \hat{L}_{\text{ctrl}} \rceil$ are recorded, but $\lfloor \hat{L}_{\delta} \rceil$ is not. Equation (4.9) on page 93 provides the means of constructing the point $\lfloor \hat{L}_{\delta} \rceil$ from them, so no data is lost.

The problem of "correcting for the loop" is really an issue with referencing transfer functions to appropriate system-state nodes. Physical measurements must originate from an excitation *out-of-loop*, such as $\widehat{\text{XFER}}\left[\lfloor \hat{L}_{\text{exc}} \rceil \Rightarrow \hat{x}\right]$. The physical measurement will ulti-

mately reference between the point that is physically *moved* by the excitation, $\hat{L}_\delta$, and the destination, $\hat{x}$, locked-in to the excitation-reference, $\widehat{\text{XFER}}\Big[\hat{L}_\delta \Rightarrow \hat{x}\Big]\lfloor\hat{L}_{\text{exc}}\rceil$. Ignoring for a moment the distinction between $\lfloor\hat{L}_\delta\rceil$ and $\hat{L}_\delta$, the "loop correction" is always a factor like $\widehat{\text{XFER}}\Big[\lfloor\hat{L}_{\text{exc}}\rceil : \lfloor\hat{L}_{\text{exc}}\rceil \Rightarrow \lfloor\hat{L}_\delta\rceil\Big]$ which moves the reference point from the out-of-loop excitation to the in-loop moving-actuator. If the transfer-functions are as between two in-loop points, the loop-correction is actually applied implicitly. Nevertheless it is useful to understand the correction applied implicitly or not, as it can affect the statistics and biasing of the calibration through the loop, as well as the stability of the system controlled.

In using signal-flow graphs, the language of loop-corrections is swallowed in to the language of "referencing points" using transfer functions. In this sense loop gain is merely a special type of coupling that is discovered as scattering network (signal-flows) are solved. Nevertheless, Loop-gain measurements tend to be useful for determining control stability and can impact the ability to reference between points with loop-corrections. There are two apparent ways of generating an estimate for $\hat{G}_{\text{loop}}$ which ultimately must be equivalent, but are worth comparing for the sake of the semantics and statistics of the measurement.

The first is the gain between "two-in-loop" points method, which is often used for quick measurements help in optimizations for control-stability.

$$\overline{\text{XFER}}\Big[\lfloor\hat{L}_{\text{exc}}\rceil : \lfloor\hat{L}_{\text{ctrl}}\rceil \Rightarrow \lfloor\hat{L}_\delta\rceil\Big] = \frac{\overline{\text{CSD}}\Big[\lfloor\hat{L}_\delta\rceil, \lfloor\hat{L}_{\text{exc}}\rceil\Big]}{\overline{\text{CSD}}\Big[\lfloor\hat{L}_{\text{ctrl}}\rceil, \lfloor\hat{L}_{\text{exc}}\rceil\Big]} = \hat{G}_{\text{loop}} \tag{4.15}$$

$$\Downarrow$$

$$\hat{G}_{\text{loop}} = \widehat{\text{XFER}}\Big[\lfloor\hat{L}_{\text{exc}}\rceil : \lfloor\hat{L}_{\text{ctrl}}\rceil \Rightarrow \lfloor\hat{L}_\delta\rceil\Big] \tag{4.16}$$

This certainly works, but it has some strange semantics in its strong *implicit* requirement that the lock-in channel $\lfloor\hat{L}_{\text{exc}}\rceil$ is added between the first ($\lfloor\hat{L}_{\text{ctrl}}\rceil$, denominator) point and second ($\lfloor\hat{L}_\delta\rceil$, numerator) point in the signal-flow such as shown in fig. 4.1 on page 90.

Furthermore, the loop affects the statistics of the measurement

$$\overline{N} = \left|\overline{\textsc{Csd}}\left[\lfloor\hat{L}_\delta\rceil, \lfloor\hat{L}_{\text{exc}}\rceil\right]\right|, \qquad \overline{D} = \left|\overline{\textsc{Csd}}\left[\lfloor\hat{L}_{\text{ctrl}}\rceil, \lfloor\hat{L}_{\text{exc}}\rceil\right]\right| \tag{4.17}$$

$$\begin{aligned}\textsc{Var}\left[\widehat{\textsc{Xfer}}\left[\lfloor\hat{L}_{\text{exc}}\rceil : \lfloor\hat{L}_{\text{ctrl}}\rceil \Rightarrow \lfloor\hat{L}_\delta\rceil\right]\right] = \frac{1}{\overline{D}^2}\textsc{Var}\left[\widehat{\textsc{Csd}}\left[\lfloor\hat{L}_\delta\rceil, \lfloor\hat{L}_{\text{exc}}\rceil\right]\right] \\ + \frac{\overline{N}^2}{\overline{D}^4}\textsc{Var}\left[\widehat{\textsc{Csd}}\left[\lfloor\hat{L}_{\text{ctrl}}\rceil, \lfloor\hat{L}_{\text{exc}}\rceil\right]\right] \\ + \frac{\overline{N}}{\overline{D}^3}\textsc{Cov}\left[\widehat{\textsc{Csd}}\left[\lfloor\hat{L}_\delta\rceil, \lfloor\hat{L}_{\text{exc}}\rceil\right], \widehat{\textsc{Csd}}\left[\lfloor\hat{L}_{\text{ctrl}}\rceil, \lfloor\hat{L}_{\text{exc}}\rceil\right]\right]\end{aligned} \tag{4.18}$$

The noise external to the loop is highly covariant between the two channels. This has the property of *always* biasing the measurement towards $\hat{G}_{\text{loop}} \to 1$, but this method of measurement does not indicate such bias without careful consideration of this complicated covariance (not done here).

The more semantically clear method is to always make loop measurements using the estimator.

$$\overline{\textsc{Xfer}}\left[\lfloor\hat{L}_{\text{exc}}\rceil : \lfloor\hat{L}_{\text{exc}}\rceil \Rightarrow \lfloor\hat{L}_\delta\rceil\right] = \frac{\overline{\textsc{Csd}}\left[\lfloor\hat{L}_\delta\rceil, \lfloor\hat{L}_{\text{exc}}\rceil\right]}{\overline{\textsc{Psd}}\left[\lfloor\hat{L}_{\text{exc}}\rceil\right]} = \frac{1}{1 - \hat{G}_{\text{loop}}} \tag{4.19}$$

$$\Downarrow$$

$$\hat{G}_{\text{loop}} = 1 - \frac{1}{\widehat{\textsc{Xfer}}\left[\lfloor\hat{L}_{\text{exc}}\rceil \Rightarrow \lfloor\hat{L}_\delta\rceil\right]} \tag{4.20}$$

The semantics of this measurement are much more clear as the form $\frac{1}{1-G}$ comes directly from the signal flow. If the excitation were moved anywhere else, then the loop-reduced signal flow would show a different form and be clear that the estimator must change to compensate. The aforementioned biasing is apparent from the nonlinearity of the loop estimator. For high-gain loops, The magnitude of $\textsc{Xfer}$ is small and the reciprocal recovers $G + 1$. Poor

SNR in the measurement will tend to make the XFER larger and the reciprocal will be biased too small to estimate $G+1$. Furthermore, the excitation measurement is noise-free, so there can be no covariance between the PSD and CSD and the SNR is easy to estimate. Since this estimator is equivalent to eq. (4.16) on page 96, this analysis applies to explain the large covariance of the two-in-loop gain measurement.

Equivalently, referencing to the control point before the insertion of the excitation generates a loop-gain estimate.

$$\overline{\mathrm{XFER}}\left[\lfloor\hat{L}_{\mathrm{exc}}\rceil : \lfloor\hat{L}_{\mathrm{exc}}\rceil \Rightarrow \lfloor\hat{L}_{\mathrm{ctrl}}\rceil\right] = \frac{\overline{\mathrm{CSD}}\left[\lfloor\hat{L}_{\mathrm{ctrl}}\rceil, \lfloor\hat{L}_{\mathrm{exc}}\rceil\right]}{\overline{\mathrm{PSD}}\left[\lfloor\hat{L}_{\mathrm{exc}}\rceil\right]} = \frac{\hat{G}_{\mathrm{loop}}}{1-\hat{G}_{\mathrm{loop}}} \tag{4.21}$$

$$\Downarrow$$

$$\hat{G}_{\mathrm{loop}} = \frac{\widehat{\mathrm{XFER}}\left[\lfloor\hat{L}_{\mathrm{exc}}\rceil \Rightarrow \lfloor\hat{L}_{\delta}\rceil\right]}{1+\widehat{\mathrm{XFER}}\left[\lfloor\hat{L}_{\mathrm{exc}}\rceil \Rightarrow \lfloor\hat{L}_{\delta}\rceil\right]} \tag{4.22}$$

The biasing of this measurement again arises from the nonlinear transform. The XFER here is near -1 for large, negative feedback G. Poor SNR will push the measurement away from -1, and for large noise N and measurement X, the equation will be biased according to $\frac{X+N}{1+X+N} \to 1$ as $N \to \infty$.

All of the loop considerations mentioned come together in the creation of the distilled timeseries discussed in section 4.7 on page 112. When these timeseries are averaged further, the loop-corrections are averaged before their nonlinear-transformations. This reduces the biasing from the nonlinearities.

4.4 Calibration from one-pass Michelson (ex-situ)

Operating the interferometers with the Power-recycling mirror misaligned sufficiently to prevent power recycling storage changes the optical system to a one-pass Michelson. This keeps the entire controls and electrical setup constant, particularly the endmirror PZTs. The

main change is that the light level on the beamsplitter is reduced in the cavity by a factor of $\sim 10^6$, from 2kW to 1mW. This changes dynamic-range requirements and noise levels for measurements taken in one-pass mode.

The one pass mode serves a number of purposes. For the final science result, it provides a very direct measurement of the PZT calibration, $\hat{C}_{[\frac{\mathrm{m}}{\mathrm{v}}]\mathrm{PZT}}$. This is done first by sweeping $\hat{L}_\delta$ to see the sinusoidal power output. The upper and lower limits set a natural scaling for the virtual-PD point $P_{\mathrm{low}} < \lfloor \hat{P}_{\mathrm{AS}} \rceil < P_{\mathrm{high}}$. With this scaling, the virtual point must relate to the differential arm-length as

$$\lfloor \hat{P}_{\mathrm{AS}} \rceil = P_{\mathrm{low}} + \left(P_{\mathrm{high}} - P_{\mathrm{low}}\right) \overbrace{\sin^2\left(2\pi \frac{\hat{L}_\delta}{\lambda}\right)}^{x} \tag{4.23}$$

$$\Downarrow \text{ one-pass Michelsons are broadband, so linearize}$$

$$x = \frac{\lfloor \hat{P}_{\mathrm{AS}} \rceil - P_{\mathrm{low}}}{P_{\mathrm{high}} - P_{\mathrm{low}}} \tag{4.24}$$

$$\widehat{\mathrm{XFER}}\Big[\lfloor \hat{L}_{\mathrm{exc}} \rceil : \hat{L}_\delta \Rightarrow \lfloor \hat{P}_{\mathrm{AS}} \rceil\Big] = \frac{4\pi}{\lambda}\sqrt{x(1-x)} \tag{4.25}$$

This equation has the fantastic property of relating a physical quantity into a virtual (measurable) quantity. Moving signal-flow arrows around, this transfer can solve for the calibration $\hat{C}_{[\frac{\mathrm{m}}{\mathrm{v}}]\mathrm{PZT}}$ by:

$$\widehat{\mathrm{XFER}}\Big[\lfloor \hat{L}_{\mathrm{exc}} \rceil : \lfloor \hat{L}_\delta \rceil \Rightarrow \lfloor \hat{P}_{\mathrm{AS}} \rceil\Big] = \widehat{\mathrm{XFER}}\Big[\lfloor \hat{L}_{\mathrm{exc}} \rceil : \hat{L}_\delta \Rightarrow \lfloor \hat{L}_\delta \rceil\Big]\widehat{\mathrm{XFER}}\Big[\lfloor \hat{L}_{\mathrm{exc}} \rceil : \hat{L}_\delta \Rightarrow \lfloor \hat{P}_{\mathrm{AS}} \rceil\Big] \tag{4.26}$$

$$\Downarrow$$

$$\hat{C}_{[\frac{\mathrm{m}}{\mathrm{v}}]\mathrm{PZT}} = \widehat{\mathrm{XFER}}\Big[\lfloor \hat{L}_{\mathrm{exc}} \rceil : \hat{L}_\delta \Rightarrow \lfloor \hat{L}_\delta \rceil\Big] = \frac{\widehat{\mathrm{XFER}}\Big[\lfloor \hat{L}_{\mathrm{exc}} \rceil : \lfloor \hat{L}_\delta \rceil \Rightarrow \lfloor \hat{P}_{\mathrm{AS}} \rceil\Big]}{\frac{4\pi}{\lambda}\sqrt{x(1-x)}} \tag{4.27}$$

Which are all measurable quantities. The initial formula (4.23) is insensitive to alignment, beam-quality and mode overlap. All of those degradations will set the low and high power

ranges, but will not affect the sinusoidal response which comes purely from the phase-offset between the transverse-mode vector between the two arms. Even the full representation of the Michelson in Hermite-Gauss mode vectors, no matter how poorly they may cancel between the arms, will interfere with sinusoidal response from the laser wavelength. Other than the arm-lengths, only Gouy phase can effect the phase-interference terms, but it is wildly insensitive compared to the longitudinal-motion phase. There is one large systematic term affecting this calibration, and that is residual cross-couplings or impurities that actually put the virtual DARM into angular modes $\lfloor \hat{L}_\delta \rceil \Rightarrow \hat{\theta}_{\delta x}$. Those will be discussed in section 4.6 on page 107.

Although eq. (4.27) on page 99 is valid at any alignment or operation, the terms are sensitive to *changes* of alignment and operational terms. The transfer-function measurement must occur with the exact same alignment and parameters as the DARM-sweep in order to apply the cross calibration.

With a consistent and unbiased measurement scheme, the statistics of the measurement should be considered. None of the control-systems photodiodes operate at the shot-noise limit, even in the power-recycled (PR) Michelson. The ground-noise for the control-system to suppress, passing through the instrument conversion, is so much larger than the length-sensitivity that the photodiodes would require very special frequency-dependent gains and other engineering to hit a quantum limit in the acoustic control band. Furthermore, operating in that regime it would not help the instrument. The residual noise of the DARM control loop up to the Unity-Gain-Frequency (UGF) where the loop suppresses no noise could only be lowered slightly but could not be made to hit sensor-noise limits.

The control systems are largely not dominated by photodiode amplifier noise either, they are dominated by the bit-noise of the ADC. For the one-pass mode, lower light-levels cause a relatively-larger bit-noise floor. This is remedied through two mechanisms, photodiode voltage gains and interferometer optical gain set by fringe-offset. For the former, the control-

port photodiode gain is increased 100x, and the input amplifier to the ADC is increased by 10. Voltage-gain adjustment compensates for 10^3 of the 10^6 drop in bit-noise limited sensitivity of the control-system. Although the interferometer lost optical-gain, some may be recovered between the PR and one-pass Michelsons. The PR interferometer must operate with the transmission out of the AS port, here (x), very small to maintain the high-power resonance-condition. In the one-pass, the gain dependence $\sqrt{x(1-x)}$ can be optimized at $x = \frac{1}{2}$ to give an increase in optical gain from $\sqrt{100\text{PPM}} = 1\%$ up to 50%. The operating point change with voltage gain recovers almost all of the control-system bit-noise limited sensitivity for the measurement.

Figure 4.4 on the next page and 4.5 show the final calibrations. The poor SNR at low frequencies is created by physical seismic-noise on DARM. It is usually effective to increase the excitation amplitude, but here the loop excitation is limited to the linear region of the Michelson sinusoidal response. The linear region corresponds to a smaller motion than the ground noise is actually moving. In general, SNR is difficult to improve when the *open-loop* noise is larger than the linear response of a discriminant signal - as is the case here. Above 200Hz the ground is relatively more quiet, and the measurement becomes sensitive. These calibrations show small variations over time which are larger than the statistics of the measurement, so some external systematic may be affecting the calibration itself.

The fits use 2 complex-poles and 2 complex-zeros, fitting the data well without over-fitting, although this fit is only necessary to evaluate/interpolate the data at calibration line frequencies. The use of pole-zero fits is further explained in section 5.4 on page 123, although this fit is phase-sensitive unlike those explained. A few interesting features are notable - the first being the bucket-shape with 10 degrees of lost phase at only 100Hz. The analog high-voltage amplifier DAC-bitnoise-whitening filters which turn on around 60Hz may not be perfectly compensated digitally to form a flat-response. The low-frequency bucket-shape could otherwise be from statistical biasing from low-SNR below 100Hz, but the phase-lag

measured suggests an effective lead-lag filter due to mismatch of filters.

The second feature is the increasing phase-lag at high-frequencies. The measurement makes a round-trip from DAC-to-ADC and picks up one sample-time of delay in addition to a nearly equivalent amount of delay from the Filter-Buffer-Board Nyquist-filters. The phase-lag is the accumulation of these delays.

The third feature is the rising magnitude at high-frequencies. This is the Lorentzian tail of a piezo resonance, along with some additional mismatch of whitening and compensation filters. A rising gain should also deliver a phase-advance, but the sample-time and Nyquist filters overpower the expected advance.

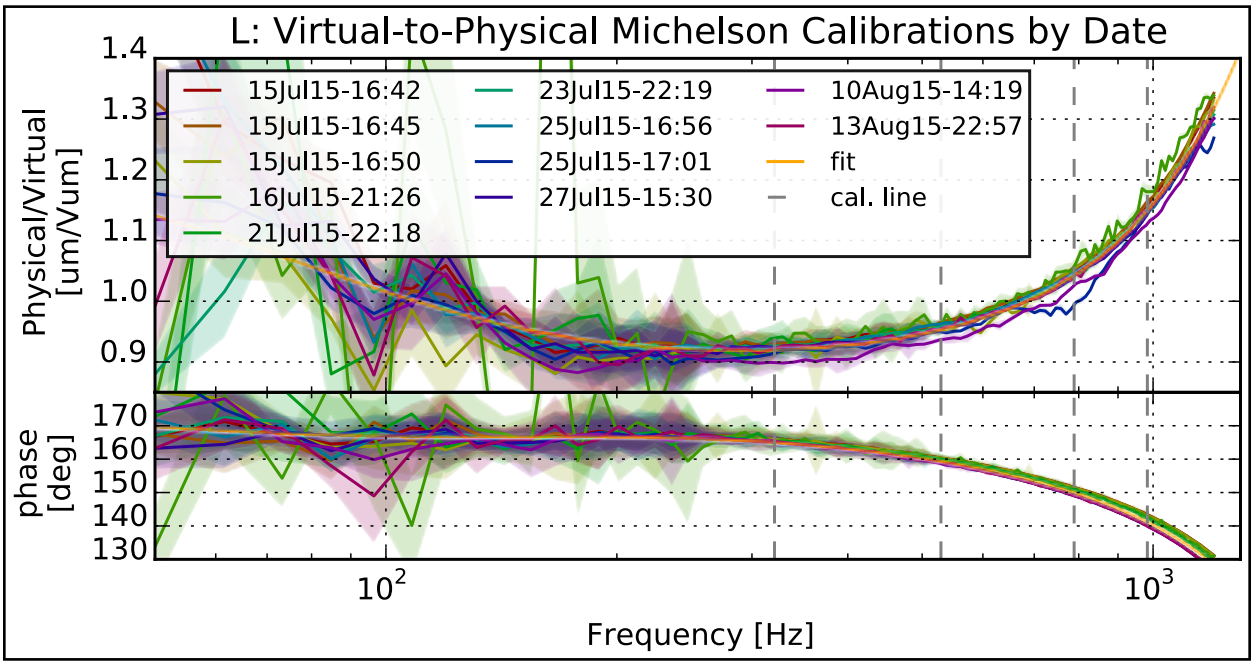

Figure 4.4: Swept-sine transfer-functions of the one-pass Michelson of the **L** interferometer driven in differential-arm-length, referred to real motion using the laser wavelength. The units express the physical to virtual transfer-function $\widehat{\text{XFER}}\left[\lfloor\hat{L}_{\text{exc}}\rceil : \hat{L}_\delta \Rightarrow \lfloor\hat{L}_\delta\rceil\right] = \hat{C}_{[\frac{\text{m}}{\text{v}}]\text{PZT}}$ which is depicted graphically in fig. 4.2 on page 91. The physical units are microns RMS longitudinal mirror motion of differential arm length. The Vum units then are the virtual expression of these units. This transfer-function would be identically 1 for a control system with perfect compensation filters. The deviation from 1 is not significant for the calibration insofar as this plot can account for it. To that end, the series of measurements indicates that the calibration is stable to around 2%.

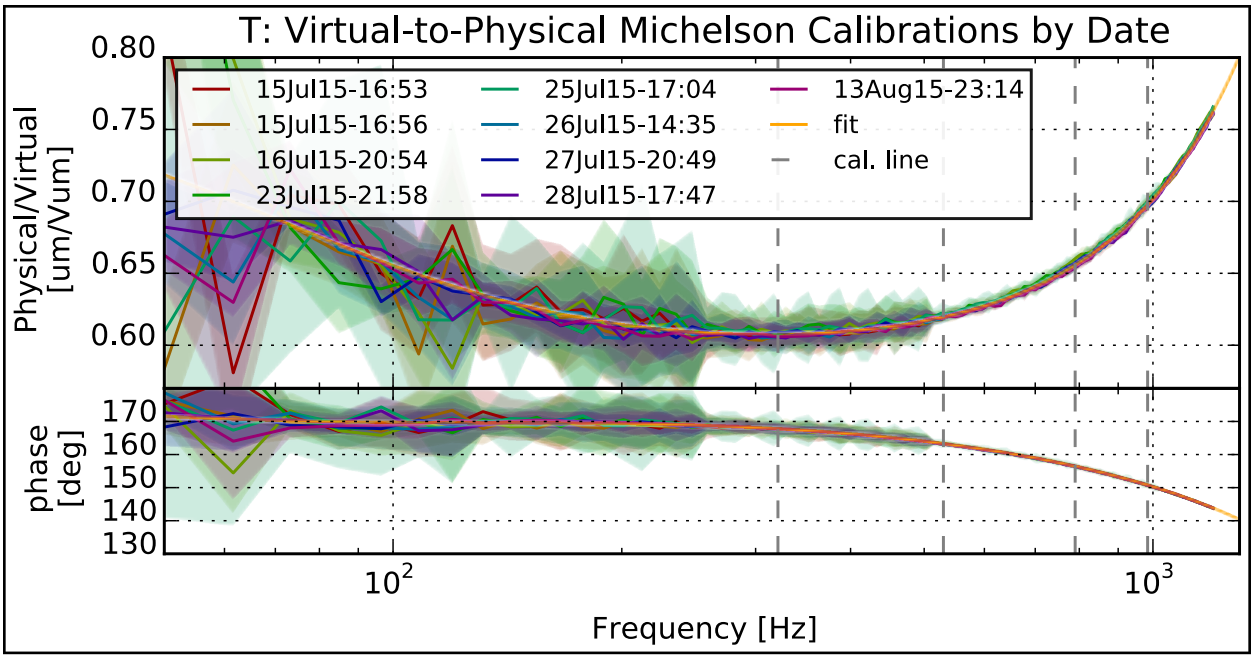

Figure 4.5: Swept-sine transfer-functions of the one-pass Michelson of the **T** interferometer driven in differential-arm-length, referred to real motion using the laser wavelength. It may be interpreted similarly to fig. 4.4 on page 102.

4.5 Interferometer Model-Corrections

The power recycled Michelson contains an important new coupling compared to the one-pass - the input power to the "internal Michelson," composed of the of the beamsplitter and two endmirrors, now depends on the output power. The signal-carrying light out of the AS port acts as a loss affecting the power buildup. The Finesse or cavity-pole of the recycling cavity sets the frequency scale below which modulations of the AS port coupling can strongly affect the BS power, and above which the recycling considers the cavity stationary.

As pointed out in section 2.5 on page 34, the picture of the AS-port-coupling as a direct function of $\hat{L}_\delta$ is not sufficient to predict delay line effects in the Michelson. The insufficiencies of the function picture grow for the power recycled case where delay-line phasing can affect constructive or destructive interference of the Fabry-Perot. With the full perturbed-steady-

state model of the interferometer, the calibration factors can be solved directly.

As mentioned, the model does require additional internal state which must be fit-for using all of the data available. Photodiodes monitor and stored data for the AS-port, N-transmission, and REFL ports. All of these monitors provide DC outputs and transfer-functions with the $\lfloor \hat{L}_{\mathrm{exc}} \rceil$ calibration lines. Surprisingly, this data can contain all of the important internal-state of the model relevant for th AS-port transfer-functions described in section 3.2.1 on page 72.

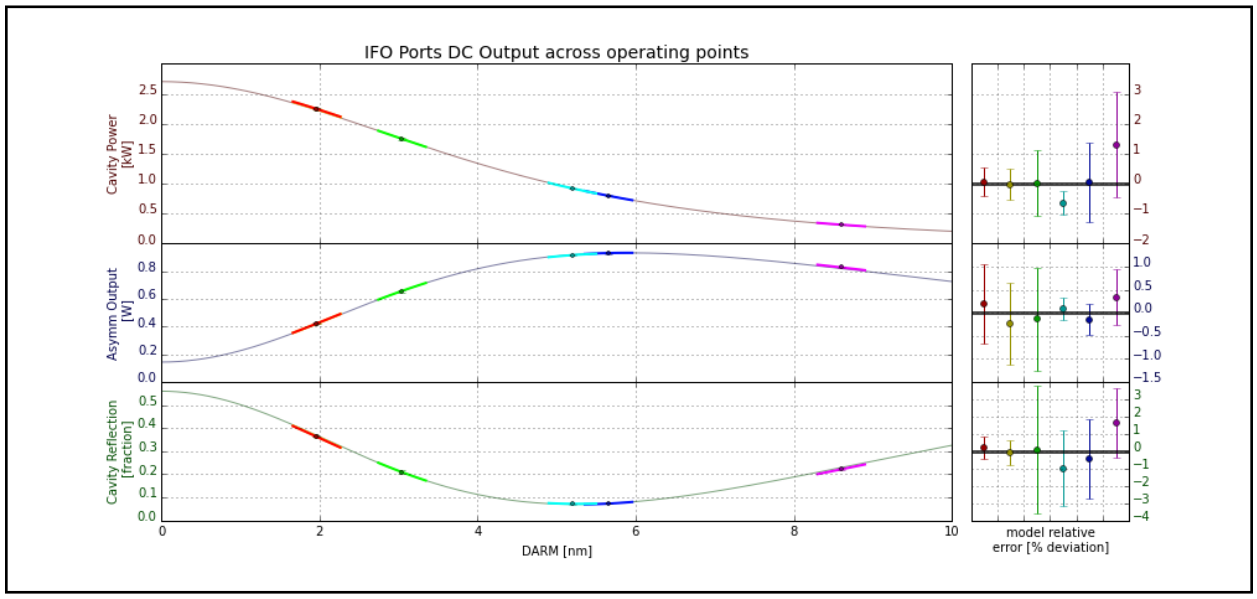

Figure 4.6: The DC values of the interferometer were fit simultaneously with their AC-transfer-functions, but across widely varying operating-points (represented by each color). This fits all of the internal parameters of the power-recycled Michelson without any degeneracy. These plots project the fit-parameters back through the model of the three major DC signal output by the interferometer (akin to fig. 3.4). The model then sits well on the data at each operating point. These "Model Sets" are generated at many moments, and can be generated directly from the calibration line data. They are not widely used in this analysis but to show that the model-correction term for the 983Hz line is small. The lines colored lines along the DARM-signal model are not errorbars, rather they are the local curves at that operating point. Between the operating points more parameters are changing and being fit than just DARM, so the common curve represents the average of those other marginalized parameters and the colored lines are the true curves that the data points are compared against. The errorbars are shown on the right ias percent deviation from the local interferometer model curves. Their magnitude is generated from the sample variance of the data section used in the fit.

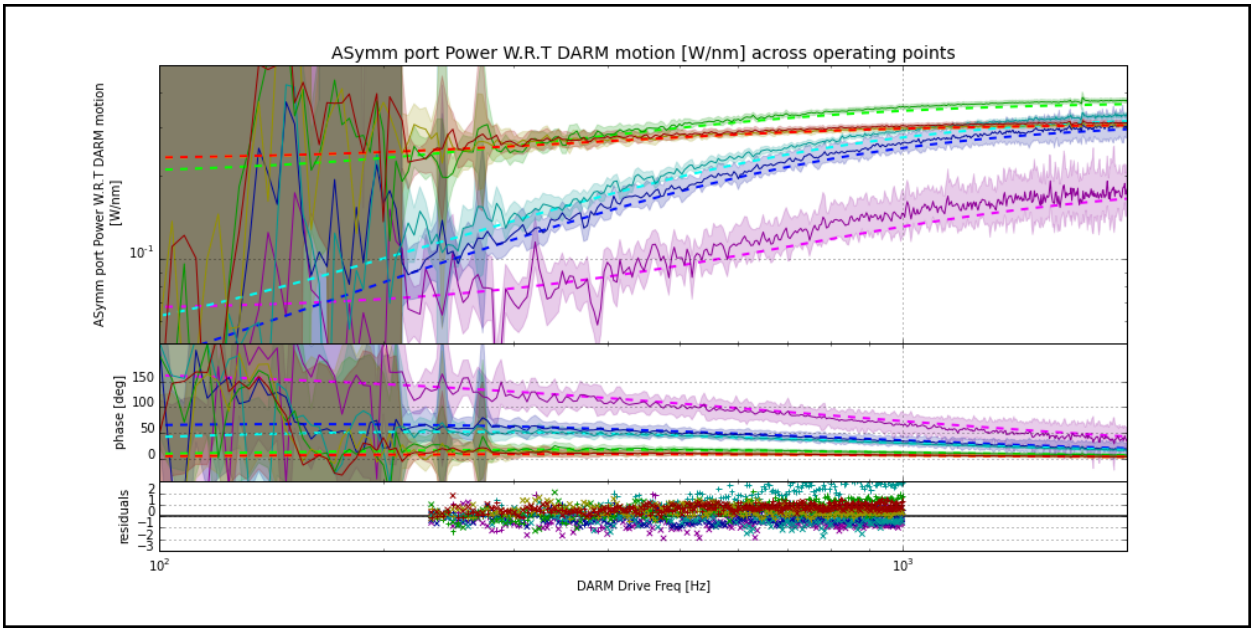

Figure 4.7: Here the model fits (dashed lines) of are plotted vs. data of the AS-port transfer functions (solid lines) described in section 3.2.1 on page 72. This allows a model-correction between the low-frequency calibration lines into the high-frequency sensitivity fully outside of the cavity-bandwidth. The colors correspond to the DC operating points of fig. 4.6 on page 105. The operating-point during data-collection is most reflected by the red-line. The model correction term shows smaller gain at the calibration line than the gain at RF, but only by around 3%. Unaccounted, this factor projects the data to show *worse* sensitivity to length than it actually has. The residuals of the bottom plot show that these data went into the model fitting, but only from 200Hz to 1kHz.

4.6 Assessing the Purity of Calibration Longitudinal Drive

A number of measurements in this chapter make the caveat that $\lfloor \hat{L}_\delta \rceil$ does *not* cause strong excitations of angular modes in the interferometer. If angular modes are created coherently in the calibration, then they can cause coherent systematic biasing if they manage to convert into signals stacking on the calibration lines which are created through mechanisms not reflective of the actual Holographic noise signal to be studied.

As it turns out, the degeneracy that could stack these signals on the calibration makes them difficult to isolate and limit. To fully detail this stacking requires an explanation of the

4.6.1 Hermite Gauss notation for transverse-spatial power modulations

The interferometer acts as a large scattering matrix between the frequency and spatial modes of resonant optical beam. The scattering matrix is solved and the steady state output in the indexed modes must then be intermodulated to convert from optical fields into photodiode power. The frequency indexes of the modes cause time-dependent beating in photodiodes given by the frequency separation. The spatial modes also have beating effects, but most photodiodes can only see the spatial analog to the DC beating term. Modes separated in transverse index beat such that their average power is zero[1]

The notation used here expresses the indices needed for this beating. In field-space, the optical modes are are expressed by $|A_{\text{single}}\rangle = |{}^{\text{H}}_{\text{G}}{:}ij,F{:}F_{\text{carrier}}\rangle$ which represents the field in Hermite-Gauss mode i, j at frequency F. For a field with multiple modes, the superposition can be expressed $|A_{\text{2-mode}}\rangle = C_0|{}^{\text{H}}_{\text{G}}{:}i_0j_0,F{:}F_0\rangle + C_1|{}^{\text{H}}_{\text{G}}{:}i_1j_1,F{:}F_1\rangle$. The fields then must be expressed in terms of power modulation for the photodiodes. For the two mode case, all of

1. The "negative power" terms of these terms are always seen with the positive DC terms and the spatially-resolved power never actually becomes negative. This is analogous to the frequency intermodulation case - any AC signal must be sitting on a DC signal at least as large.

the intermodulations then appear as

$$|P_{\text{2-mode}}\rangle = \langle A_{\text{2-mode}}|A_{\text{2-mode}}\rangle \tag{4.28}$$

$$= |C_0|^2 \,|{}^{\text{H}}_{\text{G}}\!:\langle i_0 j_0|i_0 j_0\rangle,\, F\!:\!F_0\!-\!F_0\rangle + |C_1|^2 \,|{}^{\text{H}}_{\text{G}}\!:\langle i_1 j_1|i_1 j_1\rangle,\, F\!:\!F_1\!-\!F_1\rangle$$

$$+ C_0 C_1^* |{}^{\text{H}}_{\text{G}}\!:\langle i_0 j_0|i_1 j_1\rangle,\, F\!:\!F_0\!-\!F_1\rangle + C_1 C_0^* |{}^{\text{H}}_{\text{G}}\!:\langle i_1 j_1|i_0 j_0\rangle,\, F\!:\!F_1\!-\!F_0\rangle \tag{4.29}$$

Equation (4.29) is split into two classes of terms. Ones with self-modulating transverse modes and those with cross modulations. The actual actual distribution in space follows from the conjugate multiplication of the two Hermite-Gauss spatial wavefunctions. The salient feature is that the multiplied modes are all positive for the self-modulating terms, so those terms represent average power, and the terms are odd functions for the cross-modulations. The odd functions are powers beating differentially and those terms may only be detected in a quadrant photodiode or other detector whose overlap integral with the cross-Hermite-Gauss modes is nonzero and therefor not centered in the Hermite-Gauss basis.

The notation of eq. (4.28) is admittedly a bit unusual. The difficulty is that the power observation is also a statistical or quantum mechanical state, but arises from a nonlinear operation. It is possible to generate the effective quantum mechanical operators to represent the field mode conversion to power and to represent the summing and quadrant photodiode detections of those power modes. It is not attempted here as the notation is cumbersome and unenlightening over this basic modal analysis that abuses the notation slightly.

4.6.2 Analysis of parasitics

In the following discussion, only one axis of the Hermite-Gauss modes is mentioned for simplicity. These modes are represented by their transverse wavefunction $|{}^{\text{H}}_{\text{G}}\!:ij\rangle$, but for this section only one axis is notated. $|{}^{\text{H}}_{\text{G}}\!:1\rangle$ can represent any superposition of $|{}^{\text{H}}_{\text{G}}\!:10\rangle$ or $|{}^{\text{H}}_{\text{G}}\!:01\rangle$.

For DARM modulation without parasitics, the motion couples every interferometer mode

into upper and lower sidebands of the *same* mode. For angular modulations, the strong $|{}^{\text{H}}_{\text{G}}{:}0,F{:}F_{\text{carrier}}\rangle$ mode will generate $|{}^{\text{H}}_{\text{G}}{:}1,F{:}F_{\text{carrier}}\pm F_{\text{mod}}\rangle$ modes at the endmirrors. The interferometer naturally has some level of imperfect alignment, so the steady-state mode at the AS Port is itself some superposition of $|{}^{\text{H}}_{\text{G}}{:}0,F{:}F_{\text{carrier}}\rangle$ and $|{}^{\text{H}}_{\text{G}}{:}1,F{:}F_{\text{carrier}}\rangle$. The sideband field modes at the endmirrors then beat with the steady state mode to generate some amount of $|{}^{\text{H}}_{\text{G}}{:}\langle 0|1\rangle, F{:}F_{\text{mod}}\rangle$, and some $|{}^{\text{H}}_{\text{G}}{:}\langle 1|1\rangle, F{:}F_{\text{mod}}\rangle$. The former is an odd mode and will only show as a modulation in a quadrant photodiode, but the latter will show as a modulation on top of the usual $|{}^{\text{H}}_{\text{G}}{:}\langle 0|0\rangle\rangle$ in signal PDs.

This additional parasitic signals bias calibrations which are supposed to indicate purely differential arm motion. Moreover, it is difficult to measure the modulated $|{}^{\text{H}}_{\text{G}}{:}\langle 0|1\rangle\rangle$ to characterize the $|{}^{\text{H}}_{\text{G}}{:}\langle 1|1\rangle\rangle$ because the *DC* $|{}^{\text{H}}_{\text{G}}{:}1\rangle$ mode also beats with the AC $|{}^{\text{H}}_{\text{G}}{:}0\rangle$ mode to also create an odd $|{}^{\text{H}}_{\text{G}}{:}\langle 1|0\rangle\rangle$, degenerate with $|{}^{\text{H}}_{\text{G}}{:}\langle 0|1\rangle\rangle$.

The resolution of this degeneracy is to realize that in optical field-amplitude, the concept of "DC field" does not exist. The concept is useful during power detection because the convolution of modes by their associated frequency cancels many carrier-frequencies down to DC. Sidebands show as modulations typically from beating against the carrier. In essence, all power signals are intermodulations. Typically intermodulation products should be avoided, but in the picture where all signals arise from intermodulation they can be used to avoid the confounding mode content of the carrier. Multiple modulation frequencies are effective at finding parasitics through locking into the intermodulation beat notes for $|{}^{\text{H}}_{\text{G}}{:}\langle 0|1\rangle\rangle$ modes in a quadrant photodiode.

Let ϵ be the parasitic coupling of length modulation into angular modes. The $\hat{L}_\delta$ is then modulated at two frequencies F_1 and F_2 as calibration-lines which generate phase-modulation depth γ, and F_{c} is the optical carrier frequency. Including the steady-state carrier modes,

this generates the AS port field (with some overall normalization $\mathcal{N}$):

$$\begin{aligned}\frac{1}{\mathcal{N}}|A_{\mathrm{AS}}\rangle = \quad & |\text{HG}{:}0,F{:}F_{\mathrm{c}}\rangle && +x|\text{HG}{:}1,F{:}F_{\mathrm{c}}\rangle \\ & +\gamma_1|\text{HG}{:}0,F{:}F_{\mathrm{c}}+F_1\rangle && +\epsilon\gamma_1|\text{HG}{:}1,F{:}F_{\mathrm{c}}+F_1\rangle \\ & +\gamma_2|\text{HG}{:}0,F{:}F_{\mathrm{c}}+F_2\rangle && +\epsilon\gamma_2|\text{HG}{:}1,F{:}F_{\mathrm{c}}+F_2\rangle \\ & +(\text{lower sidebands}\ldots)\end{aligned} \tag{4.30}$$

This expression shows that there are intermodulation terms during power detection to with many modal products uniquely visible in a quadrant photodiode across the intermodulation frequencies.

$$\frac{1}{|\mathcal{N}|^2}|P_{\mathrm{AS}}\rangle = \Big((1{+}2\gamma_1^2{+}2\gamma_2^2)|\text{HG}{:}\langle 0|0\rangle,\, F{:}\mathrm{DC}\rangle$$

$$+ (x^2{+}2\epsilon^2\gamma_1^2{+}2\epsilon^2\gamma_2^2)|\text{HG}{:}\langle 1|1\rangle,\, F{:}\mathrm{DC}\rangle\Big) \tag{4.31}$$

$$+x\Big(|\text{HG}{:}\langle 0|1\rangle,\, F{:}\mathrm{DC}\rangle \quad +|\text{HG}{:}\langle 1|0\rangle,\, F{:}\mathrm{DC}\rangle\Big) \tag{4.32}$$

$$\begin{aligned}+\Big(\quad & 2\gamma_1|\text{HG}{:}\langle 0|0\rangle,\, F{:}F_1\rangle && +2x\epsilon\gamma_1|\text{HG}{:}\langle 1|1\rangle,\, F{:}F_1\rangle \\ & +2\gamma_2|\text{HG}{:}\langle 0|0\rangle,\, F{:}F_2\rangle && +2x\epsilon\gamma_2|\text{HG}{:}\langle 1|1\rangle,\, F{:}F_2\rangle\Big)\end{aligned} \tag{4.33}$$

$$\begin{aligned}+\Big(\quad & \epsilon\gamma_1|\text{HG}{:}\langle 0|1\rangle,\, F{:}F_1\rangle && +x\gamma_1|\text{HG}{:}\langle 0|1\rangle,\, F{:}F_1\rangle \\ & +\epsilon\gamma_2|\text{HG}{:}\langle 0|1\rangle,\, F{:}F_2\rangle && +x\gamma_2|\text{HG}{:}\langle 0|1\rangle,\, F{:}F_2\rangle + \text{C.M.}\Big)\end{aligned} \tag{4.34}$$

$$\begin{aligned}+\epsilon\gamma_1\gamma_2\Big(\quad & |\text{HG}{:}\langle 0|1\rangle,\, F{:}F_1{+}F_2\rangle && +|\text{HG}{:}\langle 0|1\rangle,\, F{:}F_1{-}F_2\rangle \\ & +|\text{HG}{:}\langle 0|1\rangle,\, F{:}{-}F_1{+}F_2\rangle && +|\text{HG}{:}\langle 0|1\rangle,\, F{:}{-}F_1{-}F_2\rangle + \text{C.M.}\Big)\end{aligned} \tag{4.35}$$

$$+\mathcal{O}(\epsilon^2)$$

This expression provides information about the parasitic angular coupling. The difficulty is in finding terms which do not contain factors of the DC residual HOM content x. The phrase "C.M." is short for conjugate-modes which are the same terms as in $|\text{HG}{:}\langle 0|1\rangle\rangle$ repeated on the

$|_{\mathrm{G}}^{\mathrm{H}}\!:\langle 1|0\rangle\rangle$. A breakdown of the terms in this expression into PD-visibility and information content is:

Terms of 4.31 This is the DC power on a sum-total photodiode (SPD, the term representing the usual meaning of a photodiode with no transverse discrimination). The contrast-defect from misalignment is contained in the x^2 term.

Terms of 4.32 This is the DC misalignment on a QPD (quadrant-photodiode, one that can distinguish transfers modes in power created from the collapse of even optical-amplitude modes with odd modes). Ideally one could use this x measurement to correct others, but in a power-recycled interferometer there are many more terms HOM terms influence the DC term of a QPD.

Terms of 4.33 These are the direct-modulation products (intermodulation of motion sidebands with the "DC" carrier) which appear in an SPD. These are useful. Assuming small ϵ and x, these normalize the drive strengths γ, so that ϵ can be selected from terms 4.35.

Terms of 4.34 These are the direct products appearing in a QPD. There is a strong degeneracy between ϵ and x indicating that direct-products cannot be trusted as unbiased measurements of ϵ.

Terms of 4.35 These are the products unique to this double-drive measurement. They require knowledge of both drive strength γ's, but do not have any presence of the DC misalignment x. These terms only show in a QPD as well.

This 2-drive modulation measurement was made in both one-pass and PR recycled mode and found that the ϵ residual couplings of DARM into the X and Y Hermite-Gauss modes were less than 5%. During operation, the contrast defect term from high-order-modes leaking power is minimized. The defect term is dominated by $>$ order-2 modes through mirror

astigmatism and the alignment allows the order-1 aligment mode to be minimized. The defect contributes $< \frac{1}{2}$ of the output Asymmetric port light and the misalignment term is during nomininal operation only a small addition to the defect. If the order-1 mode defect term is less than 20% of the fringe light, then the field power is $\sqrt{10\%} \approx 0.3$ of the fringe 0-mode field. This is the field that the AC 1-mode must beat against to generate a power signal in the diode, and so the 5% limit is reduced further to a 2% systematic biasing of the calibration from misalignment and geometric impurity.

4.7 Implementation of Down-Sampled Calibration Timeseries

The live calibration measurements are ultimately composed into a timeseries of the photodiode signals, loop excitations and actuation signals. The distillation process generates averages of all of the measured signal DC values, as well as the transfer functions at the four calibration frequencies, only the highest of which is used for calibration analysis. All of the controls-channel data is stored as 32kHz timeseries. The distillation code Nyquist-filters, and downsamples the DC levels of all sensors as well transfer functions between pairs of sensors and actuators locked-in to each excitation frequency in $\lfloor \hat{L}_{\mathrm{exc}} \rceil$. The downsampling creates output signals at 16Hz, which is fast enough to see typical disturbances at high SNR, but slow enough to easily process and merge calibration data to the 1s timescale CSD matrices stored in the RF-DAQ.

So far, transfer functions to $\lfloor \hat{L}_{\mathrm{exc}} \rceil$ are shown being built using CSD-estimators. For timeseries' of transfer-functions, CSD estimates have a number of flaws.

- Typical implementations such as the Welch-method are computationally intensive from using FFT's across many frequencies, even those not containing excitation amplitude.
- The calibration-line frequencies are not necessarily centered on the FFT bins.
- Coherence-estimates require many averages of a traditional CSD-estimator which is

not acceptable in maintaining time-resolution.

The frequency-shifted templates in CSD estimates such as the Welch method act as a convolution by a filter which is evaluated at a given point.

$$\mathcal{K}_{t,F}\{\hat{x}\} = \int_{-\infty}^{+\infty} \mathcal{K}(t'-t)\hat{x}(t')dt' \tag{4.36}$$

$$= \{\mathcal{K}_F *_{\mathrm{T}} \hat{x}\}(t) \tag{4.37}$$

This convolution operation is equivalent to a filter application in the time-domain. This makes the CSD estimator work as a pair of time-evaluations of filtered inputs. In this expression the multiplication in the Fourier-domain corresponds to the convolution in the time-domain.

$$\widehat{\mathrm{CSD}}[\hat{x},\hat{y};F,t] = \left\langle \mathcal{K}_{t,F}\{\hat{x}\}\,\mathcal{K}^*_{t,F}\{\hat{y}\} \right\rangle \tag{4.38}$$

$$= \mathscr{F}^{-1}\big\{\mathcal{K}_F(F')\cdot\hat{x}(F');t\big\}\cdot\mathscr{F}^{-1}\big\{\mathcal{K}^*_F(F')\cdot\hat{x}(F');t\big\} \tag{4.39}$$

This method suggests a much more efficient method for implementing CSD's evaluated at few frequencies - time-domain filters. Although templates tend to correspond to Finite-impulse-response (FIR) filters. The theory is generic enough that infinite-impulse-response (IIR) filters may also be used and IIR filters have the advantage of compact, efficient implementations.

The filters corresponding to complex templates are unusual from the perspective of typical filter design. Complex templates create filters that convolve with real timeseries to create complex timeseries. Frequency-translated templates like those in the Welch method correspond to narrow-band Hilbert-transform (NBHT) filters. A Hilbert transform has the property of selecting purely positive frequency components from a signal. This corresponds to a Heaviside step function in frequency space, or a convolution with $\frac{1}{t}$ in the time-domain.

One cannot physically implement or compute with such a singular kernel, but for narrow-band implementations, the Hilbert-transform is easily realizable. An effective NBHT only requires minimizing passband in negative frequencies.

For the 983Hz calibration line, the timeseries spectral estimation filter is created first by generating a 16Hz order-8 Butterworth filter as a digital second-order-section. This creates a filter with purely-real coefficients, which has Hermitian symmetry under $F \to -F$. This is equivalent to having all poles and zeros as balanced complex-conjugates in either the digital domain (z-variable) or the analog Laplace-domain (s-variable). A brief introduction to filter-fitting using the language of poles and zeros is given in section 5.4 on page 123 in the context of an inverse problem. The roots (both poles and zeros) of the Butterworth filter are then rotated in the Z-domain to center on the calibration line frequency. The high-order of the filter ensures rapid attenuation at frequencies separated from the positive calibration line frequency, including negative frequencies. This filter is denoted $H_{F_{\text{cal}}}(t)$.

The excitation channel, when this filter is applied, transforms from balanced delta-functions in frequency into a single selected positive frequency:

$$\lfloor \hat{L}_{\text{exc}} \rceil = L_1 \sin(2\pi F_{\text{cal1}} t + \hat{\phi}_1) + L_2 \sin(2\pi F_{\text{cal2}} t + \hat{\phi}_2) + \dots \tag{4.40}$$

$$\Big\{ H_{F_{\text{cal1}}} *_{\text{T}} \lfloor \hat{L}_{\text{exc}} \rceil \Big\}(t) = \mathscr{F}^{-1}\Big\{ H_{F_{\text{cal1}}}(F) \cdot \lfloor \hat{L}_{\text{exc}} \rceil (F); t \Big\} \tag{4.41}$$

$$\approx \frac{L_1}{2} e^{2\pi \mathrm{i} F_{\text{cal1}} t + \mathrm{i}\hat{\phi}_1} \tag{4.42}$$

eq. (4.42) defines the filtered-timeseries estimator as the convolution with the filter.

Now a peculiar reduction can be made to a CSD estimate using this template on the

noise-free excitation.

$$\widehat{\mathrm{XFER}}\Big[\lfloor\hat{L}_{\mathrm{exc}}\rceil \Rightarrow \hat{x}\Big]_t = \frac{\widehat{\mathrm{CSD}}\Big[\hat{x}, \lfloor\hat{L}_{\mathrm{exc}}\rceil; t\Big]}{\widehat{\mathrm{CSD}}\Big[\lfloor\hat{L}_{\mathrm{exc}}\rceil, \lfloor\hat{L}_{\mathrm{exc}}\rceil; t\Big]} \tag{4.43}$$

$$= \frac{\big\{H_{F_{\mathrm{cal1}}} *_{\mathrm{T}} \hat{x}\big\}(t) \cdot \Big\{H^*_{F_{\mathrm{cal1}}} *_{\mathrm{T}} \lfloor\hat{L}_{\mathrm{exc}}\rceil\Big\}(t)}{\Big\{H_{F_{\mathrm{cal1}}} *_{\mathrm{T}} \lfloor\hat{L}_{\mathrm{exc}}\rceil\Big\}(t) \cdot \Big\{H^*_{F_{\mathrm{cal1}}} *_{\mathrm{T}} \lfloor\hat{L}_{\mathrm{exc}}\rceil\Big\}(t)} \tag{4.44}$$

$$= \frac{\big(\big\{H_{F_{\mathrm{cal1}}} *_{\mathrm{T}} \hat{x}\big\}(t)\big)\left(\frac{L_1}{2}e^{-2\pi \mathrm{i} F_{\mathrm{cal1}} t - \mathrm{i}\hat{\phi}_1}\right)}{\left(\frac{L_1}{2}e^{2\pi \mathrm{i} F_{\mathrm{cal1}} t + \mathrm{i}\hat{\phi}_1}\right)\left(\frac{L_1}{2}e^{-2\pi \mathrm{i} F_{\mathrm{cal1}} t - \mathrm{i}\hat{\phi}_1}\right)} \tag{4.45}$$

$$= \frac{\big\{H_{F_{\mathrm{cal1}}} *_{\mathrm{T}} \hat{x}\big\}(t)}{\frac{L_1}{2}e^{2\pi \mathrm{i} F_{\mathrm{cal1}} t + \mathrm{i}\hat{\phi}_1}} \tag{4.46}$$

$$= \frac{\big\{H_{F_{\mathrm{cal1}}} *_{\mathrm{T}} \hat{x}\big\}(t)}{\Big\{H_{F_{\mathrm{cal1}}} *_{\mathrm{T}} \lfloor\hat{L}_{\mathrm{exc}}\rceil\Big\}(t)} \tag{4.47}$$

This simplification is *not* general, and only applies here because all of the excitations are coherent lines with no noise terms, separated by many filter bandwidths. It further requires that the filter not be a typical resonance, but rather a one-sided resonance acting as a NBHT.

The simplified time-resolved transfer-function estimator of equation (4.47) is how the various calibration lines are extracted for the moment-to-moment calibration. The filter applied is additionally shaped to better suppress noise. The loop-inversion or reference against the actuation point $\lfloor\hat{L}_{\delta}\rceil$ carries all of the noise that the loop is removing. This noise has a seismic $1/F^2$ spectrum. To select coherent lines, the entire noise spectrum away from the line must be suppressed by the filter. Figure (4.8) shows the shape used for the filter. Even an order-8 Butterworth cannot suppress the noise around DC without an additional notch attached around 0Hz. Compare the source and filtered signal to the calibration line appearing in the 1811 DC channel of fig. 4.9 on page 117. This channel can only see the residual DARM noise converted through the interferometer. The boosted control loop whitens even $1/F^2$ external noise for sensors, so the additional notch is overkill, but the filters were not adjusted to simplify analysis.

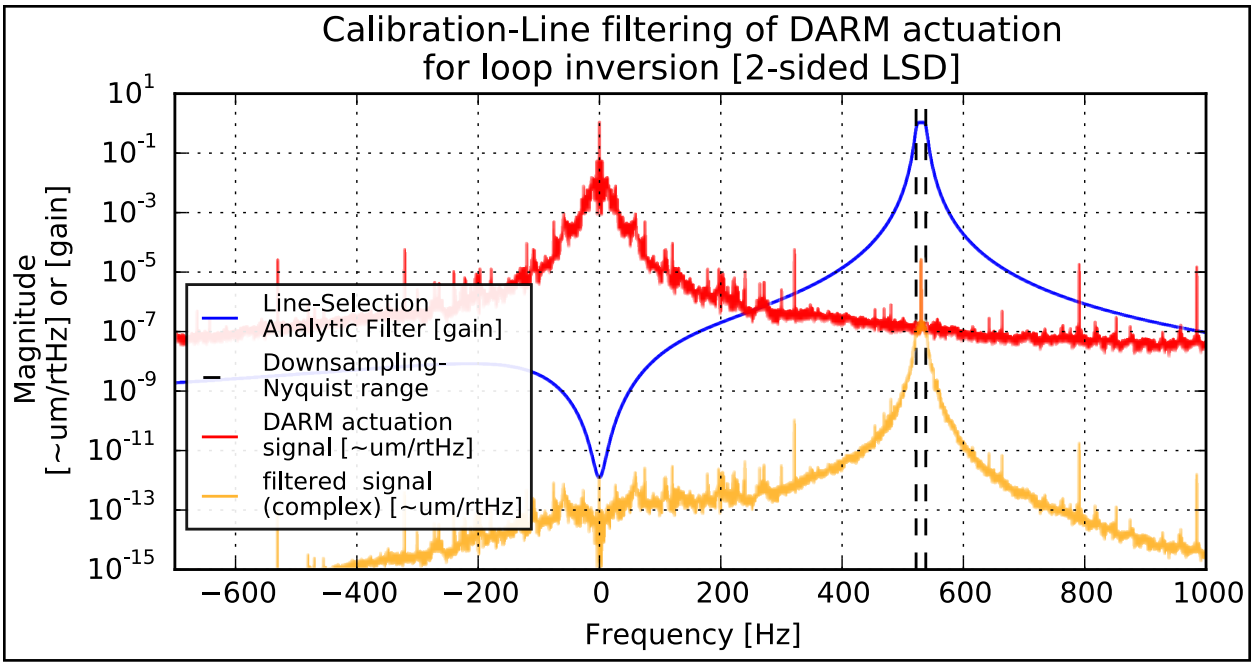

Figure 4.8: Analytic filtering of the actuation-point $\lfloor \hat{L}_\delta \rceil$. This is an *two-sided* power spectrum which extends into negative frequencies. The large $1/F^2$ falloff of the source-signal around DC ($F = 0$) must be sufficiently attenuated to prevent its aliasing as the signal is down-sampled. An order-8 Butterworth filter is translated to the positive calibration-line frequency and extended with a notch-filter tuned to remove the DC power (shown blue). The filter is applied in the time-domain and the output is plotted (orange) showing the sufficient attenuation and selection of the calibration line. The tilde on the units expresses that these are in the virtual-micron units of the control system. The calibrations are later applied to the data generated from these lines.

The analytic filter technique enables further useful analysis. The complex signal that is produced can be "folded" through the filter center-frequency to create an amplitude modulation spectrum as well as phase. The interferometer's conversion of the excitation into voltage drives the AM signal, but there is no physical mechanism driving the line into the PM signal other than very small Doppler-effects. The PM quadrature of the folding does allow a noise analysis to determine the SNR of the calibration line at each 16Hz sample. An example of the AM/PM folding of fig. 4.8 is given in figure (4.10). The folded signals are really the real and imaginary parts of an analytic-bandpass testpoint after dividing by the similarly-filtered excitation. The division shifts the signal spectrum so that the coherent excitation-line sits

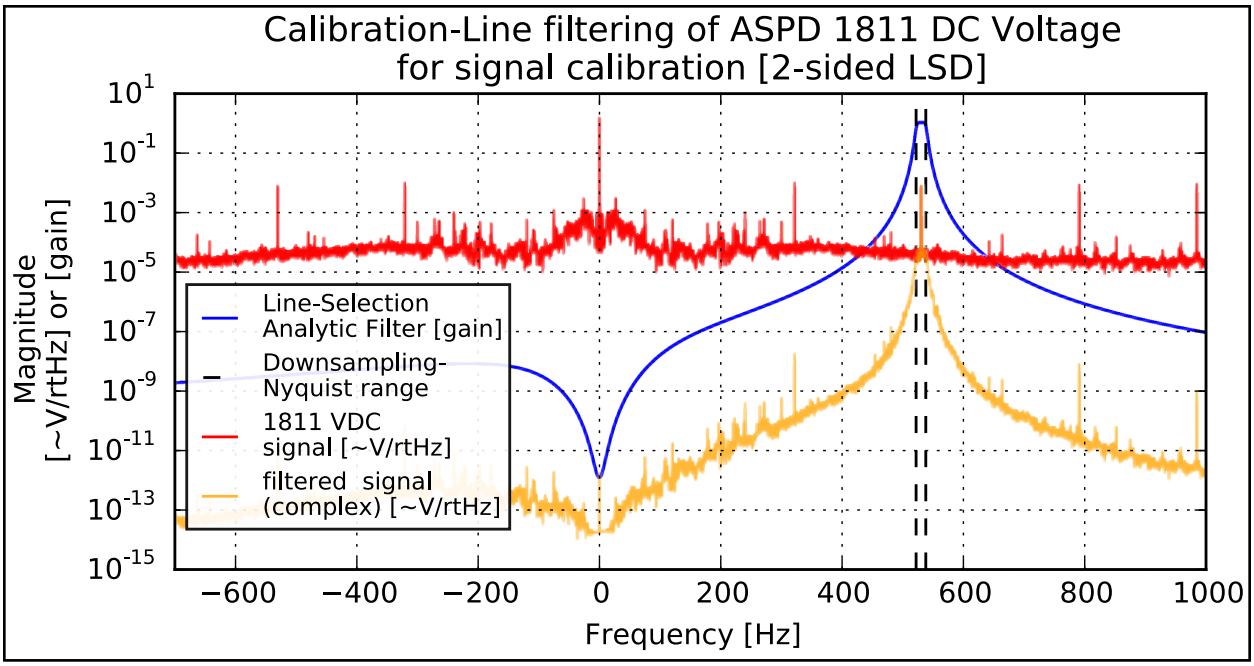

Figure 4.9: Analytic filtering of a photodiode signal testpoint $\hat{V}_{\mathrm{aspd1}}$. The filter used for fig. 4.8 on page 116 is applied for consistency, even though the calibration line for this testpoint is hidden within the whitened DARM noise of the loop-residual.

at DC in the spectrum of the "real" signal. The real real part of the signal then represents AM modulation of the excitation line and the imaginary part is the PM modulation of the coherent line in the testpoint. Taking the real and imaginary parts separately recovers two separate real signal, allowing the one-sided power spectrum to be used again. This is why the term "folding" is used for the conversion of the two-sided spectrum into separate one-sided spectra.

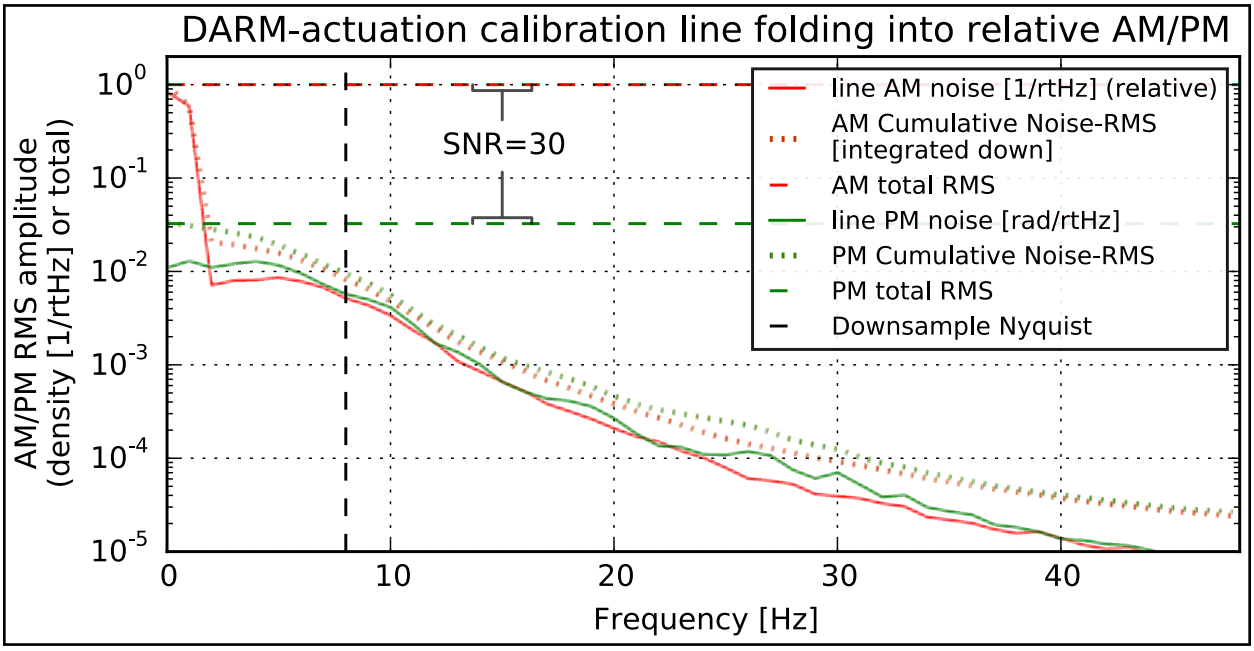

Figure 4.10: Analytic filtering of the actuation-point $\lfloor \hat{L}_\delta \rceil$ divided by the filtered excitation-reference $\lfloor \hat{L}_{\text{exc}} \rceil$ shifts the orange signal of fig. 4.8 on page 116 to DC and normalizes by the drive-amplitude. The shift maintains the complex-form of the signal. Instead of plotting again a two-sided power spectrum, the real and imaginary parts to this signal are each non-complex signals comprising the amplitude-modulated component of the calibration-line and the phase-modulated component of the line. This plot shows that the AM carries calibration magnitude, and the interferometer does not imprint significant PM on the calibration-line. The noise folding between the two provides a comparison of the noise floor and determines the single-sample signal to noise ratio.

Chapter 5

CHARACTERIZATION SCHEME FOR PHOTODIODES

5.1 Overview of Calibration and Fitting Scheme

Chapter 4 details the goal of the calibration scheme to generate basis-change matrix for converting voltages reported by photodiodes/ADCs into physical units. This conversion has two pieces, one internal to the diode, converting voltage into incident photocurrent, Watts, or photons. The other, external, representing the sensitivity of the optical instrument in converting physical motion into optical fluctuation. The transimpedance component of these calibrations is detailed in this chapter.

The formulas of eq. (4.12) on page 93 and eq. (4.14) on page 94 motivate the requirements on the calibrations in the context of balancing error across the many constituent factors. The Vertex AS-port calibrations referred by those equations reference low-frequency port measurements (DC, $<$ 10kHz) to the RF high-frequency measurements (RF, $>$ 100kHz). The many factors that this reference carries from DC to RF represent the first of two styles of calibration applicable to the instrument.

Transimpedance calibration This is a direct method to convert ADC-signals back to photocurrent. With this reference to photocurrent an external model or system-calibration must also be applied to convert photopower on-diode into physical units. Systematic errors propagate from both sides in this method - the PD calibration is imperfect as is knowledge of the optical apparatus.

Cross-Reference calibration This is an indirect method to modulate or lock-in to a common reference signal between one reference PD and another. Only systematic uncertainties from the optical system remain after this technique, and only then for *deviations* in the operating point that would make the reference at the time of the calibration unreflective of the in-situ measurements where the calibrations are applied.

The cross-reference method is generally preferred, except it is often infeasible to find a suitable excitation modulation at RF frequencies. It will be used in later chapters for the systematic-background studies to reference between optical noise at the laser to noise seen at the AS port length-sensors. In those special cases modulations can be generated or detected at the laser table.

The first method is more general and used to validate the calibration from the cross-references against the expectation of a full photopower-model. This chapter covers the scheme used for transimpedances calibrations. For the vertex photodiodes, this is a fundamental necessity to reference between the RF channel, the DC calibration and interferometer end-to-end length-sensitivity. No practical means are known to drive a strong length modulation into the endmirrors at RF frequencies.

All of the auxiliary photodiodes are used in the Cross-Reference manner to reference laser noise to the AS port. To trust those references, the laser noise is fully budgeted into AM and PM noise using transimpedance calibrations of the intensity-monitors and the REFL-PDH-mixer systems. Furthermore, the calibrations of the intensity-monitors allows their use in a Mach-Zehnder configuration to better cross-check the complicated PDH signal-chain.

5.2 Shot-noise in Photodiodes

Photon shot-noise provides an effective reference for calibrating the photodiode output transimpedances. It has the advantage of being inherently white, broadband noise from Poisson statistics, and it is easily related to the DC photocurrent. Poisson statistics are not otherwise intrinsic statistics for electrical current, because impedances cause voltages cause back-reaction which adjusts the statistics. Current derived from the photoelectric effect inherits the statistics of the light incident, as long as the back-reaction terms are insignificant for the photoconversion. Reverse-biased photodiodes with a sufficiently low-impedance cur-

rent sink act in this manner. Thermal light[1] or ideal coherent-state laser light both have Poisson statistics corresponding to independent arrival times of a mean-photon-flux. These statistics are related through the one and two-point correlation functions:

$$\hat{I}_{\mathrm{PD}} = \xi_{\mathrm{PD}}\hat{P}_{\mathrm{PD}} + \hat{N}_{\gamma\to\mathrm{e}} \tag{5.1}$$

$$\left\langle \hat{P}_{\mathrm{PD}}(t)\right\rangle = P_{\mathrm{in}} \qquad \left\langle \hat{P}_{\mathrm{PD}}(t)\hat{P}_{\mathrm{PD}}(t')\right\rangle = P_{\mathrm{in}}E_\lambda\delta(t-t') + \underbrace{P_{\mathrm{in}}^2}_{\left\langle \hat{P}_{\mathrm{PD}}(t)\right\rangle^2} \tag{5.2}$$

Omitted from this table are the statistics for $\hat{I}_{\mathrm{PD}}$ which must account for the photon-electron conversion efficiency. For perfect conversion, the light statistics are inherited as mentioned, but for imperfect conversion, there is a binary process selecting for converted photons. This process is independent, so imprints on the variance of the current the additional variance of a large-N binomial distribution, which behaves for a continuous source like a new Poisson term. The binomial term can actually combine with the photon-Poisson term to create an effective "current source" Poisson term.

$$Q_{\mathrm{eff}} = \xi_{\mathrm{PD}}E_\lambda(1/q_{\mathrm{e}}) \tag{5.3}$$

$$\left\langle \hat{I}_{\mathrm{PD}}(t)\hat{I}_{\mathrm{PD}}(t')\right\rangle = Q_{\mathrm{eff}}(1-Q_{\mathrm{eff}})\hat{P}_{\mathrm{PD}}(t)E_\lambda\delta(t-t') + \xi_{\mathrm{PD}}^2\left\langle \hat{P}_{\mathrm{PD}}(t)\hat{P}_{\mathrm{PD}}(t')\right\rangle \tag{5.4}$$

$$= (1-Q_{\mathrm{eff}})\xi_{\mathrm{PD}}\hat{P}_{\mathrm{PD}}(t)q_{\mathrm{e}}\delta(t-t') + \xi_{\mathrm{PD}}Q_{\mathrm{eff}}\frac{q_{\mathrm{e}}}{E_\lambda}\left\langle \hat{P}_{\mathrm{PD}}(t)\hat{P}_{\mathrm{PD}}(t')\right\rangle \tag{5.5}$$

$$= q_{\mathrm{e}}\left\langle \hat{I}_{\mathrm{PD}}(t)\right\rangle\delta(t-t') + \left\langle \hat{I}_{\mathrm{PD}}(t)\right\rangle^2 \tag{5.6}$$

Equation (5.2) shows the Poisson statistics of the light, whereas eq. (5.4) propagates those statistics, but includes an additional term for the large-N binomial distribution. The effective Poisson term used representing a perfect independent current source is shown in

1. Thermal light has the additional effect of containing "bunched" photon states, where multiple photons are delivered simultaneously. These states themselves have Poisson statistics with a lower effective counting rate per current delivered and can be accounted for with additional Poisson second-moment terms. For incandescent light near 1 micron wavelength, the adjustment to final statistics is $< 1\%$.

eq. (5.6) on page 121.

5.3 Calibration Layout using Shot-Noise

The statistics terms shown for $\hat{I}_{\mathrm{PD}}$ are all white-noise, which propagates through the electronics into a voltage.

$$\begin{aligned}\hat{V}_{\mathrm{PD:DC}}(F) &= Z_{\mathrm{DC}}(F)\hat{I}_{\mathrm{PD}}(F) + \hat{N}_{\mathrm{amp:DC}} \\ \hat{V}_{\mathrm{PD:RF}}(F) &= Z_{\mathrm{RF}}(F)\hat{I}_{\mathrm{PD}}(F) + \hat{N}_{\mathrm{amp:RF}}\end{aligned} \tag{5.7}$$

The transimpedances here represented by Z are frequency dependent. The labels DC and RF distinguish the multiple readouts of the photocurrent through separate ports of the 1811 photodiodes used in the experiment. The white noise then appears in a one-sided power-spectrum of the voltage as:

$$\overline{\mathrm{PSD}_{(+)}}\left[\hat{V}_{\mathrm{PD:RF}}; F\right] = 2q_{\mathrm{e}}\overline{I}_{\mathrm{PD}}|Z_{\mathrm{RF}}(F)|^2 + \overline{\mathrm{PSD}_{(+)}}\left[\hat{N}_{\mathrm{amp:RF}}; F\right] \tag{5.8}$$

Z_{RF} can be solved-for provided that the DC current $\overline{I}_{\mathrm{PD}}$ is known. One of the DC or RF channels must then have a known, non-zero $Z(F = 0\mathrm{Hz})$. Using the DC channel, the estimator for the transimpedance magnitude is expressed:

$$\left|\widehat{Z}_{\mathrm{RF}}(F)\right| = \left(\frac{2q_{\mathrm{e}}\widehat{\mathrm{AVG}}[\hat{V}_{\mathrm{PD:DC}}]}{Z_{\mathrm{DC}}\left(\widehat{\mathrm{PSD}_{(+)}}\left[\hat{V}_{\mathrm{PD:RF}}; F\right] - \widehat{\mathrm{PSD}_{(+)}}\left[\hat{N}_{\mathrm{amp:RF}}; F\right]\right)}\right)^{\frac{1}{2}} \tag{5.9}$$

which requires the separate measurement with no incident photopower

$$\widehat{\mathrm{PSD}_{(+)}}\left[\hat{N}_{\mathrm{amp:RF}}\right] = \widehat{\mathrm{PSD}_{(+)}}\left[\hat{V}_{\mathrm{PD:RF}}; F\right]\Bigg|_{\widehat{\mathrm{AVG}}[\hat{V}_{\mathrm{PD:DC}}]=0} \tag{5.10}$$

5.4 Phase Recovery via Kramers-Kronig Relations

The previous section demonstrates an estimator for the square-transimpedance magnitude, but it cannot measure the phase. Fortunately, the Kramers-Kronig relations constrain the phase information. The transimpedance is determined by the electronics of the photodiode which use feedback amplifiers and linear techniques. The natural domain for electronics is the Laplace domain. This domain is more generally applicable to all linear-time-invariant (LTI) systems such as the control system as well. The frequency response (Fourier domain) of an LTI system such as the transimpedance is related to the Laplace domain through a well-known correspondence of the two transforms. The correspondence exists for sufficiently well-defined (or analytically well-behaved) impulse-responses of LTI systems, which physical realizability always provides.

$$\mathscr{F}\{Z(t); F\} = \mathscr{L}\{Z(t); s = 2\pi \mathrm{i} F\} \tag{5.11}$$

The transimpedance is determined from the connections of lumped-components, with an additional delay-line term for the cables' connection to the equipment. In the Laplace-domain the impedance can then be expressed as a rational function of s, here broken into roots. The root decomposition adds an additional factor Z_G for the overall gain. Only a limited number of roots are necessary given the schematic of the components. The roots of the numerator are *zeros* and the denominator, *poles*. Together, the rational-roots, overall gain and delay terms combine to form the expression:

$$Z(s) = Z_G \frac{(s - z_0)(s - z_1)(s - z_2)\dots}{(s - p_0)(s - p_1)(s - p_2)\dots} e^{-sT_{\text{delay}}} \tag{5.12}$$

The number of poles and zeros is not usually the same. Any imbalance in the number determines the asymptotic frequency response of the system. An excess of poles makes the system asymptotically a (multi-) integrator or low-pass, and excess zeros a high-pass or

(multi-) differentiator.

This expression contains all of the magnitude and phase information for the system. For physical systems which are stable, there are additional constraints on the roots. The poles must all live in the left-hand plane for the impulse response to be exponentially decaying, rather than growing. The zeros can live on either-side of the plane, but zeros on the right do not represent differentiation - unlike usual factors of s in Laplace-domain expressions. Right-side zeros are high-delay differentiators and require specific electrical topologies to implement. Note also that if the delay term exponential were broken into its constituent roots, it contains both kinds of zeros. For *real* LTI-system impulse responses, the expression of $Z(s)$ must be conjugate-invariant[2], $Z(s) = Z(s^*)$

Using the estimator of the previous section, and some knowledge of asymptotics and analytical features of the electrical topology, the transimpedance Z_{RF} can be fit purely in magnitude using eq. (5.12) on page 123 and (5.11) with an expected number of pole/zero degrees of freedom. This fit will recover all of the phase information except that from the delay-term.

The name from this form of analytic-function phase recovery are the Kramers-Kronig relations and they can be proven rigorously using the Cauchy integral theorems. They affect many relations in physics and imply broad results, for example - an inductor with its susceptibility (real-part) changing by frequency also implies some resistivity (imaginary part).

There are some data-analysis issues in recovering phase-information. The pole terms require the fits to be intrinsically nonlinear. Nonlinear fits can have biasing issues when the noise is large which occur when the local linearization approximation is invalid over the uncertainty interval/errorbar. For the fits shown here, the noise is very small compared to the nonlinear sensitivities and the dominant fit errors are from measurement systematics.

2. By eq. (5.11) on page 123, this is equivalent to the Fourier-transform being Hermitian on real signals.

Another issue for the fits is that the fit occurs in a finite region of frequency. If too many pole/zero degrees of freedom exist, they can be erroneously moved out of the fit-region and the altered, yet unmeasured asymptotics can effect the phase-information even inside of the fit-region. For this reason, the number of degrees-of-freedom should be the minimum necessary to recover a residual-reduced chi-square of order-1. Measurements only requiring the magnitude data appropriately-smoothed can use more D.O.F. The measurements of the amplifier-noise power spectrum take this approach.

5.5 Differential Phase Recovery from cross-referenced measurements

The RF measurements of the Holometer are all expressed with the CSD-matrix over the channels. The action of the basis-change matrix to express the RF data in calibrated units has a some symmetries that the calibration-scheme exploits to reduce error. The common-phase is one of them. For a calibration matrix where all elements share some phase-delay in common, the matrix may be expressed

$$\mathbf{C} = \begin{bmatrix} e^{2\pi \mathrm{i}\omega(F)}C_{11} & e^{2\pi \mathrm{i}\omega(F)}C_{12} & \cdots \\ e^{2\pi \mathrm{i}\omega(F)}C_{21} & e^{2\pi \mathrm{i}\omega(F)}C_{12} & \\ \vdots & & \ddots \end{bmatrix} = e^{2\pi \mathrm{i}\omega(F)} \underbrace{\begin{bmatrix} C_{11} & C_{12} & \cdots \\ C_{21} & C_{12} & \\ \vdots & & \ddots \end{bmatrix}}_{\mathbf{C}'} \tag{5.13}$$

which from the basis-change formulas through section 2.10 on page 53 implies:

$$\hat{\mathbf{M}}_{\text{science}} = \mathbf{C}\hat{\mathbf{M}}_{\mathbf{V}}\mathbf{C}^{\dagger} = \mathbf{C}'\hat{\mathbf{M}}_{\mathbf{V}}\mathbf{C}'^{\dagger} \tag{5.14}$$

This simplification is particularly important for the *delay line* phasing that the pole-zero expression cannot restore. The need only for differential phase-differences allows a cross-reference measurements to be sufficient to fully restore phase information on the full system

CSD-matrix. In practice, this is done on a *per system* basis. All of the interferometer PDs are cross-referenced for this phasing, but the auxiliary PDs are only cross-referenced in smaller units that require such information to be useful. In particular, the basis change of two PDs arranged as a Mach-Zehnder requires basis changes with a strong cancellation of the common AM signal to produce the PM/FM signal, so the two intensity (Imon) PDs are cross referenced for that calibration. In effect, the delay can be trusted to be zero for CSDs representing channels in a given cross-referenced system, but not for channels between systems. However, with the zero-pole correction, the phase error between systems can be represented as a differential delay. The representation of the calibration matrix in terms of block-diagonal systems then becomes.

$$\mathbf{C}_{\text{full}} = \begin{bmatrix} \mathbf{C}_{\text{vertex}} & & & \\ & \left(e^{-2\pi \mathrm{i} FT_1}\mathbf{C}_{\text{L:Imon}}\right) & & \\ & & \left(e^{-2\pi \mathrm{i} FT_2}\mathbf{C}_{\text{L:PDH}}\right) & \\ & & & \left(e^{-2\pi \mathrm{i} FT_3}\mathbf{C}_{\text{T:Imon}}\right) \\ & & & & \left(e^{-2\pi \mathrm{i} FT_4}\mathbf{C}_{\text{T:PDH}}\right) \end{bmatrix} \tag{5.15}$$

The T_n terms are all unknown delay lengths. These unknown terms show only for CSD's referencing channels between calibrated systems. Phase-sensitive measurements between such channels must perform statistical tests which marginalize over this delay-time.

The various matrices in practice have certain shapes and calibrations corresponding to their construction. In general more factors than the transimpedances should be included, but this list is to motivate the electronics-characterization strategies for each of the subsystems.

- $\mathbf{C}_{\text{vertex}}$: 4in-by-4out diagonal-matrix with the correct differential phases to represent in-phase interferometer photocurrent to length as per eq. (4.14) on page 94. This provides 2 length-measurements per PR-Michelson, so an additional 4in-by-2out averaging matrix is also constructed to combine the measurements into a single effective length-

sensor per machine. These diodes will be referenced to length via the calibrations of the previous chapter, so the strategy is to minimize error in the transimpedance ratios needed for the length conversion.

- $\mathbf{C}_{\mathrm{L:Imon}}$ and $\mathbf{C}_{\mathrm{T:Imon}}$: For in-situ data, these will be 1in-by-1out for a single intensity-monitor channel which is referenced either as laser-AM or cross-referenced to the vertex channels to represent AM leakage coadded to the length signal. For a small subsection of in-situ data, these matrices will be 2in-by-2out calibration of 2x intensity monitors for a sub-shotnoise measurement of the laser AM spectrum. For ex-situ measurements, the 2x intensity monitors are physically arranged in a Mach-Zehnder (MZ) configuration to provide separate AM/PM sensors. The calibration for the MZ configuration applies an addition basis change into sum (average) and difference channels. The average channel for MZ output provides AM, whereas the difference channel provides PM/FM with its scale set through additional geometric factors.

- $\mathbf{C}_{\mathrm{L:PDH}}$ and $\mathbf{C}_{\mathrm{T:PDH}}$: These are always 1in-by-1out for the PDH mixer output. This channel is the output of the PDH-electronics mixer and quite complicated. In-situ, it is cross-referenced to the ASPDs to provide the PM-conversion-to-length systematic limit, but it can also be referenced to PDH-mixed-sideband photocurrent or to laser-phase-noise.

5.6 Vertex Photodiodes

The photodiodes at the vertex underwent many modifications and revisions from stock 1811 model diodes in order to accept 100mW of photocurrent without distortion. As mentioned, they have both a DC and RF channel. The DC channel is used to measure the total incident photocurrent, and the RF channel to measure the signal sitting on fluctuations of the incident current. The calibration scheme into length uses both channels to project a dither magnitude

in the DC channel into the RF channel.

5.7 Features of the Schematics

The schematics of the 1811 Photodiodes are given in full by fig. 5.1 on page 131 and a simplified form fig. 5.2 on page 132. The simplified form assumes all perfect components, and imperfections are absorbed into parasitic components. The full schematic centers around the photodiode. Starting at the top, the DC bias to the diode is generated through the LM340 voltage regulator, which is itself tuned from 5V to 7V with the feedback resistors. This component actually works poorly in low-loading conditions. It's output impedance, usually assumed low, reaches as high as 10 Ohms when the loading is < 10 mA. Furthermore, the feedback is relatively low-bandwidth which causes the regulator to act as an inductor with a 30kHz crossing-frequency from its output resistance. The 700 Ohm resistor loads the regulator and keeps its current above 10mA under all conditions.

The bias voltage then passes through a 5 Ohm resistor (R_{DC}) and the voltage drop is monitored by the DC channel signal chain. That signal chain is an instrumentation amplifier that is buffered. The bias voltage is then filtered with staged R-C pairs for 2-poles of noise suppression from the regulator and supplies. The overall configuration is actually somewhat non-ideal as the low-pass loops serve to shunt photodiode current from the monitor resistor, R_{DC}, for an overall 80kHz low-pass on the DC channel. It does not affect any in-situ measurements, but the otherwise broadband components in the DC signal chain would have otherwise crossed-over with the RF component bandwidth. As it is, the DC signal is strongly suppressed at any frequency where the RF signal is well-calibrated.

The DC signal chain has an overall transimpedance gain $Z_{\mathrm{DC}} = 10\mathrm{Ohms}$ coming from the R_{DC} and the gain-2 instrumentation amplifier.

The photodiode itself is a 2mm InGaAS surface. The 7V bias voltage increases the depletion depth, reducing the capacitance and speeding up the diode. The dark-current

from this bias is the order of micro-Amps. Such a bias is large for many applications, but against a 100mW incident power it is insignificant. Furthermore, the referencing scheme used to calibrate the RF channel includes this current as it flows through $R_D C$.

The modifications above the diode in the schematic were to apply the specific 7V bias with an unusually low impedance, so that the ∼100mA photocurrent does not overly affect the bias. The large current also warranted smaller gains in the DC amplifiers. The bias still drops by $\sim 10\%$ between unloaded and loaded states.

Below the photodiode are the components for the RF readout. The amplifiers for shot-noise-limited readout have dynamic-range constraints, so the photodiode is strongly high-passed with two-zeros using an inductor to shunt the DC current to ground and a capacitor to high-pass to the transimpedance amplifier. The NE5210 used for this is a monolithic transimpedance amplifier with the feedback-path internal to the chip and differential outputs. This has major stability advantages in reducing parasitic feedback for this fast amplifier. The idealized schematic of fig. 5.2 on page 132 shows what this device looks like as an ideal op-amp. It unusually has a large input impedance. The monolithic chip internally uses a 3.5k Ohm feedback resistance, shown as 7k Ohm through the differential output. The actual forward gain inside the monolithic chip is smaller than usual for op-amp circuits - giving the effective impedance shown. This R_{in} matches against the C_{HP} and L_{HP} to generate the high-pass filters.

This circuit has some undesirable features in the layout of its high-pass. The photodiode observes two paths to ground, one through the inductor to real ground and one through the capacitor to the 62 Ohm virtual ground of the amplifier. The real and virtual grounds are equivalent up to the amplifier bandwidth, so the photodiode actually sees a resonant LC tank circuit. This tank resonance modifies the conversion of photocurrent to voltage through the amplifier, as the amplifier ultimately measures voltage, using its R_{trans} to convert from current. Simulations of this resonance with the listed components suggest that the resonance

should have a quality factor of 4-5, but the measurements show it is ~ 2. The parasitic loss on the inductor is the reason. This loss is not the usual series wire-resistance of an inductor, rather it is the frequency limit for the core-substrate magnetization cutoff. The powder substrate has a $\mu \approx 1000\mu_0$ and is extremely linear even at the large loading, but frequency response is rather slow. As the susceptibility rolls down, the resistance must roll-up and behaves as the effective parallel resistance shown. This resistance, along with the 62 Ohms of the virtual-ground, reduce the Q of the tank-resonance.

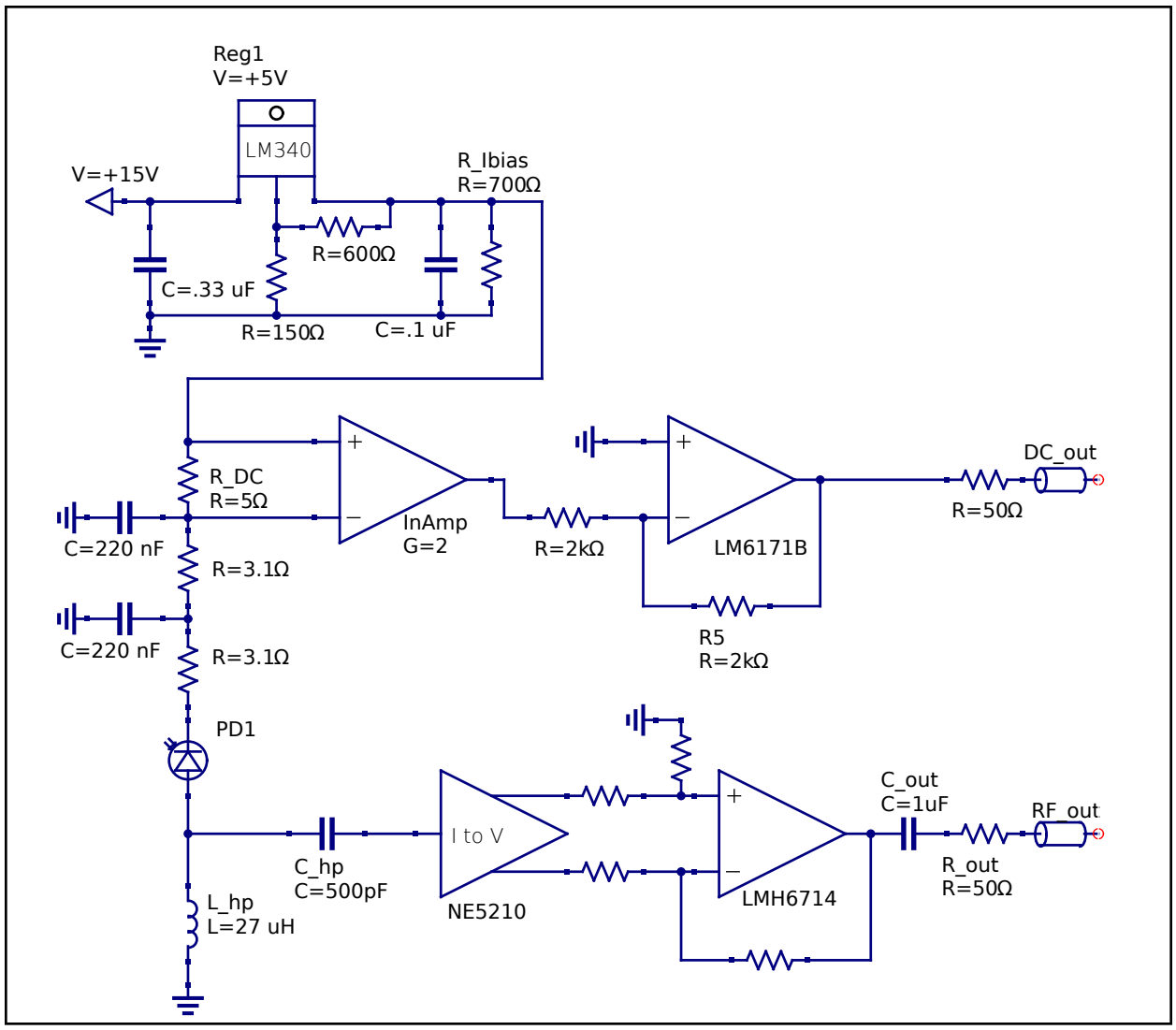

Figure 5.1: Reverse engineered schematic of the vertex 1811 photodiodes with modifications applied.

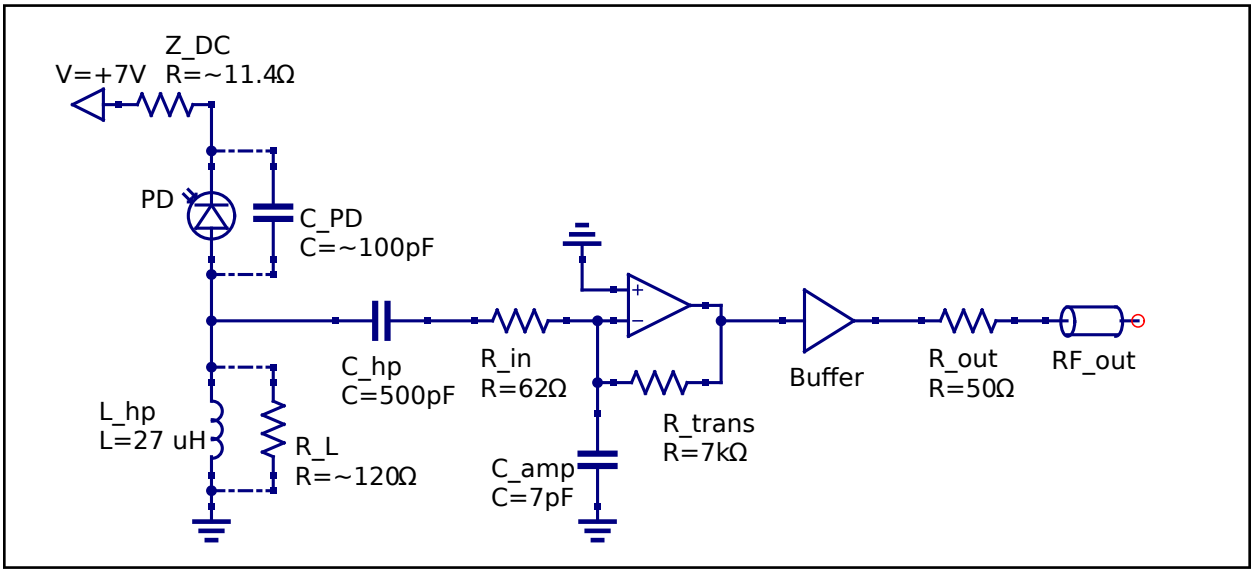

Figure 5.2: Modified Vertex photodiode schematic, simplified to use ideal components with parasitics. The prominent parasitics are the photodiode capacitance, the input impedance of the transimpedance amplifier, and the lossy inductor.

5.8 High-Power Characteristics

The extreme conditions that these photodiodes handle in-situ requires particular diligence of the calibration to account for the load on the electronics. The calibration scheme, in cross-referencing the DC and AC channels, cancels any sensitivity to changes to the conversion-efficiency, ξ_{InGaAS}, as long as it is not frequency-sensitive. Accounting for amplifier-noise, the power spectrum of shotnoise in the RF channel does not scale perfectly linearly in the DC photocurrent as is expected. The apparent nonlinearity of eq. (5.9) on page 122 to DC current is consistent with a Z_{RF} which is itself dependent on photocurrent. From the estimator, Z and ξ are degenerate, but pushing the effect into Z is motivated from the electronics as well as reference-sweep measurements (shown in fig. 5.9 on page 143).

The photodiode ejects electrons through the semiconductor band-gap at the interface of the two substrates. The reversed-biased diode has a physical *depletion-zone* acting as a insulating dielectric. The space acts on the circuit as a parasitic capacitance, modifying the gain of the RF amplifier. As the incident power increases, the diode-bias changes with load from the non ideal voltage-source providing the bias ($\sim 8\Omega$ on 100mA photocurrent drops the 7V bias 10%). The changing bias causes the total transimpedance, Z_{RF}, of the RF channel to change through the changing photodiode parasitic capacitance. The RF-transimpedance must then be evaluated as a function of the load current. The high load also heats the components upwards of 60°C. This could also change more of the component values, so the transimpedance is best measured after some operating time at the steady-state thermal load.

The total DC-transimpedance, Z_{DC}, could also be changing as a function of load, though this is not motivated by a known physical mechanism. All of the components of the DC-signal chain are rated with low thermal sensitivity ($\sim 10^{\mathrm{PPM/C}}$), so that loading should not cause even 1% effects. Furthermore, the in-situ power-calibrated laser incident on the PDs using the expected conversion efficiency of the substrate, $0.7^{A/W}$ reproduces the expected photocurrent when referenced through the schematic-specified DC transimpedance. This is an important

observation for the DC transimpedance, for which directly measurements are difficult because the DC signal-chain is not shot-noise limited, and a reliable estimator of the form of eq. (5.9) on page 122 cannot be made. The photocurrent appearing within a few percent of the nominal expectation from efficiency and schematics allows one to conclude that either a) the quantum-efficiency is high and the transimpedance is low - unlikely as the efficiency is about the standard reported for InGaAS - or b) the efficiency is low and the DC-transimpedance is higher than nominal. The second conclusion could be problematic. Propagating it through the calibrations indicates that the sensitivity in that case is worse than reported. The work to characterize this case was done by Jonathan Richardson for the Holometer and composes the RF shotnoise, RF reference and an additional DC reference measurements to constrain the DC transimpedance. The data shows some systematic effects, but reliably reports the DC transimpedances are near 9.7Ω, even when under heavy photocurrent loading. The analysis in this thesis use the nominal values, which err conservative on the calibration.

The calibration systematics are primarily affected by the RF components changing under load. These cause not only Z_{RF} to change with load, but also the amplifier noise,$\hat{N}_{\mathrm{amp:RF}}$ as well. The change in the noise is relatively small, at most 10% itself for a 10% capacitance-change. For measurements of eq. (5.9) on page 122, where the eq. (5.10) term is small, this change is neglected. These neglected frequencies are indicated in the amplifier-noise budget of fig. 5.8 on page 142 and the influence to the fit is discussed with reference to the analytic constraints chosen. The noise-change effect does explain the large erroneous excess impedance of the estimators vs. the fits (at frequencies $<$ 500kHz) shown in fig. 5.3 on page 137.

5.8.1 Analytic Constraints on the Pole-Zero fit

The 1811 RF-transimpedance is AC-coupled across 2-zeros at frequencies below 100kHz. Two zeros located at $0Hz$ of the Laplace-plane provide the appropriate F^2 response. Knowledge of

the schematic places these zeros without any sensitivity to other components, so they are not marginalized in the fit. There are crossover frequencies for the amplifier input-impedance vs. both the high-pass inductor and the high-pass capacitor, these provide a pole each to cancel the original high-pass zeros. The current-source at the PD actually sources an LC tank-circuit between the high-pass inductor and capacitor, even though the inductor connects to the true-ground while the capacitor is connected to the amplifier virtual-ground. The resonance requires the addition of one complex-pole and one complex-zero to the ZP-model. The photodiode capacitance crosses-over the amplifier input-impedance for an additional overall pole. Accounting for complex roots having two degrees-of-freedom vs. real roots having one, the total D.O.F. budgeted through this basic analysis of the circuit is 7. For the actual fits, the number of parameters was marginalized, adding a pole-zero pair until the residual chi-squared stopped precipitously falling.

The chi squared is not expected to fully reach 1 because the model does not account for the systematics of the amplifier noise-gain changing with load. Adding too many parameters to attempt to lower it will impact the phase-recovery by over-fitting as per section 5.4 on page 123.

Ideally, the full analytic form of the amplifier electronics could be fit. This actually was attempted, but requires too detailed of knowledge for the components, particularly the loss in the high-pass inductor (via susceptibility dependence on F). The expressions are not included here, but the load-sensitivity of Z_{RF} seen in fig. 5.3 on page 137 are followed qualitatively when changing capacitance (and some inductor susceptibility-saturation) are expressed in the electrical model.

Along with the predetermined two 0Hz-zeros, the 20MHz-Bessel-Nyquist-Filter of the RF-ADC was modelled as poles/zeros and added to the fit. The Nyquist-compensation was further modified from the digital-boxcar-averaging that takes the RF DAQ from 100MHz sample-rate to 50MHz. This required some additional fitting of the digital transfer function

(Z-domain) back into poles/zeros of the Laplace domain. The final PD fit can compensate for any error in those adjustments through detuning the budgeted degrees of freedom, assuming that the error can be expressed as a detuning and does not need additional D.O.F. During initial fitting, however, the budgeted real-pole of diode-capacitance low-pass was required to be complex for stable fits on all of the PDs. This doubles the asymptotic low-pass response of the PD. It is possible in the limited bandwidth measured that the fit merely needed more D.O.F, potentially to correct for errors of the Nyquist filter model or cables.

5.8.2 Fit Data for representative 1811 Vertex Photodiode

Included in this section are the data plots for a single diode of the four used at the vertex. These plots are representative of the qualitative features between the diodes, to the point that showing other diode data is redundant. The next subsection shows aggregate data for the vertex-system where the diodes may be compared. All of the statistics of the fits are small enough that errorbars are not included. More important is an analysis of the systematic errors to the measurements.

These data for the Vertex diode were collected by Jonathan Richardson, but applied to this unique analysis. The data for the other diode systems was collected by the author.

These data are indexed and colorized by the DC-channel voltage representing the photocurrent load-detuning of the RF-transimpedances. The NF1811.4 label of the photodiode is an internal labelling scheme accounting for the diodes and is unimportant except to select this particular representative.

Figure 5.3 on the following page and fig. 5.4 on page 138 demonstrate that the previous considerations accurately describe the diode qualitative shape and parameters (the analytic response). Figure 5.5 on page 139 displays the residuals to show both that the fit is well-modelled and that the detuning by photocurrent-load is also expressed within the D.O.F of the fit. The residual errors then must be systematic in nature or otherwise not represented

through the limited D.O.F available to the fit. This figures also show the resonant response of the diode indicated by section 5.7 on page 128.

Figure 5.6 on page 140 displays the extent to which the photocurrent-load affects Z_{RF}. Interpolating the fits through the VDC dependence can eat the calibration systematics, but otherwise the error is small when considered as a Z_{RF} change, but somewhat large if interpreted as a ξ_{PD} change.

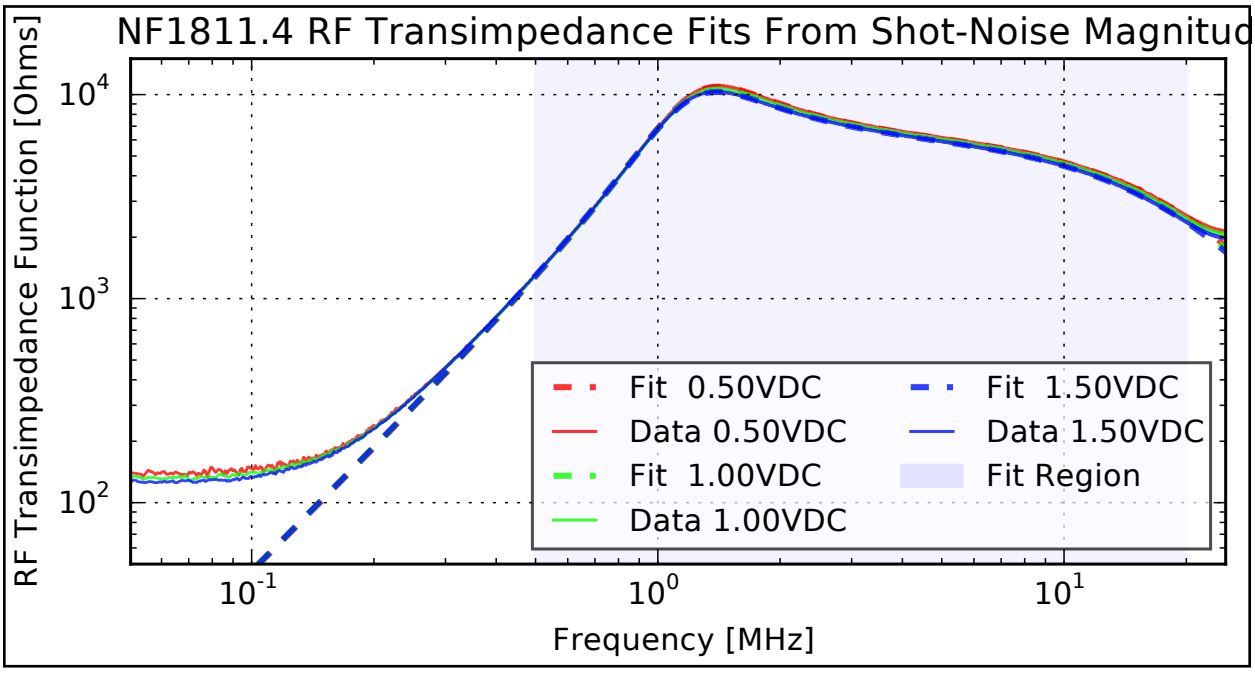

Figure 5.3: Shot-noise derived fits of the Vertex photodiode transimpedance used in calibrating the experiment. The overall shape is determined through the analytic constraints of section 5.8.1, showing an F^2 high-pass, followed by resonant enhancement, crossover to low-pass and finally Nyquist filtering. The low-F fit-mismatch is from amplifier-noise systematics and the high-F mismatch is from ADC sample-aliasing foldback.

The baseline, "dark" amplifier noise, $\widehat{\mathrm{PSD}}_{(+)}[\hat{N}_{\mathrm{amp:RF}}]$, is shown in fig. 5.7 on page 141. This includes some pickup of power supply switching frequencies, some noise internal to the RF-DAQ ADCs and other undesirable line-features. The fit is included as a compact representation of the noise-floor for later budgeting. It is used in fig. 5.8 on page 142 along with the transimpedance that is fit and interpolated to derive the level of excess noise in the

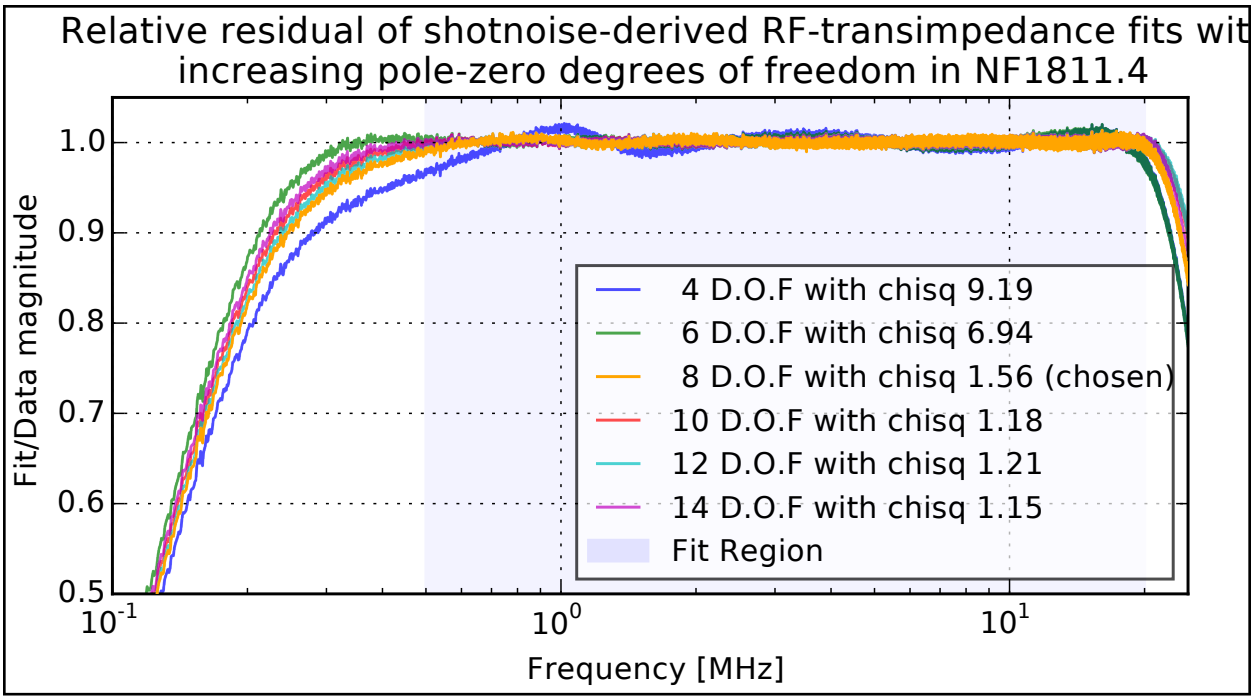

Figure 5.4: Shown are the transimpedance zero-pole fit divided by the data. Each line represents an additional pole and zero in the fit. The low D.O.F. data shows an oscillation similar to the Gibbs-phenomenon. The reduced chi-square falls precipitously from 6 to 8 D.O.F. where the fit contains as many degrees as budgeted by the schematic. Past that budget, the chi-sq falls slowly and the fit manages to reduce residuals even outside of the fit-region, displaying signs of over-fitting.

experiment due to "non fundamental" sources like the electronics noise. The budget shows that the experiment must run around 1%-2% longer for the same significance due to excess electronics noise.

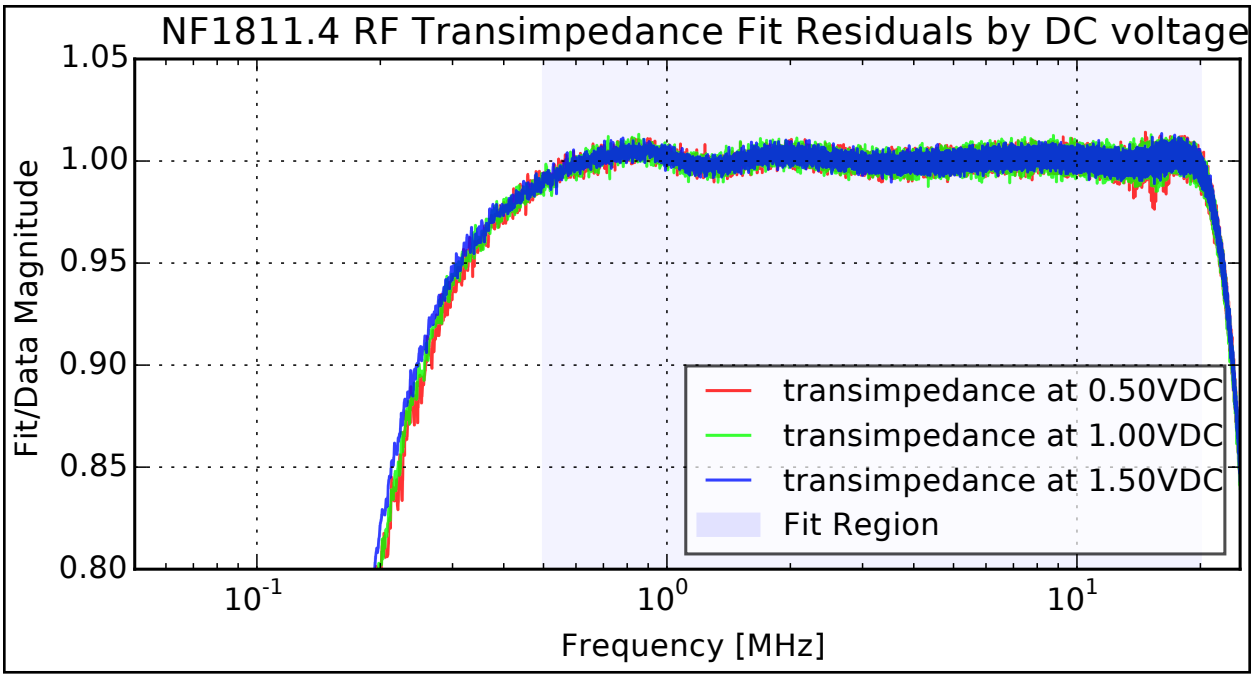

Figure 5.5: The residuals as a function of diode-load show that the model is sufficient to marginalize the detuning of the response by load. The common shape remaining expresses systematics not budgeted as parameters in the fit. Their effect is $< 1\%$, sufficiently subdominant to other systematics as to be neglected.

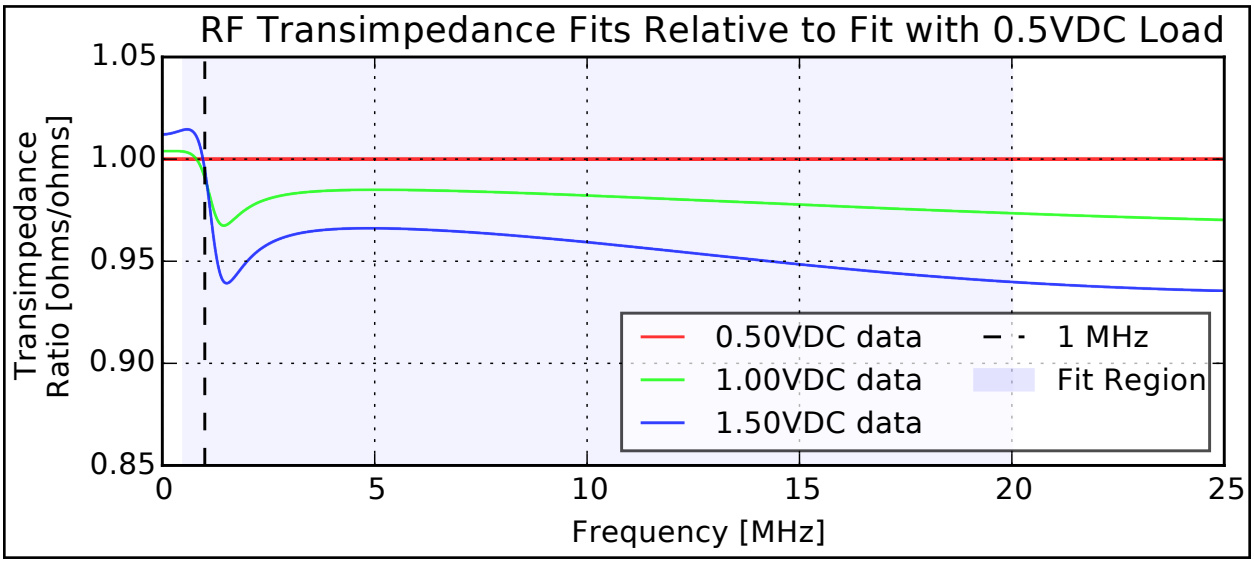

Figure 5.6: The differences in transimpedance relative to the low baseline load at 0.5VDC (50mA or 70mW incident). The change to the shaping is small and is consistent with a photodiode capacitance change affecting the circuit. Higher load *increases* the capacitance, lowering the resonance and crossover frequencies with other components. The net effect increases gain below the mean crossover and lowers it above.

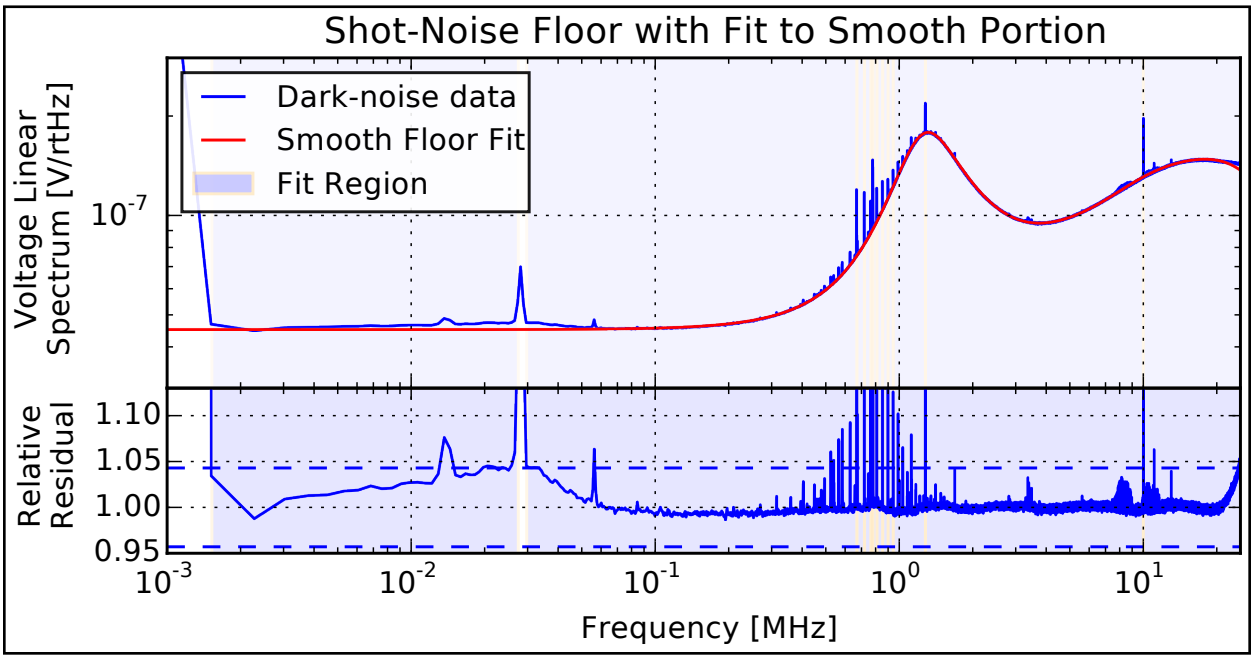

Figure 5.7: The amplifier "dark" noise of the detectors, with included fit of the shape. This fit is used purely as a compact representation of the shape (phase undefined for a noise-spectrum of superimposed sources). It uses many D.O.F. to overfit all but the narrowband features. Those features come largely from background in the ADC digitization, but also contain some residual power-supply switching elements.

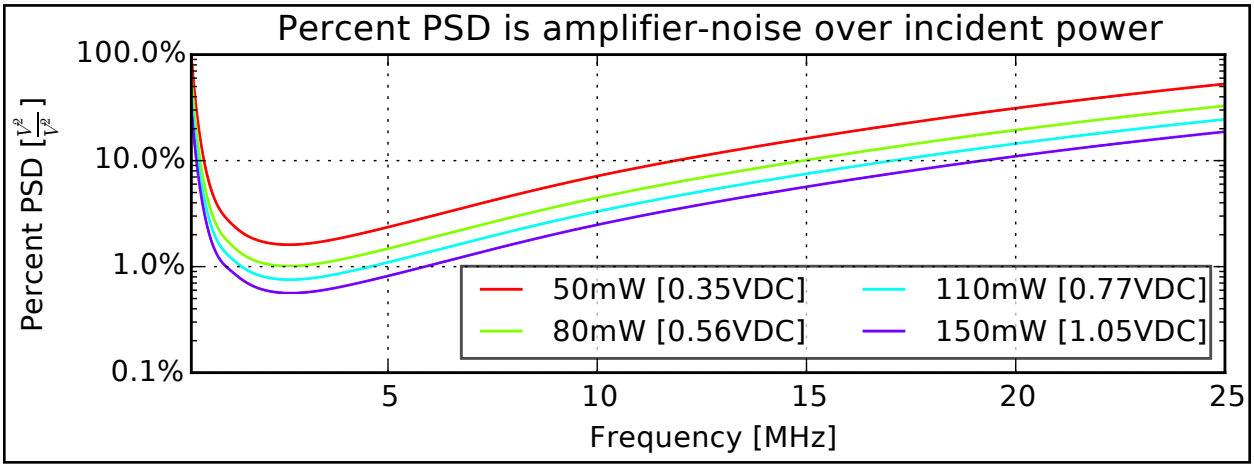

Figure 5.8: The percent amplifier noise background over "fundamental" quantum-noise of the laser signal-carrier. The final significance of the experimental result is lowered by this factor. At low-F the transimpedance becomes small compared to the amplifier input-voltage noise, at high-F the current-noise of the amplifier-input sees a relatively larger transimpedance than the current referred to the photodiode output due (subtly) to the high-pass capacitor in-between.

5.8.3 *Fit Data for Vertex cross-referenced system*

The four vertex photodiodes (ASPD) are all measured and fit in magnitude against the shot-noise. To gain the additional cross-reference for determining the differential-phase delay, an infrared LED was driven simultaneously into the vertex 1811 PD and a reference photodiode. This was done individually for each of the vertex PDs, generating one cross-reference measurement, $H_{\mathrm{ref}}(F)$, apiece. The overall gain of this reference measurement was not constrained by the setup, so each sweep plot sets the gain arbitrarily to 1 at 1MHz for the sake of comparing between the photodiodes. $H_{\mathrm{ref}}(F)$ for each ASPD initially includes the shapes and phases of: the ASPD, the reference-PD (RPD) and the cable-delay to each. The shot-noise calibration is applied to remove the ASPD shape and phase. In all of these figures the LED sweep rate skipped some CSD-bins, leaving them with small SNR. Only the bins above SNR > 20 were plotted to reduce visual-noise. The fits used all data with the appropriate weighting against the SNR.

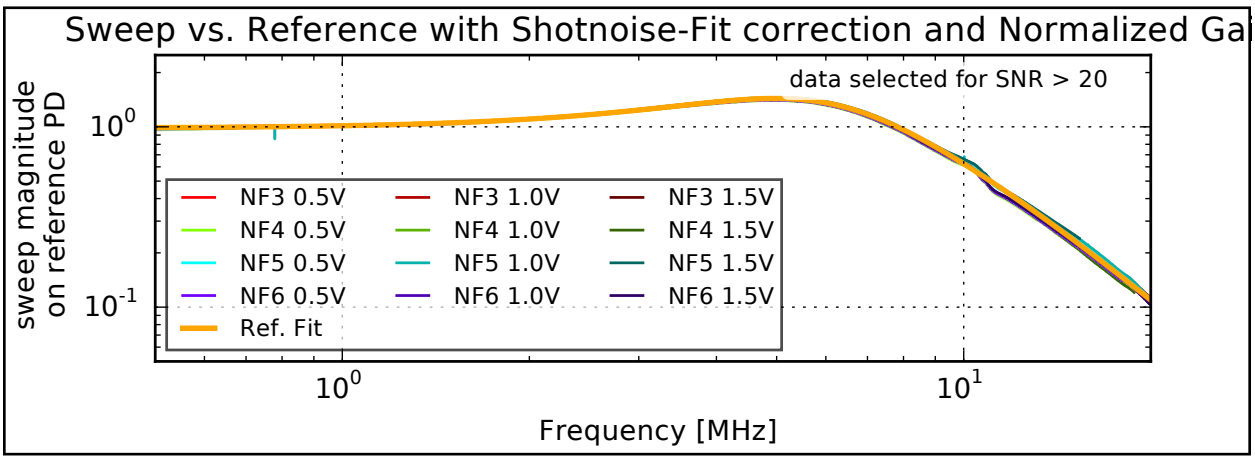

Figure 5.9: Plotted are the magnitude residuals of many LED-sweeps between a common reference PD and each ASPD operating a given photocurrent load. All of the data sit beneath the fit for the mean reference-PD transimpedance-magnitude. At high-F, the reference sees systematic effects in the reference or the vertex-diode fits are themselves imperfect. The reference photodiode spoon-like shape indicates a gain-peaking instability of the diode circuit.

The residual transfer-function $H_{\mathrm{ref}}(F)$, now contains just the RPD and relative cable-

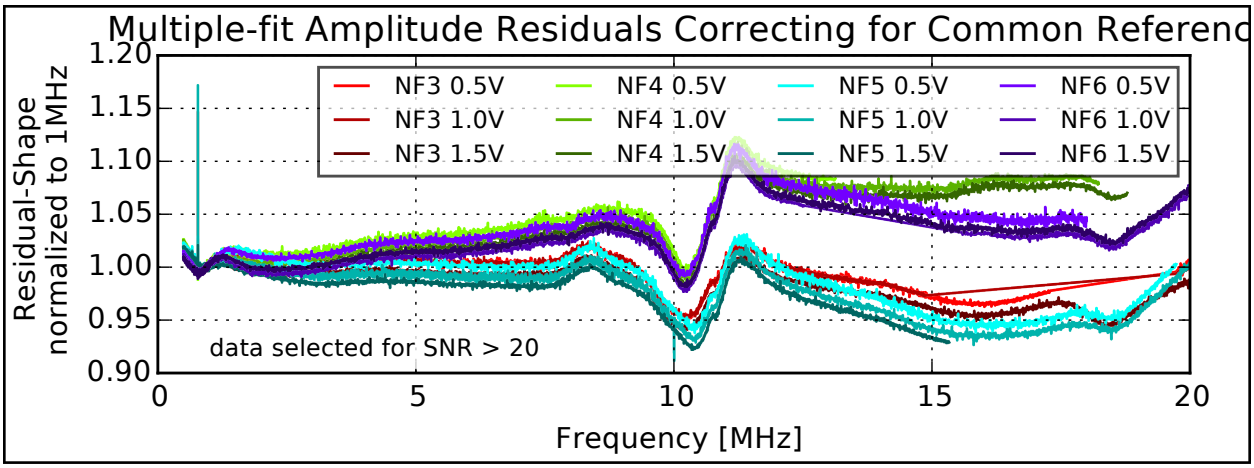

Figure 5.10: Plotted are the magnitude residuals of the LED-sweeps after correcting for the ASPD fits as well as for the common reference. The residual error is small yet grows with frequency, this is likely due to bandwidth limitations of the reference, but the inconsistency indicates the reference fit may have some small bias in the phasing due to the changing reference operating above its bandwidth.

delays between the ASPD and RPD. All of these are plotted, along with a fit to the mean RPD magnitudes in fig. 5.9 on page 143. Fitting to purely the magnitude of the sweep-measurement allows the purely-RPD component to be removed from all of the $H_{\text{ref}}(F)$ measurements, leaving only the relative cable delays. The residual magnitudes are shown in fig. 5.10. The remaining error is likely from systematic changes to the reference PD operating at the edge of its (claimed) 10MHz bandwidth, although fig. 5.9 on page 143 shows that this 3db bandwidth is only achieved through marginally-stable amplifier gain-peaking in the RPD.

Finally the residual delays are fit using a phase-sensitive delay-line model. The residual phase error after correcting the 2x-phase-restoring ZP models with an additional extraction of the delay demonstrates the effectiveness of the magnitude-phase-restoration of the ZP-fitting. These residuals are displayed in fig. 5.11 on the following page.

The fits to the RPD-differential delay are attached to the shotnoise-ZP-fits of the ASPD's.

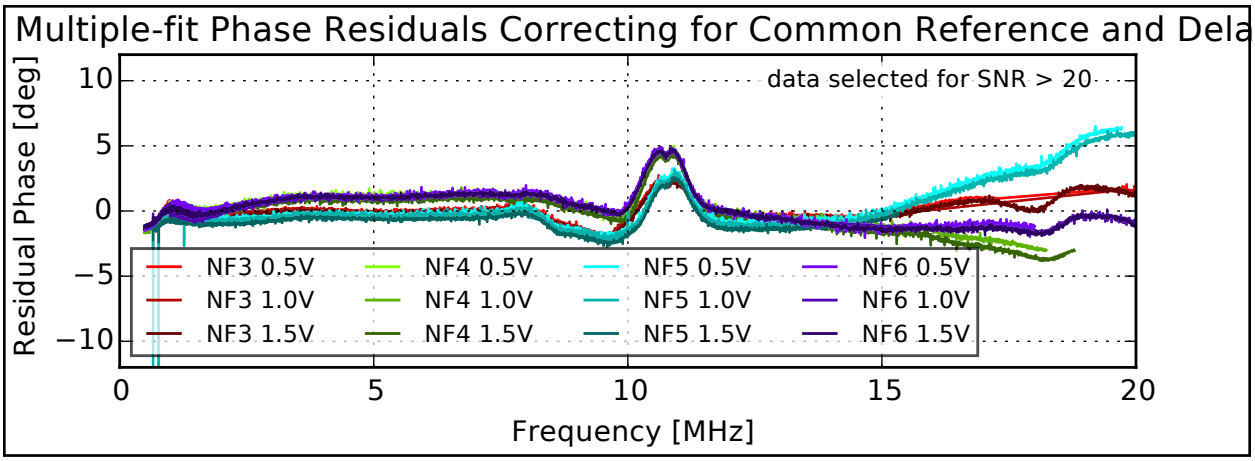

Figure 5.11: These are the final residuals after phase-correcting from two magnitude ZP-model fits and the overall differential delay-lines to each vertex PD. The small residual error indicates the ZP-fits are correctly accounting for the phasing of the transfer functions and that the only remaining effect on the phase is from signal-delay.

The delay value includes unknown delay to the reference[3]. This delay is common to all of the reference measurements, so sits within the symmetry invariance of the calibration-basis CSD matrix and does not introduce error to CSDs between vertex photodiode, but does introduce phase error between the vertex and other systems.

5.9 Comparison of ASPD fit data to electrical model

The complexity of the circuit and loading conditions of the photodiode inspires worry about the sensitivity of the response to the changing environemnt. The figures fig. 5.12 on the next page and fig. 5.13 on page 147 show a comparison of the real data to the worry of a potentiall strong phase-affect from the thermal sensitivity of the high-pass capicitor resonating in the circuit.

The comparisons of model show that the loss of signal by poor phase-correction of the calibrations is highly unlikely. Both the capacitance would have to change a full 20% and

3. The reference delay is actually corrected-for in the datasets, but to unknown accuracy.

the strong magnitude effects whould have to be missed.

The data and model both show a large phase rotation, but the residual displayed in fig. 5.11 on page 145 shows that the phase-restoring fits properly account for this.

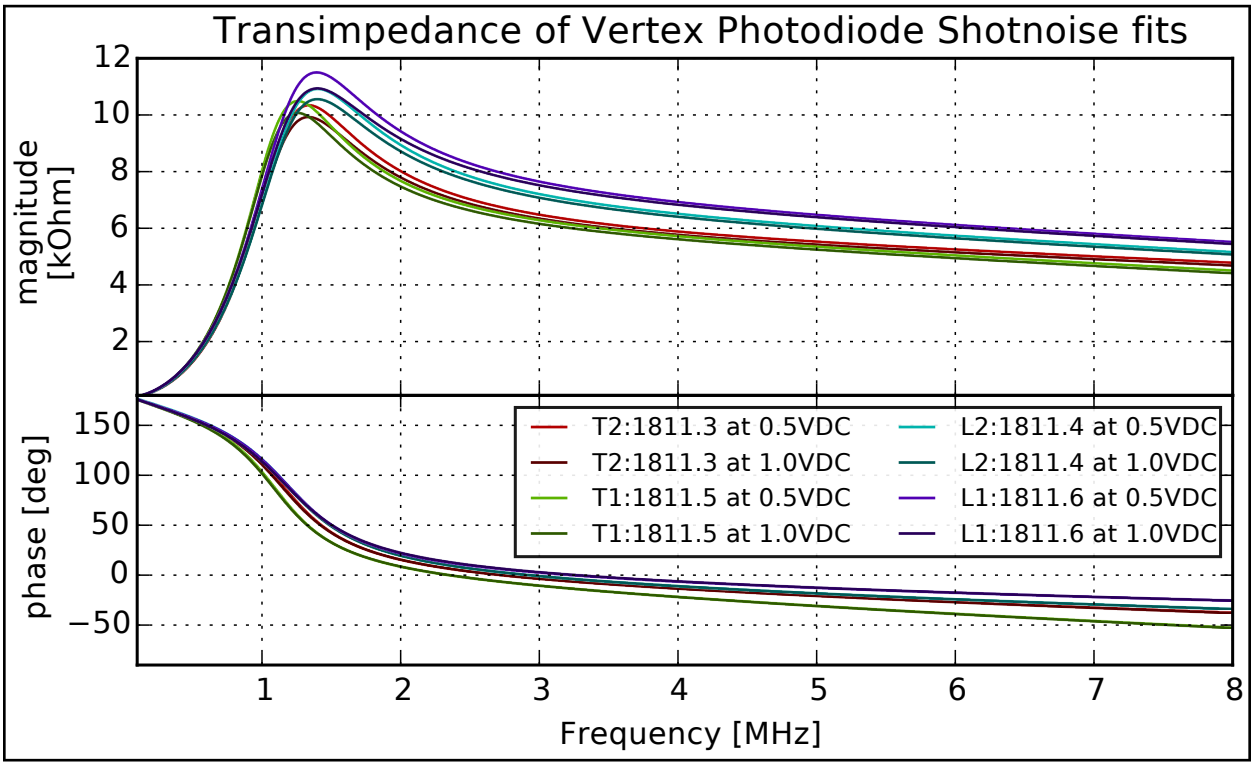

Figure 5.12: The ensemble of ASPD shot-noise phase-corrected fits above/below the nominal loading. These exclude the delay line fits from the reference for better comparison with fig. 5.13 on the next page. All of the data here are implicitly contained in previous plots, but shown here for reference.

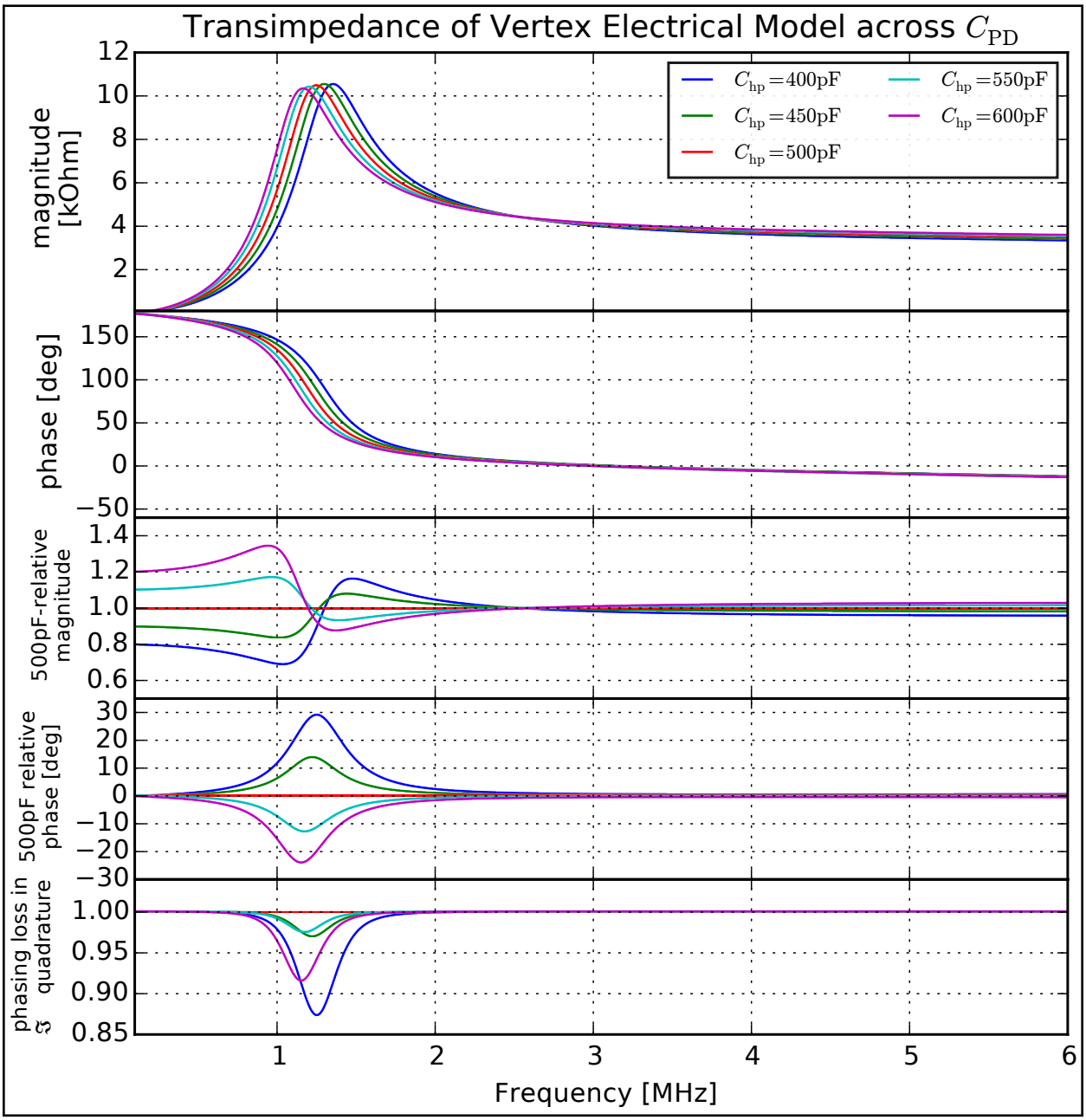

Figure 5.13: Schematic model of Vertex 1811s with a variation of the nominal high-pass capacitance. The model here does not perfectly capture the responses fit. The largest uncertainty is from the lossy-inductor's effect on the resonance width. Any variation of the capacitance would show in-situ through in the shape of the shot noise power spectrum at the 10% level.

5.10 Pound-Drever-Hall Photodiodes

The photodiodes used for Pound-Drever-Hall operate with very different optimization constraints than the AS-port diodes. They also are capable of sinking large-photocurrent for shot-noise limited phase sensitivity, but in practice they are actually limited by the dynamic-range changes between lock-acquisition and steady-operation. There are multiple aspects affecting their design, centered around the sideband optical conversion and signal mixing that constitutes the Pound-Drever-Hall technique. The schematic is provided in fig. 5.14 on page 150. It and other considerations on the PDH signal-chain are motivated by:

1. The Pound-Drever-Hall sideband frequencies used for this dataset are 20.6MHz for the **L** interferometer and 24.49MHz for the **T**. These are set from the desire to prevent external drive on the laser within 10MHz of the signal band to reduce spurious RF injection. For the **T**, the range of frequency was limited by the resonance of the Electro-Optic-Modulator (EOM) used for the sideband-drive. It could be used off-resonance just as well to lock the cavity, but not with sufficient modulation-depth for the high phase-sensitivity required to limit correlated phase-noise systematics. Both interferometers used a PDH drive amplitude around 10 milli-radians (mrad) determine from the EOM manufacturer specifications.

2. Signals outside of 10MHz of the sideband drive are irrelevant in the photodiode. Particularly those around DC where real physical motion generates large optical signals-that can saturate the diode. To solve this, the circuit has a higher frequency AC coupling using a smaller high-pass inductance to shunt low-F photocurrent to ground. This adds more parameters affecting phasing dependence of the circuit, but only the center point of the resonance must be set, and the components were chosen for a very wide resonance with little sensitivity to the components. The fit data pshow the resonance width of many MHz.

3. The photodiode capacitance and its effect on amplifier noise is a large issue. It is solved using an additional parallel-inductor to form a tank-resonance with the diode. The L_{tank} must include a very large isolation C_{iso} so that the diode may retain its reverse-bias without the isolation capacitance detuning the resonances (it must behave like a wire).

4. High amplifier transimpedance usually helps to overcome amplifier-voltage noise, but it can be a hindrance with limitations on the linear response dynamic-range. Ultimately the attenuation to the photodiode and sideband drive amplitude were adjusted to meet the range requirements, but this came at a higher cost to noise performance than could be solved through adjusting the amplifier-transimpedance. The all-in-one amplifier chip could not have that parameter adjusted. The same net effect through adjusting the effective transimpedance externally with additional shunt-resistance to ground was rejected as it increases the noise-gain of the amplifier to an unacceptable level.

5. The sideband downconversion-mixer between the PD and the Local-Oscillator (LO) also saturates. This is easily solved using filters and attenuators between the mixer and diode, not affecting the noise but adding more components to compensate-for in the calibration.

6. During steady-state operation the PDH sideband is minimized to a residual by the control system. If this residual saturates it can drive a nonlinear "motorboat" oscillation pushing large noise into the control loop and phase-detector. This falls into a sub-case of the dynamic-range issues already mentioned, but it is a unique issue to note.

7. The square-wave double-balanced diode mixer itself is complicated. It requires proper termination of the PD as it reflects diode-transition nonlinear products through the local-oscillator and PD ports. The stock 30-ohm output impedance of the diodes was

adjusted to be the standard 50-ohms, and bandpass filters were added to attenuate the reflected nonlinear products, at no cost of noise but at some cost of system complexity and modelling. The recommendations of "Tutorial on the double balanced mixer[11]" were followed both for setup and modelling of the mixer-response.

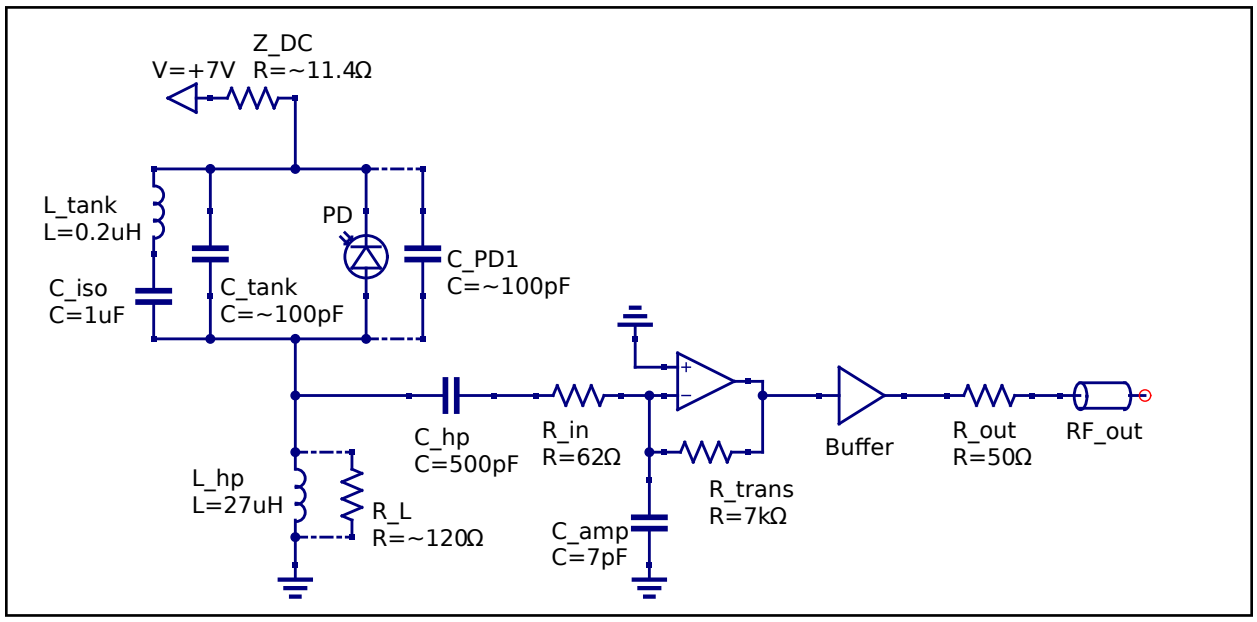

Figure 5.14: Idealized schematic of the PDH photodiodes. They are identical to the vertex diodes except for the additional tank-resonance circuit wrapped around the photodiode. This provides a narrowband escape from the parasitic photodiode capacitance around the PDH modulation frequencies and furthermore optimizes the noise-gain at those same frequencies.

Together these considerations affected both the signal chain around the diode and the diode itself. For characterizing the PD transimpedance, only the shot-noise measurements were used, but they were taken with the DAQ at full 100MHz sample-rate to measure to 50MHz. The fits were done at different intervals of photocurrent-load. The chosen operating point keeps around 0.14 VDC (14 mA) of light on the diodes with an unlocked IFO. For a locked instrument this level actually decreases through critical coupling and settles at 1/3 to 1/2 of maximum for the **L** and **T** respectively.

All of the fits show the direct transimpedance of the photodiode, with no included signal

chain components. Later modelling combines the fit measurements with the signal-chain components to derive the predicted PDH response.

5.10.1 Fit Data for L interferometer PDH photodiode

The transimpedance fits of fig. 5.15 on the next page show the broad tank resonance centered around the PDH drive frequency. It is relatively broad to give a high-bandwidth phase-sensitivity after mixing. The isolation capacitor used to maintain the DC bias is the cause of the undesirable large gain around 1MHz. That capacitor forms a resonance with the large high-pass inductor (not the tank-inductor) preventing its shunt-to-ground action and instead managing to create a significant gain for the diode. Fortunately the interferometer noise at this resonance does not saturate the amplifier and the bandpass filters successfully remove this gain for the mixer.

The noise of these measurements is poor from 1 to 5MHz for the low-photocurrent (generating shotnoise) datasets. This is biasing the fits around those frequencies, but the fit is good around the actual sideband, so the model including the mixer is sufficient as long as high-frequency mixer output isn't folding into these frequencies.

The residuals of fig. 5.16 on page 153 mirror these concerns, showing that the fit is excellent near the PDH-drive, but poor at the low photocurrent measurements and outside of the optimized region for the diode.

The relative gain plot of fig. 5.17 on page 154 shows that there are some load-systematics on the RF transimpedance. The "lump" around 30MHz is notable, but may be due to new crossover-frequencies that exist with the changing photodiode capacitance. Otherwise the systematic errors are fairly limited and a 10% level calibration could be expected for this diode.

The dark noise shown in fig. 5.18 on page 155 and corresponding amplifier-limited sensitivity budget of fig. 5.19 on page 156 are the most important results of the fits. They

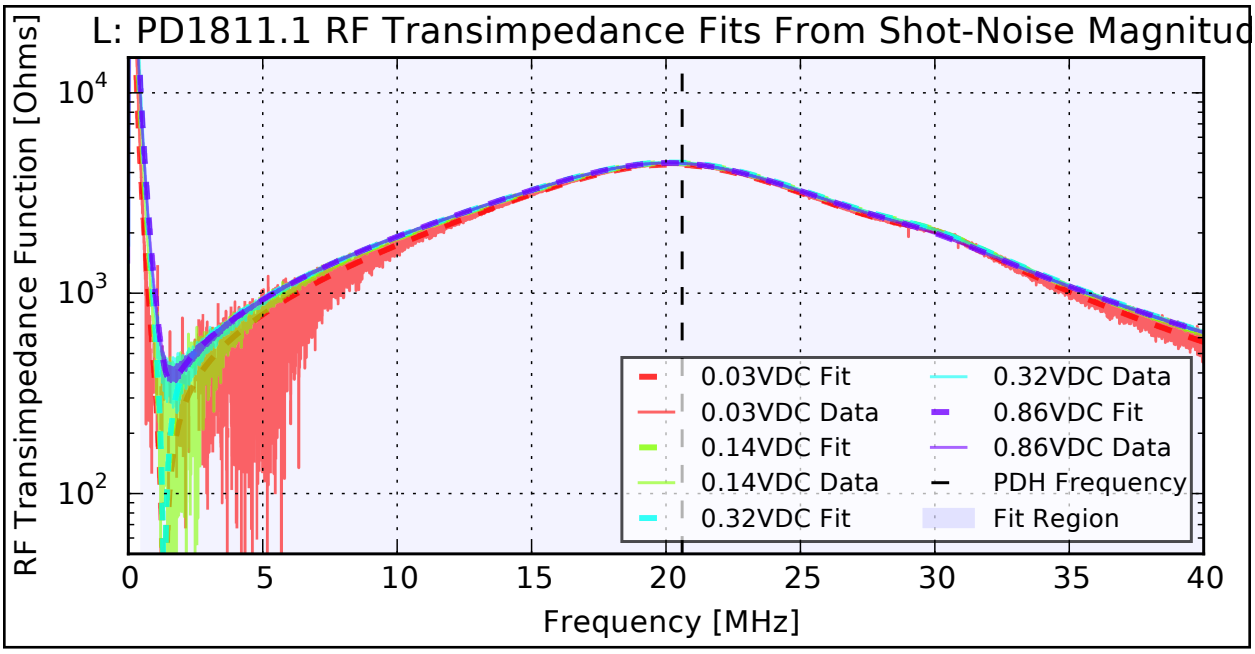

Figure 5.15: Fits of the **L** PDH photodiode transimpedance, showing broad resonant-gain around the PDH-line. These fits are used to model the final phase-noise sensitivity of the PDH system.

indicate that the chosen operating point will actually be *marginally* shot-noise limited. Of course it could do inherently much better if the cavities were operated at critical coupling and had sideband-limited shot-noise, but the Holometer was not designed to optimize the phase sensitivity of these detectors, and shot-noise limited measurement is the best possible given the optical-setup.

5.10.2 Fit Data for T interferometer PDH photodiode

The data and analysis for the T PDH photodiode follows closely to the L. The primary difference is the tuning of the tank resonance to the **T** sideband frequency. For historical reasons, the T PDH photodiode is actually a 1mm diode rather than the usual 2mm of the other high-photocurrent diodes. The smaller diode has a smaller total capacitance as well, making the tank-resonance more broad as it needs a correspondingly lower inductor.

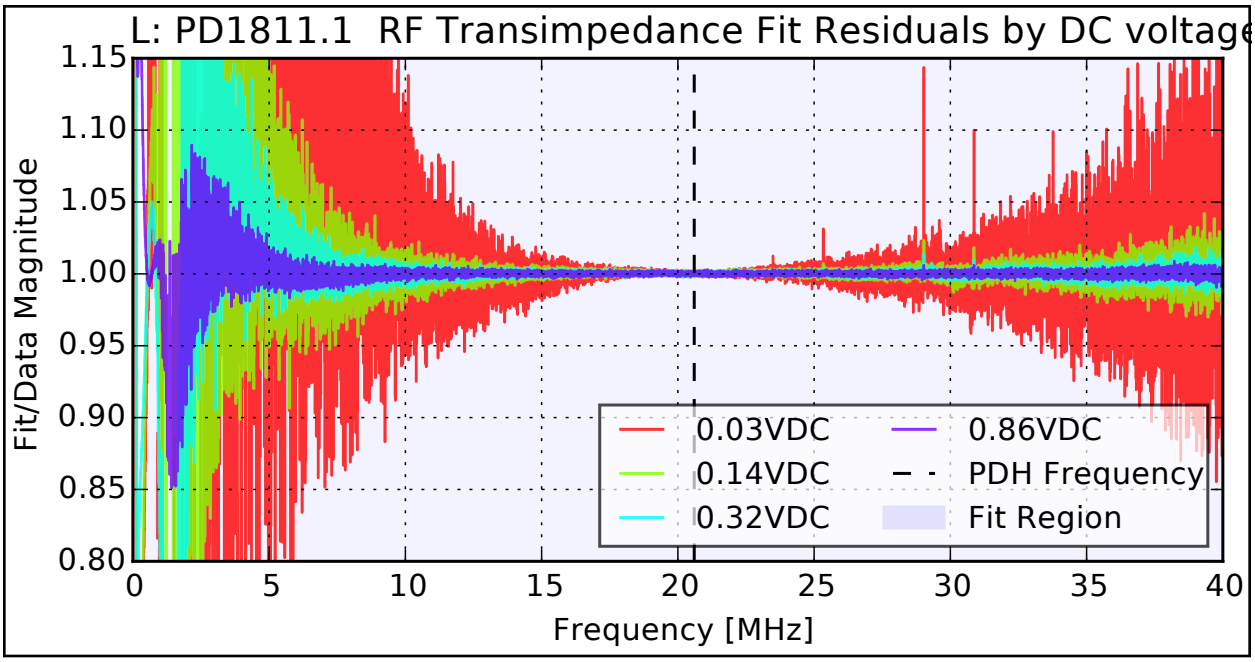

Figure 5.16: Transimpedance fit residuals for the **L** PDH photodiode showing high data quality centered at the PDH sideband frequency.

This appears to have some significant effects for the amplifier noise shown in fig. 5.23 on page 158. The large number of crossover frequencies from the additional components makes the difference between the L and T photodiodes difficult to fully account.

Another feature between the gain fits and dark-noise is the change in the center-frequency between the gain resonance and the noise-notch. The different reference points of the circuit for photocurrent and amplifier noise-current are the cause for this. Each respective point may see the same resonance detuned differently from intermediate components.

5.10.3 Modelling Post-Mixer signal chain

As mentioned in section 5.10 on page 148, each interferometer photodiode-mixer setup has a chain of conditioning filters to construct an optimized PDH signal. The data-sheets of each MiniCircuits BNC components were fit to recover the amplitude and phase of the passing signal. These fits only account for the forward scattering (S12) through the filters, and

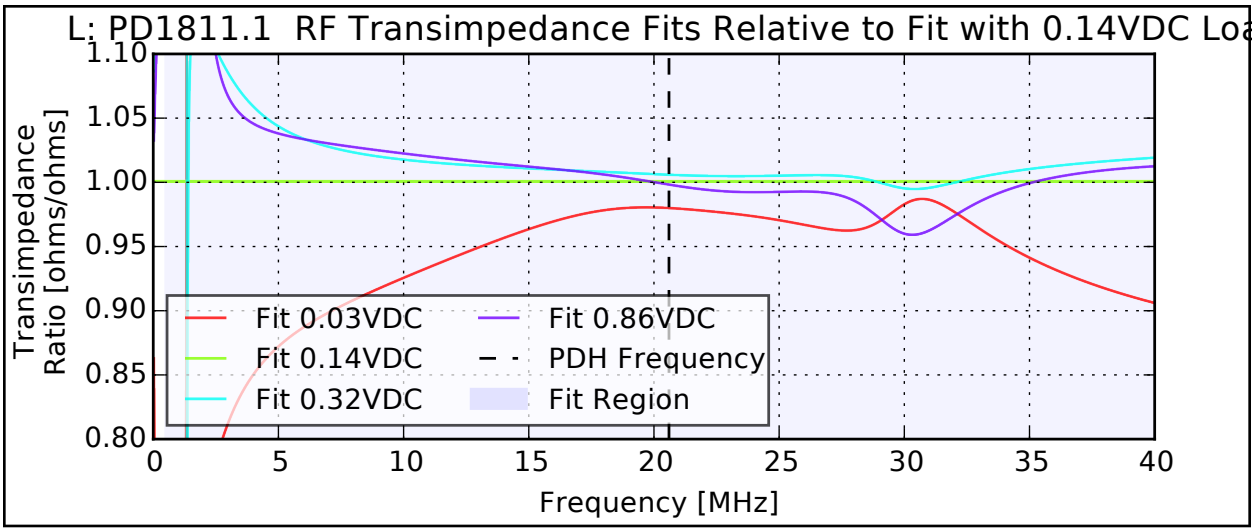

Figure 5.17: Relative gain changes of the **L** PDH-diode from the unlocked nominal 0.14VDC load state. The transimpedance shape is different for low-load due to the poor, biased fit. At high load electronic effects change the response as the photodiode capacitance increases with the load.

cannot be applied for a more ambitious scattering-matrix model of the signal chain. Nevertheless all of the attenuations and filters are propagated (including counter-corrections for the photodiode-fits including Nyquist filters). The mixer is modelled as an ideal unsaturated double-balanced mixer with a known LO-amplitude [11]. The LO amplitude sets a dead-time attenuation which is accounted accounted.

The transimpedance for "photocurrent around the PDH sidebands" is created for each photodiode and shown in fig. 5.25 on page 159. The folding operation is also applied to the noise-floor to provide the phase-noise sensitivity limits shown in fig. 5.26 on page 160.

To generate these limits, some knowledge and assumptions must to be made about the operating of the interferometers. The Watts-per-radian sensitivity of the Pound Drever Hall can be computed in the small-drive-limit ($\theta_{\mathrm{PDH}} \ll 1\mathrm{rad}$) as

$$C_{[\frac{\mathrm{W}}{\mathrm{rad}}]\mathrm{PDH}} = \frac{P_{\mathrm{PDH:PD}}}{P_{\mathrm{src}}} \theta_{\mathrm{PDH}} \sqrt{T_{\mathrm{prm}} \cdot P_{\mathrm{src}} \cdot P_{\mathrm{cavity}}} \tag{5.16}$$

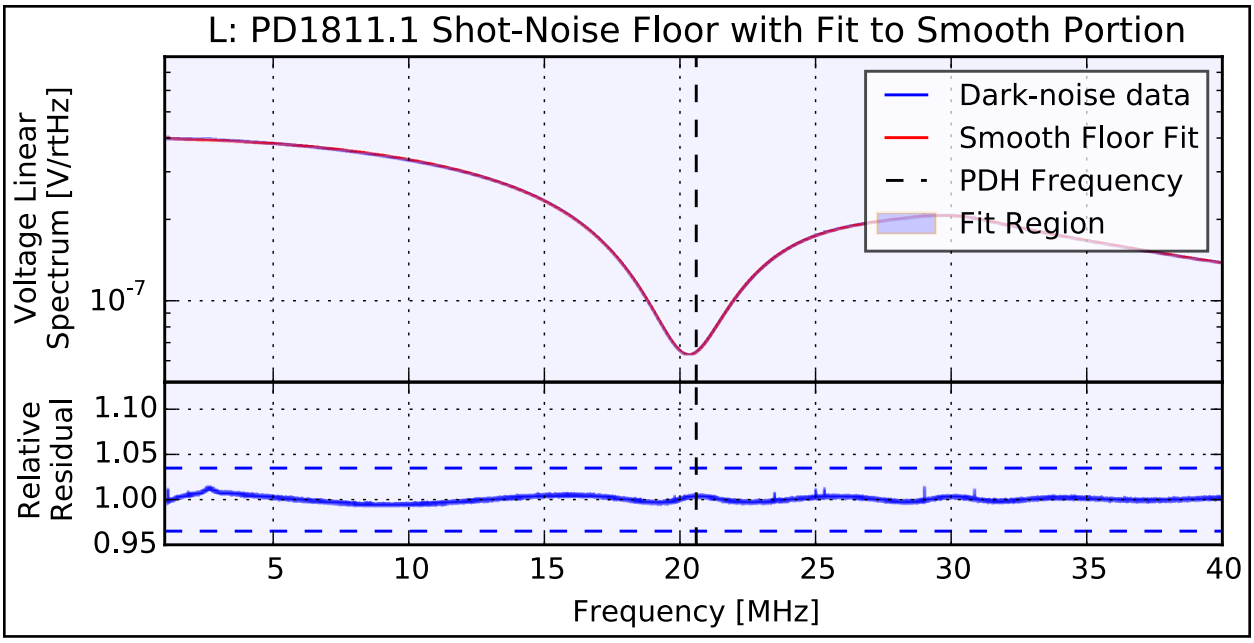

Figure 5.18: Data with fit for the **L** PDH photodiode amplifier noise. The resonant tank-circuit installed provides not only the gain-boost shown in earlier fits, but also a reduction in the amplifier noise-gain centered also at the resonance.

The first term of which represents the attenuation into the PDH diode, the second is the PDH EOM drive amplitude in radians and the terms in the square-root are from the optical gain factors. This formula was derived through simulation of the PDH response. Although its derivation is not analytic, it appears to fully account for all effects on the signal sensitivity. The sensitivity plots used rounded numbers of the real instrument performance:

$$\begin{aligned} P_{\text{src}} &= 1\text{W}, & P_{\text{cavity}} &= 2.5\text{kW}, & P_{\text{PDH-PD}} &= 10\text{mW} \\ T_{\text{prm}} &= 0.1\%, & \theta_{\text{PDH}} &= 10\text{mrad}, \end{aligned} \tag{5.17}$$

The sensitivity model only applies to frequencies higher than the cavity pole, which is too low to see on these plots. The conversion from PM to FM is done by multiplying through F.

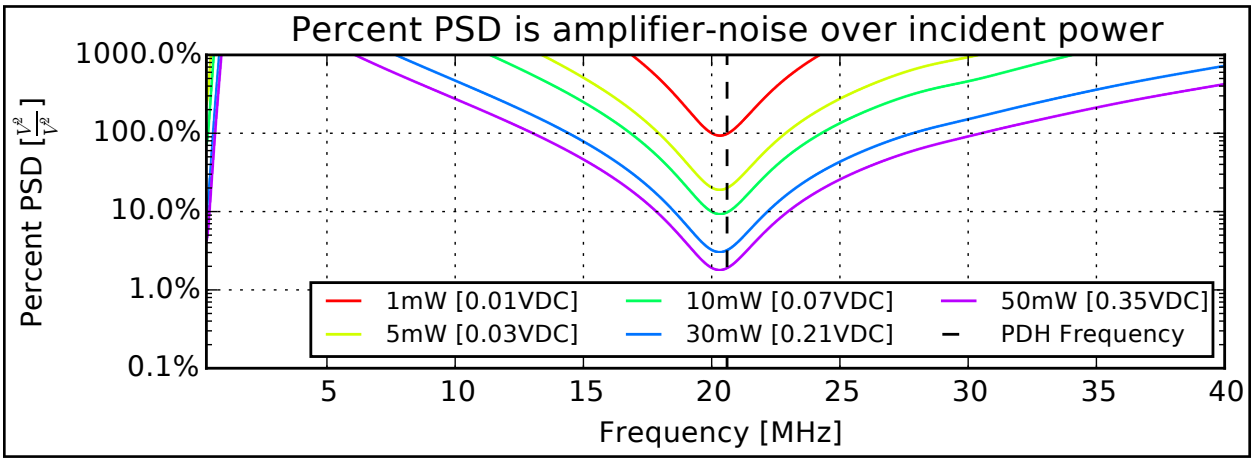

Figure 5.19: **L** amplifier-to-shot noise ratio budget in the PDH photodiode generated by the gain and noise fits. At the nominal operation of 10mW on-diode, the phase-sensitivity is quantum-limited in a 3-MHz bandwidth around the PDH-sideband line.

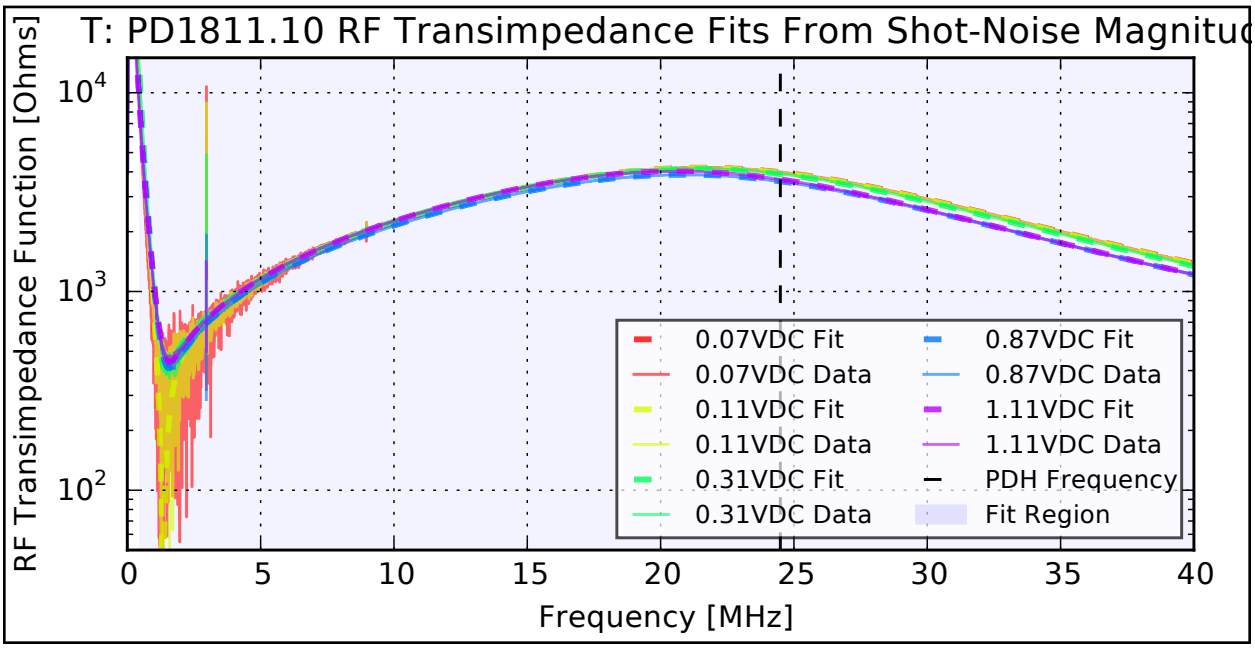

Figure 5.20: Fits of the **T** PDH photodiode transimpedance, showing broad resonant-gain around the PDH-line. These fits are used to model the final phase-noise sensitivity of the PDH system.

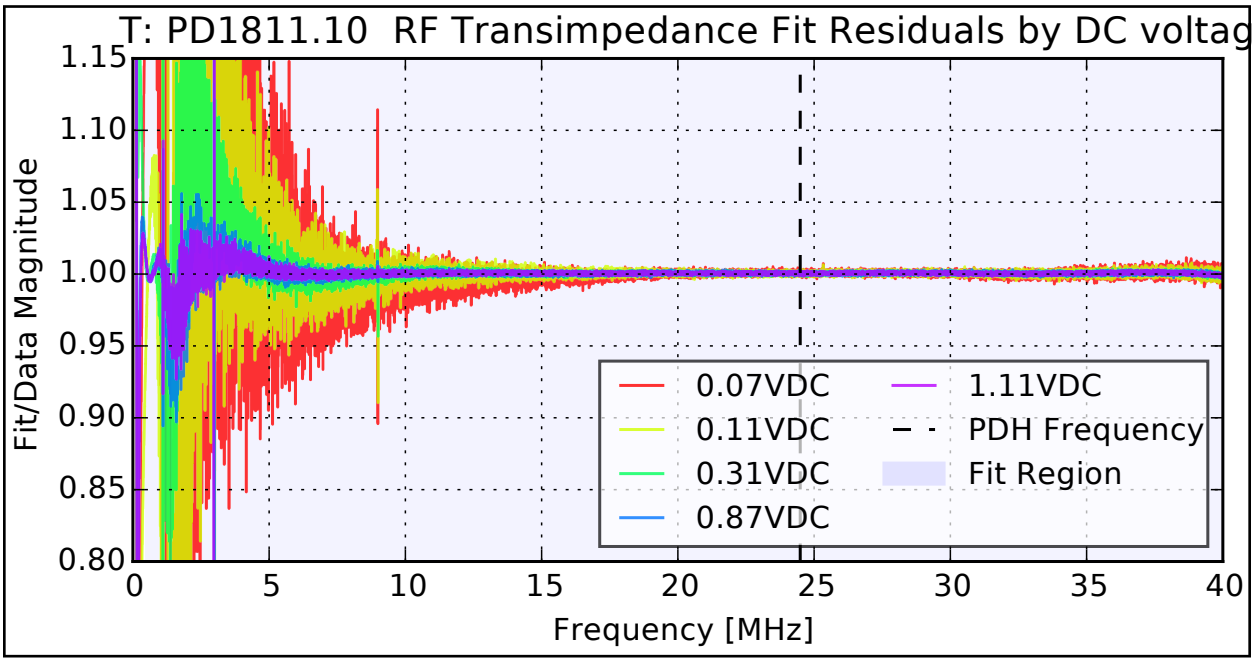

Figure 5.21: Transimpedance fit residuals for the **L** PDH photodiode showing high data quality centered at the PDH sideband frequency.

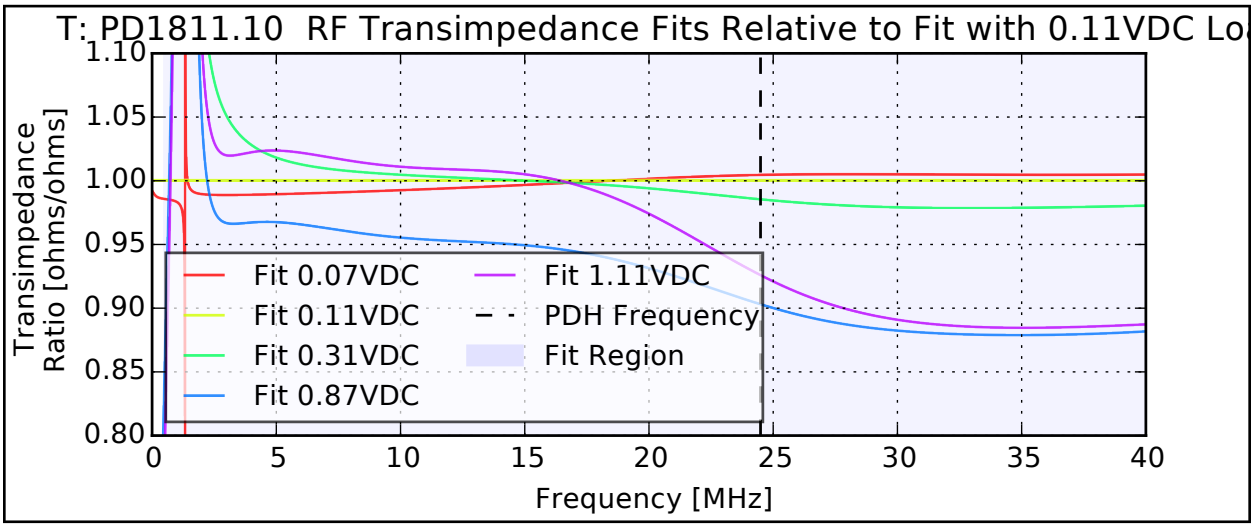

Figure 5.22: Relative gain changes of the **T** PDH-diode from the 0.11VDC load state (the measurement nearest to the nominal load). The fits below 5Mhz are all somewhat biased, but around the PDH frequency they are consistent. The large-load cases above .5VDC show a strong detuning of the photodiode-tank resonances. The nominal operation is far from these loads.

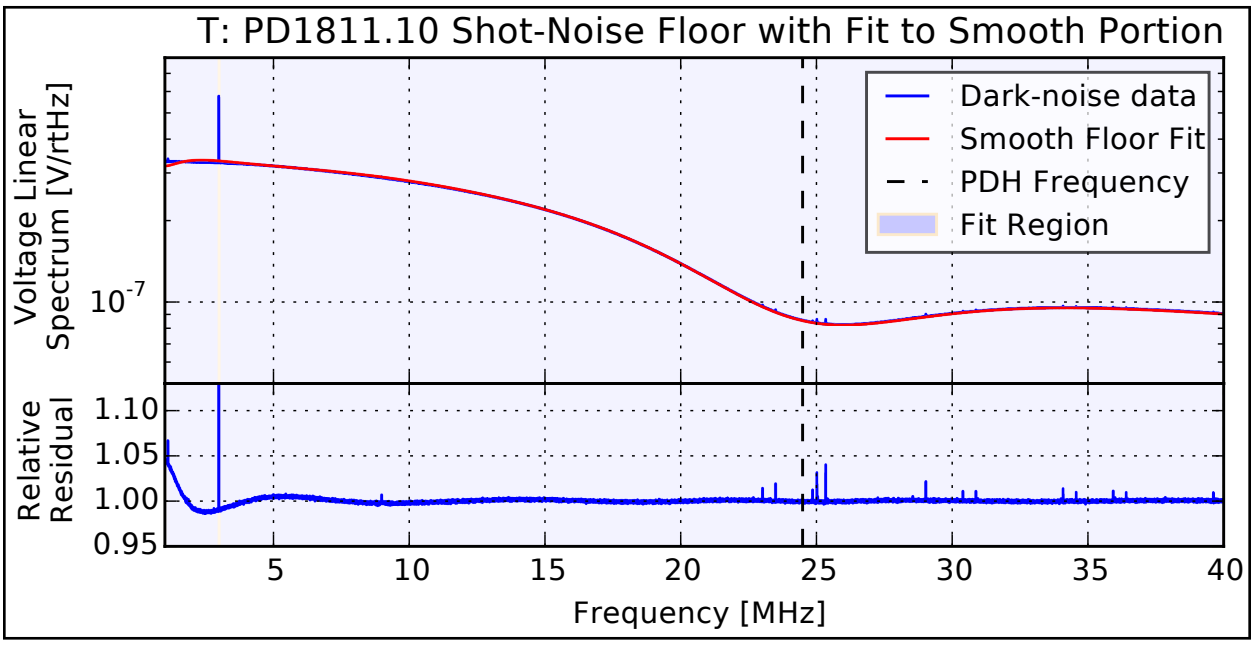

Figure 5.23: Amplifier (dark) noise data and fit for the **T** PDH-diode. The noise-minimum is slightly off-center the drive frequency. After the mixer folds the response around the drive frequency, the noise will be dominated by the larger side.

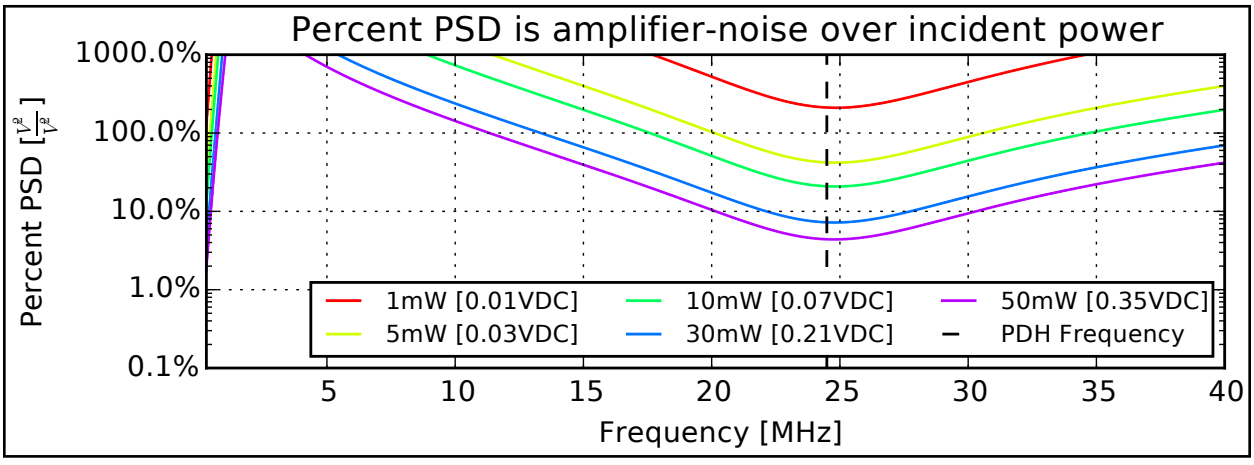

Figure 5.24: Noise ratio for the **T** PDH-diode. This diode performs slightly worse than the **L** PDH PD, but has a larger bandwidth before shotnoise is overcome by amplifier noise.

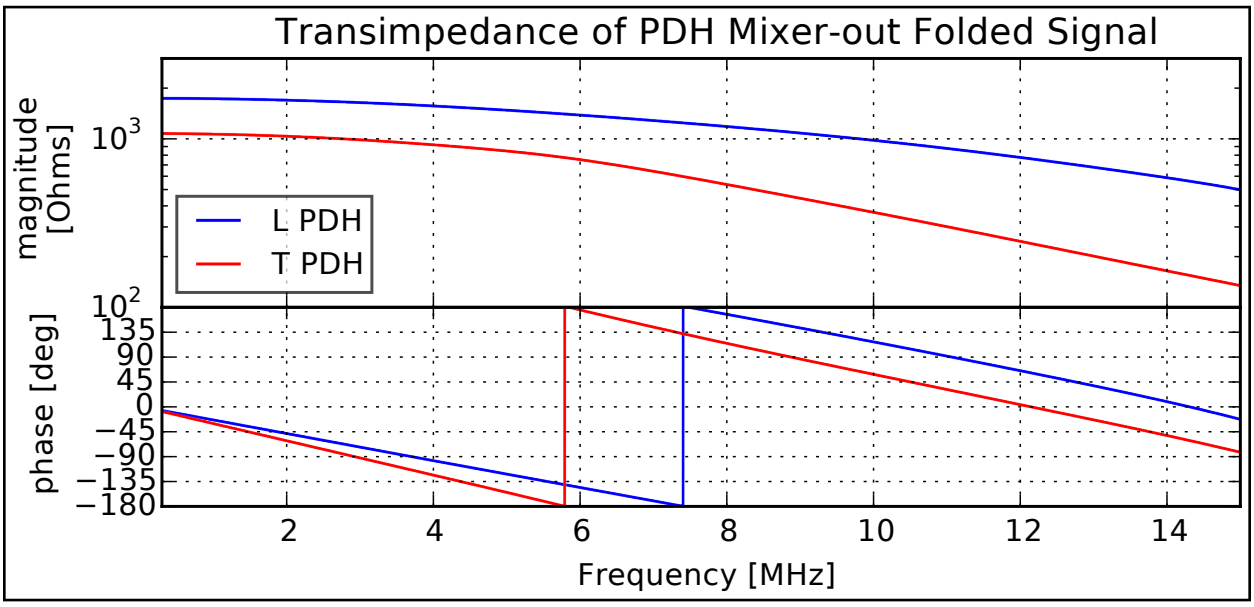

Figure 5.25: The photodiode transimpedance fits for the **L** and **T** propagated through models of the PDH-system signal chain and mixer to provide the transimpedance for measuring the photocurrent modulated around the PDH sideband.

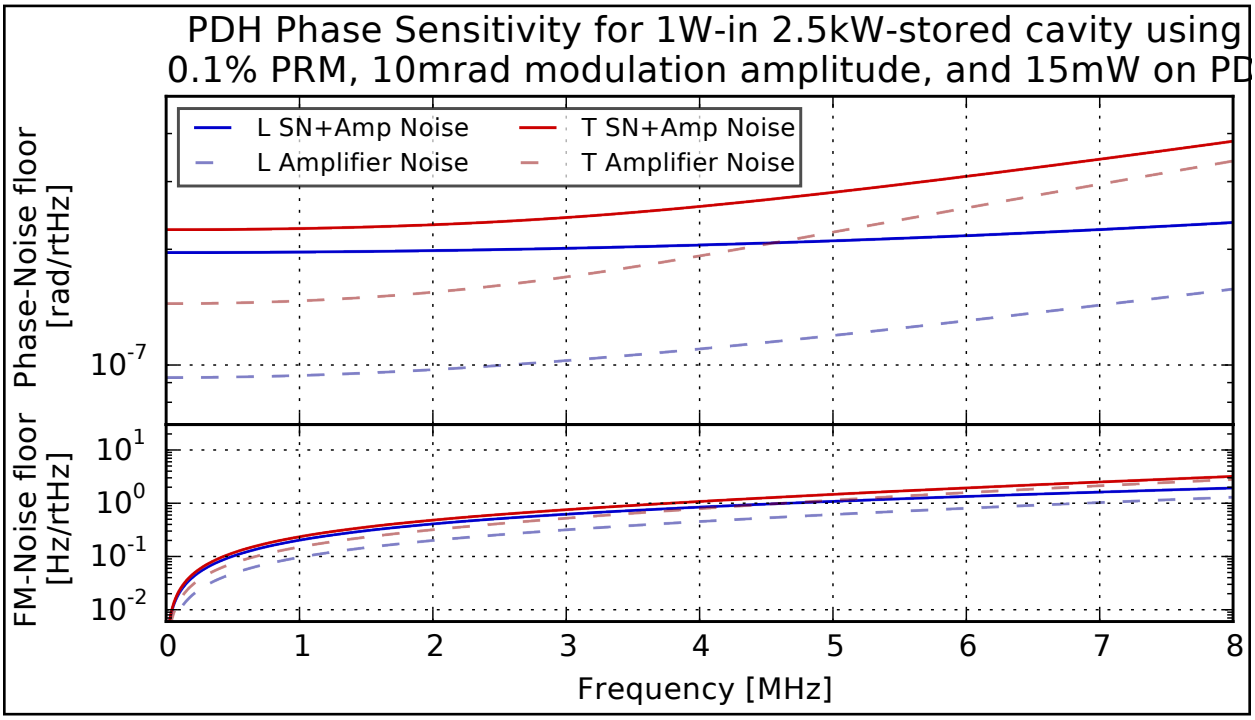

Figure 5.26: The full PDH model applied to the photodiode shot-noise and amplifier noise to budget the available sensitivity to monitor the laser phase noise. Both diodes are shot-noise limited, but only for 4MHz, with the L diode performing better. The noise floor raises at large frequencies as the diode moves outside of the optimized circuit resonance, which appears around DC from the demodulation with the mixer.

5.11 Intensity-Monitor photodiodes

Each of the interferometer tables has a beam pickoff to monitor and characterize the laser. The pickoff is transported through a highly-asymmetric Mach-Zehnder (MZ) layout with both output ports having a detector. This configuration can be used three ways

1. The MZ is locked and active, using its large arm-length asymmetry to convert phase-noise to amplitude with the additional phase-delay of a longer arm. Both photodiodes are recorded in the DAQ system, and a later basis-change can invert the MZ response back to purely AM and PM monitors.

2. The MZ is disabled with one arm blocked, and both diodes are monitored to provide a sub-shot-noise measurement of the laser AM.

3. The MZ is disabled and a single detector monitors the laser AM.

For the in-situ science operation, mode 3 was used almost entirely due to the limited number of channels. A single hour of science data was integrated for each interferometer using mode 2. The sub-shot-noise measurement across two channels allows the second monitor to be used as a lock-in reference for transfer-functions of the ASPD or other interferometer-ports with the first monitor.

The first mode of operation is the only mode actually using the full Mach-Zehnder geometry. The MZ basis-rotated PM-sensor has very poor phase-sensitivity compared to the PDH signal, but is a more simple instrument without the complicated mixer and signal-chain. The MZ PM sensor was used in ex-situ measurements to cross-calibrate the PDH sensor and ensure that it was truly sensitive to phase noise.

5.12 Fit Adjustments for Stock Intensity Monitor PDs

For the MZ on each laser table, stock 1811's were used rather than the high-power modified diode used in the rest of the experiment. The stock diodes have a specified RF-channel transimpedance of 40kOhms, and DC-coupled channel with 10kOhm transimpedance. These diode are not designed for high incident power, saturating supply in the DC channel at only 1mA incident photocurrent.

These diodes also required nearly maximum power to operate at the shot-noise limit. They were ultimately useful for setting limits on correlated AM noise in the lasers, in spite of "non-fundamental" noise sources.

The additional amplifier noise incurs systematics on their shot-noise calibration. Especially below the AC-high-pass frequencies, the fits cannot match the data from an imperfect dark-noise subtraction.

These unmodified 1811 diodes display no photocurrent-loading effects. Fits were done across multiple loads, but the data was average and displays also a "avg" (average) fit to the datasets. This average-data fit is used for the calibration of the transimpedance.

Finally, the cabling to the photodiodes applied a small standing wave resonance to the transfer functions into the DAQ system, which hindered budgetting the degrees of freedom needed for the fits. Their internal transfer-functions are actually less complex than high-power modified diodes, however the unmodified diodes have a stock output-impedance of their RF channel at 30-ohms. This mismatch to the typical 50-ohms was attached to $\sim$ 80ns Heliax cables and transported to the DAQ system. The combination of cables and termination puts a small ($\sim$ 1%) but highly significant voltage-standing-wave-ratio (VSWR) error onto the ADC-referred transfer function. This ripple is seen in the fits, and its regularity requires many degrees-of-freedom to suppress. The number D.O.F. for the fits is still insufficient for perfect modelling the ripple, which indicates that even the high number of parameters are not overfitting to data outside of the fit band.

5.13 Fit Data for Intensity Monitor Photodiodes

Like the many vertex ASPDs, these stock diode are largely identical, so only plots from a single representative are shown. Their internal-accounting label $D0$ indicates this is the first of an unmodified set.

The fits, residuals and relative comparison are shown in fig. 5.27 on the following page, fig. 5.28 on page 165, fig. 5.29 on page 165. As mentioned, the data systematics prevent the model from fitting well below 100kHz. The residuals show the effect of the VSWR ripple in the transfer functions. Finally the relative comparison shows $\sim 1\%$ calibration inconsistency. Since these diodes are not changing from photocurrent load, this inconsistency is real measurement systematic and likely due to a poor mounting scheme used for the thermal shot-noise source.

As mentioned earlier, these diode have an output transimpedance stated to be 40kOhms, but the data of fig. 5.27 on the next page do not reflect this value. The 40kOhm spec is strange for an 50Ohm load assuming the diode is also 50 Ohm. The ADC indeed uses standard 50 Ohm termination, but the diode uses 30 despite its specifications. Adjusting for this factor of $50/30$ restores the specification.

The dark noise was fit as well in fig. 5.29 on page 165 to form a noise budget for these diode in fig. 5.31 on page 166. The noise budget reiterates that these diodes have marginal noise performance even where their amplifiers nearly saturate.

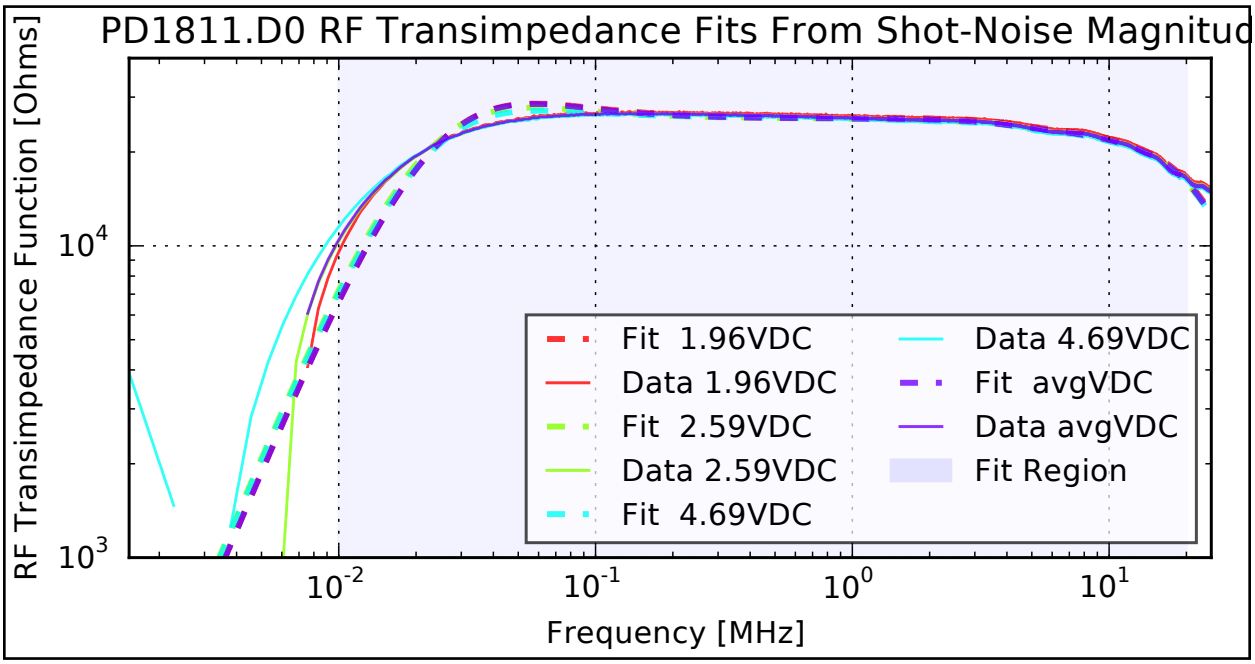

Figure 5.27: The shot-noise fits for one table intensity-monitor PD across load. These diode circuits do not display loading effects, but have ripple from the cabling to the ADCs performing the measurements.

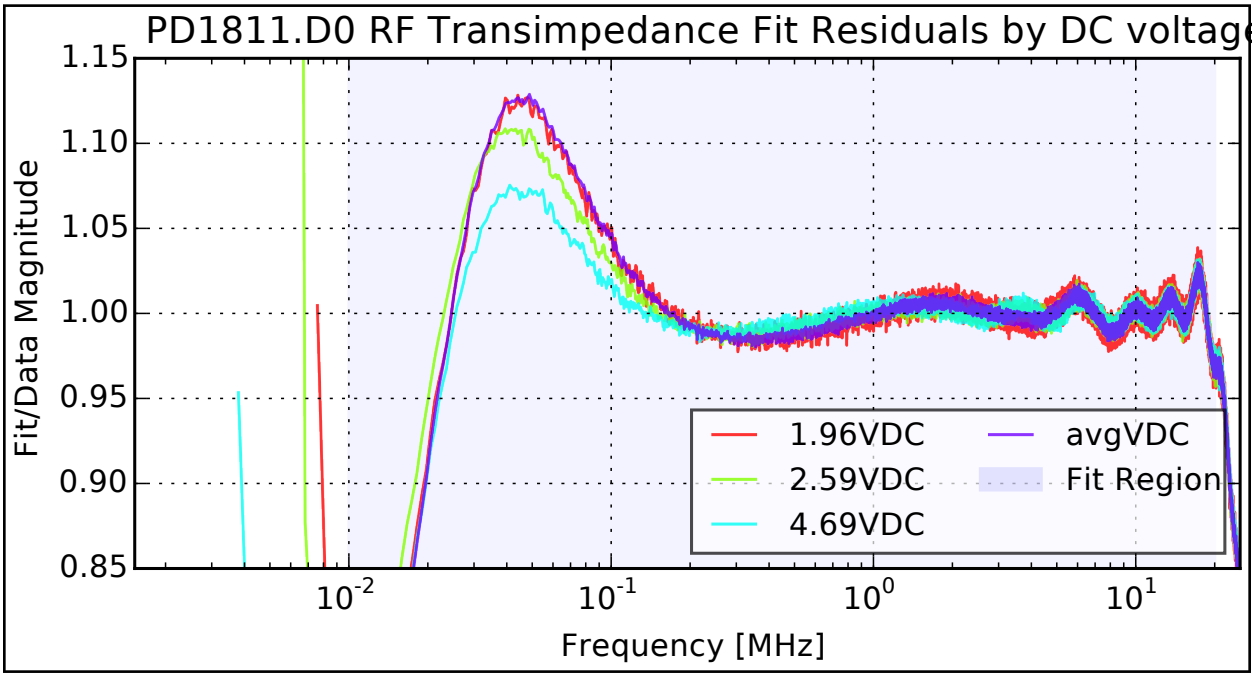

Figure 5.28: Residuals for the intensity monitor diode fit. The small VSWR ripple is highly significant here. Some of it is absorbed into the fit, but the many peaks defy fitting without an unreasonable number of parameters.

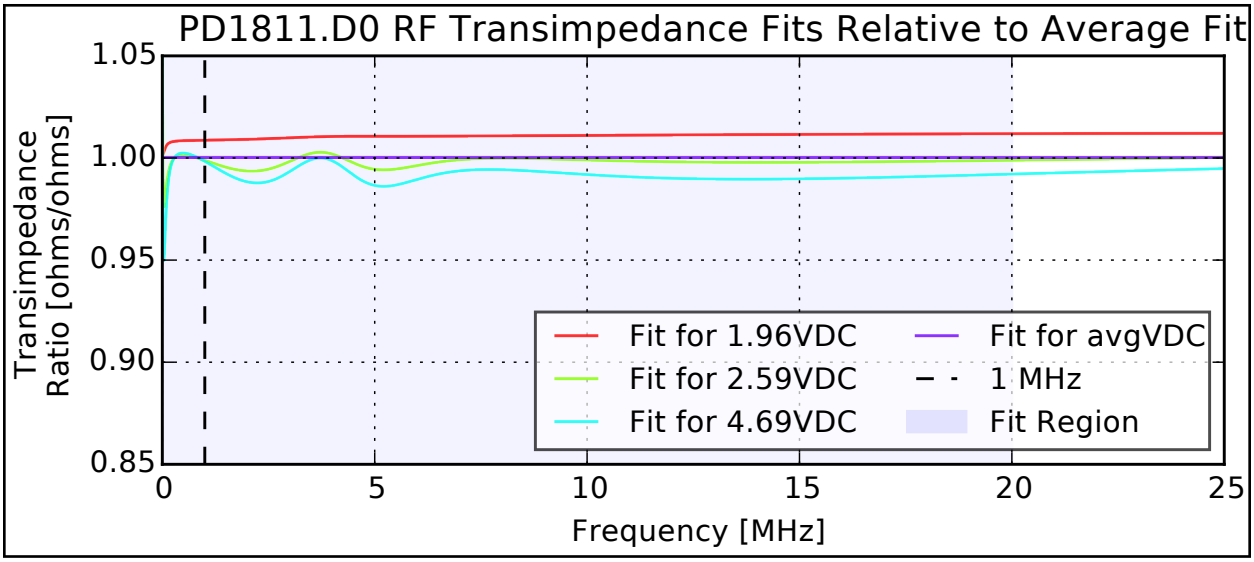

Figure 5.29: Relative fits responses for the intensity monitors. The ripple indicates imperfect fitting near the edges of the data regions. The flat overall gain mismatch can only be attributed to systematic errors in the DC photocurrent values used to normalize the fits.

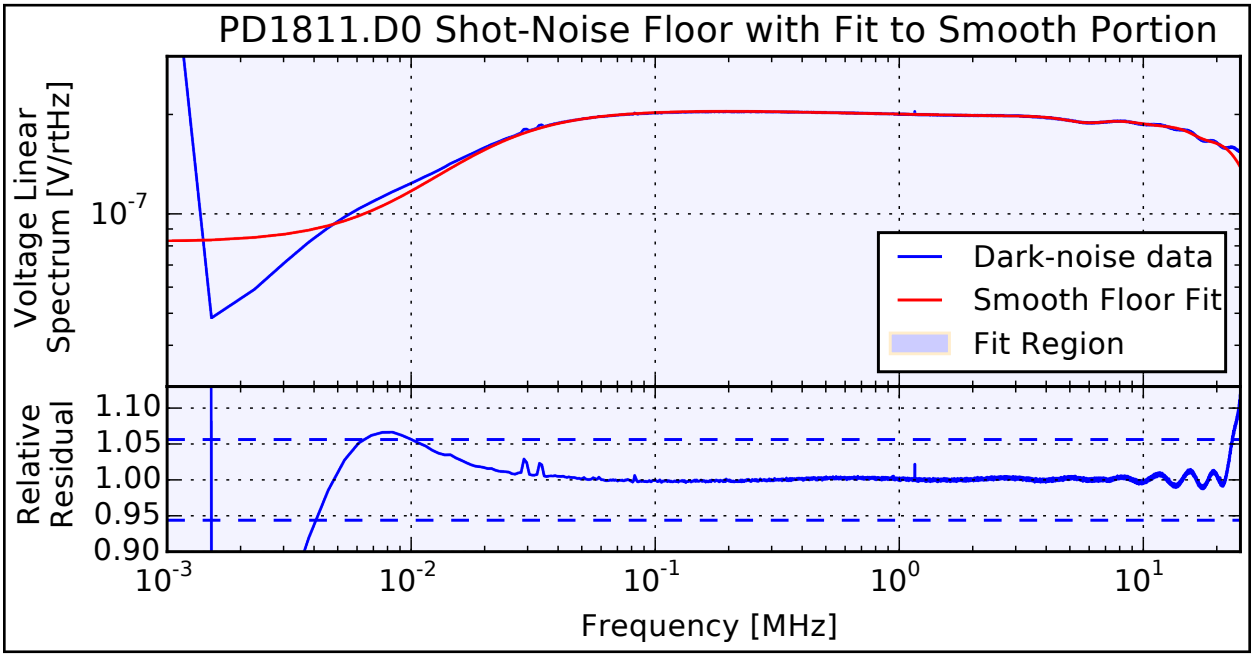

Figure 5.30: Amplifier noise of the stock intensity-monitor photodiodes.

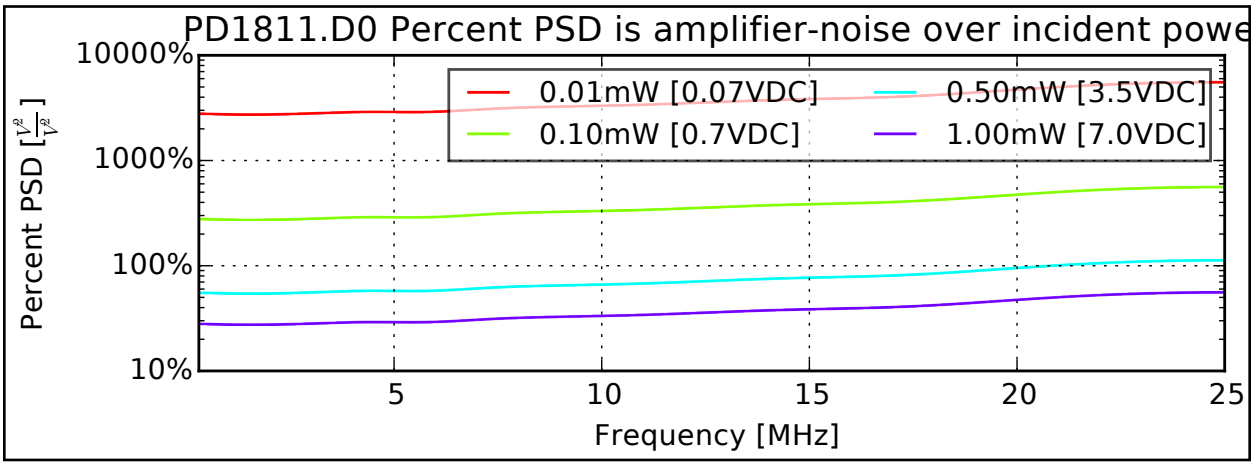

Figure 5.31: Noise budget of the stock intensity-monitor photodiodes. 1mW represent near saturation of the DC channel output or maximum allowable incident current. Only near saturation is the noise performance near the shot-noise limit.

5.14 Optimizing for Mach-Zehnder PM/FM sensitivity

The use of these diode in a Mach-Zehnder configuration requires them to be a differential-phase-calibrated system as described in section 5.5 on page 125. An LED sweep drive was placed along an arm of the Mach-Zehnder to split into both photodiode. The common cross reference provides the full phase information, as well as a differential correction to the transimpedance magnitudes in both diodes.

These corrections are applied in order for the second intensity-monitor to be calibrated exactly to the reference of the first. For the Mach-Zehnder basis-change into PM, the AM-signal present in both outputs of the MZ must be subtracted exactly to construct a good PM signal from the two channels. The differential correction to both phase and amplitude aids in this subtraction, even if the amplitude correction otherwise imposes the calibration error of MZ-channel 1 into the calibration of MZ-channel 2.

The LED sweep was performed at low and high frequency sweeps, applying much more drive power per CSD bin below 1MHz than above. The data reflect the change in SNR between these two sweep regimes.

Like the vertex PD cross calibration, the shot-noise-fit transimpedances are applied to these cross-reference measurements to show only the residual mismatch.

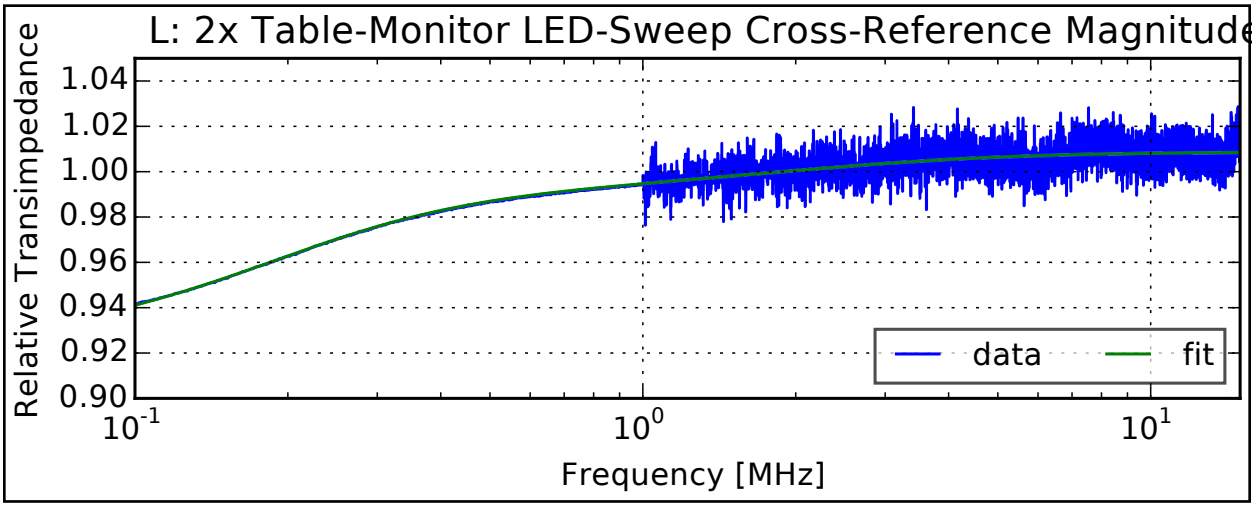

Figure 5.32: Relative residual mismatch in the calibrations of the **L** table intensity monitors. Where the fits of fig. 5.27 on page 164 were mismatched between fit and data, these residuals also show some relative mismatch. At higher frequencies, the low mismatch demonstrates that the fit calibrations can be trusted.

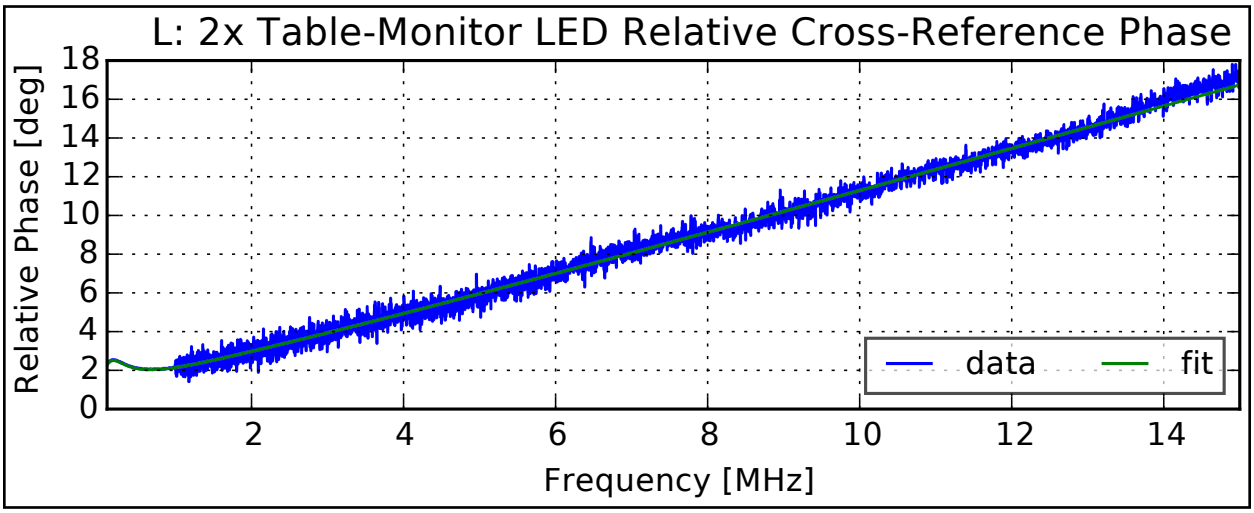

Figure 5.33: Relative residual mismatch of the phasing of photodiodes. The small error at low-F reflects the same fit error as fig. 5.32. At higher frequencies the residual is consistent with a differential delay-line length between the diodes and ADCs.

Chapter 6

RF CHARACTERIZATION AND NOISE BUDGETS

The purpose of the auxiliary channels is to budget the noise from external sources appearing *as length* in the ASPD science channels. The budgets shown in this chapter all reflect *single interferometer* measurements, showing that all of the excess noise over shotnoise is coming from known physical sources. The stronger goal of the auxiliary channels, shown in the next chapter, are *cross interferometer* budgets of background systematic correlations, where auxiliary channels account for ASPD correlated noise between the machines.

6.1 Auxiliary Channel Referencing for Noise Budgets

The AM-to-AM and AM-to-PM functions from the laser tables to the interferometer outputs are the H_{even} and H_{odd} transfer functions of eq. (D.35) on page 264 in section section D.1 on page 261. The caveat is that actually *many modes* are expressed in these transfer functions. All of the modes have different coupling-constants, but the resonant mode (approximately a Hermite-Gauss 00 TEM mode) is the only mode with a coupling of order one. All of the other mode-carriers are filtered by the cavity. As described in appendix D, the transfer functions represent signals on the sidebands, but the final couplings of of AM/PM into photocurrent also depends on the carrier amplitude. Each of the higher-order modes (HOM) of the cavity has its carrier strongly suppressed, although the final basis-change into the aperture of the photodiode can restore some HOM-carriers from parasitic coupling of the beam-referred fundamental mode into the PD-aperture-referred HOM mode. This mechanism can bypass the HOM-carrier suppression of the cavity, but moderately well-aligned photodiodes prevent the parasitic couplings becoming order-1.

Labelling all of the HOM AM transfer functions by their mode $H_{\text{ij:even}}$. The formulas of section D.4 on page 267, can be calculated using each-mode's Gouy-phase and combined

with coupling constants for each mode. The fundamental mode coupling, $H_{00:\mathrm{even}}$, should use instead the formulas of section D.3 on page 265 which contain the Schnupp asymmetry but no Gouy-phase shift term.

$$H_{\mathrm{AM}}(F) = H_{00:\mathrm{even}}(F) + B_{10}H_{10:\mathrm{even}}(F) + B_{01}H_{01:\mathrm{even}}(F) \\ + B_{20}H_{20:\mathrm{even}}(F) + B_{02}H_{02:\mathrm{even}}(F) + B_{11}H_{11:\mathrm{even}}(F)\ldots \tag{6.1}$$

This expression is identical to the PM propagation except using the odd optical functions. The transfer functions represent the transport of *relative intensity AM* (RIN) or *phase* into the RIN at the ASPD. These are unitless quantities where RIN represents optical-power fluctuation over optical DC power, the ratio manages to carry data purely about the sideband field-amplitudes relative to the carrier. In this picture, the B coupling constants should represent the ratio of the modal field power in the basis of the photodiode aperture.

$$B_{\mathrm{ij}} \approx \frac{P_{\mathrm{DC}\langle ij|ij\rangle}}{P_{\mathrm{DC}\langle 00|00\rangle}} \tag{6.2}$$

This representation must be incomplete however, as the mode-indices of the H_{even} optical functions must be in the basis of the optical system. This entire representation is really an approximation to a large linear system propagating states indexed by three frequencies (lower-SB, carrier, upper-SB) and indexed by transverse-mode through different couplings that a are function of both indices, then propagating those states through the basis-change from vacuum paraxial-modes to the independent modes of a photodiode aperture, all of these data are then convolved into the DC and RF terms created during power-detection.

The measurements cannot actually resolve individual B constants, only the full H_{AM} or H_{PM} is measurable and expresses the shape of the all-mode-power-detection transfer-functions between for channels expressed in RIN (AM) or radians (PM). The shape will express primarily the shape of H_{00} due to the order-1 coupling, but there will be perturbations

on top of this transfer from the H_{ij} HOM transfer functions because at mode-resonances, H_{ij} becomes order-1, and the cavity-filtering on the otherwise-dominant fundamental can cause $B_{ij} > H_{00}$. The mode Gouy-phase shift for the Holometer resonant cavities is (slightly lower than) $\sim \frac{\pi}{2}$, which means that these perturbations will appear at each quarter of a free-spectral-range.

6.2 Expansion of Calibration Scheme to include AM-Auxiliary channels

Chapter 4 covered the components generating the length-calibration matrix for the ASPD subsystem. The ASPD's have natural conversion to length given their placement on the interferometer, but the auxiliary channels are all in photocurrent and require a conversion into the same units as the ASPD-channels. The basis change into ASPD-referred-DARM must happen with the same time-resolution as calibrating the ASPD's because at every-moment, the auxiliary channels are detecting background noise which must be budgeted with the moment-by-moment calibration just as the science-data averaged.

The conversion for the auxiliary channels is most naturally expressed as optical transfer functions from AM-to-AM for the intensity monitors and PM-to-AM for the PDH monitors. The to-AM unit then refers to photocurrent fluctuation at the ASPDs, so the ASPD calibration from photocurrent to length is used again in changing the units of the auxiliary channels fully to ASPD-referred-DARM. For the AM/intensity monitors, the voltage

measuring photocurrent is converted to ASPD-DARM using the following factors.

$$\hat{L}_{\mathrm{Imon}} = \hat{C}_{[\frac{\mathrm{m}}{\mathrm{v}}]\mathrm{Imon:RF}}\hat{V}_{\mathrm{Imon}}(F) \tag{6.3}$$

$$\begin{aligned}\hat{C}_{[\frac{\mathrm{m}}{\mathrm{v}}]\mathrm{Imon:RF}}(t,F) = \underbrace{Z^{-1}_{\mathrm{Imon:RF}}(F)}_{\text{to photocurrent}} \cdot \overbrace{\left(\frac{Z_{\mathrm{Imon:DC}}}{\widehat{\mathrm{AVG}}[\hat{V}_{\mathrm{Imon:DC}};t]}\right)}^{\text{to Imon-RIN}} \\ \cdot \underbrace{H_{\mathrm{AM}}(F)}_{\text{to ASPD-RIN}} \cdot \overbrace{\left(\frac{\widehat{\mathrm{AVG}}[\hat{V}_{\mathrm{AS:DC}};t]}{Z_{\mathrm{AS:DC}}}\right)}^{\text{to ASPD W}} \cdot \underbrace{\frac{Z_{\mathrm{ASPD:RF}}(F)}{\hat{C}_{[\frac{\mathrm{v}}{\mathrm{m}}]\mathrm{ASPD:RF}}(t,F)}}_{\text{to DARM}}\end{aligned} \tag{6.4}$$

In this way, the auxiliary detectors are cross-referenced to the ASPDs, using some ex-situ measurement of the H_{AM} or H_{PM}. The average DC voltages in the Imon and ASPDs are read from control-system data. The implementation is mildly more complicated to cross reference to the "common" ASPD composed of two separate length-measurements, but just requires the "to ASPD W" and "to DARM" terms to be combined into the same weighted average as the composite sensor basis-transformation.

The terms, building incrementally, can construct a reference from any of the intermediate. In practice the calibration process is split, only immediately applying values available from the controls data. The reason is that some terms are difficult to measure (like H_{AM}) yet constant, while some terms are easy to measure yet time-sensitive. While merging the datasets into an average, only the transimpedance terms and time-sensitive terms were collected. The transfer-function to determine H_{AM} then collects all of the remaining terms of the calibration and the ex-situ measurement is representative of the usual optical coupling into the instrument. The use of a directly-measured cross-reference will ultimately absorb and compensate for any calibration error applied by the transimpedance measurements. This makes the calibration extremely strong under the caveat that the H_{AM} measured in whatever units must be representative of the average coupling through the laser cavity. The

measurements shown in the following sections were taken on a 1-hour subset of the in-situ data and should therefore be representative.

6.3 AM sub-shotnoise measurements

The first characterization to determine with the intensity monitors is the laser-AM spectrum in units of RIN. This measurement is pimportant to make while the laser is in-loop, being actuated to stabilize the frequency to the cavity. The cables and electrical components attached create parasitic couplings of background RF which can correlate between instruments. During 1-hour of the science-run, each interferometer ran in the 2x-Imon configuration. This allows one-channel to provide a lock-in reference to another for a sub-shotnoise measurement of the laser AM. These are shown in fig. 6.1 on the next page and fig. 6.2 on the following page. This largely matches the manufacturer specs, yet correlates further down to see some small additional resonant structure. This structure is unimportant for the experiment, and might be some residual effect from the manufacturer's internal relaxation-oscillation suppressing loop.

The flat delay-free phase of the CSD demonstrates the precision of the photodiode calibrations applied to convert the voltages into phase-comparable photocurrents in the two monitors.

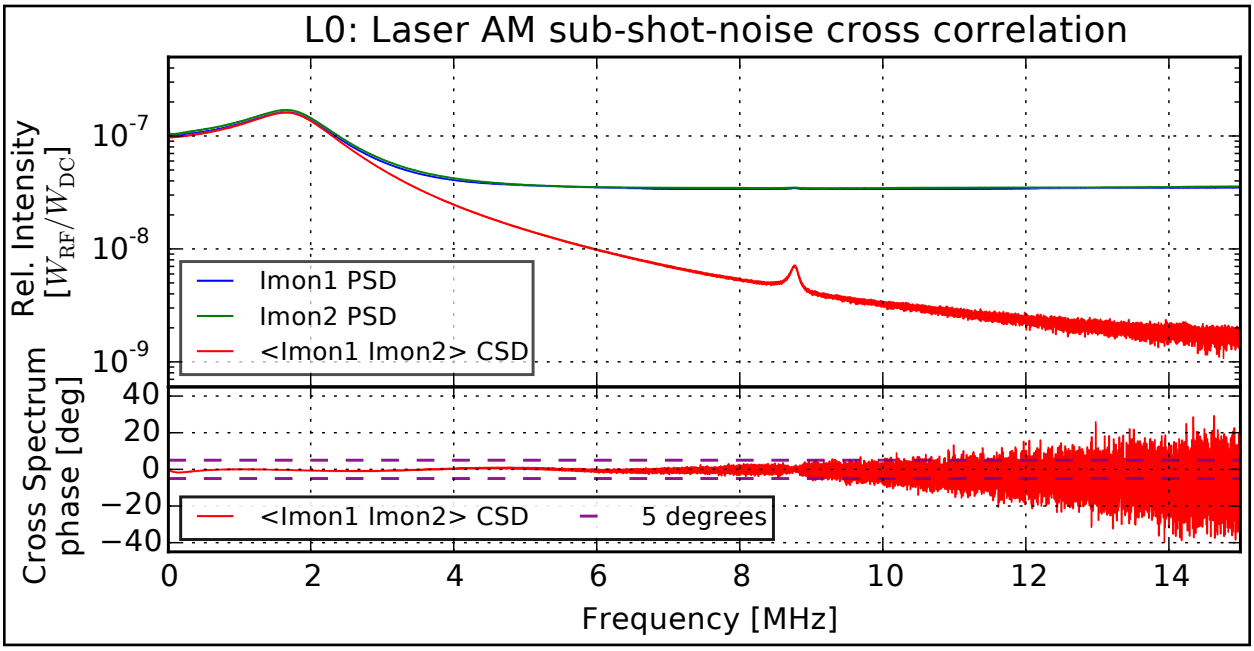

Figure 6.1: Measurement of the relative intensity noise in the **L** laser using 1 Hr of data.

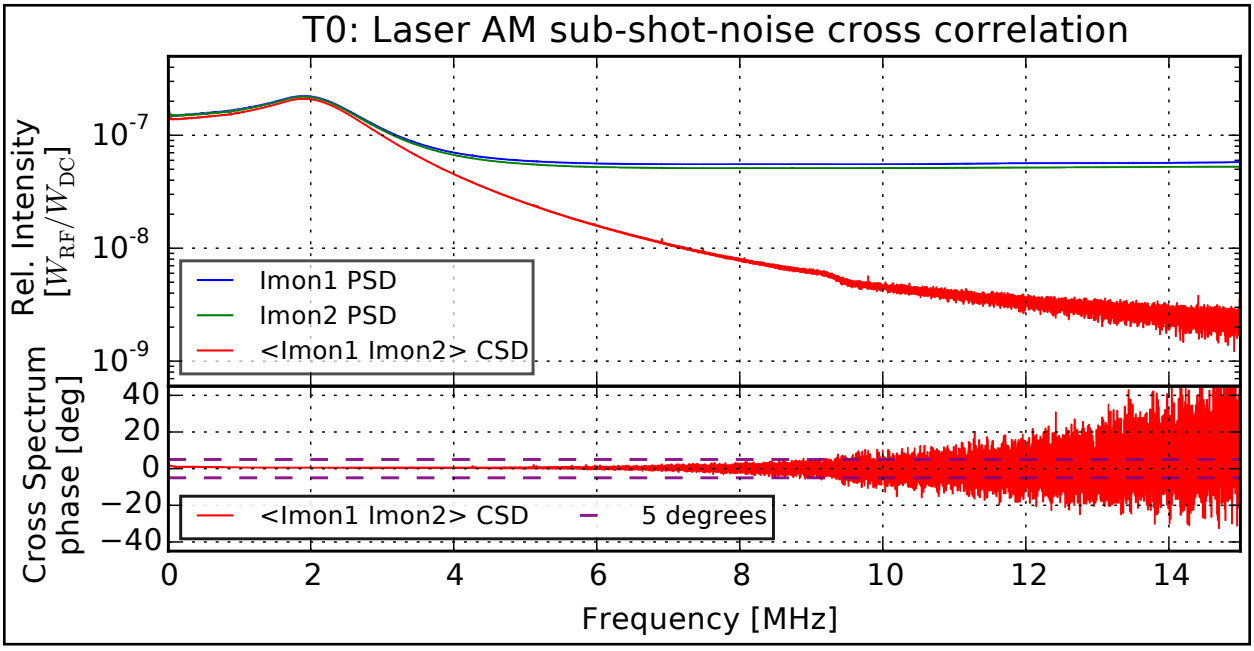

Figure 6.2: Measurement of the relative intensity noise in the **T** laser using 1 Hr of data.

6.4 AM transfer to AS port

Following the discussion of section 6.2 on page 171, the reference of the auxiliary channel into the cavity is shown in Figure 6.3 on the following page and fig. 6.4 on page 177. These cross-references are in units of $^{\text{ASPD-RIN}}/_{\text{Imon-RIN}}$, and therefore unit-less. The same measurement was generated for the fully-calibrated channels in $^{\text{ASPD-DARM}}/_{\text{Imon-DARM}}$ which is similarly unit-less and it generates the same measurement as it should.

The two figures show the physics of HOM side-channel leakage through the laser cavity. These measurements show the strong dominance of the $H_{00:\text{even}}$ term over any higher-order mode terms. The 180 degree-flips of the phase show the comb of cavity resonances rolling through the Lorentzian at each free-spectral range. Both interferometers show the perturbations of HOM $H_{\text{ij:even}}$ terms leaking into the cavity at each quarter of the FSR. The **T** in particular shows another effect, a split-degeneracy in the Gouy-phase of horizontal and vertical TEM modes. The **T** vertex camera shows a contrast-defect from astigmatism. The astigmatism must apply different radii of curvature in different planes to detune the Gouy-phase of TEM modes with higher index in each respective plane of the astigmatism (dropping the names vertical/horizontal as the astigmatism is on the diagonal).

The measurements represent the transfer-functions of taken with the estimator:

$$\widehat{\text{XFER}}\Big[\hat{L}_{\text{Imon2}} : \hat{L}_{\text{ASPD}} \Rightarrow \hat{L}_{\text{Imon1}}\Big] = \frac{\widehat{\text{CSD}}\Big[\hat{L}_{\text{Imon1}}, \hat{L}_{\text{Imon2}}\Big]}{\widehat{\text{CSD}}\Big[\hat{L}_{\text{ASPD}}, \hat{L}_{\text{Imon2}}\Big]} \tag{6.5}$$

The $\hat{L}_{\text{Imon1}}$ represent the data-channels of the calibrated-basis from volts into DARM-meters.

This estimator has a variance or equivalently signal-to-noise, which was also estimated using the techniques of Appendix C. The SNR plotted represents the measurements averaged through adjacent bins if necessary attempting to reach an SNR of 5. If a larger ΔF must be averaged than 3 kHz, the averaging stops to prevent an excessive loss of resolution for SNR. For the science band all the way through the second FSR around 8 MHz, the SNR is

large averaging just within the 3 kHz, and the bin-averages are unnecessary below 4 MHz. The reason for the low SNR is that this is a *passive* measurement, using the laser's "natural" noise instead of an excitation. The cross spectrum in the sub-shotnoise AM measurements of fig. 6.1 on page 174 and figure 6.2 shows a falling coherence when normalized by the geometric-mean of the two PSDs. This falling coherence sets the SNR of the transfer-function measurement.

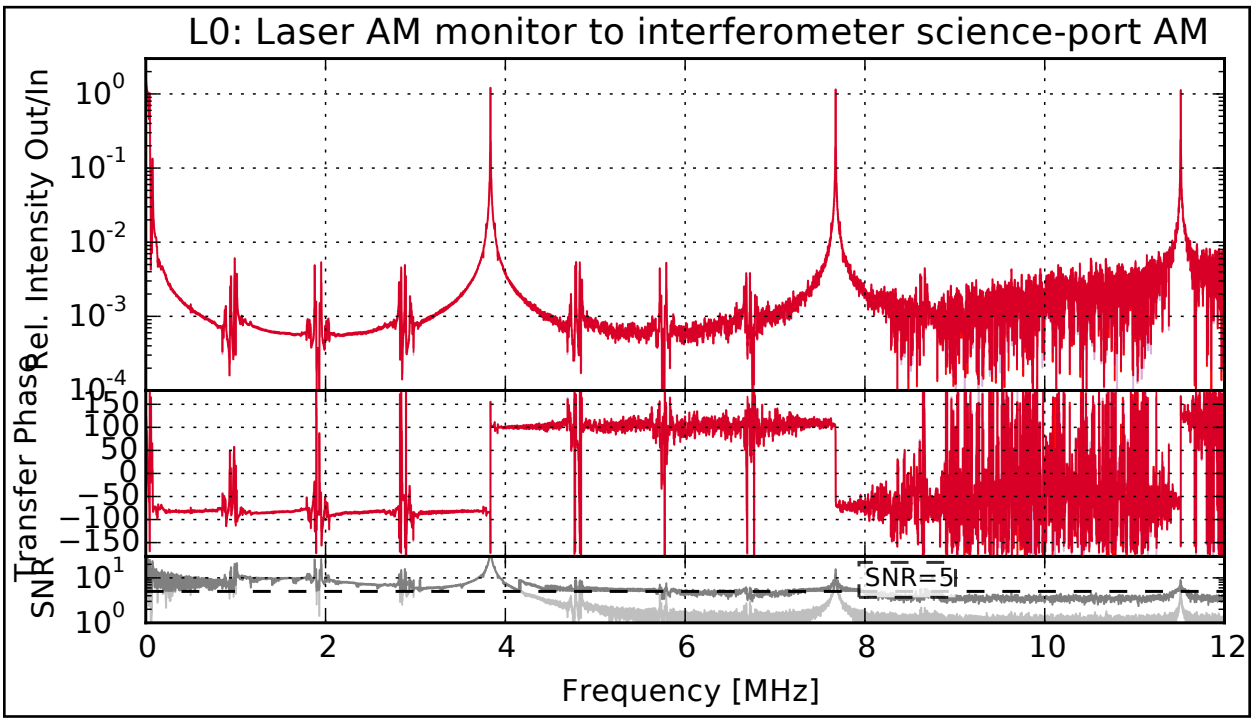

Figure 6.3: Transfer function of relative amplitude noise through the **L** interferometer cavity.

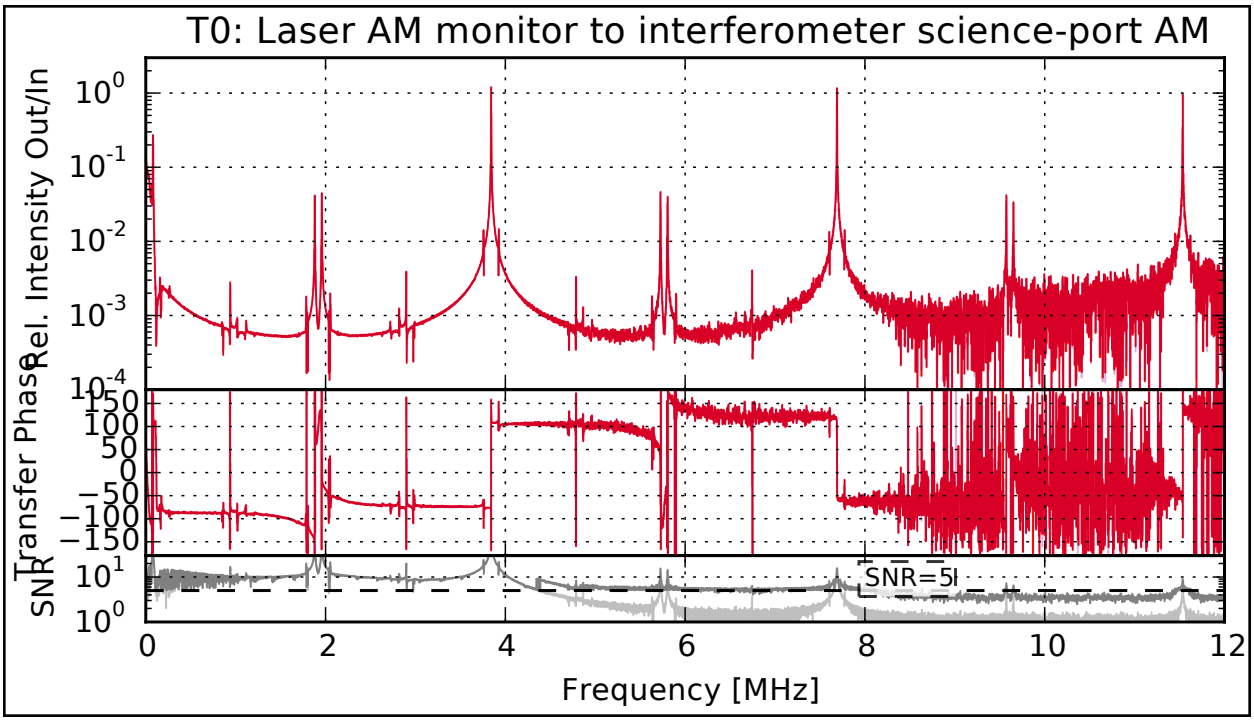

Figure 6.4: Transfer function of relative amplitude noise through the **T** interferometer cavity.

6.5 AM Budget at AS port

With the H_{AM} references determined, the excess-noise at the asymmetric-port can begin to be dissected. The cross-spectrum between the ASPD-referred auxiliary-channels and the true ASPD channels selects for noise common to both. In particular this generates a sub-shotnoise measurement of the laser-AM leaking through the cavity to appear through the interferometer calibration as an *apparent* length fluctuation. Each of these plots for the **L** and **T** represents the same data, but zooms and emphasizes where the laser AM is saturating the shotnoise-excess. The X in the label refers to the full recalibration reference from AM into ASPD-DARM represented in eq. (6.7) on page 182. Three measurements are plotted, representing aspects of the budget.

orange The actual DARM PSD noise floor for the interferometer in DARM-length units.

This should ideally show perfectly-flat white shot-noise limited measurement, but has shape from external "non-fundamental" noises, some of which could carry systematic backgrounds correlating between the two interferometers.

purple This is the cross-spectrum with the referred intensity monitor. This picks out the contribution of AM leaking through the filter-cavity onto the signal.

faded blue This is the intensity monitor PSD referenced into the DARM units. This should overlay the cross-spectrum measurement at frequencies where the Imon sees true AM-noise over shotnoise and amplifier noise. It is included in the plots to demonstrate the accuracy of the calibration. This measurement includes two calibration, X, factors rather than one, so if X carries large error, then this plot will not overlay the 1x-reference when it should. The figures (6.1) and (6.1) show that the Imon does see true AM noise and the overlay should persist until around 4 MHz,.

The additional faded overlay is useful to demonstrate that the calibration is representative as the X-reference was on 1-hour of data, whereas these plots represent the full dataset[1].

1. Due to limited channels, the Imon channels were occasionally replaced with an antenna, and the measurements only represent $\sim 60\%$ of the full dataset

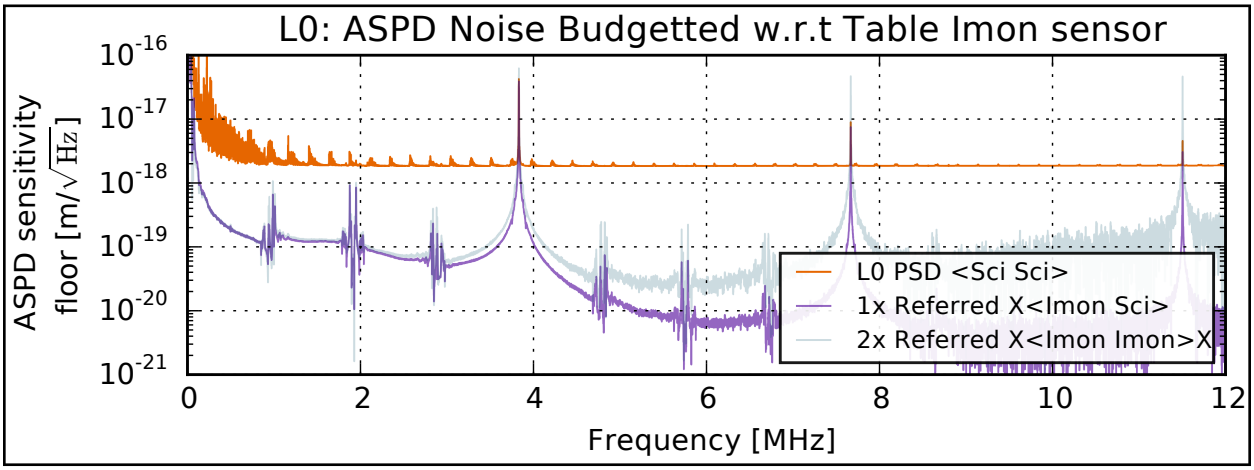

Figure 6.5: Intensity-noise budget of the **L** ASPD channel plotted linearly in frequency. The excess noise at each FSR is accounted by this budget.

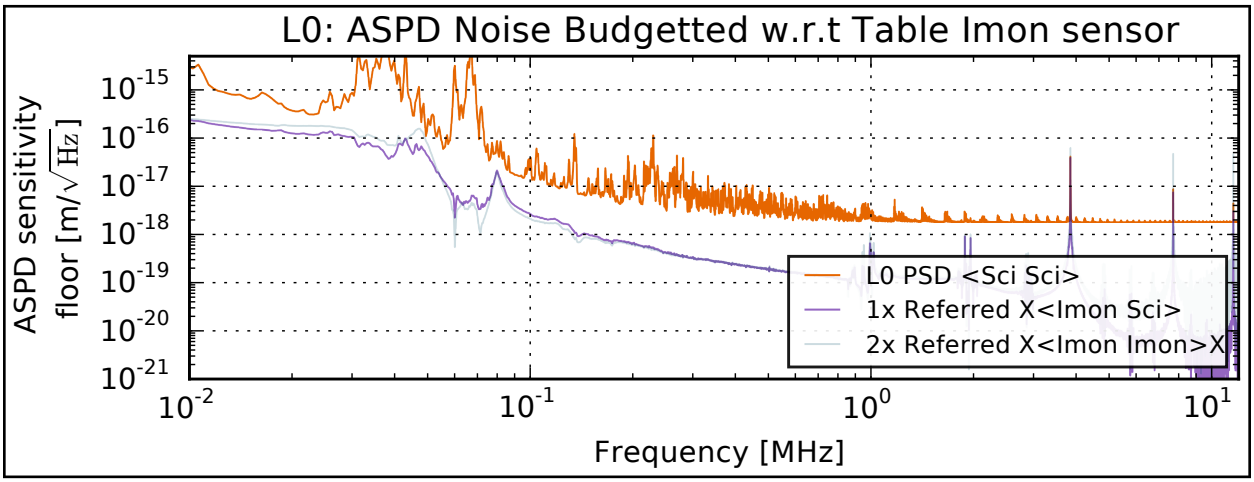

Figure 6.6: Intensity-noise budget of the **L** ASPD channel plotted logarithmically in frequency. The low frequency excesses cannot be accounted-for from laser-AM.

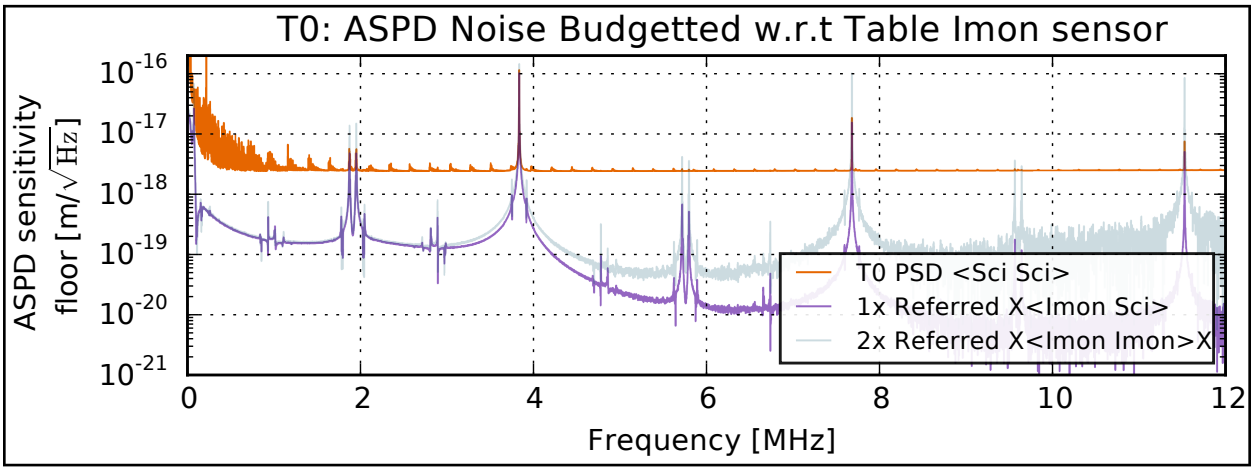

Figure 6.7: Intensity-noise budget of the **T** ASPD channel plotted linearly in frequency. The excess noise at each FSR is accounted by this budget. Additionally some peaks around TEM02 and TEM20 HOM frequencies are saturated in this budget.

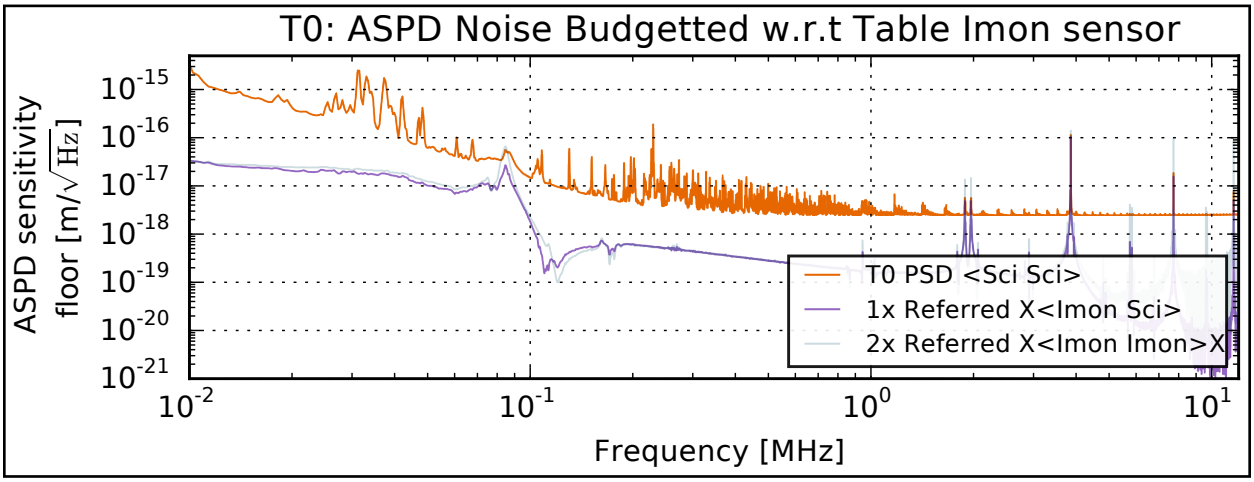

Figure 6.8: Intensity-noise budget of the **T** ASPD channel plotted logarithmically in frequency. A small section of low-F excess is accounted-for from laser-AM.

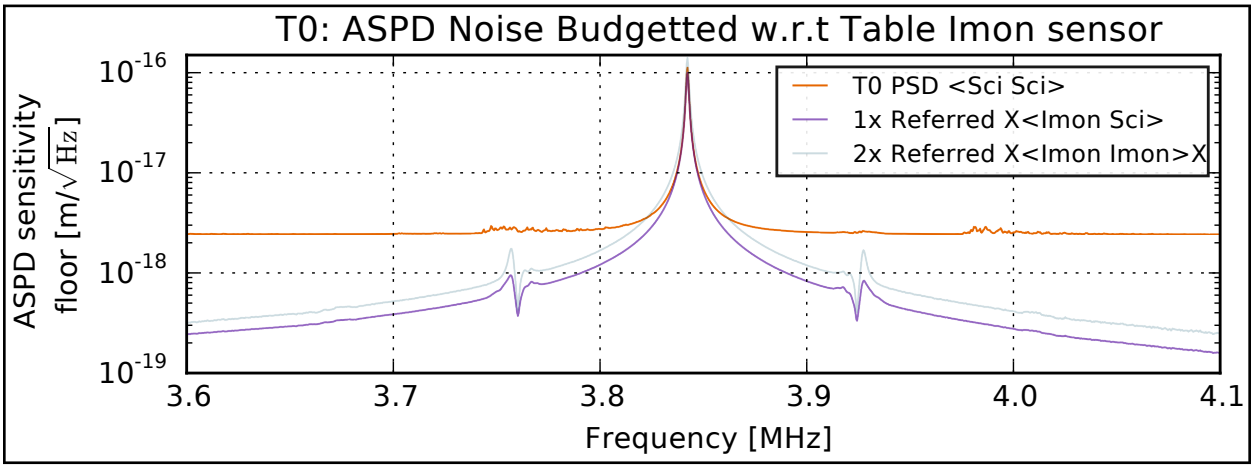

Figure 6.9: Intensity-noise budget of the **T** ASPD channel plotted linearly in frequency with a zoom around the first free-spectral-range. The FSR excess noise is conclusively AM noise of the laser.

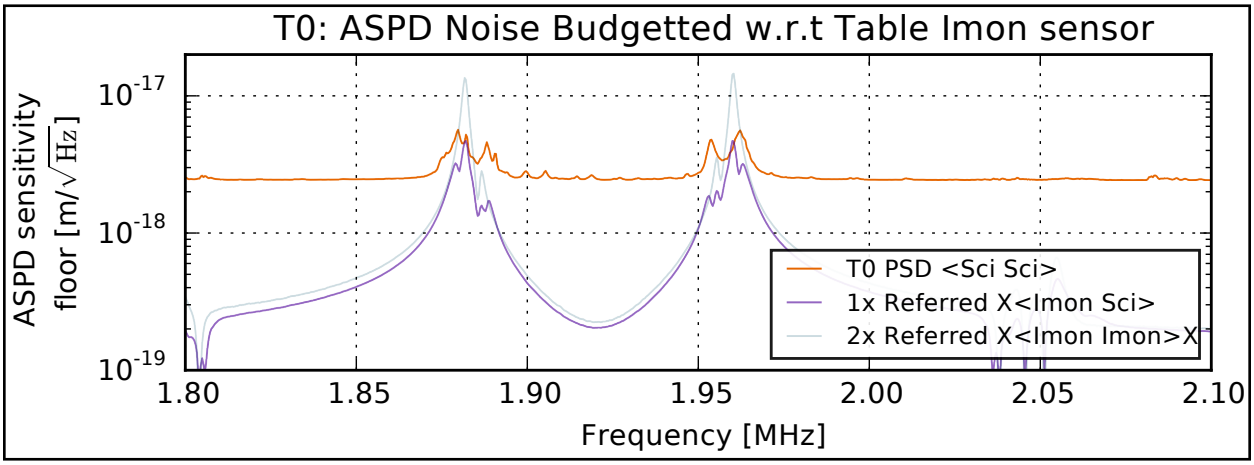

Figure 6.10: Intensity-noise budget of the **T** ASPD channel plotted linearly in frequency with a zoom around the 02/20 HOM mode resonance. The excess nearly saturated from the Imon cross-reference but not conclusively.

6.6 Expansion of Calibration Scheme to include PM-Auxiliary channels

The cross-referencing from the PDH channel into the ASPD follows similarly to the AM channel. Using the PDH signal as the reference entails some additional complications from the effect of cavity-parameters on the PM-sensitivity; however, if those are accounted-for, the only major difference is that the H_{PM} equivalent to eq. (6.1) on page 170 merely requires using the *odd* single-carrier optical transfer functions as per section D.1 on page 261. The odd functions represent conversion from PM (such as from the laser) into AM (as in the ASPD signal) or vice-versa.

The conversion to PM sensitivity requires applying the factors given in eq. (5.16) on page 154. The control-system monitors the changing cavity-power, and the other parameters are static. The $P_{\text{PDH-PD}}$ represents the power on the diode while the cavity is *unlocked* and the ratio with the source adjusts the sensitivity to the effective attenuation to the diode.

$$\hat{L}_{\mathrm{PDH}} = \hat{C}_{[\frac{\mathrm{m}}{\mathrm{v}}]\mathrm{PDH:RF}}\hat{V}_{\mathrm{PDH}}(F) \tag{6.6}$$

$$\hat{C}_{[\frac{\mathrm{m}}{\mathrm{v}}]\mathrm{PDH:RF}}(t,F) = \underbrace{Z^{-1}_{\mathrm{PDH:RF}}(F)}_{\text{to photocurrent}} \cdot \overbrace{\left(\frac{P_{\text{PDH-PD}}}{P_{\mathrm{src}}}\Theta_{\mathrm{PDH}}\sqrt{T_{\mathrm{prm}}\cdot P_{\mathrm{src}}\cdot\hat{P}_{\mathrm{cavity}}(t)}\right)^{-1}}^{\text{to PDH-PM [rad]}}$$
$$\cdot \underbrace{H_{\mathrm{PM}}(F)}_{\text{to ASPD-RIN}} \cdot \overbrace{\left(\frac{\widehat{\mathrm{AVG}}[\hat{V}_{\mathrm{AS:DC}};t]}{Z_{\mathrm{AS:DC}}}\right)}^{\text{to ASPD W}} \cdot \underbrace{\frac{Z_{\mathrm{ASPD:RF}}(F)}{\hat{C}_{[\frac{\mathrm{v}}{\mathrm{m}}]\mathrm{ASPD:RF}}(t,F)}}_{\text{to DARM}} \tag{6.7}$$

As with the AM-monitors, in practice not all terms are applied to generate the full calibration. Only the terms directly-monitored in the control system that are time-dependent are applied, along with the transimpedance. The PDH transimpedance indicated here is the fully folded and modelled transimpedance for each PDH photodiode as described in section 5.10.3 on

page 153. The transfer functions to the ASPD's are generated, which absorb all of the remaining terms. To generate plots in physical units like radians, the missing parameters are filled-in from standard the reference-set of eq. (5.17) on page 155.

The measurements to calibrate and budget the phase-measurement through this signal are included in following sections. First, the PM to ASPD transfer is shown, but to validate its calibration and that of the PDH-mixer model more transfer-functions are taken against the Mach-Zehnder which calibrates the phase sensitivity through the known arm-asymmetry. The lock-in reference for these transfer-functions is provided through an Electro-optical-modulator (EOM) providing a phase-excitation. Further sections will bound the AM/PM ratio to indicate that the transfer-function is not taken purely of parasitic AM sensitivity.

6.7 PM transfer to ASPD-AM as measured through PDH

These measurements were taken by driving a phase-noise swept-sine through an EOM. The drive was recorded as a lock-in and the usual transfer-function estimator.

$$\widehat{\textsc{Xfer}}\left[\hat{V}_{\mathrm{EOM}} : \hat{L}_{\mathrm{ASPD}} \Rightarrow \hat{L}_{\mathrm{PDH}}\right] = \frac{\widehat{\textsc{Csd}}\left[\hat{L}_{\mathrm{PDH}}, \hat{V}_{\mathrm{EOM}}\right]}{\widehat{\textsc{Csd}}\left[\hat{L}_{\mathrm{ASPD}}, \hat{V}_{\mathrm{EOM}}\right]} \tag{6.8}$$

Is generated. The sweep makes this measurement considerably different than usual applications of the CSD. Each of the CSD-estimators here was not averaged in the usual fashion optimizing for high length-sensitivity at the AS-ports. Instead, the CSD's of this measurement were weighted in a frequency-and-time dependent fashion. For a series of CSDs indexed by j, that are to be combined in a weighted average, the weight function used was:

$$w(j, F) = \textsc{Snr}\left[\widehat{\textsc{Xfer}}\left[\hat{V}_{\mathrm{EOM}} : \hat{L}_{\mathrm{ASPD}} \Rightarrow \hat{L}_{\mathrm{PDH}}\right]_{j,F}\right]^2 \tag{6.9}$$

Where the SNR is derived from section C.4 on page 255. This weight function has the property of optimizing the final ratio-of-CSDs (transfer-estimator) for that SNR. As the sweep moves the signal power through bins, the coherence with the drive peaks and only bins containing drive-power at a given time/index are given significant weighting. At high SNR this measurement should be fully unbiased, but the SNR weighting potentially creates some kind of selection-bias from fluctuations that happen to raise the coherence of the numerator and denominator with the drive. These biasing fluctuations could only be significant when the channels never gain significant drive power and so should not affect measurements with $\gg 1$ SNR.

This weighting scheme is used for all of the transfer-functions measured through the EOM drive. Even those between PDH and MZ channels still use the weighting from which takes SNR from the ASPD channel coherence. This is due partly to represent a consistent measurements, partly because for high SNR it should not matter, and partly because the entire CSD Matrix for the measurements to follow (PDH, ASPD, drive, and MZ) were all accumulated in the same weighted-average computation.

The data from the sweep for each interferometer is shown in fig. 6.11 on the following page and fig. 6.12 on page 186. The complexity of the H_{odd} transfer-functions indicates a lot of physical processes competing to produce the H_{PM} presented in these figures. A bite of this physics is contained with the modelled cavity-resonance line. This line is constructed from eq. (D.58) on page 267, where the DARM term is set to $L_\delta = 1\text{cm}$, $r_{\text{prm}} = \sqrt{1 - .1\%}$, $r_{\text{ifo}} = \sqrt{1 - 300\text{PPM}}$ and finally the DARM phase (physically included in L_δ but separated for convenience) is set $\sin^2(\phi_\delta) = 100\text{PPM} \approx \tan^2(\phi_\delta)$. This model represents the odd optical-transfer of the fundamental $H_{00;\text{odd}}$, which has order-1 coupling of table-radians to ASPD-AM.

The resonance model shows that the two interferometers appear to have different arm-asymmetries, but at the same time indicates that this term is insignificant to residual phase-

noise conversion, particularly around the HOMs. The large H_{PM} gain near DC is somewhat of a mystery. It is most likely one of two things, the TEM04 HOMs could be leaking through strongly like the TEM02's, or potentially the cavity is locked slightly off-resonance and the $H_{00;\mathrm{odd}}$, term represented by eq. (D.58) on page 267, should be expressed as an HOM instead by eq. (D.63) on page 268 with the $\phi_{\mathrm{mode}} \approx 2\pi \cdot {}^{10\mathrm{Hz}}/_{3.84\mathrm{MHz}}$.

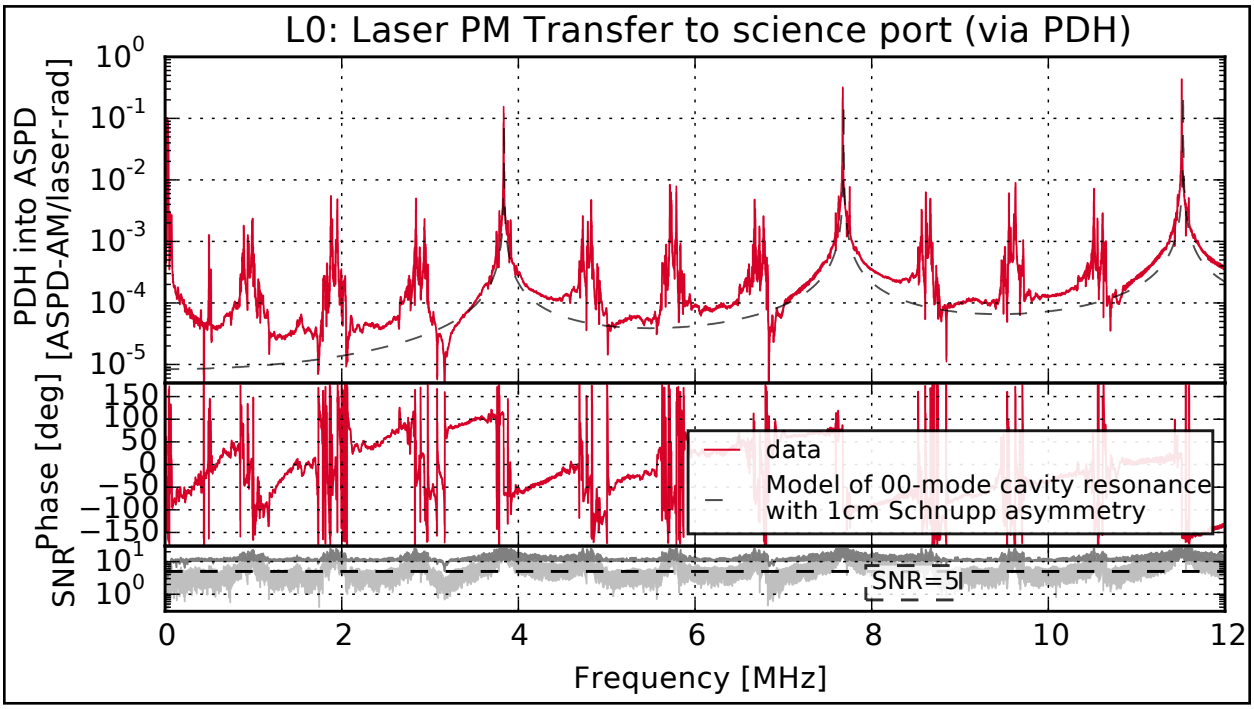

Figure 6.11: laser-referred phase noise transfer function into the ASPD-AM for the **L**. It shows the relatively weak coupling of phase into AM despite the presence of many HOM's and Schnupp asymmetry creating imbalances to the optical transfer of upper and lower sidebands. The magnitude units for AM are relative intensity and radians for PM. This leaves the transfer-function unitless and represents the ratio of odd (PM) field amplitudes of upper/lower noise sidebands at the laser converting to even sidebands through the interferometer.

The SNR of plotted for the transfer-functions is notable. It uses the same 3kHz neighborhood averaging scheme to put SNR > 5 into all points. The light-grey shows the SNR without this mechanism and the values are oscillating from bin-to-bin. The swept-sine equipment used discrete steps in frequency rather than a continuous chirp and the sweep rate was

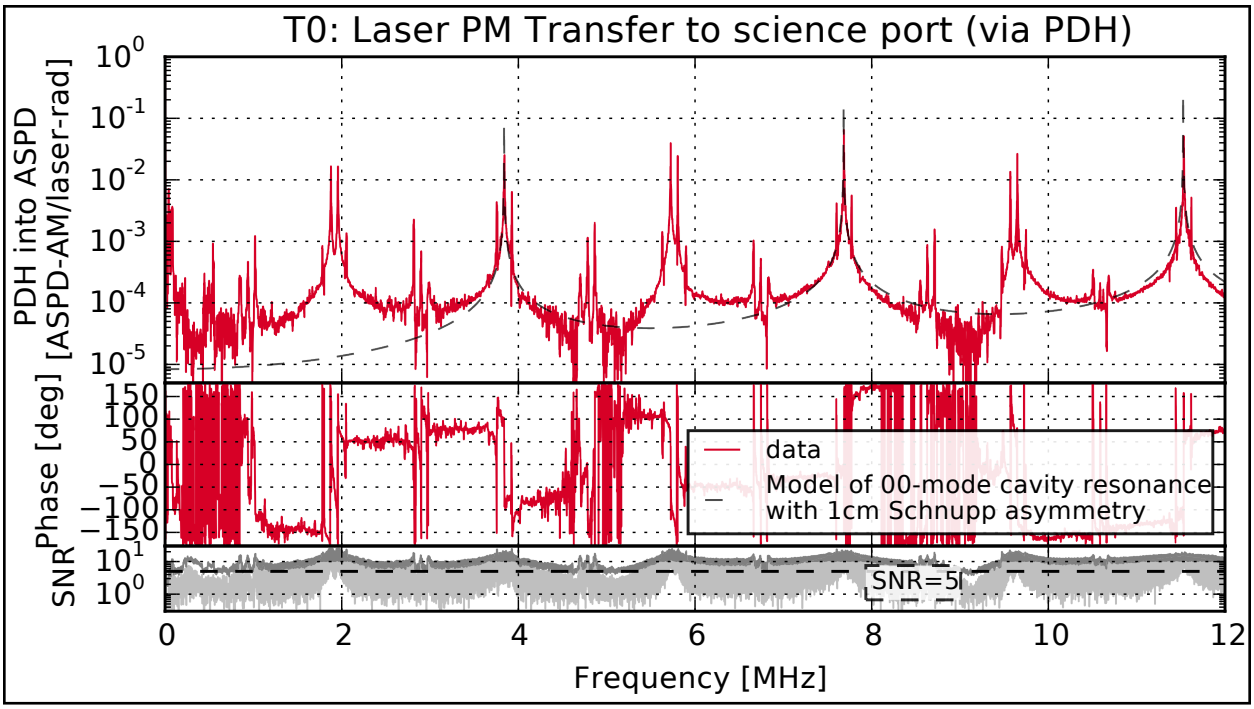

Figure 6.12: laser-referred Phase noise transfer function into the ASPD-AM for the **T**. It shows the relatively weak coupling of phase into AM despite the presence of many HOM's and Schnupp asymmetry creating imbalances to the optical transfer of upper and lower sidebands. The magnitude units for AM are relative intensity and radians for PM. This leaves the transfer-function unitless and represents the ratio of odd (PM) field amplitudes of upper/lower noise sidebands at the laser converting to even sidebands through the interferometer.

high enough that the steps skipped some bins.

Also of note is that the general magnitude of the PM transfer smaller than that of the AM. This is due to the usual cancellation that occurs in the expression of H_{odd} transfer-functions. The small magnitude also might indicate that the phase-noise should be an insignificant contribution to the ASPD noise budget, but the CARM-loop directly actuates the laser-FM with an large gain. This provides a known electrical mechanism for parasitic coupling of background RF. Furthermore, the cancellations that typically suppress PM-to-AM make PM somewhat intrinsically difficult to measure. The PDH technique circumvents this somewhat, but a quick comparison of the diode sensitivities reported in fig. 5.26 on

page 160 and fig. 5.31 on page 166 shows that the 10x reduces $H_{\rm PM}$ over $H_{\rm AM}$ is necessary to set comparable limits in background characterization.

6.8 Setup of Mach-Zehnder

The Mach-Zehnder is an "unfolded" Michelson interferometer, and operates as a phase-noise sensor through the same mechanism that the Schnupp asymmetry creates a phase-sensitivity in a Michelson. The arm-length imbalance allows sideband frequencies to advance in phase more in one-arm than the other. Upon recombining at the second beamsplitter, the differential phase-advances prevents exact cancellation and the two sidebands are rotated into the AM quadrature. The AM and PM leak in through the same even and odd terms as in eq. (D.58) on page 267 except without the initial terms representing the cavity-FSR.

The laser tables each have a MZ setup for phase-noise calibration studies and each MZ has a $L_\delta = 2$ft arm-length imbalance. The two monitor diodes are the Imon1 and Imon2 from before, though now labelled as MZ1 and MZ2[2]. The AM and PM indexes of the laser light are seen in the MZ as

$$\begin{bmatrix}\hat{P}_{\rm MZ1}(F)\\ \hat{P}_{\rm MZ2}(F)\end{bmatrix} = \sin^2(\phi_\delta)P_{\rm MZtotal}\cdot\begin{bmatrix}H_{\rm even1}(F) & H_{\rm odd1}(F)\\ H_{\rm even2}(F) & H_{\rm odd2}(F)\end{bmatrix}\begin{bmatrix}\hat{\gamma}_{\rm AM}(F)\\ \hat{\gamma}_{\rm PM}(F)\end{bmatrix} \tag{6.10}$$

$$\Downarrow \quad \text{inverting at mid-fringe and linearizing in } F$$

$$\begin{bmatrix}\hat{\gamma}_{\rm AM}(F)\\ \hat{\gamma}_{\rm PM}(F)\end{bmatrix} = \underbrace{\frac{1}{P_{\rm MZtotal}}\begin{bmatrix}\frac{1}{2} & 2\pi F\frac{L_\delta}{c}\\ \frac{1}{2} & -2\pi F\frac{L_\delta}{c}\end{bmatrix}^{-1}}_{\mathbf{C}_{\rm MZ}\ \text{basis-change}}\begin{bmatrix}\hat{P}_{\rm MZ1}(F)\\ \hat{P}_{\rm MZ2}(F)\end{bmatrix} \tag{6.11}$$

The inversion into the basis-change matrix provides the means of recovering the phase and amplitude of the laser only requiring a lock at mid-fringe and knowledge of the arm length asymmetry. Note that for $F = 1$MHz and $L = 60$cm that the odd terms are $\sim 1\%$. The gain

2. In the data-analysis, all of Imon1, 2 are actually called MZ1,2 regardless of the blockage/activation state of the MZ

calibration must be better than 1% itself to distinguish phase noise from amplitude when they are of comparable size.

6.9 PM characterization in Mach-Zehnder

Using the MZ inversion of the previous section, the PDH model can be cross checked as can the EOM drive to ensure that the PM transfer functions were not actually locked into an AM drive. The figure-of-merit for this is the AM-to-PM ratio of sidebands generated in the EOM. This sets the error level that transfer-functions could be picking up an AM-term. For an AM/PM ratio of 1%, the table-AM to ASPD-am H_{AM} would have to be 100x the PM-to-AM H_{PM} for the PDH transfer function to have an order-1 systematic. Figure 6.13 on the following page and fig. 6.14 on page 190 provide the ratios for the EOM measurements used. The **T**has a somewhat poor ratio at the 1% level, whereas the **L**is 10x better except for a resonant structure at 6MHz. As the AM transfer measured is generally 10x higher than the PM, the **T** PM transfer as measured from PDH could have as much as a 10% error from systematic AM drive leaking to the ASPD-AM.

The principle purpose of the MZ is displayed in fig. 6.15 on page 191 and fig. 6.16 on page 192. These figures compare the PDH-Mixer-signal-chain model to the direct phase-sensitivity computation of the MZ. The comparisons show that the model works to 30%. This accuracy is unsurprising given a number of unmeasured quantities. The PDH modulation-drive in particular is computed purely from the LO amplitude and the manufacturer specifications for the PDH-drive EOMs. The frequency dependence on the shape is from the limitations of fitting and modelling the multiple Mini-Circuits components that condition the photodiode signal before-and-after the mixer.

While it is encouraging that the photodiode-model works, the PDH signal works via a many-sideband measurement of the filter-cavity. It is certainly vulnerable to HOM effects affecting the AM generation around the sideband. These comparisons show narrowband

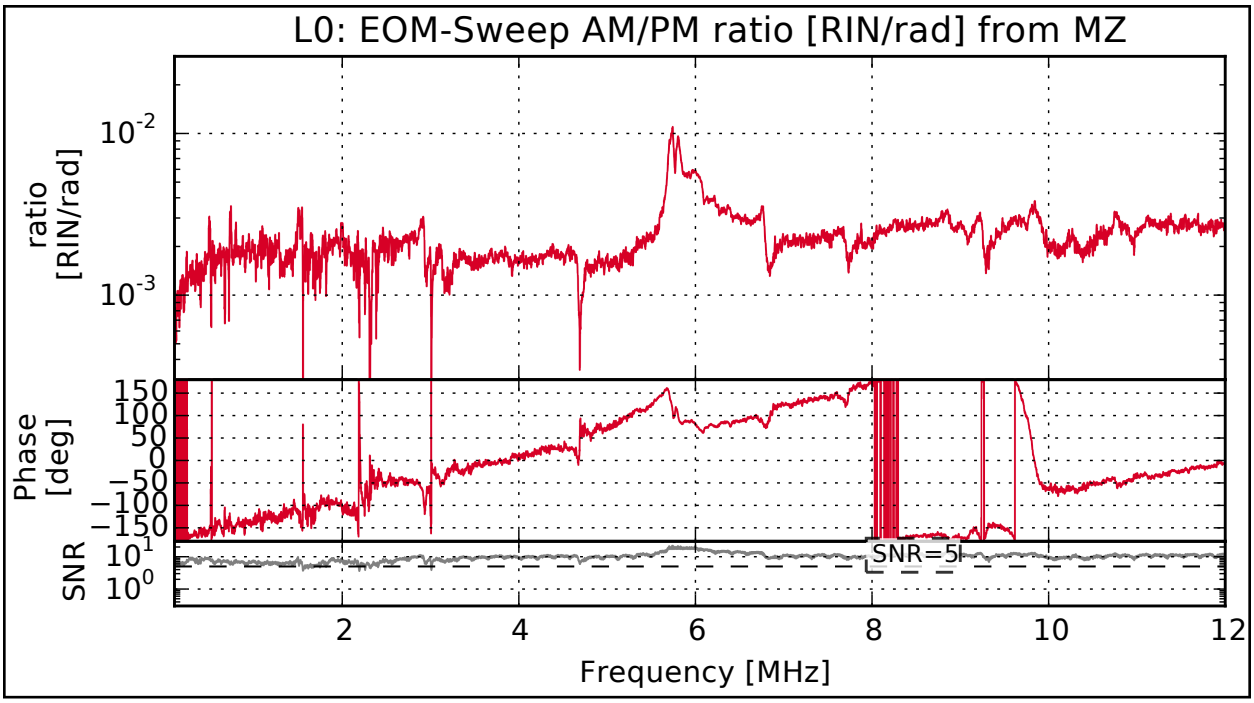

Figure 6.13: AM/PM ratio of the EOM drive used for phase-sensitivity characterization in the **L**.

shape at the 100% which could indicate HOM parasitics affecting the PDH measurement. They do not show any broadband adjustment to the sensitivity, encouraging their use a phase-discriminant.

This measurement shows an impressive SNR at all frequencies as well. This is because both channels are optimized for sensitivity, unlike the ASPD channel which has large suppression from the cavity-pole.

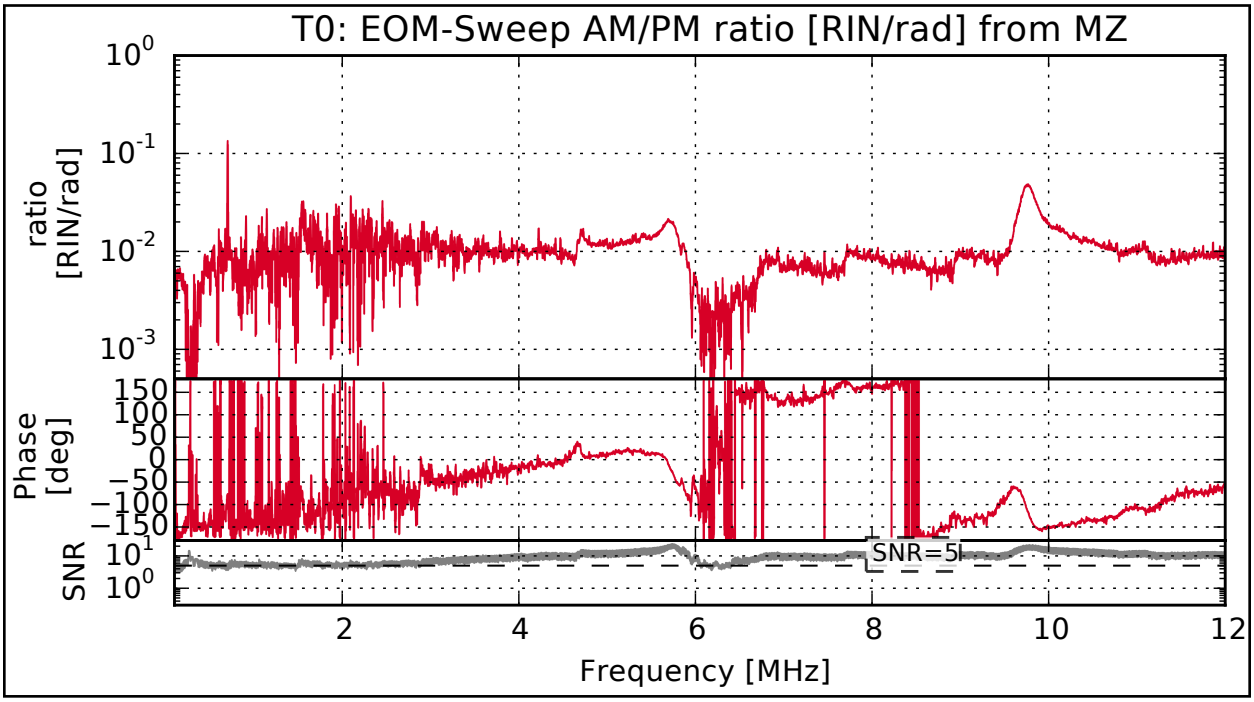

Figure 6.14: AM/PM ratio of the EOM drive used for phase-sensitivity characterization in the **T**.

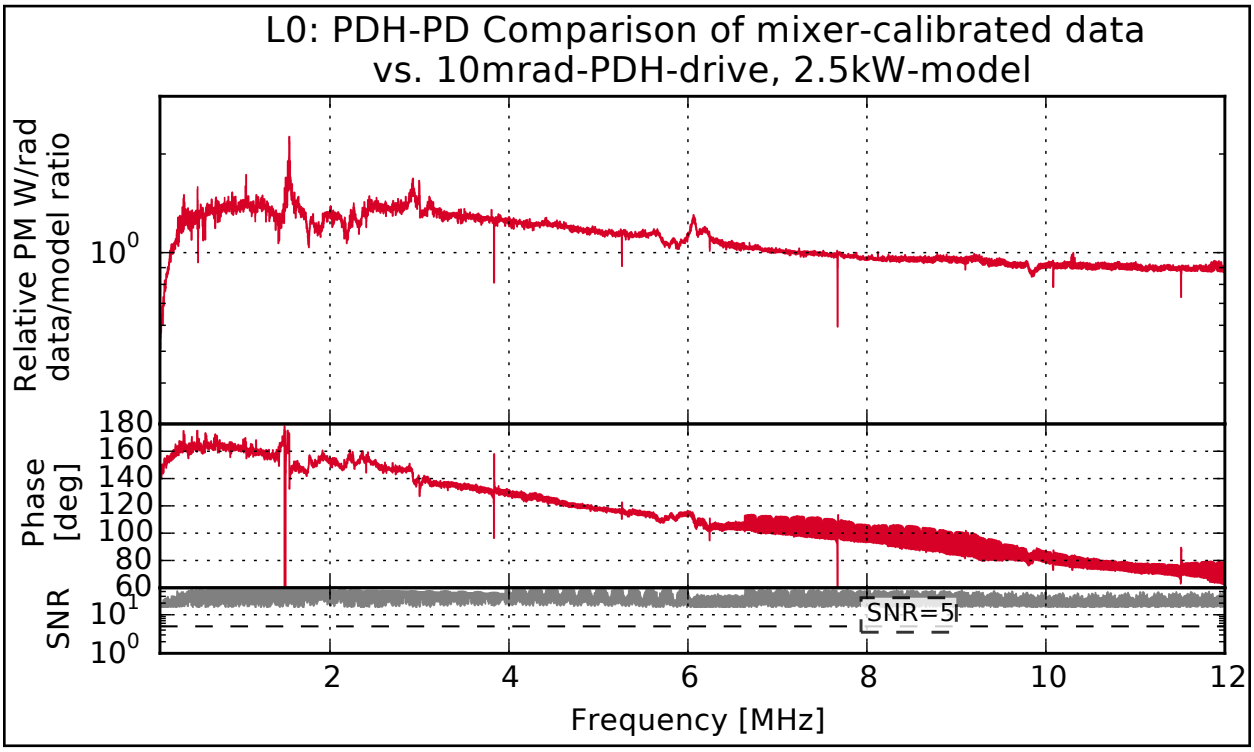

Figure 6.15: PDH sensitivity measurement of an EOM sweep compared against the Mach-Zehnder for the **L**.

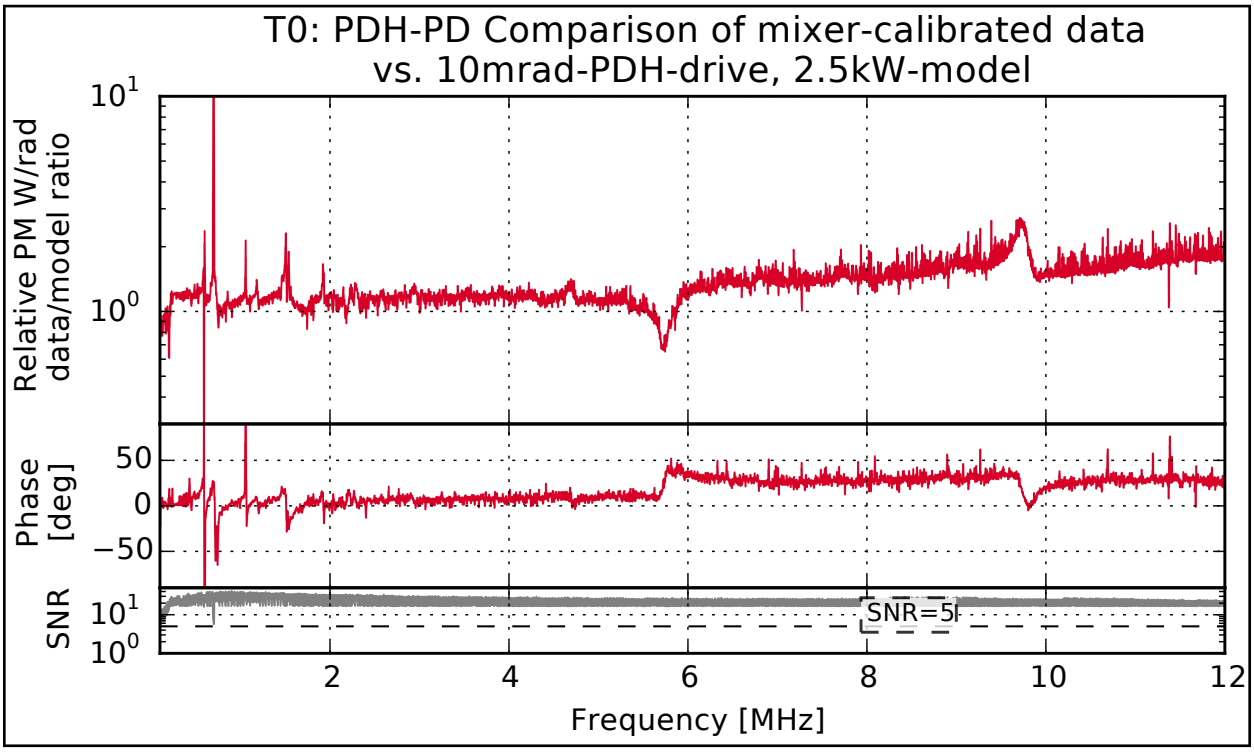

Figure 6.16: PDH sensitivity measurement of an EOM sweep compared against the Mach-Zehnder for the **T**.

6.10 PM Budget in PDH-locked laser

Double-checked calibrations of the PDH phase sensitivity are used in fig. 6.17 and fig. 6.18 on the next page to display the phase-noise spectrum of the *CARM-locked* interferometer. Due to the active electronics actuating the laser-FM, the manufacturer specifications of FM are not necessarily representative of the noise expected of the locked interferometer. The PDH discriminant, calibrated to PM through its model as well as through the MZ are displayed. The forest of resonant structure from 200kHz to 1MHz can be attributed to laser-PZT resonances. The CARM-loop itself was optimized with notch filters to attempt not to excite these resonances from output-electronics noise and the loops' sensor-noise.

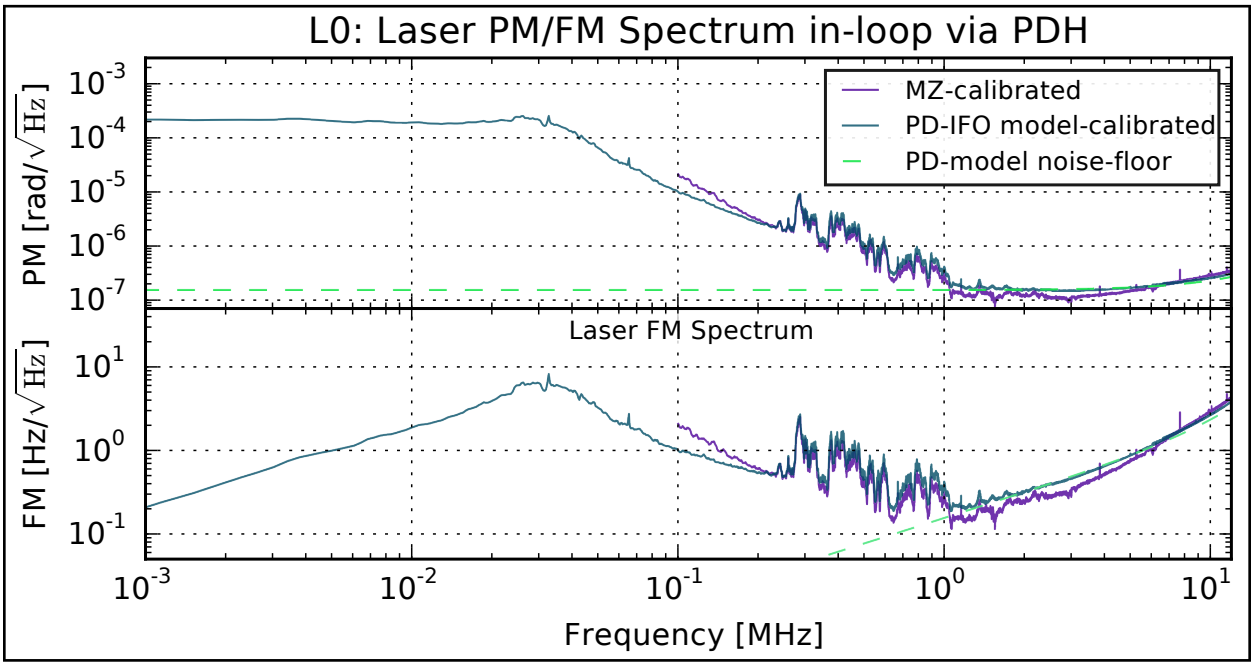

Figure 6.17: In-situ phase-noise of the laser averaged over all of the data in the **L**, as measured by PDH. The flat-top PM and F^1 rise in FM show the CARM-loop hitting a 30kHz Unity-gain-frequency. Further up to 1MHz are laser resonances possibly in the FM-drive PZT being driven by electronics.

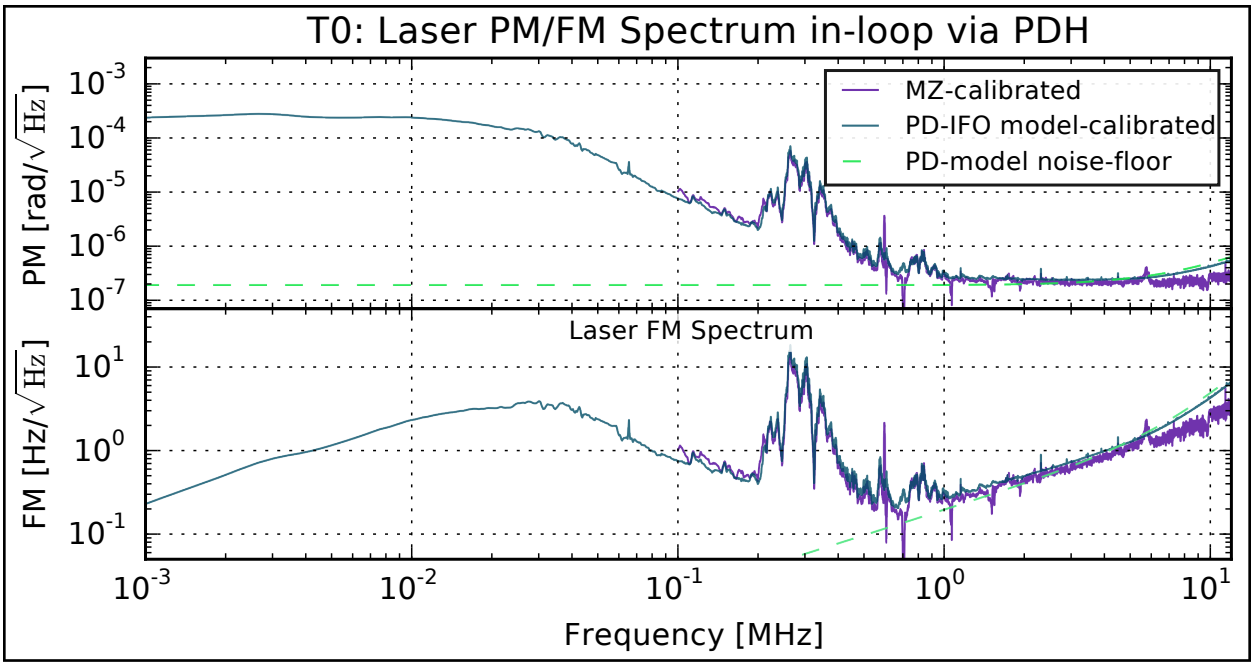

Figure 6.18: In-situ phase-noise of the laser averaged over all of the data in the **L**, as measured by PDH. The flat-top PM and F^1 rise in FM show the CARM-loop hitting a 30kHz Unity-gain-frequency. Further up to 1MHz are laser resonances possibly in the FM-drive PZT being driven by electronics.

6.11 Phase-noise Budget at AS Port

Just like the AM-noise, the PM can be viewed in cross-spectra with the ASPDs to budget excess-noise at the ASPD's due instead to phase. Refer to section 6.5 on page 177 for details on the distinction of the 1x vs. 2x measurements.

The phase-noise budgets for the L and T are shown in fig. 6.19 on the next page, fig. 6.20 on page 196, fig. 6.21 on page 196, and fig. 6.22 on page 197. By-and-large they show that the phase-noise is *not* responsible for any significant portion of the excess noise seen at the AS-port except potentially for noise between 10kHzand 100kHz. The linear zoomed plot around the free-spectral-range for the **T** in fig. 6.23 on page 197 show a peculiar feature of the odd-function of phase noise. The optical transfer function as it is increasing in frequency passes through a near cancellation of the FSR upper and lower sidebands, creating a very narrow-

notch at the FSR. The DAQ system was only measured these with 300Hz resolution, and so does not perfectly capture the zero, but the zoom-in does show the single-bin unresolved notch in the transfer-function. Interestingly, the model of eq. (D.58) on page 267 cannot express this cancellation, so at some level there must be a detuning from the cavity resonance.

The zoom of the TEM-2 modes in fig. 6.24 on page 198 also do not saturate the budget, although they do combine with the AM in fig. 6.10 on page 181 to better-fill the excess.

The final note for the PDH plots is that the 2x-referred line for the L shows a nearly factor-of-two bias down below the 1x referred line. This indicates that the PDH transfer could be as much as a factor-of-two off systematically, weakening the cross-interferometer budgets shown in the next chapter.

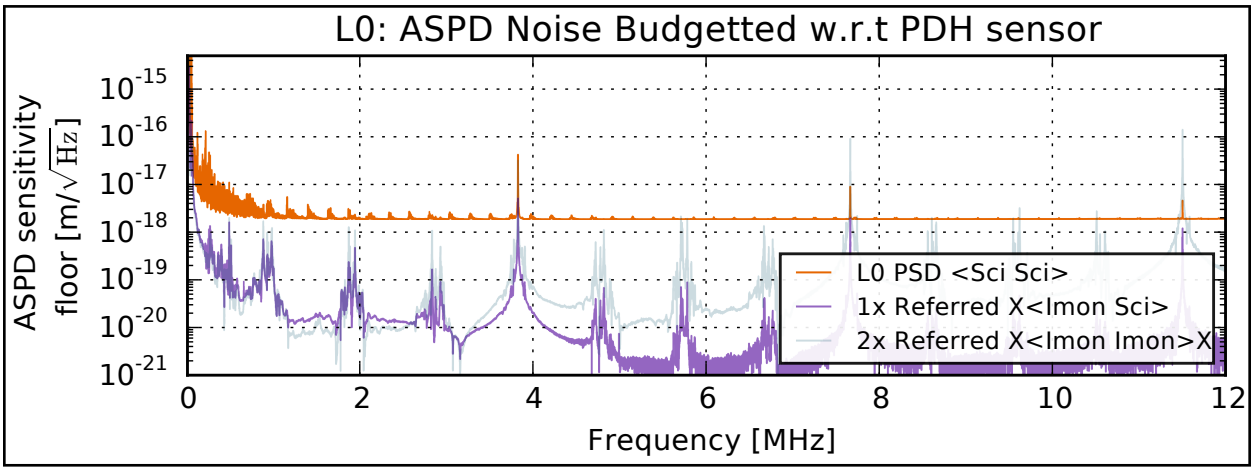

Figure 6.19: Phase-noise budget of the **L** ASPD channel plotted linearly in frequency.

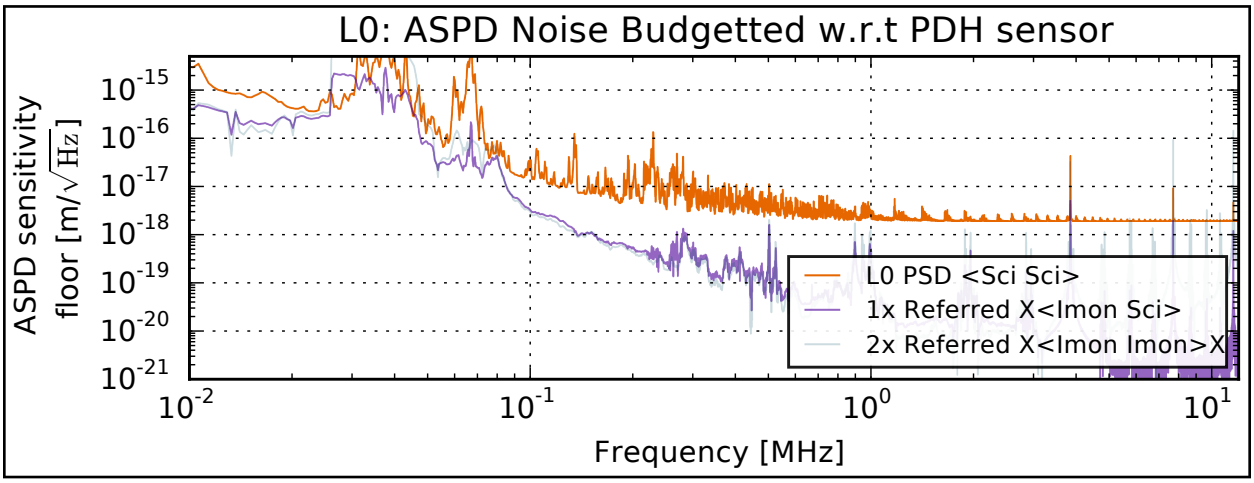

Figure 6.20: Phase-noise budget of the **L** ASPD channel plotted logarithmically in frequency. Much of the noise below 100kHz appears attributable to laser phase-noise.

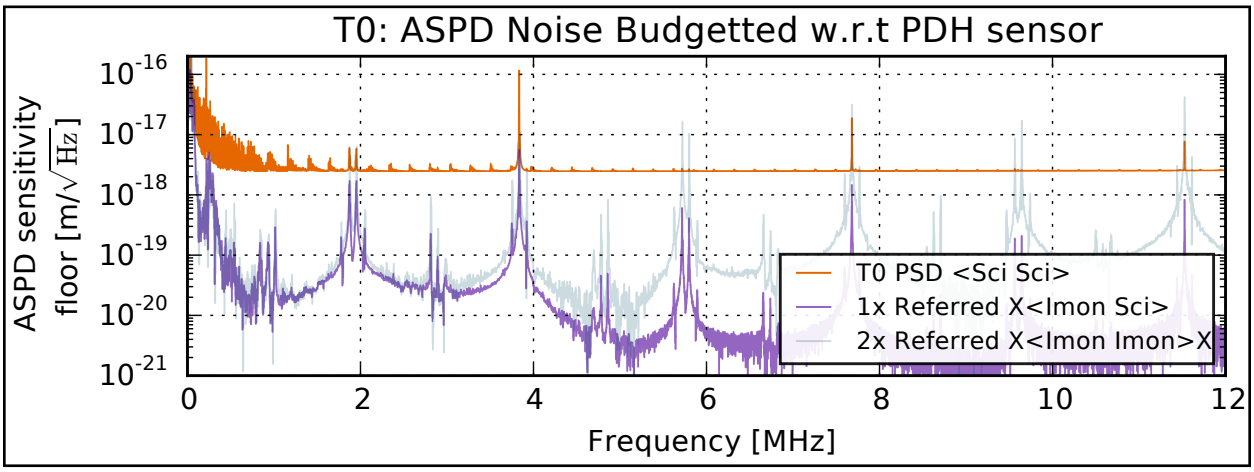

Figure 6.21: Phase-noise budget of the **T** ASPD channel plotted linearly in frequency.

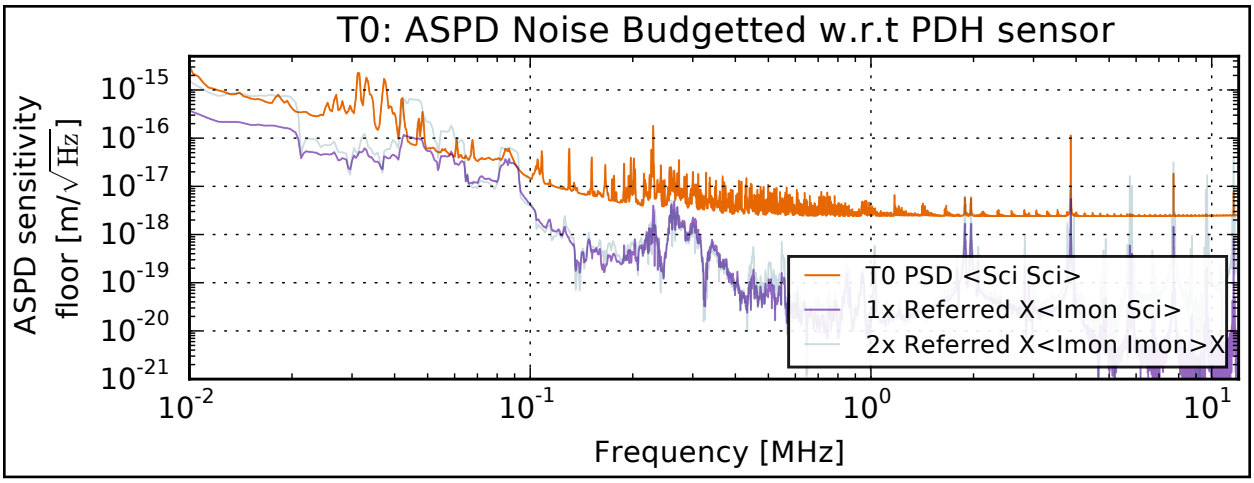

Figure 6.22: Phase-noise budget of the **T** ASPD channel plotted logarithmically in frequency. Much of the noise below 100kHz appears attributable to laser phase-noise.

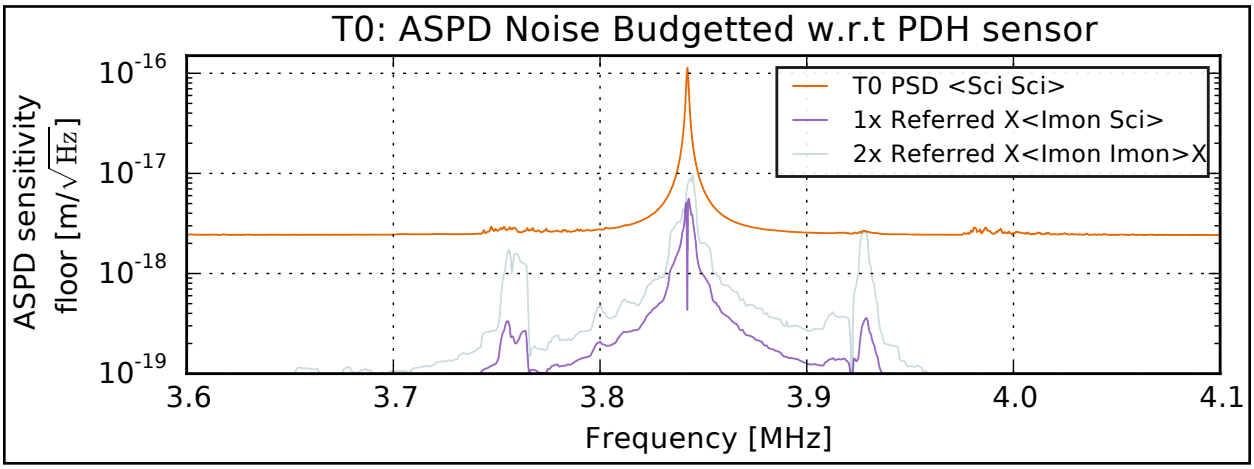

Figure 6.23: Phase-noise budget of the **T** ASPD channel plotted linearly in frequency with a zoom around the first free-spectral-range.

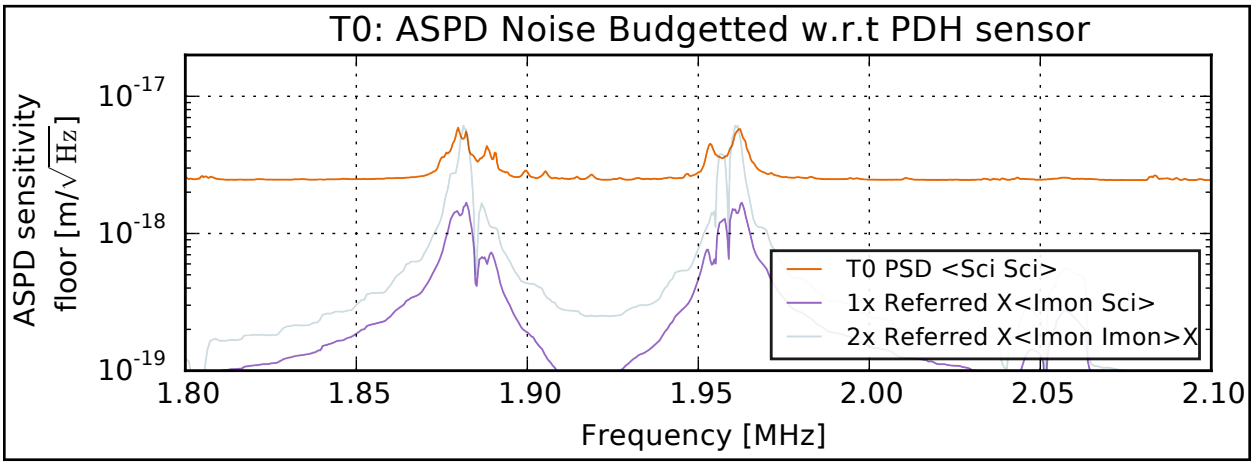

Figure 6.24: Phase-noise budget of the **T** ASPD channel plotted linearly in frequency with a zoom around the TEM02/20 HOM mode resonance.

6.12 ASPD Self-Cross Length-noise budget

The final self-interferometer budgets use the separate length-sensing photodiode measurements at the AS-port to generate a sub-shotnoise measurement of the correlated noise excess. In effect, this measurement is equivalent the "radiometer-method" measurement to detect excess noise in a Michelson as discussed in section 2.12.1 on page 61. The use of two photodiodes prevents the need for an exact budget of the shot-noise required to generate the estimator of that method. Instead, the cross-spectrum of two photodiodes through a beamsplitter allows the "common" or sum-channel to make the measurement, and the "differential" channel to estimate the shot-noise. The basis-change to PD common-differential actually expresses the PD1, PD2 cross-spectrum as the radiometer method estimator. Where the PSD of the shot-noise is not estimated, but measured.

In-any case, the cross at the AS-ports represent a "catch-all" for noise in the interferometers. Much of this noise is actual length fluctuation at the surfaces of optics. The repetitive-band structure seen matches well to the frequencies of bulk-longitudinal etalon modes of the $\frac{1}{2}$ inch fused-silica mirrors. At lower frequencies, many of the modes could be the radial and azimuthal Bessel-drumhead modes of the mirror surfaces. All of these fused-silica modes are driven through thermal fluctuations.

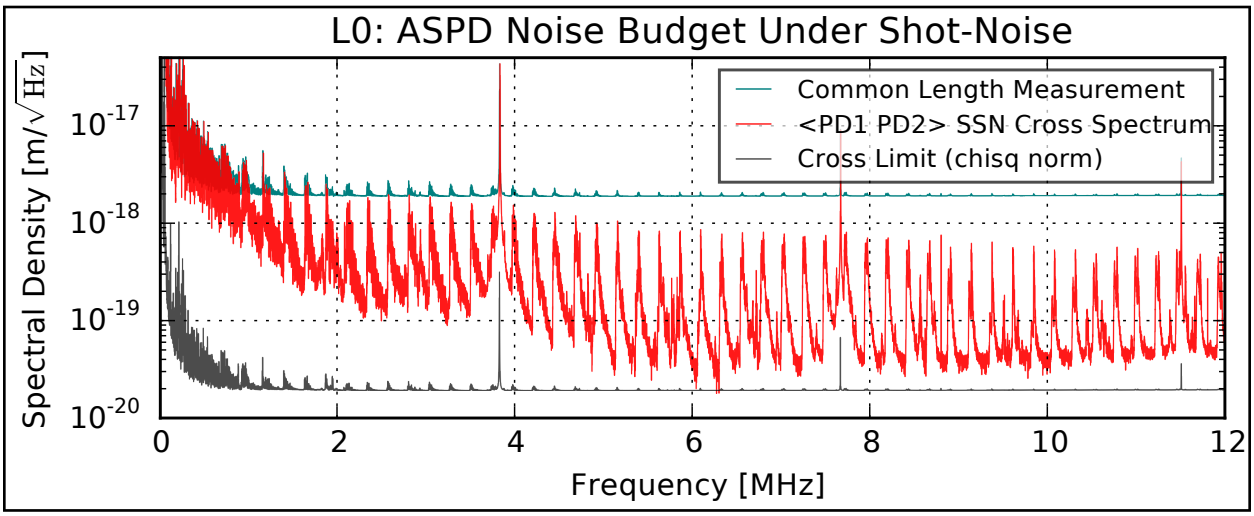

Figure 6.25: Interferometer sub shot noise cross spectrum of the **L**. This measurement detects all excess noise common to the interferometer. The regular band structure repeating every 230kHz are mirror-longitudinal modes thermally-driven.

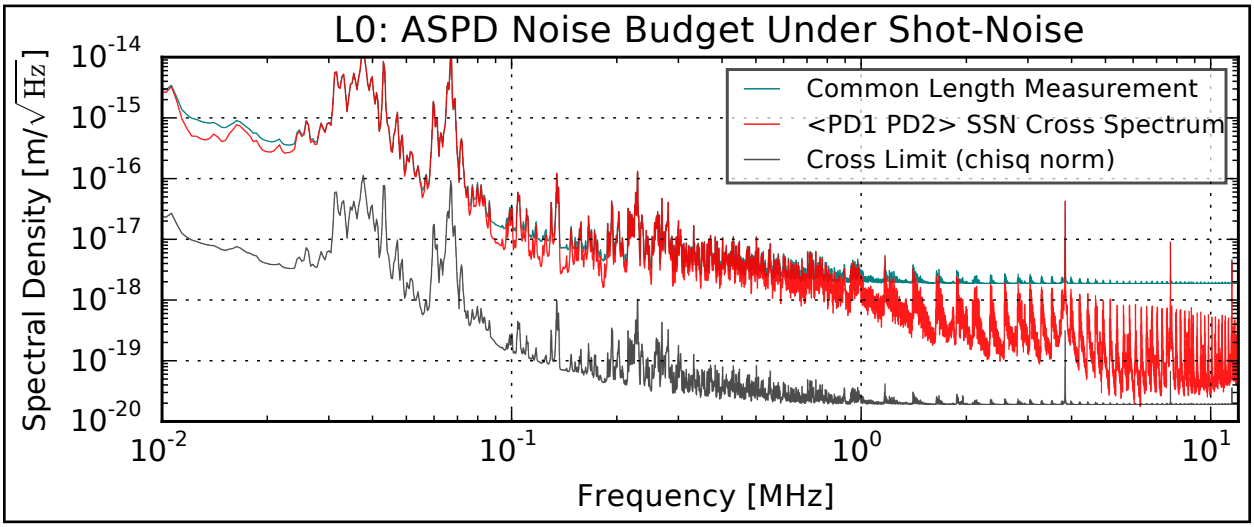

Figure 6.26: Interferometer sub shot noise cross spectrum of the **L**, plotted log-frequency. The large low-frequency excess not otherwise covered from AM and PM budgets is likely real displacement noise. The mechanical modes of constant mass and Q excited thermally fall in their resolved displacement as $1/f$ and much of the excess is likely mechanical.

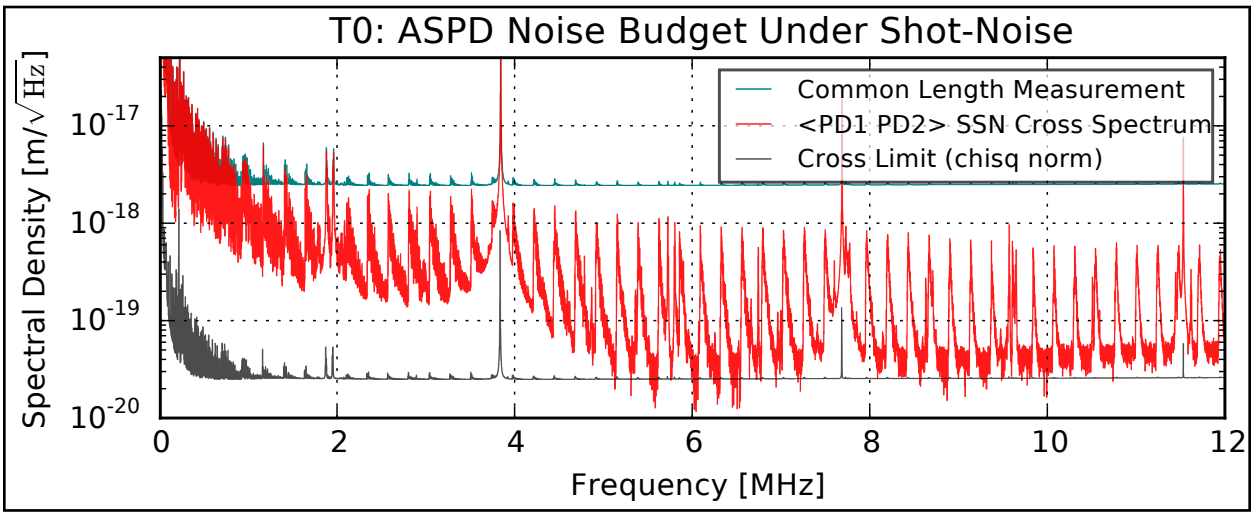

Figure 6.27: Interferometer sub shot noise cross spectrum of the **T**. This measurement detects all excess noise common to the interferometer. The regular band structure repeating every 230kHz are mirror-longitudinal modes thermally-driven.

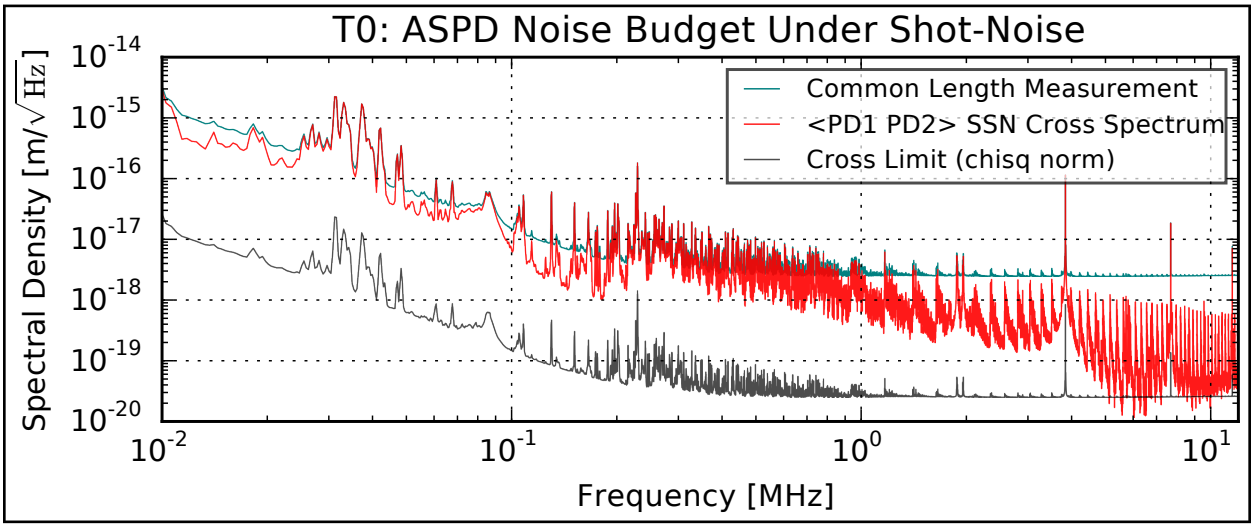

Figure 6.28: Interferometer sub shot noise cross spectrum of the **T**, plotted log-frequency. The large low-frequency excess not otherwise covered from AM and PM budgets is likely real displacement noise. The mechanical modes of constant mass and Q excited thermally fall in their resolved displacement as $1/f$ and much of the excess is likely mechanical.

Chapter 7

SYSTEMATIC BACKGROUND CORRELATIONS

The previous chapter indicated from the budget plots that the Laser systems and the ground both imprint signals at the ASPD ports that appears as spurious length-noise. The aim of two instruments was to isolated the systems sufficiently well that spurious correlations imprinting in one interferometer will not also imprint on the other. During the development of the experiment, many means were found for the background RF environment to enter in to the interferometers in ways that correlate in the two instruments. These backgrounds were reduced through great effort of monitoring the auxiliary channels to the point where their detection was - except for some tenacious narrow bands - undetectable for short operating periods.

At this time, the 100+ hour science integration was taken, without the knowledge that the auxiliary channels were background-free at the long-integration sensitivity.

7.1 Model of interference from Background Sources

With the calibrations of the previous chapter, the same budgets can be constructed for each set of auxiliary channels, but crossing L monitors to the T ASPDs and vice-versa. The budgets created in this fashion serve to constrain and budget the spurious correlation of the 2-interferometer length cross-spectrum. A simple model of the background noise can be created to demonstrate the nature of the limits.

Let $\hat{\vec{N}}_{\mathrm{BG}}$ be a vector of the intrinsic independent modes of sources representing the

background noise. It is unit-normalized to have CSD matrix for independent sources.

$$\widehat{\mathrm{CSD}}[\hat{\vec{N}}, \hat{\vec{N}}] = \begin{bmatrix} 1 & & & \\ & 1 & & \cdots \\ & & 1 & \\ & \vdots & & \ddots \end{bmatrix} \tag{7.1}$$

A similar statistical-vector exists for the excess noise modes local to the L and T respectively, $\hat{\vec{N}}_{\mathrm{L}}$, $\hat{\vec{N}}_{\mathrm{T}}$. One of the modes in each of these matrices represents the shot-noise of the combined-PD-channel and can further be expressed as a linear combination of the 2 shotnoise-modes of the constituent photodiodes.

In any case, the ASPD science channels of each interferometer can be composed as a linear combination of the potential Holographic-noise signal $\hat{S}_\delta$, and a coupling-vector into these noise-matrices. The coupling vector has units of length since the noise-vectors were defined to be unit-less.

$$\hat{L}_{\mathrm{aspd}} = \hat{S}_\delta + \vec{\Lambda}^{\mathrm{L}}_{\mathrm{AS}} \cdot \hat{\vec{N}}_{\mathrm{BG}} + \vec{\Gamma}^{\mathrm{L}}_{\mathrm{AS}} \cdot \hat{\vec{N}}_{\mathrm{L}} \tag{7.2}$$

$$\hat{T}_{\mathrm{aspd}} = \hat{S}_\delta + \vec{\Lambda}^{\mathrm{T}}_{\mathrm{AS}} \cdot \hat{\vec{N}}_{\mathrm{BG}} + \vec{\Gamma}^{\mathrm{T}}_{\mathrm{AS}} \cdot \hat{\vec{N}}_{\mathrm{T}} \tag{7.3}$$

The expected cross correlation to detect the presence of $\hat{S}_\delta$ finds the background noise terms and cannot distinguish them from the signal.

$$\overline{\mathrm{CSD}}[\hat{L}_{\mathrm{aspd}}, \hat{T}_{\mathrm{aspd}}; F] = \overline{\mathrm{PSD}}[\hat{S}_\delta; F] + \vec{\Lambda}^{\mathrm{L}}_{\mathrm{AS}}(F) \cdot \vec{\Lambda}^{\mathrm{T}*}_{\mathrm{AS}}(F) \tag{7.4}$$

The $\vec{\Lambda}^{\mathrm{L}}_{\mathrm{AS}}$ vectors are the couplings of any number of background noise modes referred into the length-units of the ASPDs. Somehow, the dot-product of these coupling-vectors must be determined or bounded through measurements. The various auxiliary channels budget out how these coupling could possibly be created through AM or PM of the laser leaking into the interferometer. They could also occur from background leaking directly into the

electronics. With the auxiliary channels all referred fully into the ASPD-length units. The expectation is that the background couplings can be expressed as

$$\hat{L}_{\mathrm{AM}} = \vec{\Lambda}^{\mathrm{L}}_{\mathrm{AM}} \cdot \hat{\vec{N}}_{\mathrm{BG}} + \vec{\Gamma}^{\mathrm{L}}_{\mathrm{AM}} \cdot \hat{\vec{N}}_{\mathrm{L}} \qquad \hat{T}_{\mathrm{AM}} = \vec{\Lambda}^{\mathrm{T}}_{\mathrm{AM}} \cdot \hat{\vec{N}}_{\mathrm{BG}} + \vec{\Gamma}^{\mathrm{T}}_{\mathrm{AM}} \cdot \hat{\vec{N}}_{\mathrm{L}} \tag{7.5}$$

$$\hat{L}_{\mathrm{PM}} = \vec{\Lambda}^{\mathrm{L}}_{\mathrm{PM}} \cdot \hat{\vec{N}}_{\mathrm{BG}} + \vec{\Gamma}^{\mathrm{L}}_{\mathrm{PM}} \cdot \hat{\vec{N}}_{\mathrm{L}} \qquad \hat{T}_{\mathrm{PM}} = \vec{\Lambda}^{\mathrm{T}}_{\mathrm{PM}} \cdot \hat{\vec{N}}_{\mathrm{BG}} + \vec{\Gamma}^{\mathrm{T}}_{\mathrm{PM}} \cdot \hat{\vec{N}}_{\mathrm{L}} \tag{7.6}$$

And the AS couplings can be broken into the constituent sources of correlated backgrounds

$$\vec{\Lambda}^{\mathrm{L}}_{\mathrm{AS}} = \vec{\Lambda}^{\mathrm{L}}_{\mathrm{AM}} + \vec{\Lambda}^{\mathrm{L}}_{\mathrm{PM}} + \vec{\Lambda}^{\mathrm{L}}_{\mathrm{v}} + \vec{\Lambda}^{\mathrm{L}}_{\mathrm{X}} \tag{7.7}$$

$$\vec{\Lambda}^{\mathrm{L}}_{\mathrm{AS}} = \vec{\Lambda}^{\mathrm{L}}_{\mathrm{AM}} + \vec{\Lambda}^{\mathrm{L}}_{\mathrm{PM}} + \vec{\Lambda}^{\mathrm{L}}_{\mathrm{v}} + \vec{\Lambda}^{\mathrm{L}}_{\mathrm{X}} \tag{7.8}$$

as well as the uncorrelated backgrounds (these were plotted in the previous chapter).

$$\vec{\Gamma}^{\mathrm{L}}_{\mathrm{AS}} = \vec{\Gamma}^{\mathrm{L}}_{\mathrm{PD1SN}} + \vec{\Gamma}^{\mathrm{L}}_{\mathrm{PD2SN}} + \vec{\Gamma}^{\mathrm{L}}_{\frac{1}{2}\mathrm{kt}} + \vec{\Gamma}^{\mathrm{L}}_{\mathrm{AM}} + \vec{\Gamma}^{\mathrm{L}}_{\mathrm{PM}} + \vec{\Gamma}^{\mathrm{L}}_{\mathrm{v}} + \vec{\Gamma}^{\mathrm{L}}_{\mathrm{X}} \tag{7.9}$$

$$\vec{\Gamma}^{\mathrm{L}}_{\mathrm{AS}} = \vec{\Gamma}^{\mathrm{L}}_{\mathrm{PD1SN}} + \vec{\Gamma}^{\mathrm{L}}_{\mathrm{PD2SN}} + \vec{\Gamma}^{\mathrm{L}}_{\frac{1}{2}\mathrm{kt}} + \vec{\Gamma}^{\mathrm{L}}_{\mathrm{AM}} + \vec{\Gamma}^{\mathrm{L}}_{\mathrm{PM}} + \vec{\Gamma}^{\mathrm{L}}_{\mathrm{v}} + \vec{\Gamma}^{\mathrm{L}}_{\mathrm{X}} \tag{7.10}$$

The terms represented for the correlated backgrounds are: the noise modes imprinted into the AM channel of the laser, the PM channel of the laser, the voltage from external RF coupling into the ASPD/DAQ signal chain and finally, X, representing any unaccounted but not-new physics.

Now all of the various combinations of cross-budgets account for the contributions of each set of terms by selecting only the common noise sources. For example:

$$\overline{\mathrm{CSD}}[\hat{L}_{\mathrm{AM}}, \hat{T}_{\mathrm{aspd}}; F] = \vec{\Lambda}^{\mathrm{L}}_{\mathrm{AM}}(F) \cdot \vec{\Lambda}^{\mathrm{T}*}_{\mathrm{AS}}(F) \tag{7.11}$$

And the electric RF-voltage background can only be measured ex-situ during "dark" running without the lasers imprinting light on the photodiode. In principle more terms could be

collected from running only a single interferometer dark at a time, but that data was not collect for this experiment, only the double-dark was collected.

$$\overline{\mathrm{CSD}}\left[\hat{T}_{\substack{\mathrm{aspd},\\ \mathrm{dark},F}}, \hat{T}_{\substack{\mathrm{aspd},\\ \mathrm{dark},F}}\right] = \vec{\Lambda}^{\mathrm{L}}_{\mathrm{v}}(F) \cdot \vec{\Lambda}^{\mathrm{T}*}_{\mathrm{v}}(F) \tag{7.12}$$

The "dark noise" or background terms can be measured extremely strongly in double-dark mode because of the passive state of the interferometer. The optical system is not running in this mode and requires no attention. Furthermore without the addition of shot-noise, the background RF environment is correlated only against the amplifier noise of the detectors, which is 1% of the shotnoise in this experiment. Removing this background required considerable work, but could be done with a quick (statistical-integration limited) iteration time when looking in double-dark mode. That term will be plotted, but absorbed into the "X" terms for the in-situ collections that follow. The in-situ measurements from the ASPD-referred AM and PM can be crossed against the opposing interferometer ASPD and summed to pick-out the remaining cross correlation. The unmeasured X-term can not be picked-up from this analysis, but each cross is sensitive to the opposite interferometer's X-terms. The concise expression is (dropping the cumbersome F indexes):

$$\overline{\mathrm{CSD}}[\hat{L}_{\mathrm{AM}}, \hat{T}_{\mathrm{aspd}}; F] + \overline{\mathrm{CSD}}[\hat{L}_{\mathrm{PM}}, \hat{T}_{\mathrm{aspd}}; F] = \vec{\Lambda}^{\mathrm{L}}_{\mathrm{AS}} \cdot \vec{\Lambda}^{\mathrm{T}*}_{\mathrm{AS}} - \vec{\Lambda}^{\mathrm{L}}_{\mathrm{X}} \cdot \vec{\Lambda}^{\mathrm{T}*}_{\mathrm{AS}} \tag{7.13}$$

$$\overline{\mathrm{CSD}}[\hat{L}_{\mathrm{aspd}}, \hat{T}_{\mathrm{AM}}; F] + \overline{\mathrm{CSD}}[\hat{L}_{\mathrm{aspd}}, \hat{T}_{\mathrm{PM}}; F] = \vec{\Lambda}^{\mathrm{L}}_{\mathrm{AS}} \cdot \vec{\Lambda}^{\mathrm{T}*}_{\mathrm{AS}} - \vec{\Lambda}^{\mathrm{L}}_{\mathrm{AS}} \cdot \vec{\Lambda}^{\mathrm{T}*}_{\mathrm{X}} \tag{7.14}$$

These sets of cross-spectra can then be integrated in frequency just as with the data to limit (up to the unknown X terms) the presence of systematic backgrounds). The only systematics that must be taken on faith are the unknown terms $\vec{\Lambda}^{\mathrm{L}}_{\mathrm{X}} \cdot \vec{\Lambda}^{\mathrm{T}*}_{\mathrm{X}}$, but for these terms to cast strong doubt, this term would have to include sufficiently-strong couplings with some physical motivation. One potential source could be the endmirror PZT's actuating from ambient RF pickup, but the coupling to length is an extremely steep function of frequency, falling $1/F^2$

from PZT-spring resonances, and an additional $1/F$ from PZT capacitance, not to mention that the PZTs are connected differentially, which was often seen to couple in a $\sim 3^{\mathrm{nV}}/\sqrt{\mathrm{Hz}}$ noise into poorly-isolated cables. The baseline conversion to length below PZT resonances is $.1^{\mathrm{um}}/V$, providing at most a $10^{-15}\mathrm{m}/\sqrt{\mathrm{Hz}}$ noise, which then is reduced from F-cubed roll-off starting at a conservative 10kHz (expected more around 1kHz), which puts the residual background at $10^{-21}\mathrm{m}/\sqrt{\mathrm{Hz}}$. It is possible that in some narrow-bands the F-cubed roll-off is somewhat bypassed from the resonant amplification by mirror-modes, but it is unlikely that both interferometers would have mode-frequencies sufficiently similar at the quality-factors required for the common pickup to be in-phase. The endmirror common-RF pickup is a potential explanation for some residual pickup at lower frequencies, where the F-cubed roll-off is not fully active and the mirrors share common geometrically-defined resonances with lower-Q and potentially consistent coupling between the two interferometers.

7.2 Conventions for plots

The plots in this chapter showcase the two-interferometer ASPD cross-spectrum. This data will be in red. All of the plots show the *magnitude* of the complex signal in the cross spectrum. As-such they cannot be directly used to detect the proposed Holographic noise. The dashed black line represents the location of the cross-spectra reduced-χ^2_2 statistic for sensitivity. This is derived from the statistics of $\widehat{\mathrm{COH}}[\cdot,\cdot]$ detailed in appendix C. It is not flat because the geometric-mean length-sensitivity power-spectra of the two interferometers is used to convert from χ^2_2 error of coherence back into the unitful cross-spectrum. Where the true cross spectrum in red is lifted above its statistical-limit in black, there is resolved systematic background cross-correlating in the two instruments.

The resolution limit for this plot is set by the 3.8kHz bin-width. Further averaging in frequency would improve this limit at the cost of resolution for narrowband features. The next chapter will take this averaging to the limit as it integrates fully in frequency to

generate the Holographic-noise model-test. These plots breakdown the visible systematics, frequency-resolved, with the data from auxiliary channels through the vector-decomposition of the previous section. The choice for 3.8kHz is not arbitrary. It is the highest resolution at which the Welch-method-resolution bins can be coadded together to have an insignificant ($< 1\%$) covariance of their errorbars. This means that every data point plotted has an independent errorbar from every other.

The lower section in all of these plots is a χ^2_2 statistic from the coherence of the auxiliary channel with the opposite ASPD. It is detecting for any background of the form $\vec{\Lambda}^{\mathrm{L}}_{\mathrm{AM}}(F) \cdot \vec{\Lambda}^{\mathrm{T}*}_{\mathrm{AS}}(F)$ over the sensitivity of the cross-spectrum measurement. Even when excess is not visible or will not affect the science 2x-ASPD cross, the auxiliary channels can detect the possibility of any background through this statistic. Ultimately, these values are used to establish a veto criterion for final frequency-averaging through the model. With the vetos decided from the auxiliary-channels and not from the principle dataset, there is no clipping of probability-tails or other effects that bias or adjust the Gaussian/chi-square statistics used for the final integration.

7.3 AM Spectrum Limits

Figure 7.1 on page 209 and fig. 7.2 on page 210 show the ASPD length data along with the ASPD-referred AM auxiliary channels. The percentage of data shown reflects the operational limit in the number of available RF-correlating channels. The intensity monitors were traded with other channels to set representative limits for the full dataset in as many channels as possible. The **L**intensity monitor (LImon) was more sensitive than the monitor in the T, so used less data in setting a comparable limit.

The red science data does show significant excess around low-frequencies and the hope is that the noise budgets may fill that excess with signal from known mechanism. The laser intensity noise is very apparently not the source of this noise. If it were, then these budgets

would be capable of seeing it and showing the excess. Despite not filling the ASPD budget, the bottom chi-square statistic is showing a significant detection of coupled noise. This statistic was used for shorted test-runs to isolate the electrical systems and the excess seen here shows that removing excess from $\tilde{1}0$ minute runs and dark-noise runs of the interferometers was sufficient in preventing the ASPD's from gaining a background from intensity-noise but naturally did not perfectly isolated the noise and it became visible after longer integration time.

Included as well is the budget from the 2x intensity monitor. This sets a limit purely from the $\vec{\Lambda}^{\mathrm{L}}_{\mathrm{AM}} \cdot \vec{\Lambda}^{\mathrm{T}*}_{\mathrm{AM}}$ term, without crosses to all other ASPD-couplings. It shows particularly well that the AM channel is clean.

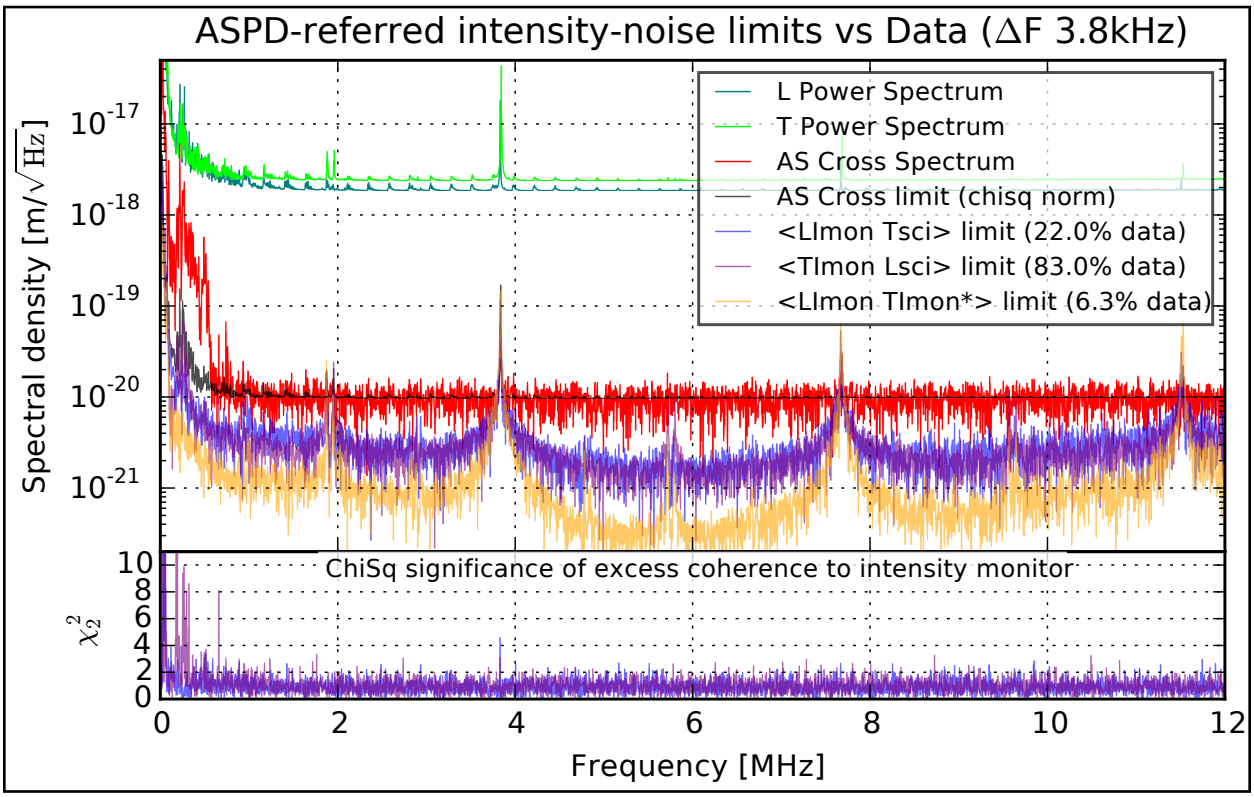

Figure 7.1: 3.8kHz-resolved inter-interferometer cross-spectrum,linear in frequency and including the model-sensitive 2x-IFO ASPD cross as well as the cross-interferometer budgets of the AM systematics noise. The three limits shown are upper bounds for noise in those respective channels. The (reduced) Chi-square indicates the level of statistical certainty of noise detection in the background limit. Chi-squares above 3 are excluded at the 95% and 3 is used as the veto threshold for a frequency-bin. Most frequencies do not show an excess and are not vetoed. The lack of excess indicates that the curve of the magnitude plot is primarily showing the statistical fluctuation.

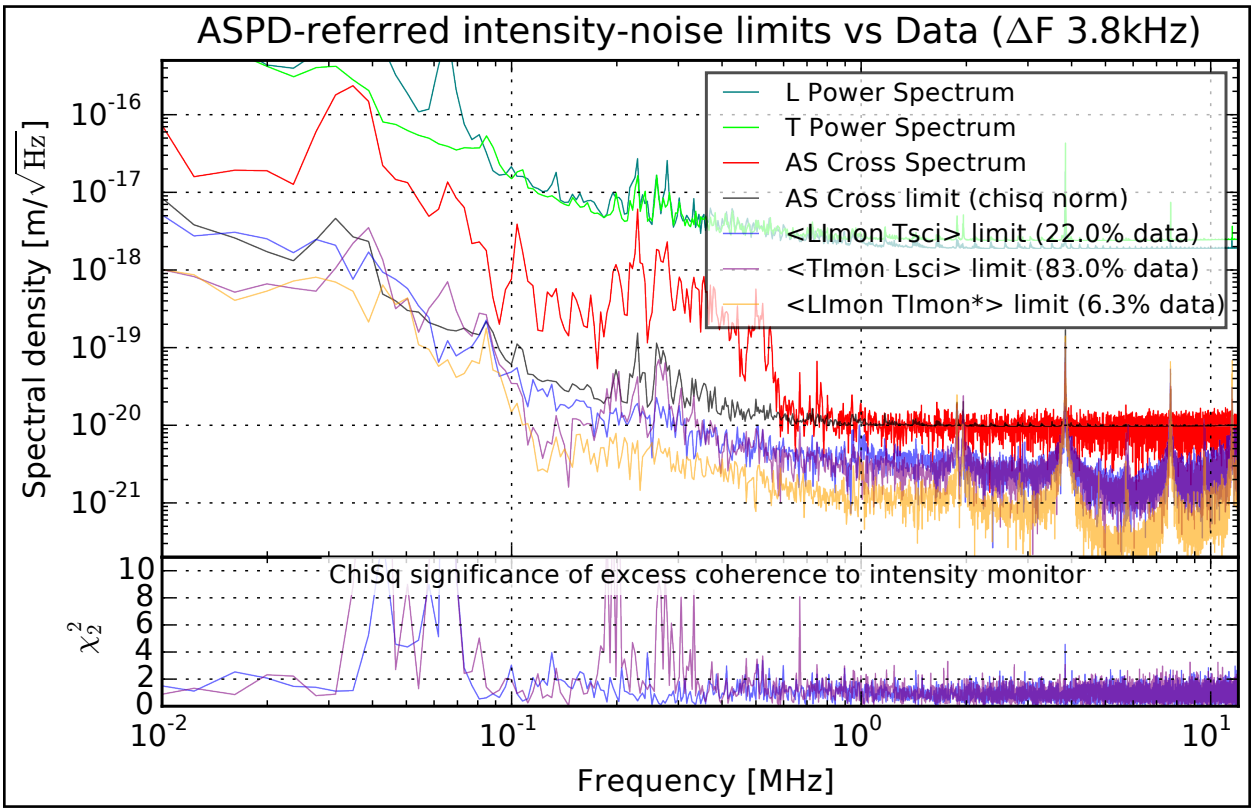

Figure 7.2: 3.8kHz-resolved inter-interferometer cross-spectrum logarithmic in frequency and including the model-sensitive 2x-IFO ASPD cross as well as the cross-interferometer budgets of the AM systematics noise.

7.4 PM Spectrum Limits

The story for the phase budget is radically different than for intensity. The phase-noise as measured through the Pound-Drever-Hall signal shows highly significant excesses in the chi-square plots, and the ASPD budget is well-saturated from the cross of the T-PM into the L-ASPD particularly around 200-300kHz. This cross describes the source of excess noise in the T-ASPD that is common to the L. This is interesting as the converse cross is not true, the L-PM can not be used to explain the excess noise of the L-ASPD common to the T. This plot underlies using each cross the ASPD's rather than purely between the PM-channels. The differences between the blue and purple data show the different appearances of the "mystery coupling" $(\vec{\Lambda}^{\mathrm{L}}_{\mathrm{PM}} \cdot \vec{\Lambda}^{\mathrm{T}*}_{\mathrm{X}})$ vs. $(\vec{\Lambda}^{\mathrm{L}}_{\mathrm{X}} \cdot \vec{\Lambda}^{\mathrm{T}*}_{\mathrm{PM}})$.

The appearance of an unaccounted presence of systematics is worrisome, but as described, only the RF-mechanical connections remain as a candidate source for these backgrounds and the unbudgeted excesses stop appearing above the noise around 500kHz, suggesting that an F-cubed or F-squared response of a mechanical mounting is suppressing these terms and their narrowband response suggests a sudden resonant coupling that becomes difficult to repeat at higher frequencies in a manner common to both machines.

The few additional budget excesses around 500, 600 and 800 kHz all can possibly be expected to not repeat further at high frequencies. If a concern persists, each of the unbudgeted excesses does show a large significance in the chi-square. This means that the veto-decisions will prevent the inclusion of the background. For an unknown background to escape the veto, it must not only leak into the interferometer, it must also manage to *not* leak into the CARM-loop laser FM drive nor the AM noise of the laser. In the opinion of the Author, this would not take just the work of Maxwell's Demon, but of Tesla's as well.

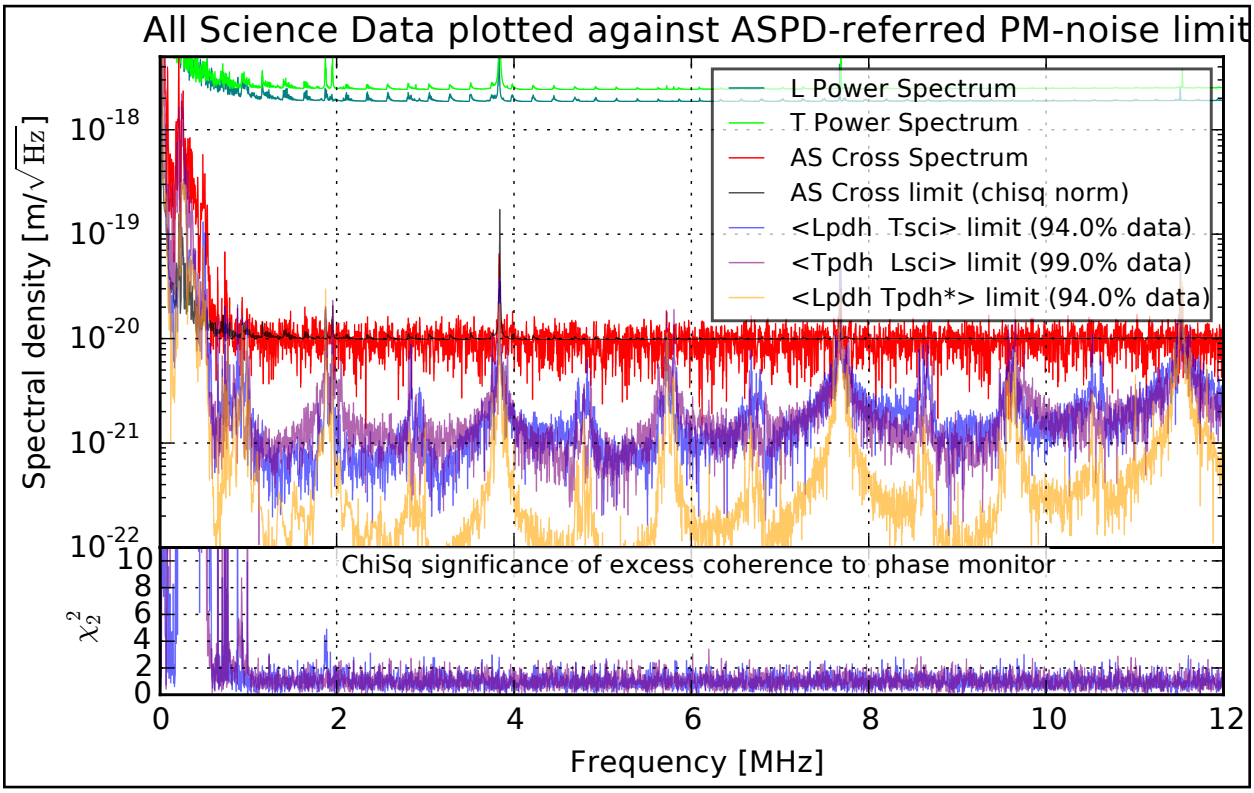

Figure 7.3: 3.8kHz-resolved inter-interferometer cross-spectrum, linear in frequency, including the model-sensitive 2x-IFO ASPD cross as well as the cross-interferometer budgets of the phase-systematics noise. The analysis is similar to fig. 7.1 on page 209.

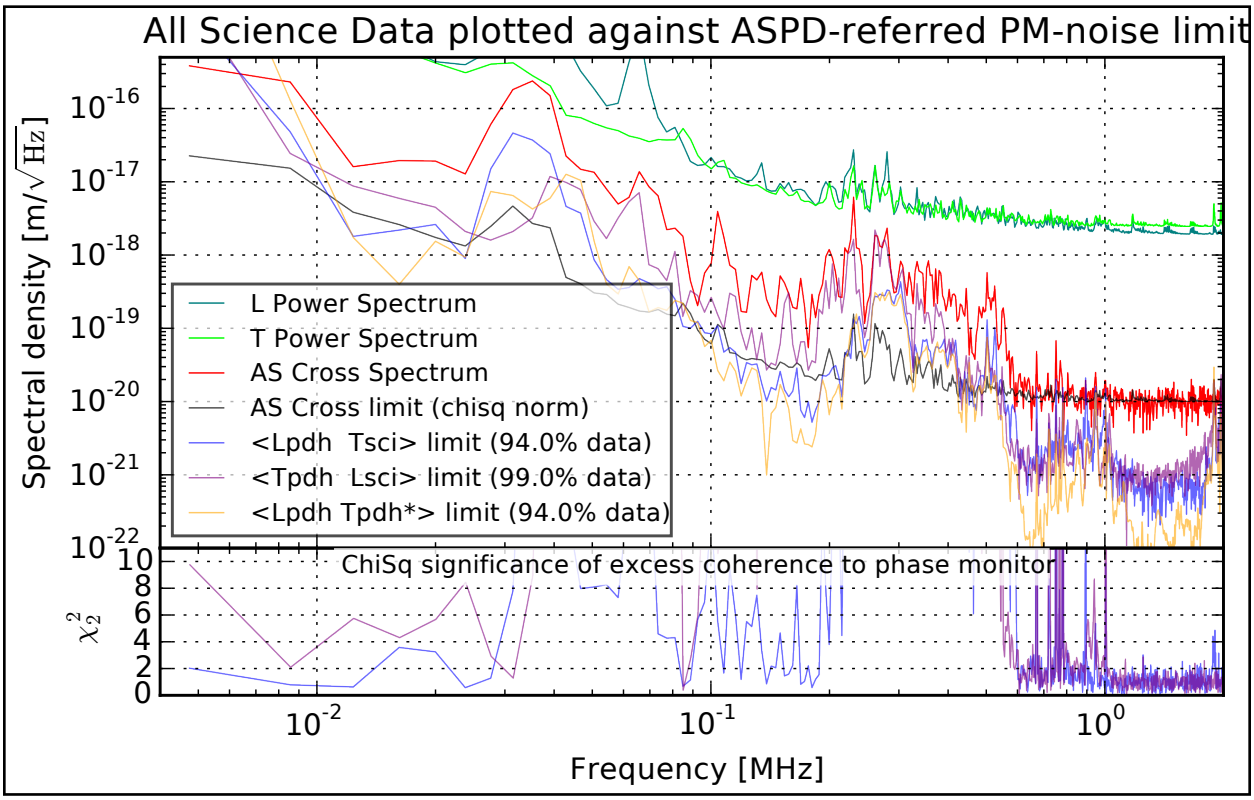

Figure 7.4: 3.8kHz-resolved inter-interferometer cross-spectrum, logarithmic in frequency, including the model-sensitive 2x-IFO ASPD cross as well as the cross-interferometer budgets of the phase-systematics noise.

7.5 Antenna lower-limits

The final limits come from an as-yet unexplained antenna channel shown linear-scale in fig. 7.5 on page 216 and logarithmic in fig. 7.6 on page 217. For most of the in-situ data, an antenna was also included to correlate with the ambient RF environment. This channel does not have much of any sensor noise and so can very strongly detect outside RF potentially coupling into the interferometer, but with no guarantees that it can see the exactly the same modes. Furthermore there is no unbiased method to reference the antenna to the ASPDs in a way that generates length-units. For this reason the antenna channel may only set lower-limits on the correlated background eventually detected by the interferometer.

As a lower-limit, this provides the experimenter a condition stating that the RF environment appears "too bad" to meaningfully run the instrument. This comes as an indiscriminate means of saturating the budget where the interferometer correlated noise happens to coincide with the mode seen by the antenna.

The statistic plotted as the Antenna limit here (F indices suppressed) is:

$$\hat{M}_{\text{ant}} = \left(\frac{\left| \widehat{\text{CSD}}[\hat{L}_{\text{aspd}}, \hat{V}_{\text{ant}}] \right|}{\widehat{\text{LSD}}[\hat{V}_{\text{ant}}]} \right)^{\frac{1}{2}} \left(\frac{\left| \widehat{\text{CSD}}[\hat{V}_{\text{ant}}, \hat{T}_{\text{aspd}}] \right|}{\widehat{\text{LSD}}[\hat{V}_{\text{ant}}]} \right)^{\frac{1}{2}} \tag{7.15}$$

$$= \frac{\left| \vec{\Lambda}^{\text{L}}_{\text{AS}} \cdot \vec{\Lambda}^{\text{LT}*}_{\text{ant}} \right|^{\frac{1}{2}} \left| \vec{\Lambda}^{\text{LT}}_{\text{ant}} \cdot \vec{\Lambda}^{\text{T}*}_{\text{AS}} \right|^{\frac{1}{2}}}{\left| \vec{\Lambda}^{\text{LT}}_{\text{ant}} \cdot \vec{\Lambda}^{\text{LT}*}_{\text{ant}} \right|^2} \tag{7.16}$$

Note that the statistic has the units of Λ which are length-noise.

The antenna statistic could be formed separately for each ASPD channel, but the geometric mean was taken to better approximate the modes showing between the two ASPDs, $(\vec{\Lambda}^{\text{L}}_{\text{AS}} \cdot \vec{\Lambda}^{\text{T}*}_{\text{AS}})$. The statistic in this form resembles the projection-operator for the ASPD-mode into the antenna-mode and the statistic $\hat{M}_{\text{ant}}$ then is the expectation when projected through

the antenna

$$\overleftrightarrow{P}_{\rm ant} = \frac{|\vec{\Lambda}^{\rm LT}_{\rm ant}\rangle\langle\vec{\Lambda}^{\rm LT}_{\rm ant}|}{\langle\vec{\Lambda}^{\rm LT}_{\rm ant}|\vec{\Lambda}^{\rm LT}_{\rm ant}\rangle} \qquad\qquad \hat{M}_{\rm ant} = \sqrt{\langle\vec{\Lambda}^{\rm L}_{\rm AS}|\overleftrightarrow{P}_{\rm ant}|\vec{\Lambda}^{\rm T}_{\rm AS}\rangle} \tag{7.17}$$

The figures show that the statistic does help fill the budget. Additional plots (not included) could identify which parts of the antenna-mode are selecting for the "X" mode over the optical modes already budgeted. The most interesting aspect of the antenna budget is the chi-square. That statistic is provided separately with the antenna CSD to the L and to the T (rather than combined as for the geometric-mean statistic). Even though the limit itself can only express a lower limit, the chi-squares state with profound certainty that ambient electrical RF is still entering the science measurement at some level. It can gain this certainty because it is a direct measurement of the background noise with very little noise itself, unlike the other auxiliary channels which detect the background under the shotnoise of their pickoff beam.

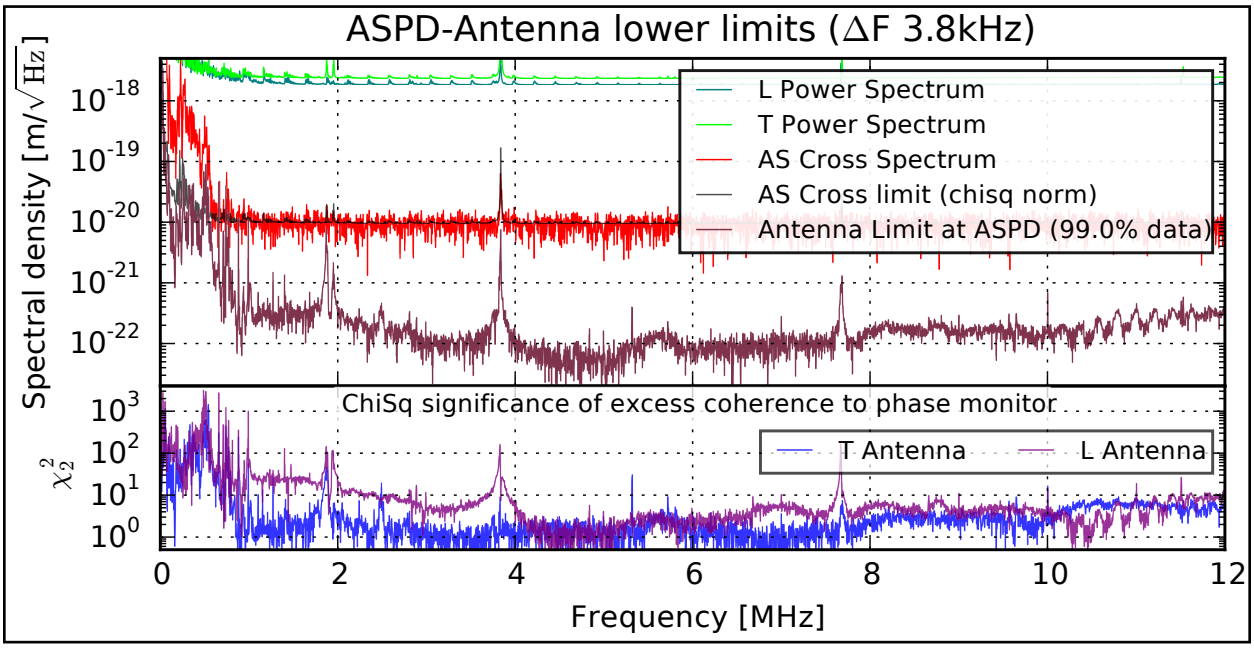

Figure 7.5: 3.8kHz-resolved inter-interferometer cross-spectrum, linear in frequency, including the model-sensitive 2x-IFO ASPD cross as well as an antenna measurement of the background setting an eventual lower-limit on the sensitivity seen in the interferometer. Note that the significance with the antenna is huge compared to that seen in the optical monitors, yet the lower limit set is much lower than their upper limits. The antenna is able to do this because it is a relatively noise-free measurement of the modes contributing to spurious correlation, but the lack of physical mechanism coupling the modes forces it to be a lower-limit.

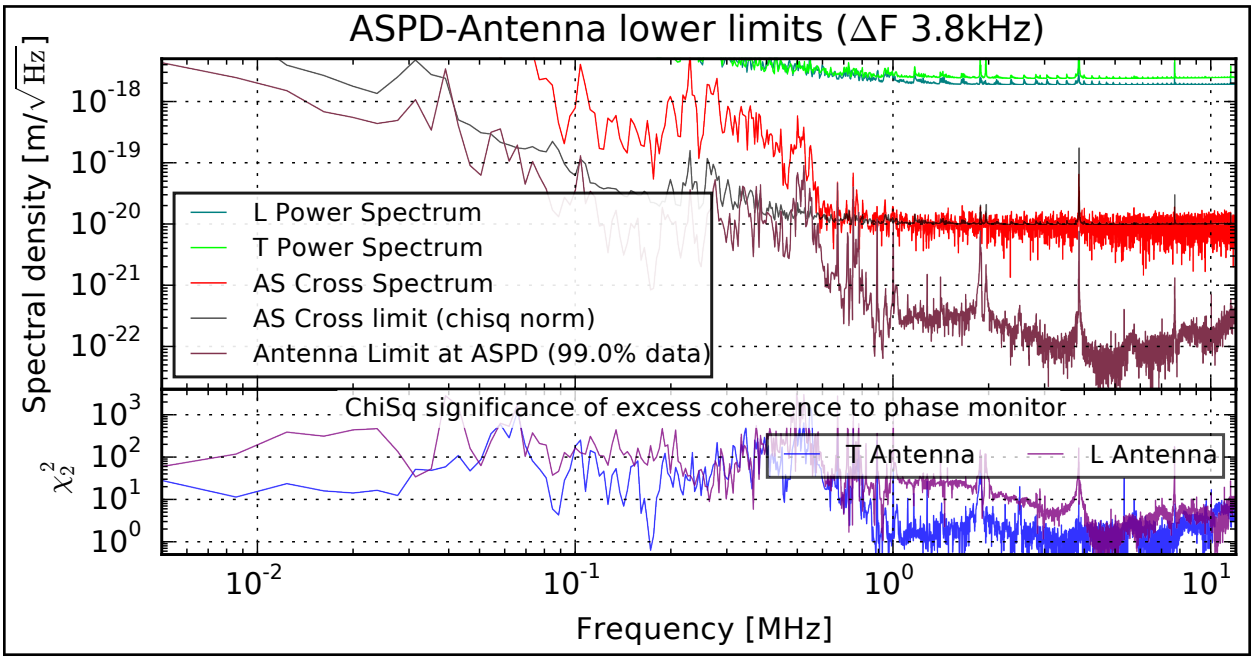

Figure 7.6: 3.8kHz-resolved inter-interferometer cross-spectrum, logarithmic in frequency, including the model-sensitive 2x-IFO ASPD cross as well as an antenna measurement of the background setting an eventual lower-limit on the sensitivity seen in the interferometer.

Chapter 8

FINAL-RESULTS

The culmination of this work tests the 2x interferometer length-sensitive cross spectrum for the presence of the correlated Holographic noise model presented in the introductory chapter. The statistics of the measurement are built and investigated through Chapter 2 to determine that the experiment after 150 hours should have sufficient sensitivity to test the model.

The details the calibration, how and why it works along with tests of its necessary assumptions are explored to determine that the calibration results should not be biased. Although all of the plots are on log-scales, the final significance is very sensitive to calibration error due to the use of two interferometers. Any calibration systematic-error doubles if it is present in both - it does not simply add in quadrature.

Finally, all of the calibrations are applied to generate budgets for the RF noise backgrounds that will be contained within the model-test to ascertain the proportion of novel excitation the model test should have over the proportion of parasitic "standard-physics" that will also appear.

8.1 Vetos Chosen for data samples in time

There are many intervals during the operation of the interferometers where one or both of the machines was not in a state to provide correct, calibrated data for integration into the final datasets. On the 1s timescale, accumulated RF CSD frames at 384Hz resolution (FFT-size 130kilo-samples) representing $2 \cdot 384$ Welch-method accumulations are provided and combined with the filtered and downsampled controls data to derive a calibration for the various channels.

As the calibration data representing that 1s frame are built, range tests and auxiliary state data are checked to determine the validity of the frame for inclusion or veto from the

average. All of the range-checks are done at the 16Hz downsampled rate of the process controls data. The calibration then averages those data, to generate the value applied to the entire frame, but the range checking watches all internal samples for validity.

1. The DC-channel voltage of the ASPDs is range-checked. This channel is a proxy for the lock status, its power fluctuating outside of the range at the moment of lock-loss and sitting quiescently at 0 until a lock is acquired and protection shutters are opened.

2. The cavity power in kW is checked to be above the threshold of an acceptable lock.

3. The shot-noise averaged separately in the frequency-bands, 2.25MHz-2.3MHz, 4.3MHz-4.4MHz, and 8MHz-9MHz, are checked against the shot-noise expected from the photocurrent reported at the ASPD-DC channel. If these do not agree in all of the channels to within 20% then the frame is dropped. The 20% requirement is loose, but occasional 10% disagreements do appear and are suspected to stem from wandering ground-offsets rather than a gain variation which could invalidate the calibration.

4. The DAQ system check for any 50MHz sample during the entire 1s section that exceeds a clipping-range. If so, the frame is vetoed. The clipping range is much smaller than the linear range of the photodiode output.

5. If the controls data is missing (e.g. from software malfunction), the frames are vetoed by default.

The most arbitrary of these is the 20% shot-noise agreement requirement. The vetos from this represent very few frames $\ll 1\%$, and the nature of the vetos suggests they caputre a rare underlying phenomenon that may reveal to have a more sensible veto policy. The veto is capture from recognition of the rare anomalously low shotnoise frames where other vetos did not reject the frame.

8.2 Vetos Chosen for data samples in frequency

The vetos for the final dataset across frequency-bins is covered in full detail in the previous chapter, but listed here.

1. The reduced χ^2_2 of significance for noise correlation in the auxiliary cross-spectra for any of the following channels at 3.8kHz resolution.

   (a) $\sqrt{N^{\text{effective}}_{\text{total}}} \cdot \widehat{\text{COH}}\Big[\hat{L}_{\text{aspd}}, \hat{T}_{\text{AM}}; F = u \cdot \Delta F\Big] > 3$

   (b) $\sqrt{N^{\text{effective}}_{\text{total}}} \cdot \widehat{\text{COH}}\Big[\hat{L}_{\text{AM}}, \hat{T}_{\text{aspd}}; F = u \cdot \Delta F\Big] > 3$

   (c) $\sqrt{N^{\text{effective}}_{\text{total}}} \cdot \widehat{\text{COH}}\Big[\hat{L}_{\text{aspd}}, \hat{T}_{\text{PM}}; F = u \cdot \Delta F\Big] > 3$

   (d) $\sqrt{N^{\text{effective}}_{\text{total}}} \cdot \widehat{\text{COH}}\Big[\hat{L}_{\text{PM}}, \hat{T}_{\text{aspd}}; F = u \cdot \Delta F\Big] > 3$

   A value of three in this statistic indicates an excess of at the 95% confidence level for any given frequency-bin. Since this statistic is independent of the science cross spectrum, the occasional bin erroneously vetoed presents only small loss of signal, but no biasing.

2. The projection of the ASPD noise through the Antenna channel is larger than the resolved sensitivity of the science ASPD-cross (suppressing notation to indicate the bin-index):

$$\text{VAR}\Big[\mathfrak{Re}\Big\{\widehat{\text{CSD}}\Big[\hat{L}_{\text{aspd}}, \hat{T}_{\text{aspd}}\Big]\Big\}\Big]^{\frac{1}{2}} < \frac{\Big|\widehat{\text{CSD}}[\hat{L}_{\text{aspd}}, \hat{V}_{\text{ant}}]\Big|}{\widehat{\text{PSD}}[\hat{V}_{\text{ant}}]^{\frac{1}{2}}} \cdot \frac{\Big|\widehat{\text{CSD}}[\hat{V}_{\text{ant}}, \hat{T}_{\text{aspd}}]\Big|}{\widehat{\text{PSD}}[\hat{V}_{\text{ant}}]^{\frac{1}{2}}} \tag{8.1}$$

   The sensitivity of the ASPD cross will actually be derived from a sample-variance statistic, $\hat{V}_u^{\text{shift0}}$ - later defined, rather than the power-spectrum formula. The difference can be collected into the definition of $N_{\text{effective}}$.

   While this veto criterion appears quite different from 1. The expression for the CSD

variance contains power spectra and the veto can be reduced to:

$$\sqrt{N_{\text{total}}^{\text{effective}}} \cdot \widehat{\text{COH}}\left[\hat{L}_{\text{aspd}}, \hat{V}_{\text{ant}}\right] \cdot \widehat{\text{COH}}\left[\hat{T}_{\text{aspd}}, \hat{V}_{\text{ant}}\right] > 1 \tag{8.2}$$

Which is of the same nature as 1, but actually requires a huge significance by comparison because their is only one root-N converting a coherence into a reduced chi-square. That means that the excess from each channel must be order $N^{\frac{1}{4}} \approx 800$ for the 150 hours of data.

3. The frequency must be > 100kHz. This veto is motivated from the seismic and mechanical noise below this cutoff. The noise lowers the coherence with the auxiliary channels such that they will not otherwise trigger a veto. The few additional points that get through indeed show as statistical outliers with significant noise excess. The dataset may actually be integrated without this veto in place and will recover the same test statistic against the model, so these outliers do not bear strong total weighting. They do not influence the model because of the excess variance over shot-noise seen at low frequencies in the budgets. The veto is included because the points skew the histogram used to verify the statistics influencing the final average. The veto, through arbitrary, excludes data that does not influence the average, yet would appear as outlier bins in the histogram.

8.3 Weighting Scheme for time-averaged data and generation of the sample variance

The methods described so far are used to calibrate the data and generate an unbiased cross-correlation of the common (co)varying length signal from two Michelson interferometers. The weighting scheme for the data has been left undefined to this point except when stating the needs of swept transfer-function statistics.

The weighting scheme chosen should never bias the data, only optimize the final significance by most efficiently merging the data gathered for a model-test. It is however possible for weighting schemes derived from the data to apply selection bias and affect the final result. It is also possible that between the Welch-method and lack of perfect stationarity to the noise at the ASPD, that the CSD-variance and covariance formulas derived in chapter 2 and in appendix C may not reflect the non-ideal system. For this reason, sample variance and cross-frequency covariance statistics are evaluated at every frequency bin during the weighted-accumulation of the full CSD, but these statistics are only evaluated for the essential L-to-T common-ASPD cross-spectrum. All of the other measurements rescale their theoretical CSD-statistics derived errorbars by the ratio of the L/T sample-statistics errorbar to its theoretical.

The weighting scheme chosen was to use the inverse of some estimate of the frame's variance for the L/T cross. Inverse-variance weights are the optimal weight to reduce the variance of the final weighted-average statistic when the variance of every sample is known. The method chosen for estimating the variance depends on the timescale of the data being averaged.

The CSD calibration-accumulation pipeline generated averages into calibrated 5-minute accumulations. These were all stored separately. During this generation stage, the weights were estimated from the CSD-variance derived in appendix C from the total reported number of sub-averages, the shotnoise derived from the DC channels and calibrated to length. This method using the shotnoise derived from a sources external to the measurement prevents any bias effects.

The pipeline then takes the 5-minute averages and fully accumulates those into final datasets. During this time, the variance is estimated again using the theoretical formulas, but the PSDs required are taken from the actual dataset rather than from an external channel. This generates a frequency-dependent weighting. It is useful to accumulate with a time-and-

frequency dependent weighting because over the data-taking campaign the alignments and other operating points drifted to couple differing levels of noise into the ASPD channels. This weighting scheme appropriately de-weights those sections and only at the frequencies where a coupling may have become worse. For instance the increase of noise around the tails of the T's 02 mode resonances will be de-weighted when the alignment makes them large. This methodology is not intended to select for reduced background couplings, but at frequencies where AM and PM noise are truly leaking into the noise budget, that is a side-effect.

The averaging ultimately is over time and frequency, but both stages of this pipeline only accumulate in time. The final average over frequency is done separately, but uses the same techniques.

With either scheme of the chosen weightings and calling them $w_{i,u}$, where i is the index in time, and u the index in frequency, The final accumulation over frequency and time for the real channel CSD to be used in the model test may be expressed as the 2D average in both indices, where the CSD expressed here may be one of many 1s frames or one of many 5-minute frames. These formulas actually include additional weightings q_u to express the final frequency-bin weighting for the model-averaging.

$$W_u = \sum_i w_{i,u} \tag{8.3}$$

$$Q = \sum_u q_u \tag{8.4}$$

$$\hat{D}_{i,u} = \mathfrak{Re}\Big\{\widehat{\mathrm{CSD}}[\hat{L}_{\mathrm{aspd}}, \hat{T}_{\mathrm{aspd}}; i, u]\Big\} \tag{8.5}$$

$$\hat{M}_{\mathrm{sci}} = \frac{1}{Q}\sum_u q_u \frac{1}{W_u}\sum_i w_{i,u}\hat{D}_{i,u} \tag{8.6}$$

$$\mathrm{E}[\hat{M}_{\mathrm{sci}}] = \overline{\mathrm{CSD}}[\hat{L}_{\mathrm{aspd}}, \hat{T}_{\mathrm{aspd}}] \tag{8.7}$$

$$\mathrm{VAR}[\hat{M}_{\mathrm{sci}}] = \frac{1}{Q^2}\sum_u\sum_v \frac{q_u q_v}{W_u W_v}\sum_i\sum_j w_{i,u}w_{j,v}\mathrm{COV}[\hat{D}_{i,u}, \hat{D}_{j,v}] \tag{8.8}$$

The expression of eq. (8.8) on page 223 is then used to generate the sample-(co)variance estimators

$$\left(\textsc{Var}[\hat{M}_{\text{sci}}] + \mathrm{E}[\hat{M}_{\text{sci}}]^2\right) = \sum_v \sum_u \frac{q_u q_v}{Q^2} \sum_j \sum_i \frac{w_{i,u} w_{j,v}}{W_u W_v} \left\langle \hat{D}_{i,u} \hat{D}_{j,v} \right\rangle \tag{8.9}$$

for 1s averages with $2 \cdot 384$ welch-frames, the time-overlap

covariance term containing (at most) .2% of the total variance is dropped

$$= \sum_v \sum_u \frac{q_u q_v}{Q^2} \sum_i \frac{w_{i,u} w_{i,v}}{W_u W_v} \left\langle \hat{D}_{i,u} \hat{D}_{i,v} \right\rangle \tag{8.10}$$

bin shifts > 5 dropped as well, small contribution for hanning window

$$= \sum_u \left(\frac{q_u^2}{Q^2} \underbrace{\sum_i \frac{w_{i,u}^2}{W_u^2} \left\langle \hat{D}_{i,u} \hat{D}_{i,u} \right\rangle}_{=\hat{V}_u^{\text{shift},0}} + 2 \frac{q_u q_{u+1}}{Q^2} \underbrace{\sum_i \frac{w_{i,u} w_{i,u+1}}{W_u W_{u+1}} \left\langle \hat{D}_{i,u} \hat{D}_{i,u+1} \right\rangle}_{=\hat{V}_u^{\text{shift},1}} \dots \right) \tag{8.11}$$

These $\hat{V}_u^{\text{shift}}$ statistics are collected during the running summations of the pipeline averaging and recorded, normalized by W_{total}^2. They are then propagated through the changing weight-scheme and recorded, of course being constructed with the brackets removed using sums of the data samples. During rebinning to 3.8kHz the $\sum_u$ is partially evaluated and the shift-terms can be recollected into a single shift-0 term (expressing the lack of bin-bin covariance at that resolution). Finally, the shift-0 variance estimators are used for the error-bars of the final data collection. The distribution of bins in the final dataset, normalized by the square-root of the sample-variances, is shown in fig. 8.1 on the next page

The actual statistic motivated by eq. (8.11) are contained below. These represent *almost* the sample variances. The difference is that the mean is not subtracted from the values before the squaring or multiplication. This actually violates the earlier assumption that the time-separated bins had a small, limited 2-point correlation. Containing a mean will actually provide correlation and dropping the terms anyway is equivalent to an *partial* subtraction of the mean. The equal-time two point correlation still contains the mean term. This has

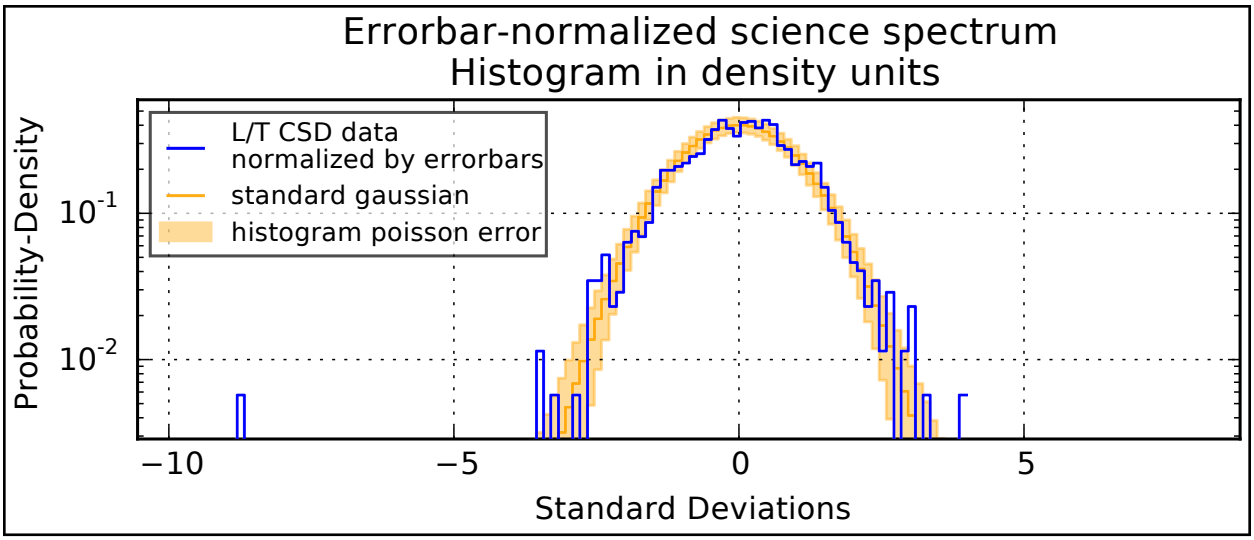

Figure 8.1: Histogram of the frequency bins of the final time-averaged dataset, vetos excluded, up to 6MHz. Around 1000 bins represented, the Poisson-statistics for the histogram-counts fails to exclude the sample-variance error model of the dataset (with the exception of a single outlier).

the effect of slightly biasing these sample-variance terms by a reduced mean. The structure of the statistics and expression of their expected value is contained below to express these concerns.

$$\hat{V}_u^{\text{shift,0}} = \sum_i \frac{w_{i,u}^2}{W_u^2} \left(\hat{D}_{i,u} \hat{D}_{i,u} \right) \tag{8.12}$$

$$\hat{V}_u^{\text{shift,v}} = \sum_i \frac{w_{i,u} w_{i,u+\text{v}}}{W_u W_{u+\text{v}}} \left(\hat{D}_{i,u} \hat{D}_{i,u+\text{v}} \right) \tag{8.13}$$

$$N_u^{\text{effective}} = \frac{\left(\sum_i w_{i,u} \right)^2}{\sum_i w_{i,u}^2} \tag{8.14}$$

$$N_{\text{total}}^{\text{effective}} = \frac{\left(\sum_u q_u \sum_i w_{i,u} \right)^2}{\sum_u q_u^2 \sum_i w_{i,u}^2} \tag{8.15}$$

Now the expression of eq. (8.11) on page 224 for the variance of $\textsc{Var}[\hat{M}_{\text{sci}}]$ can be related to the expectation of these sample statistics.

$$\mathrm{E}\left[\frac{1}{Q^2}\sum_u\left(\frac{q_u^2}{\xi_u^2}\hat{V}_u^{\text{shift},0}+2\frac{q_u q_{u+1}}{\xi_u\xi_{u+1}}\hat{V}_u^{\text{shift},1}\ldots\right)\right]=\textsc{Var}[\hat{M}_{\text{sci}}]+\frac{\mathrm{E}[\hat{M}_{\text{sci}}]^2}{N_{\text{total}}^{\text{effective}}} \tag{8.16}$$

And the biasing term from the mean is ignored for this analysis as

$$N_{\text{total}}^{\text{effective}}\approx 150\text{hours}\cdot 700\text{kHz}\approx 400{\cdot}10^9 \tag{8.17}$$

8.4 The Model-Test Statistic

Section 2.12.2 on page 62 explains in more detail the full expression of the model test performed. The exact computation used follows, using instead of the generic CSD from the Michelson chapter, the data in the DAQ system is expressed as a one-sided power-spectral density. The model expressed also in the one-sided PSD from section 1.4 on page 17 is used.

From the data, $\hat{D}_u$ and model, $\Xi_\delta^{(+)}(F)$, resolved in frequency, the model-normalized-data statistic is generated.

$$\hat{D}_u=\mathfrak{Re}\left\{\widehat{\text{CSD}}\left[\hat{L}_{\text{aspd}},\hat{T}_{\text{aspd}};F=u\cdot\Delta F\right]\right\} \tag{8.18}$$

$$\xi_u=\Xi_\delta^{(+)}(u\cdot\Delta F) \tag{8.19}$$

$$\hat{\Theta}_u=\frac{\hat{D}_u}{\xi_u} \tag{8.20}$$

Now the statistic $\hat{\Theta}$ expresses the unitless quantity for "amount of model present in signal". A value 1 indicates that the model is present, but the model must be present in all bins for this to be the case. A (statistically) significant detection in one bin could be ruled out with a significant exclusion in another, with the explanation being that a different, unknown, narrowband noise must be present. In practice, no single bin has the ability to

make significant statements about the presence of Holographic-noise. Instead, the data from all bins is averaged through the frequency-bins to generate a more informative statistic.

$$\hat{\Theta}_{\text{avg}} = \frac{\sum_u q_u \hat{\Theta}_u}{\sum_u q_u} \tag{8.21}$$

$$q_u = \frac{\xi_u^2}{\hat{V}_u^{\text{shift},0}} \approx \frac{1}{\text{VAR}\left[\hat{\Theta}_u\right]} \tag{8.22}$$

Finally the variance of this statistic may be *bounded*, using the q_u factors in eq. (8.11) on page 224. The sample statistic generated will only bound the variance because the approximations made to generate the factors V^{shift} actually do not allow them to be exactly used like the sample variance, because the mean is not subtracted from the data points. The assumption made earlier that the data points did not correlate to drop the frame-frame 2-point term actually also implicitly assumes that the mean is zero. For this reason, the variance estimate will *always* be larger than the true variance. This is OK for the model-test, where the confidence-intervals will be weakened by the approximation.

The only modification to eq. (8.11) on page 224 is from the division by the model.

$$\text{VAR}\left[\hat{\Theta}_{\text{avg}}\right] = \frac{1}{Q^2} \sum_u \left(\frac{q_u^2}{\xi_u^2} \hat{V}_u^{\text{shift},0} + 2\frac{q_u q_{u+1}}{\xi_u \xi_{u+1}} \hat{V}_u^{\text{shift},1} + 2\frac{q_u q_{u+2}}{\xi_u \xi_{u+2}} \hat{V}_u^{\text{shift},2} \dots \right) \tag{8.23}$$

$$= \frac{1}{Q^2} \sum_u \left(\frac{\xi_u^2}{\hat{V}_u^{\text{shift},0}} + 2\frac{\xi_u \xi_{u+1} \hat{V}_u^{\text{shift},1}}{\hat{V}_u^{\text{shift},0} \hat{V}_{u+1}^{\text{shift},0}} + 2\frac{\xi_u \xi_{u+2} \hat{V}_u^{\text{shift},2}}{\hat{V}_u^{\text{shift},0} \hat{V}_{u+1}^{\text{shift},0}} \dots \right) \tag{8.24}$$

The final sum for both the average and variance are later plotted, accumulating the summation upwards to the final statistic. The incremental accumulation shows the random walk of the sample mean to its final value. The excursions of the accumulated show any narrowband spurious correlation features significantly moving the average via sharp turns to the random walk. None are seen in this dataset, but the same analysis applied to the background channels shows some narrowband features within their sensitivity, but not enough to affect the science result.

8.5 Calibration Systematics Budget

With the background correlations and statistics accounted, the final additional error budget accounts for calibration systematics to relate the signals of the interferometer to the tested noise model. The deep analysis of this data is primarily in chapters 4 and 5.

Michelson Reference The Michelson references of section 4.4 on page 98 show at most a 2% deviation over a month of taking measurements. They are further corroborated with the PR Michelson model fits introduced in section 4.5 on page 103 which also have sensitivity to that calibration.

Calibration Line Purity section 4.6 on page 107 details that the conversion fraction for the longitudinal drive into angular modes is limited to 5%. These further need large misalignment to provide the DC angular mode to beat with to produce a signal degenerate with the fundamental modes. The consistency of the Michelson measurements suggest the 5% is a strong limit, and for the vast majority of the operation, the misalignment was managed both by control systems and a Human operator, so these affects should be limited to 2% at any moment, but varying depending on the misalignement mode shape.

Vertex AC transimpedance The strong agreement between the reference calibration and the many shotnoise calibrations indicated by fig. 5.10 on page 144 suggest that the shotnoise calibrations hold to 2% within the 5 MHz frequency band of interest.

Vertex DC transimpedance The analysis of section 5.8 on page 133 indicates that there are some 5% systematics in this factor, but using the nominal schematic value for this analysis errs conservative.

Data Quality Analysis done during the writing of this thesis shows that the majority of the data show consistent magnitudes for the thermal lines discussed in section 6.12 on

page 199, but there are some short sections (<5% of the dataset) where it appears to fluctuate $\sim 10\%$ with a currently uncharacterized reason. These may be modal effects interfering with the couplings of the thermal resonances and only an artifact of the cross-checking method.

Exact Geometry The exact length of the interferometers is derived from the Free-Spectral-Range frequencies shown in fig. 6.5 on page 179, which is 39.06 m. Furthermore, the two machines do not perfectly overlap, with a diagonal separation of $25\text{in} \times 25\text{in} \times 6\text{in}$, with the final distance a vertical separation. This corresponds to 0.91 m of separation. The nominal 40m model uses the 39.06 m length affecting the magnitude and frequency response, the model accounts for the separation by reducing the power-spectrum response by an additional factor $\left(1 - \frac{0.91\text{m}}{39.06\text{m}}\right)$. Together, these geometries reduces the model amplitude by 5%, but are accounted in the data that follows.

All accounted, the quadrature sum of these systematic uncertainties is dominated by the data quality checks and the Vertex PD DC transimpedance. A flat uncertainty of 10% is taken to weaken the result through a calibration-scaling error.

8.6 Final Result - A Hypothesis test for Hogan noise between co-located Interferometers

Figure 8.2 on the next page Shows the actual phase sensitive data ready to be integrated. The scale of the errorbars is dependent on the frequency bandwidth, but trades-off with resolution for the vetos. The final integrated dataset is instead shown using a cumulative average to allow all scales of rebinning to be shown. Figure 8.3 on page 231 represents the final dataset, fully calibrated, weighted and accumulated. The real-part of the cross-spectral-density between the two interferometers is normalized by the expected cross-spectrum of the Hogan prediction and the average is accumulated upwards through the frequency-bins. The

endpoint of the accumulation at the right of the plot signifies the separation of the data from the model, normalized to one. The final significance is a 6σ exclusion of the nominal prediction, and the Null-hypothesis is not excluded by the $< 1\sigma$ separation of the data from the Null-amplitude model.

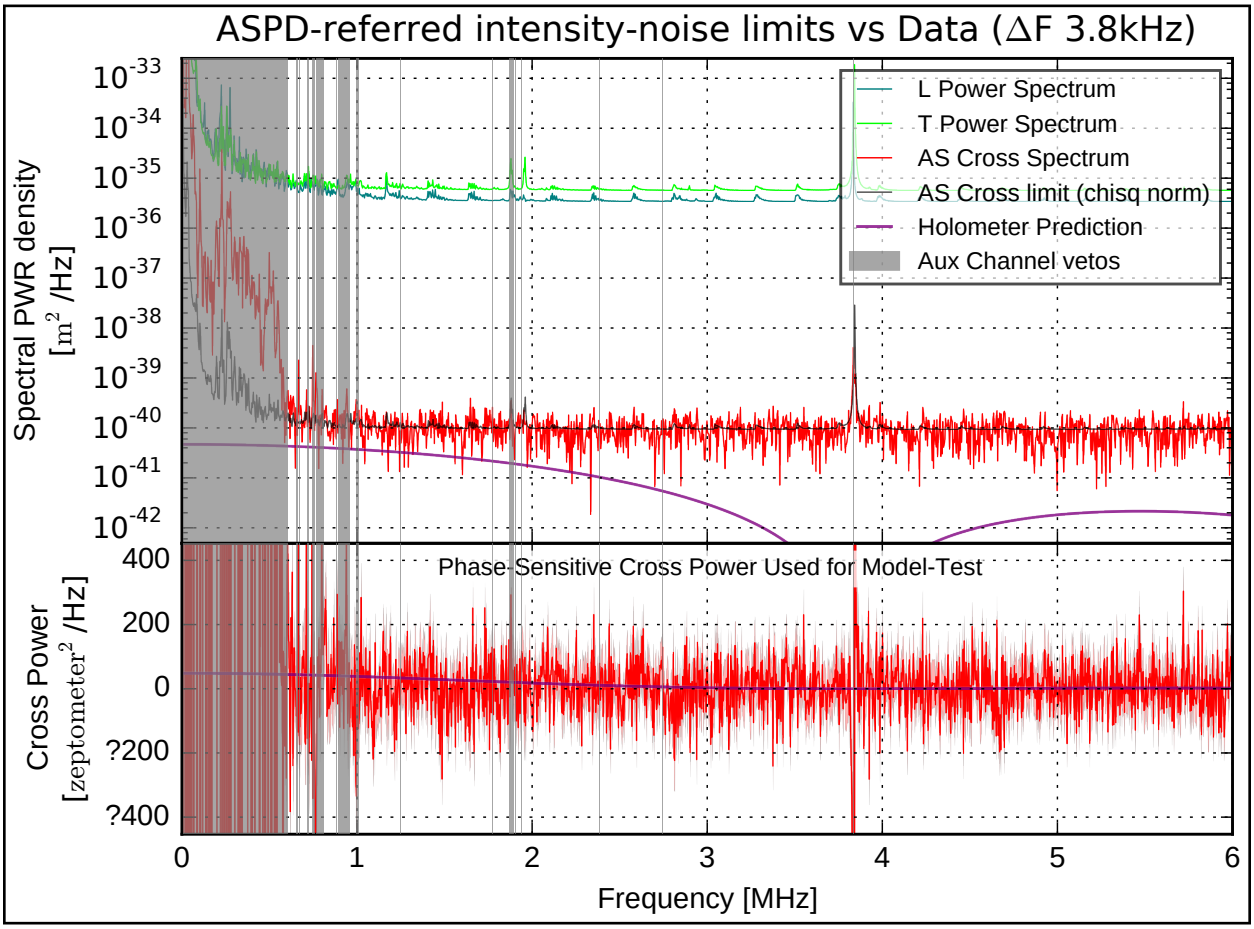

Figure 8.2: The two interferometer cross-spectrum used for the model test. The frequency resolution is just high enough for the bin-bin covariance to be small. The model is shown but without further averaging is not tested in this projection of the data. The model tests is most naturally expressed in power-specral density units, unlike the linear-spectral densities used for the budgetting plots.

The errorbars are accumulated appropriately with the data to show the growing exclusion between the data-average in sharp red vs. the model-cumulative power in purple as the data is integrated. The apparent random walk of the data is consistent with *no* signifi-

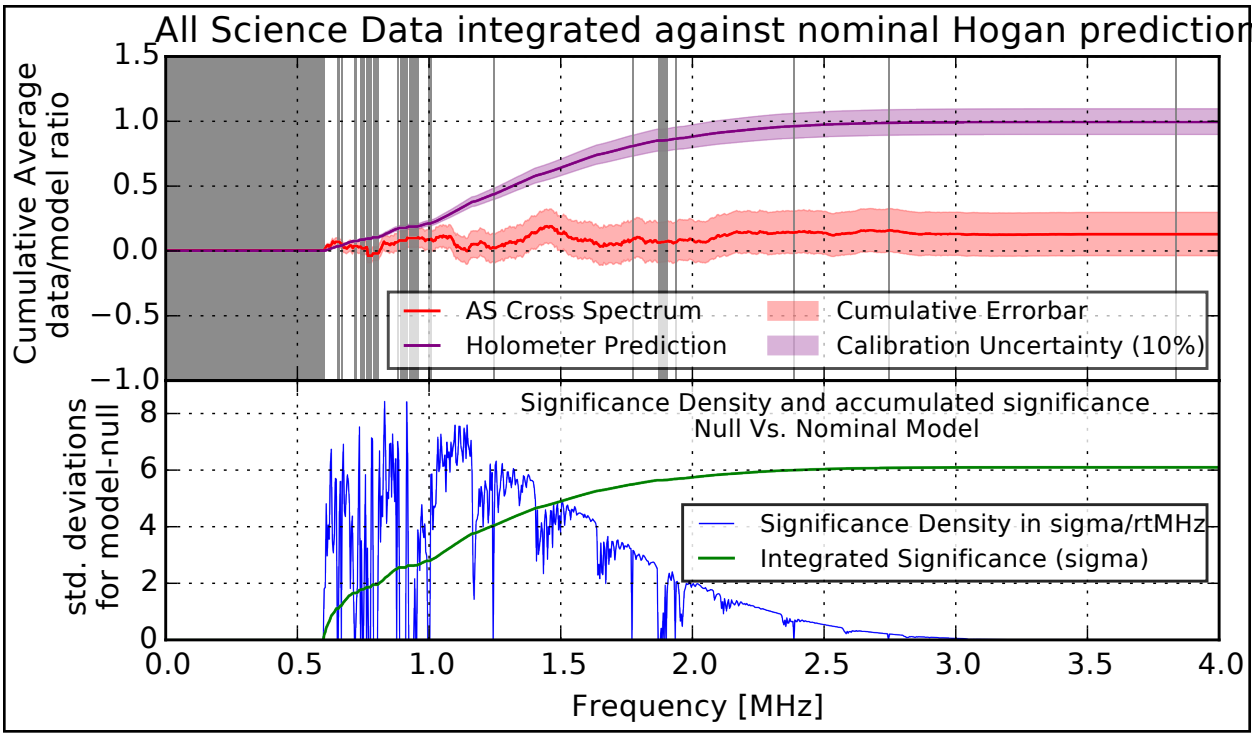

Figure 8.3: The final time-averaged cross-spectral-density for apparent length fluctuation common to two co-located Michelson Interferometers. The independent data in each frequency-bin is averaged, with the cumulative average plotted. This indicates a random-walk of the model-normalized statistic to the final value on the right. The data separates 6.1σ from the model to be consistent with the Null-hypothesis (within 1σ of 0). The lower plot indicates the relative weight of the data to the final result, determining the errorbars. Data vetos are shown in grey. The exact separations are: 6.108σ between the nominal model and Null, 5.27σ between the model and data sample mean, and 4.75σ between the lower 10% systematics uncertainty on the model and the data sample mean.

cant narrowband sources and the display of the cumulative average indicates that arbitrary subsections of the data would reach the same conclusion with less final significance.

The lower plot of fig. 8.3 indicates the data quality in a comparison to the theoretical predictions of sensitivity analyzed in section 2.12.2 on page 62. In blue, the SNR-density of the data is plotted and green represents the sum-in-quadrature for the total SNR incrementing with the average. The shape of the blue reflects a number of features. Up to 1MHz the shape reflects a forest of bin-vetos along the criteria enumerated in section 8.2 on page 220. Above 1MHz the abundance of vetos diminishes and the shape is determined by two major

feature. 1: the spectral-shape of the model vs. shotnoise determines the envelope. This is the sinc-function model power-spectrum to the fourth-power generating the weightings q_u of section 8.4 on page 226. 2: the "dip" features are the shotnoise-excess from the mirror-etalon resonances displayed in section 6.12 on page 199.

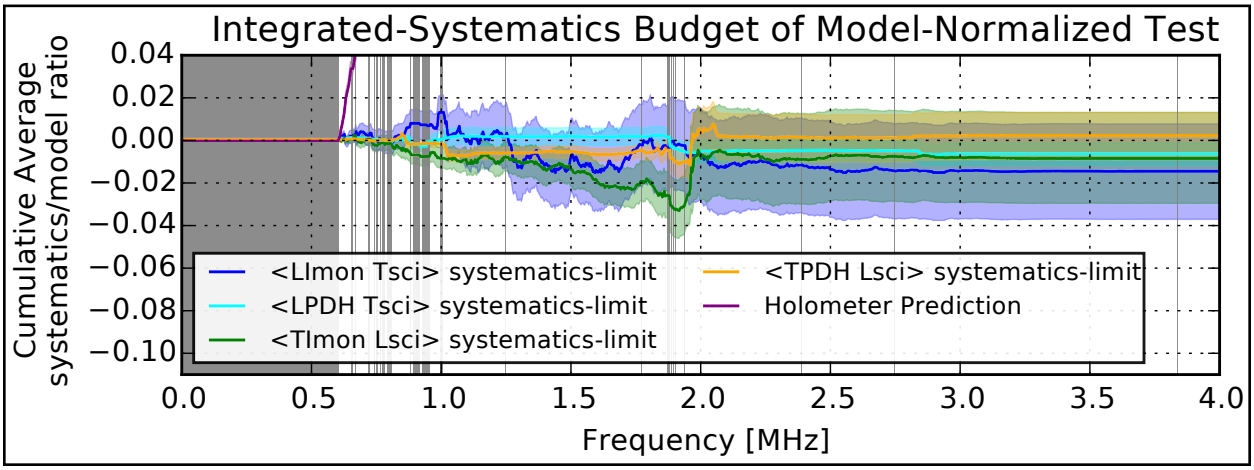

Figure 8.4: The data analysis for the 2x interferometer cross-spectral-densities applied to the 4 length-referred auxiliary-channel cross-limits. The random-walk of the accumulated data displays statistically-significant narrowband influences on the data-signal. Although significant detections of background, the amplitudes indicate a minimal influence of these backgrounds in the test of the Hogan-noise model.

The same data analysis can be applied to the auxiliary channels, where the weightings used for the auxiliary-background tests are the same as for the real dataset. This projects each of the auxiliary channels into the same statistic to find the contribution to $\hat{\Theta}_u$ that is due to each of AM and PM of either interferometer. The analysis relating the contribution of this statistic of potential broadband background noise is detailed in section 7.1 on page 202. The plots in the remainder of that chapter show budgets of the resolved-noise from those channels. Figure 8.4 projects those background limits into the model-space of fig. 8.3 on page 231.

The sharp motions in the data indicate that there is some residual pickup of the external channels, but that pickup accounts for at most 1% of the model-amplitude. If systematic

backgrounds had any larger influence on the data than the 1% errorbars, then they would be resolved through these tests. In-total, the nominal Hogan noise model has been excluded to 5σ without any possible influence from broadband external background noise conspiring to cancel the appearance of the predicted signal.

Appendix A

DERIVATIONS BY CHAPTER

A.1 Timeseries analysis of the Michelson Interferometer

A.1.1 On the mathimatics of phasor, port-parameter and physical representations

The distinction between optical (scattering-port) amplitudes and phasors is subtle, yet important to avoid confusion especially when beginning to work with quantized light. Both representations are used for calculational convenience, but neither perfectly maps to the Maxwell equations describing light. Maxwell's equations are a set of linear partial-differential equations which can evolve/calculate initial-data of field sources into future-data useful to predict measurements. The equations, being linear, allow the final system to be described as a superposition of initial sources each acted on by a linear-operator representing the evolution by the PDE's. These linear operators can always be represented by a convolution with a Greens-function kernel determined by the equations and boundary conditions.

This representation is complete, yet still very cumbersome for laser-systems where the light-paths are all lines and reflections. A compact representation without vector-fields and boundaries can more concisely describe the series of paths and forks paraxial beams follow through optics. The port and phasor representations both attempt to simplify calculations by packaging the real initial data into a complex form and then having the free-space Greens-function merely become phase-shifts and translation operators (delta functions). The initial data of the Maxwell's equations must ultimately package the electric-field, magnetic-field and their respective time-derivatives.

Phasors keep both Electric and Magnetic fields and in physical units, but package the first-derivatives into the complex term. This is why the imaginary part must be projected away

- time-evolution is not by-itself an observable. They can be further simplified to represent the fields along lines by carrying only $\vec{E}$ and $\vec{H}$ in directions transverse to propagation. A selection of formulas allows one to project the phasors into polarizations and foreward/reverse propagating waves. These projection formulas rely on all 4 components of the initial-data, so use the full complex description of the two 2-vector fields to convert into 4 complex-modes.

Port-amplitudes are direct representations of the 4 separate modes useful in the lab. The are also complex like the field-phasors, but represent the beam specfically by propagation-direction and polarization. This maintains the convenience of the Greens-functions having the form of phase-shifts and translations, while using a basis in measurable/actuatable quantities. The units are root-Watts as mentioned above which makes power-detection easy to calculate. port-amplitude parameters are convertable back into phasors and consequently physical units with the specification of the characteristic speed $(n * c)$ and the characteristic impedance Z_0. Equivalently the permittivity and permiability of the propagating space allow the conversion.

$$Z_0 = \sqrt{\frac{\mu_0}{\epsilon_0}} = \frac{1}{c\epsilon_0} \tag{A.1}$$

$$c = \frac{1}{\sqrt{\epsilon_0 \mu_0}} \tag{A.2}$$

Port-amplitudes are equivalent to the scattering parameters description of RF dbm amplitudes along transmission-lines/cables. The RF-cables description has fewer modes (generally no polarization in coaxial cables), but does have foreward/reverse propagation. The RF cable description also operates typically at 50Ω impedance rather than the impedance of free-space 376.7Ω.

The port-amplitudes for a set of modes in an electrical system are:

$$\vec{A}_{\text{foreward}} = \frac{1}{2}\mathbf{k}(\vec{V} + \mathbf{Z_p}\vec{I}) \tag{A.3}$$

$$\vec{A}_{\text{reverse}} = \frac{1}{2}\mathbf{k}(\vec{V} - \mathbf{Z_p}\vec{I}) \tag{A.4}$$

where $\mathbf{Z_p}$ is the diagonal matrix of port impedances and

$$\mathbf{k} = \mathfrak{Re}\{\mathbf{Z_p}\}^{-\frac{1}{2}} \tag{A.5}$$

Is the impedance-scale converting to root-watts.

For optical plane-waves where the assumed direction of propagation is in positive-Z, the magnetic field is related to the electric field

$$H_y = E_x/Z_0 \tag{A.6}$$

$$H_x = -E_y/Z_0 \tag{A.7}$$

So only the complex-phasors of the Electric-field are needed. This is the Jones' vector, and it is a kind of phasor description, however the assumed direction of propagation allows it to be conflated up-to units (electric-field vs. root-Watts) to equivalently be optical field-amplitude parameters. The full conversion is analogous to the electrical case.

$$A_{\text{x,z-foreward}} = \frac{1}{2}k(E_x + Z_0 H_y) \tag{A.8}$$

$$A_{\text{x,z-reverse}} = \frac{1}{2}k(E_x - Z_0 H_y) \tag{A.9}$$

$$A_{\text{y,z-foreward}} = \frac{1}{2}k(E_y - Z_0 H_x) \tag{A.10}$$

$$A_{\text{y,z-reverse}} = \frac{1}{2}k(E_y + Z_0 H_x) \tag{A.11}$$

Why is this pedantic distinction necessary? Classically there isn't a huge distinction, although tradionally the Jones vectors are not separated to be used as individual modes in a much larger interacting. They are used in systems intercoupling polarizations with wave-plates more than systems with beamsplitters, bifurcated and recombined optical paths. The port-amplitude notation and its units is traditionally seen in multi-path scattering networks,

signal-flow-graphs and resonant (frequency-dependant) systems. Labeling the polarization and propagation modes separately gives a larger freedom to generate signal-flow graphs.

With quantized light the picture is more in favor of the port-amplitude picture. The quantized states can be collected into the physical-representation $\vec{E}$ and $\vec{H}$ field operators. Phasors become confusing because the particle states carry around their own phase signatures and phasors can only describe single-particles. port-amplitudes however correspond exactly to coherent states of the quantized modes.

Setting up the system equations takes a particular form for Laser physics. The problems do not start with the optical fields specified but rather where the coherent lights sources are located and the direction that they emit. The port-amplitude or scattering matrix formulation provides a prescription for setting up the steady-state fields using matrix techniques. One of the particular conveniences of the representation is that foreward and reverse propagating modes have the *same* value for lasers traversing a distance L. This property is not shared for the phasor and physical representations in physical units except with carefully-defined sign-conventions in Jones vectors and Jones' matrices. The port-amplitude representation carries these sign-conventions with it.

For two systems described by having a field source, one at z_1 emitting in the foreward direction to z_2 and the other in the reverse direction z_2 to z_1. The fields are described by $A_{\text{foreward}}(z_1 + L) = A_{\text{emitted}} e^{-2\pi \mathrm{i} F \frac{L}{c}}$ and $A_{\text{reverse}}(z_2 - L) = A_{\text{emitted}} e^{-2\pi \mathrm{i} F \frac{L}{c}}$. These representations indicate that the field at all points along the ray is related to the field at the emission point by a linear relation. Furthermore, since the beam is propagating and each point with incoming beam appears in the steady-state to also be an emitter, these linear relations can be chained together. This allows a particularly clean representation of mirrors in terms of signal-flow diagrams.

A.1.2 Frequency-dependence of the Michelson Transfer function

$$A_{\mathrm{AS}}(t) = \frac{1}{2}e^{4\pi \mathrm{i}F\frac{L_C}{c}}\left(e^{2\pi \mathrm{i}F\frac{L_D}{c}} - e^{-2\pi \mathrm{i}F\frac{L_D}{c}}\right)A_{\mathrm{in}}e^{2\pi \mathrm{i}Ft} \tag{A.12}$$
$$+ \frac{\mathrm{i}2\pi FL_\delta}{4c}e^{2\pi \mathrm{i}(2F+F_{\mathrm{mod}})\frac{L_C}{c}}\left(e^{2\pi \mathrm{i}(2F+F_{\mathrm{mod}})\frac{L_D}{c}} + e^{-2\pi \mathrm{i}(2F+F_{\mathrm{mod}})\frac{L_D}{c}}\right)A_{\mathrm{in}}e^{2\pi \mathrm{i}(F+F_{\mathrm{mod}})t}$$
$$+ \frac{\mathrm{i}2\pi FL_\delta}{4c}e^{2\pi \mathrm{i}(2F-F_{\mathrm{mod}})\frac{L_C}{c}}\left(e^{2\pi \mathrm{i}(2F-F_{\mathrm{mod}})\frac{L_D}{c}} + e^{-2\pi \mathrm{i}(2F-F_{\mathrm{mod}})\frac{L_D}{c}}\right)A_{\mathrm{in}}e^{2\pi \mathrm{i}(F-F_{\mathrm{mod}})t}$$

$$= \mathrm{i}A_{\mathrm{in}}e^{4\pi \mathrm{i}F\left(\frac{L_C}{c}+t\right)}\left(\begin{array}{l} -\sin\left(2\pi F\frac{L_D}{c}\right) \\ \quad + \frac{2\pi FL_\delta}{2c}e^{+2\pi \mathrm{i}F_{\mathrm{mod}}(\frac{L_C}{c}+t)}\cos\left(2\pi(2F+F_{\mathrm{mod}})\frac{L_D}{c}\right) \\ \quad + \frac{2\pi FL_\delta}{2c}e^{-2\pi \mathrm{i}F_{\mathrm{mod}}(\frac{L_C}{c}+t)}\cos\left(2\pi(2F-F_{\mathrm{mod}})\frac{L_D}{c}\right)\end{array}\right) \tag{A.13}$$

$$= \mathrm{i}A_{\mathrm{in}}e^{4\pi \mathrm{i}F\left(\frac{L_C}{c}+t\right)}\left(\begin{array}{l} -\sin\left(2\pi F\frac{L_D}{c}\right) \\ \quad + \frac{2\pi FL_\delta}{2c}e^{+2\pi \mathrm{i}F_{\mathrm{mod}}(\frac{L_C}{c}+t)}\cos\left(2\pi F\frac{L_D}{c}\right)\cos\left(+2\pi F_{\mathrm{mod}}\frac{L_D}{c}\right) \\ \quad - \frac{2\pi FL_\delta}{2c}e^{+2\pi \mathrm{i}F_{\mathrm{mod}}(\frac{L_C}{c}+t)}\sin\left(2\pi F\frac{L_D}{c}\right)\sin\left(+2\pi F_{\mathrm{mod}}\frac{L_D}{c}\right) \\ \quad + \frac{2\pi FL_\delta}{2c}e^{-2\pi \mathrm{i}F_{\mathrm{mod}}(\frac{L_C}{c}+t)}\cos\left(2\pi F\frac{L_D}{c}\right)\cos\left(-2\pi F_{\mathrm{mod}}\frac{L_D}{c}\right) \\ \quad - \frac{2\pi FL_\delta}{2c}e^{-2\pi \mathrm{i}F_{\mathrm{mod}}(\frac{L_C}{c}+t)}\sin\left(2\pi F\frac{L_D}{c}\right)\sin\left(-2\pi F_{\mathrm{mod}}\frac{L_D}{c}\right)\end{array}\right) \tag{A.14}$$

$$P_{\mathrm{AS}}(t) = |A_{\mathrm{AS}}|^2 \tag{A.15}$$

$$\approx P_{\mathrm{in}}\sin\left(2\pi F\frac{L_D}{c}\right)\left(\begin{array}{l} \sin\left(2\pi F\frac{L_D}{c}\right) \\ \quad - \frac{2\pi FL_\delta}{2c}e^{-2\pi \mathrm{i}F_{\mathrm{mod}}(\frac{L_C}{c}+t)}\cos\left(2\pi(2F+F_{\mathrm{mod}})\frac{L_D}{c}\right) \\ \quad - \frac{2\pi FL_\delta}{2c}e^{+2\pi \mathrm{i}F_{\mathrm{mod}}(\frac{L_C}{c}+t)}\cos\left(2\pi(2F-F_{\mathrm{mod}})\frac{L_D}{c}\right) \\ \quad - \frac{2\pi FL_\delta}{2c}e^{+2\pi \mathrm{i}F_{\mathrm{mod}}(\frac{L_C}{c}+t)}\cos\left(2\pi(2F+F_{\mathrm{mod}})\frac{L_D}{c}\right) \\ \quad - \frac{2\pi FL_\delta}{2c}e^{-2\pi \mathrm{i}F_{\mathrm{mod}}(\frac{L_C}{c}+t)}\cos\left(2\pi(2F-F_{\mathrm{mod}})\frac{L_D}{c}\right)\end{array}\right) \tag{A.16}$$

$$\approx P_{\mathrm{in}}\sin\left(2\pi F\frac{L_D}{c}\right)\left(\begin{array}{l} \sin\left(2\pi F\frac{L_D}{c}\right) \\ \quad - \frac{2\pi FL_\delta}{c}\cos(2\pi F_{\mathrm{mod}}(\frac{L_C}{c}+t))\cos\left(2\pi(2F+F_{\mathrm{mod}})\frac{L_D}{c}\right) \\ \quad - \frac{2\pi FL_\delta}{c}\cos(2\pi F_{\mathrm{mod}}(\frac{L_C}{c}+t))\cos\left(2\pi(2F-F_{\mathrm{mod}})\frac{L_D}{c}\right)\end{array}\right) \tag{A.17}$$

$$P_{\mathrm{AS}}(t) \approx P_{\mathrm{in}} \sin\left(2\pi F \tfrac{L_D}{c}\right) \left(\begin{array}{l} \sin\left(2\pi F \tfrac{L_D}{c}\right) \\ \quad - \cos\left(2\pi F \tfrac{L_D}{c}\right) \cos\left(2\pi F_{\mathrm{mod}} \tfrac{L_D}{c}\right) \dfrac{4\pi F L_\delta}{c} \cos\left(2\pi F_{\mathrm{mod}} (\tfrac{L_C}{c} + t)\right) \end{array} \right) \tag{A.18}$$

Appendix B

BRIEF OVERVIEW OF CROSS-SPECTRUM ESTIMATES, LOCK-IN, AND SIGNAL FLOW

The interferometer as an optical system can be described accurately using linear techniques, as long as appropriate linearization approximations are made at square-law detectors and hold true during operation. Similarly, the control system may also be described by linear systems of equations. As a practical matter, these systems often must be approximated heavily to reduce the number of terms and defined variables which must referenced.

Signal flow graphs provide a very convenient means of visually describing and labeling linear systems. Furthermore, they provide a consistent means of viewing the optical resonance as a feedback system just as the control system is. There are two pictures to view the technique in. Usually the simplified picture is sufficient, but when the system becomes confusing, lifting the view into the rigorous can resolve ambiguities or help demonstrate that approximations are appropriate.

Simplified Picture - The Signal flow graphs shown will almost always be in a frequency-basis. Put another way, every state in the system state space is a node on the signal flow and is referenced by a given frequency. The edge-weights are complex scattering amplitudes between these nodes, and the scattering amplitudes are often functions of the frequency of the connected nodes. Connected nodes usually reference the same frequency, but as seen for the Michelson, electrical or optical intermodulation can bridge nodes of different frequency.

Rigorous Picture - every node x on the space is some kind of Quantum ($\check{x}$) or Statistical ($\hat{x}$) variable and every node-coupling is a linear operator in the functional space of the two variables. A single graph can be representative of the system *at all frequencies* but the computations necessary are less straightforward. For systems with stationary noise and no modulation, these linear operators are diagonal in the frequency-basis. This provides the picture that the variables are *implicitly* indexed by frequency and the couplings are

as well. The ability to reference frequencies implicitly breaks down for intermodulation. Intermodulation provides off-diagonal terms in the frequency basis, requiring nodes to be *explicitly* labelled by frequency and approximations to be made to truncate infinite series' to nodes of large frequency.

B.1 Lock-in via the Cross-Spectral-Density Estimator

Flow Graphs in this document is for more mundane bookkeeping of calibration constants. The graphical method allows many terms from the experimental setup to be included without requiring an abundance of new variables. The spectral-estimators $\widehat{\text{CSD}}[\cdot,\cdot;F]$ developed in Chapter (2) on the Michelson-statistics provides both a mathematical concept and implementation for selecting measurements from the graphs. The CSD provides estimates of the two-point correlation functions in the Frequency domain. These functions serve a dual purpose. They lock-in to excitation sources to select subgraphs between fewer points. The reduction to subgraphs then simplifies calculations and eliminates extraneous terms. Such subgraph-elimination is done all the time implicitly by physicists, but the CSD provides a canonical measurement associated with the process.

Measurements then are the second purpose. Depending on the graph of the system, most edges can be made using two-point correlation functions amongst either two or three timeseries-nodes on the graph. Figure B.1 on the next page illustrates. The series of edges relating $\hat{x}$ to $\hat{y}$ is measured with just one CSD with the noise falling out of the average, then normalized with the PSD of the source excitation. Note that this is akin to the lock-in measurement to the Michelson except the normalization is not in the amplitude of $\hat{x}$ projected into $\hat{y}$, but relative amplitude between the two. Later in this chapter the measurement

statistics will be considered in an ad-hoc model of superimposed noise.

$$\overline{\mathrm{CSD}}[\hat{y},\hat{x};F] = A(F)\cdot B(F)\cdot C(F)\cdot D(F)\overline{\mathrm{CSD}}\left[\left(\hat{x}+\frac{\hat{N}_A}{A(F)}+\cdots\right),\hat{x};F\right] \tag{B.1}$$

$$= ABCD\overline{\mathrm{PSD}}[\hat{x}] \qquad \text{(with F dependence implicit)} \tag{B.2}$$

The noise terms as represented are incoherent with the $\hat{x}$ timeseries, so the CSD cuts them out of the graph, leaving only the remaining edges. Those are collected and returned by the estimator.

The linear nature of this graph turns out to make measurements convenient in spite of the noise. If $\hat{z}$ is also recorded, the CD coupling can also be measured. The derivation of the following requires expanding out all of the noise terms, but the assumption that they are incoherent drops cross terms and the linearity of the CSD/PSD in both arguments allows all of the precursor sources to be collected back into the $\widehat{\mathrm{PSD}}[\hat{z}]$ term.

$$\overline{\mathrm{CSD}}[\hat{y},\hat{z}] = CD\overline{\mathrm{PSD}}[\hat{z}] \tag{B.3}$$

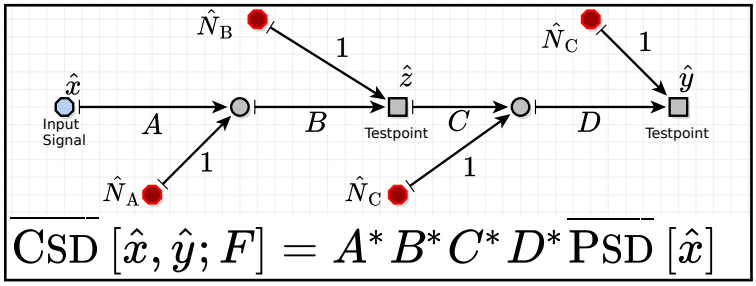

Figure B.1: Signal-flow between measured timeseries $\hat{x}$, $\hat{y}$, and potentially-measured $\hat{z}$. Across points in the system superimposed noise is added. The CSD cuts out the superimposed noise under the assumption that independent sources are uncorrelated - i.e. all correlation-creating couplings are either indicated on the graph or purposefully excluded in approximation.

B.2 Transfer functions to determine Coupling Constants

Typical graphs do not look nearly so linear as Figure B.1 on page 242, but the measurement described by eq. (B.3) on page 242 is actually only one of two ways to measure that transfer function. The second method requires locking both signals into $\hat{x}$ to form the relation

$$\frac{\overline{\mathrm{CSD}}[\hat{y},\hat{x}]}{\overline{\mathrm{CSD}}[\hat{z},\hat{x}]} = \frac{ABCD}{AB} = CD \tag{B.4}$$

This 3-point transfer function is what appears on most spectrum-analyzers, which provide a source, $\hat{x}$ and two measurement channels akin to $\hat{y}$ and $\hat{z}$. While the linear topology measures direct-transfer, the 3-point transfer estimate more generally measures *relative* transfer to the common source. Figure B.2 on the following page depicts this relation. Again the lock-in cuts off noise branches, which the two point $\widehat{\mathrm{CSD}}[\hat{y},\hat{z}]$ cannot, but the represented edge is virtual and has the value of.

$$\frac{\overline{\mathrm{CSD}}[\hat{y},\hat{x}]}{\overline{\mathrm{CSD}}[\hat{z},\hat{x}]} = \frac{ABC}{AD} = BC \cdot D^{-1} \tag{B.5}$$

The three point transfer function is fundamental to the measurements in the control system as well as the optical system. For the control system, loops and calibration lines are simultaneously measured using this technique. For the optical system, the systematics limits are set by measuring the graph-edges at one time, then cross-referencing background-noise detectors during the science integration using the measurements. Because of its common usage, the three-point transfer function is given special notation.

$$\widehat{\mathrm{XFER}}[\hat{x}:\hat{z}\Rightarrow\hat{y}] = \frac{\widehat{\mathrm{CSD}}[\hat{y},\hat{x}]}{\widehat{\mathrm{CSD}}[\hat{z},\hat{x}]} \tag{B.6}$$

An analysis of the statistics of this estimator are provided in Appendix C. The transfer function is essentially an orthogonal measurement to the coherence. The former is a

measurement of the system, and the latter a measure of the noise. The derivations in that Appendix show the conversions into signal to noise ratios.

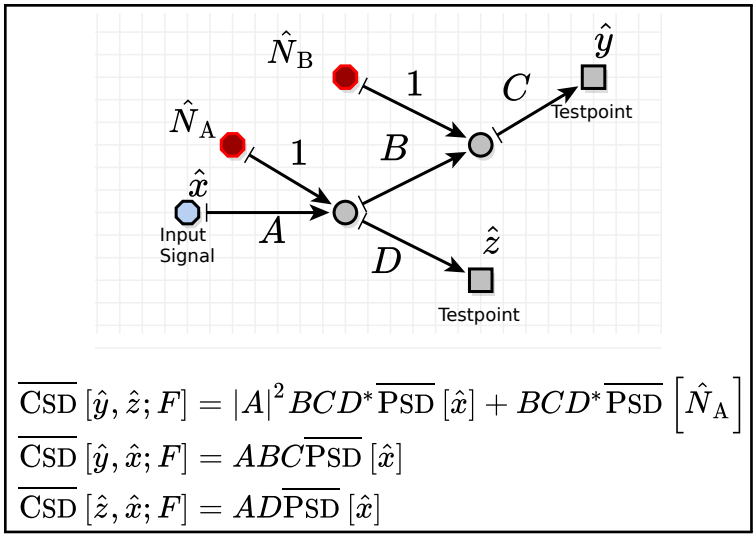

Figure B.2: Signal-flow between measured timeseries $\hat{x}$, $\hat{y}$, and potentially-measured $\hat{z}$. Across points in the system superimposed noise is added. The CSD cuts out the superimposed noise under the assumption that independent sources are uncorrelated - i.e. all correlation-creating couplings are either indicated on the graph or purposefully excluded in approximation.

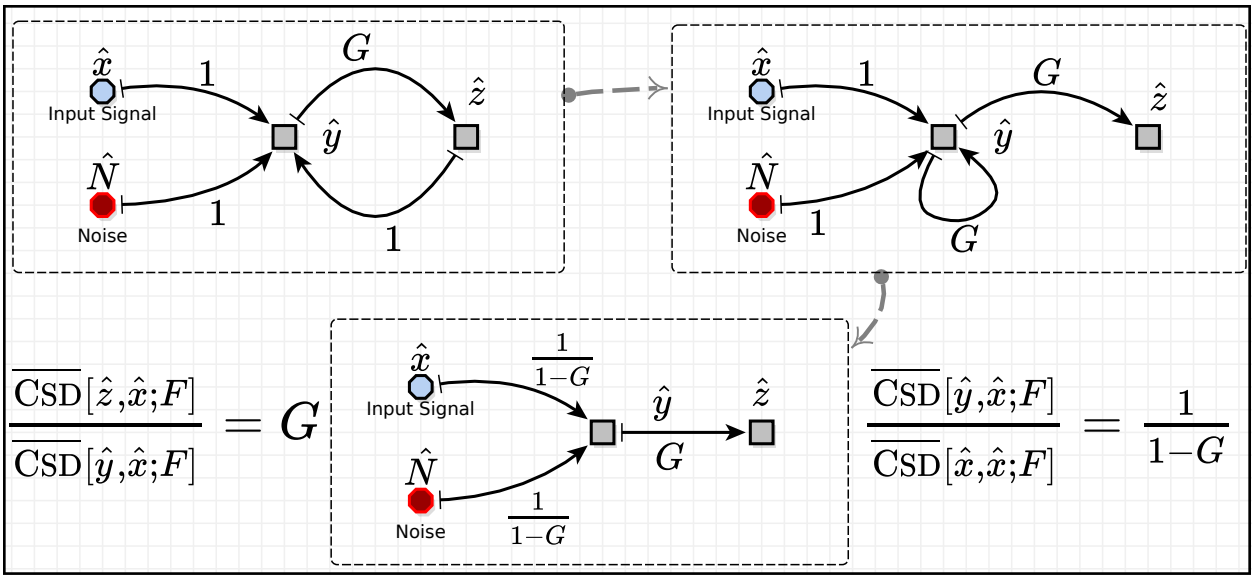

Figure B.3: The signal flow shown here includes a feedback loop relating the state variables. The loop can be algebraically solved to reduce the graph to a simple linear form.

B.3 Observed, vs. Unobserved Nodes in graphs

When thinking through a laboratory system, there are often many unmeasurable states that connect between observed states. Tracking these couplings of internal states is especially important to consider parasitic feedback couplings, side channel couplings, etc. Observed states require more care when using graph techniques for linear reduction. Internal states, being unobserved are conveniently representation independent. This allows great freedom when simplifying graphs as nodes and edges can be collected together and moved in a way to represent that "some" unobserved noise or state exists to affect measurable quantities, but without requiring the care to preserve the node's exact meaning.

Circles or other markers are used in this document to indicate states that should or are measured. Other nodes may be moved, edge-collected or whatever is needed, but the circled states are preserved in graph simplifications.

B.4 Relation of signal-flow to Feynman Diagrams

Signal flow graphs certainly look like Feynman diagrams, and if no approximations in the rigorous-picture are sacrificed, they can be equivalent. The correspondence being that the linear operators are physical propagators and nodes represent particle states. Signal-flow graphs of optical systems such as a Fabry-Perot have a strong correspondence to quantum scattering calculations and the inter-frequency coupling of mirror modulation corresponds to a 3-edge vertex of three scalar fields - the mirror, the in-optical-field and the out-optical field (the light field becoming scaler merely for the polarization insensitive interaction). Mirror motion can alternately be a four-edge vertex to allow radiation-pressure back-action on the mirrors. The three-line vertex represents an infinite-mass mirror, where the mirror line couples to an excitation-drive moving the mirror. The four-line case works for finite-mass mirrors - one line is the mirror position and the other the conjugate momentum and there is a always a loop between momentum and position depending on the mass and picking up poles from the spring-constant of the mounts. > 2 edge vertices in Feynman diagrams indicate nonlinear processes; however, signal flow graphs only represent linear systems of equations. The graphs then can represent only a kind of "mean field" perturbation theory. Feynman diagrams containing such vertices must be approximated by diagrams containing additional background "classical" mean-fields, which splits the vertex into many. The classical fields are then absorbed into the definition of the vertices so that they all become 2-edge type. A two-edge vertex represents the edge between two internal unobserved particle-states.

Appendix C

ADDITIONAL PROPERTIES AND STATISTICS OF CSD ESTIMATORS

C.1 Many-N Statistics of CSD-derived estimators

$$\textsc{Var}\left[\widehat{\textsc{Psd}}[\hat{y};N]\right] = \frac{1}{N}\overline{\textsc{Psd}}[\hat{y};N]^2 \tag{C.1}$$

$$\textsc{Var}\left[\widehat{\textsc{Csd}}[\hat{x},\hat{y};N]\right] = \frac{\overline{\textsc{Psd}}[\hat{x};N]\overline{\textsc{Psd}}[\hat{y};N]}{N} \tag{C.2}$$

$$\textsc{Var}\left[\widehat{\textsc{Xfer}}[\hat{y}\Rightarrow\hat{x};N]\right] = \frac{\left|\overline{\textsc{Xfer}}[\hat{y}\Rightarrow\hat{x};N]\right|^2}{N+1}\left(\frac{1}{\widehat{\underline{\textsc{Coh}}}[\hat{x},\hat{y};N]^2}-1\right) \tag{C.3}$$

$$\widehat{\underline{\textsc{Coh}}}[\hat{x},\hat{y};N] \approx \frac{1}{2}\left((N+1)-\sqrt{(N+1)^2-4N\cdot\widehat{\textsc{Coh}}[\hat{x},\hat{y};N]}\right) \tag{C.4}$$

Where $\widehat{\underline{\textsc{Coh}}}[\hat{x},\hat{y};N]$ represents the *squeezed* coherence estimator. The following sections derive these estimators. Note that the method used is different than for the timeseries chapter. For many-N computations, the integral-transform representation is too cumbersome. Instead each measurement is assumed independent and that the internal complex template integrates into variable with a complex-Gaussian distribution. White-noise has this property, but coherent sources do not.

C.2 2 Channel PSD, CSD, and transfer statistics

Starting with variables used to define the data at 1 frequency

$$\hat{s}_k = \hat{g}_{\Re,s,k} + i\cdot\hat{g}_{\Im,s,k} \tag{C.5}$$

Where $\hat{g}\_\_$ are Gaussian distributed random variables. Then $\hat{s}_k$ is a *complex* Guassian

number representing the drive strength for measurement number k.

$$\langle \hat{s}_k \rangle = \langle \hat{s}_k \rangle = 0 \tag{C.6}$$

$$\left\langle \hat{s}_k^* \right\rangle = \left\langle \hat{s}_k^* \right\rangle = 0 \tag{C.7}$$

$$\left\langle \hat{s}_k \hat{s}_k^* \right\rangle = \left\langle \hat{s}_k \hat{s}_k^* \right\rangle = \left\langle |\hat{s}_k|^2 \right\rangle = \left\langle \hat{g}_{\mathfrak{R},s,k}^2 + \hat{g}_{\mathfrak{I},s,k}^2 \right\rangle = s^2 \tag{C.8}$$

So un-hatted s outside of the angle brackets corresponds to the mphlinear spectral density of the drive signal. The random variable $|\hat{s}_k|^2$ then has χ_2^2 (chi-square statistics on 2 parameters) with a scaling to have a mean of s^2.

Similarly, noise-drive variables are defined

$$\left\langle \hat{n}_{\hat{x},k} \right\rangle = \left\langle \hat{n}_{\hat{x},k} \right\rangle = 0 \tag{C.9}$$

$$\left\langle \left| \hat{n}_{\hat{x},k} \right|^2 \right\rangle = n_{\hat{x}}^2 \tag{C.10}$$

$$\left\langle \hat{n}_{\hat{y},k} \right\rangle = \left\langle \hat{n}_{\hat{y},k} \right\rangle = 0 \tag{C.11}$$

$$\left\langle \left| \hat{n}_{\hat{y},k} \right|^2 \right\rangle = n_{\hat{y}}^2 \tag{C.12}$$

Now to define the channels that are measurable, first define transfer functions that are of interest. Since these definitions are for a measurement at a single frequency bin, these transfer functions are complex numbers $H_{\hat{x}}$, $H_{\hat{y}}$. The channel variables are defined as:

$$\hat{C}_{\hat{x},k} = H_{\hat{x}}(\hat{s}_k + \hat{n}_{\hat{x},k}) \tag{C.13}$$

$$\hat{C}_{\hat{y},k} = H_{\hat{y}}(\hat{s}_k + \hat{n}_{\hat{y},k}) \tag{C.14}$$

Now the spectrum estimators between the channels are defined

$$\widehat{\mathrm{PSD}}[\hat{x}; N] = \frac{1}{N} \sum_{k}^{N} \hat{C}_{\hat{x},k} \hat{C}_{\hat{x},k}^* \tag{C.15}$$

$$\widehat{\mathrm{CSD}}[\hat{x},\hat{y};N] = \frac{1}{N}\sum_{k}^{N}\hat{C}_{\hat{x},k}\hat{C}^{*}_{\hat{y},k} \tag{C.16}$$

And the estimators can be shown to have the predicted response. The PSD has the signal and noise terms added in quadrature.

$$\begin{aligned}
\overline{\mathrm{PSD}}[\hat{y};N] &= \left\langle \frac{1}{N}\sum_{k}^{N}\hat{C}_{\hat{y},k}\hat{C}^{*}_{\hat{y},k} \right\rangle \text{ no cross-k terms} && \text{(C.17)}\\
&= \left\langle \hat{C}_{\hat{y},k}\hat{C}^{*}_{\hat{y},k} \right\rangle && \text{(C.18)}\\
&= |H_{\hat{x}}|^2 \left\langle (\hat{s}_k + \hat{n}_{\hat{x},k})(\hat{s}^{*}_k + \hat{n}^{*}_{\hat{x},k}) \right\rangle \text{ no cross-source terms} && \text{(C.19)}\\
&= |H_{\hat{x}}|^2 \left\langle |\hat{s}_k|^2 + \left|\hat{n}_{\hat{x},k}\right|^2 \right\rangle && \text{(C.20)}\\
&= |H_{\hat{x}}|^2 \left(s^2 + n^2_{\hat{x}}\right) && \text{(C.21)}
\end{aligned}$$

And the CSD picks out the signal terms.

$$\begin{aligned}
\overline{\mathrm{CSD}}[\hat{x},\hat{y};N] &= \left\langle \frac{1}{N}\sum_{k}^{N}\hat{C}_{\hat{x},k}\hat{C}^{*}_{\hat{y},k} \right\rangle \text{ no cross-k terms} && \text{(C.22)}\\
&= \left\langle \hat{C}_{\hat{x},k}\hat{C}^{*}_{\hat{y},k} \right\rangle && \text{(C.23)}\\
&= H_{\hat{x}}H^{*}_{\hat{y}}\left\langle (\hat{s}_k + \hat{n}_{\hat{x},k})(\hat{s}^{*}_k + \hat{n}^{*}_{\hat{y},k}) \right\rangle \text{ no cross-source terms} && \text{(C.24)}\\
&= H_{\hat{x}}H^{*}_{\hat{y}}\left\langle |\hat{s}_k|^2 \right\rangle && \text{(C.25)}\\
&= H_{\hat{x}}H^{*}_{\hat{y}}s^2 && \text{(C.26)}
\end{aligned}$$

The first big exercise is then to determine the variance of the PSD and CSD, starting with the variance formula, which holds for formulas with no covariance between their real and imaginary parts. The average-squared is added back to the variance at the beginning

to form the expectation.

$$\textsc{Var}[\hat{O}] = \left\langle |\hat{O} - \mathrm{E}[\hat{O}]^2| \right\rangle = \left\langle |\hat{O}|^2 \right\rangle - \left| \langle \hat{O} \rangle \right|^2 \tag{C.27}$$

$$\textsc{Var}[\hat{O}] + \left| \langle \hat{O} \rangle \right|^2 = \left\langle |\hat{O}|^2 \right\rangle \tag{C.28}$$

Which is used to simplify the variance expressions:

$$\textsc{Var}\left[\widehat{\textsc{Psd}}[\hat{y}; N]\right] + \mathrm{E}\left[\widehat{\textsc{Psd}}[\hat{y}; N]\right]^2 = \tag{C.29}$$

$$= \left\langle \left(\frac{1}{N} \sum_k^N \hat{C}_{\hat{y},k} \hat{C}^*_{\hat{y},k} \right) \left(\frac{1}{N} \sum_k^N \hat{C}^*_{\hat{y},k} \hat{C}_{\hat{y},k} \right) \right\rangle \tag{C.30}$$

$$= \left\langle \frac{1}{N^2} \sum_k^N \sum_j^N \hat{C}_{\hat{y},k} \hat{C}^*_{\hat{y},k} \hat{C}^*_{\hat{y},j} \hat{C}_{\hat{y},j} \right\rangle \tag{C.31}$$

$$= \left\langle \frac{1}{N^2} \sum_k^N \hat{C}_{\hat{y},k} \hat{C}^*_{\hat{y},k} \hat{C}^*_{\hat{y},k} \hat{C}_{\hat{y},k} \right\rangle + \left\langle \frac{1}{N^2} \sum_k^N \sum_{j \neq k}^N \hat{C}_{\hat{y},k} \hat{C}^*_{\hat{y},k} \hat{C}^*_{\hat{y},j} \hat{C}_{\hat{y},j} \right\rangle \tag{C.32}$$

$$= \frac{1}{N^2} \sum_k^N \left\langle \hat{C}_{\hat{y},k} \hat{C}^*_{\hat{y},k} \hat{C}^*_{\hat{y},k} \hat{C}_{\hat{y},k} \right\rangle + \frac{1}{N^2} \sum_k^N \sum_{j \neq k}^N \left\langle \hat{C}_{\hat{y},k} \hat{C}^*_{\hat{y},k} \right\rangle \left\langle \hat{C}^*_{\hat{y},j} \hat{C}_{\hat{y},j} \right\rangle \tag{C.33}$$

$$= \frac{1}{N} \left\langle \hat{C}_{\hat{y},k} \hat{C}^*_{\hat{y},k} \hat{C}^*_{\hat{y},k} \hat{C}_{\hat{y},k} \right\rangle + \frac{1}{N^2} N \overline{\textsc{Psd}}[\hat{y}; N](N-1) \overline{\textsc{Psd}}[\hat{y}; N]^* \tag{C.34}$$

Now moving the average term back to solve only for the variance

$$\textsc{Var}\left[\widehat{\textsc{Psd}}[\hat{y}; N]\right] = \frac{1}{N} \left\langle \hat{C}_{\hat{y},k} \hat{C}^*_{\hat{y},k} \hat{C}^*_{\hat{y},k} \hat{C}_{\hat{y},k} \right\rangle - \frac{1}{N} \overline{\textsc{Psd}}[\hat{y}; N]^2 \tag{C.35}$$

$$= \frac{|H_{\hat{x}}|^4}{N} \left\langle (\hat{s}_k + \hat{n}_{\hat{x},k})(\hat{s}^*_k + \hat{n}^*_{\hat{x},k})(\hat{s}^*_k + \hat{n}^*_{\hat{x},k})(\hat{s}_k + \hat{n}_{\hat{x},k}) \right\rangle - \frac{1}{N} \overline{\textsc{Psd}}[\hat{y}; N]^2 \tag{C.36}$$

$$= \frac{|H_{\hat{x}}|^4}{N} \left\langle |\hat{s}_k|^4 + 4 |\hat{s}_k|^2 \left|\hat{n}_{\hat{x},k}\right|^2 + \left|\hat{n}_{\hat{x},k}\right|^4 \right\rangle - \frac{1}{N} \overline{\textsc{Psd}}[\hat{y}; N]^2 \tag{C.37}$$

The computation should pause here, as it seems like this is going to go to zero, replacing the $|\hat{s}_k|^4$ by s^4; however, the replacement is different than that. The problem is that $|\hat{s}_k|^4$ is actually a composite product of 4th and 2nd Gaussian moments (due to the internal Gaussian variables). These moments are equivalently lower-order chi-square-variable moments. This allows calculating the moments using the chi-square *moment generating function*.

$$\text{MGF}\left\{\chi_k^2 : t\right\} = (1-2t)^{-k/2} \tag{C.38}$$

$$\text{MGF}\left\{|\hat{s}_k|^2 : t\right\} = (1-s^2t)^{-1} \tag{C.39}$$

since $|\hat{s}_k|^2$ is a 2-parameter chi-square with mean s.

Now derivatives of the MGF evaluated at $t=0$ then give the moments

$$\left\langle |\hat{s}_k|^2 \right\rangle = \left.\frac{d}{dt}\text{MGF}\left\{|\hat{s}_k|^2 : t\right\}\right|_{t=0} = \left.s^2(1-s^2t)^{-2}\right|_{t=0} = s^2 \tag{C.40}$$

$$\left\langle |\hat{s}_k|^4 \right\rangle = \left.\frac{d^2}{dt^2}\text{MGF}\left\{|\hat{s}_k|^2 : t\right\}\right|_{t=0} = \left.2s^4(1-s^2t)^{-3}\right|_{t=0} = 2s^4 \tag{C.41}$$

$$\left\langle |\hat{s}_k|^{2n} \right\rangle = \left.\frac{d^n}{dt^n}\text{MGF}\left\{|\hat{s}_k|^2 : t\right\}\right|_{t=0} = \left.n!s^{2n}(1-s^2t)^{-(1+n)}\right|_{t=0} = n!s^{2n} \tag{C.42}$$

Now going back to the calculations of the variances:

$$\text{VAR}\left[\widehat{\text{PSD}}[\hat{y};N]\right] = \frac{|H_{\hat{x}}|^4}{N}\left\langle |\hat{s}_k|^4 + 4\,|\hat{s}_k|^2\left|\hat{n}_{\hat{x},k}\right|^2 + \left|\hat{n}_{\hat{x},k}\right|^4\right\rangle - \frac{1}{N}\overline{\text{PSD}}[\hat{y};N]^2 \tag{C.43}$$

$$= \frac{|H_{\hat{x}}|^4}{N}\left(2s^4 + 4s^2n_{\hat{x}}^2 + 2n_{\hat{x}}^4\right) - \frac{1}{N}\overline{\text{PSD}}[\hat{y};N]^2 \tag{C.44}$$

$$= \frac{|H_{\hat{x}}|^4}{N}\left(2s^4 + 4s^2n_{\hat{x}}^2 + 2n_{\hat{x}}^4\right) - \frac{1}{N}\overline{\text{PSD}}[\hat{y};N]^2 \tag{C.45}$$

$$= \frac{2}{N}\overline{\text{PSD}}[\hat{y};N]^2 - \frac{1}{N}\overline{\text{PSD}}[\hat{y};N]^2 \tag{C.46}$$

$$\text{VAR}\left[\widehat{\text{PSD}}[\hat{y};N]\right] = \frac{1}{N}\overline{\text{PSD}}[\hat{y};N]^2 \tag{C.47}$$

which was expected the expected result. The variance of the CSD is similar, but actually

includes fewer high-order terms. Here the CSD is assumed to be between channels with independent noise terms (only sharing the signal term).

$$\textsc{Var}\Big[\widehat{\textsc{Csd}}[\hat{x},\hat{y};N]\Big] + \Big|\overline{\textsc{Csd}}[\hat{x},\hat{y};N]\Big|^2 = \tag{C.48}$$

$$= \left\langle \left(\frac{1}{N}\sum_k^N \hat{C}_{\hat{x},k}\hat{C}^*_{\hat{y},k}\right)\left(\frac{1}{N}\sum_k^N \hat{C}^*_{\hat{x},k}\hat{C}_{\hat{y},k}\right)\right\rangle \tag{C.49}$$

$$= \left\langle \frac{1}{N^2}\sum_k^N\sum_j^N \hat{C}_{\hat{x},k}\hat{C}^*_{\hat{y},k}\hat{C}^*_{\hat{x},j}\hat{C}_{\hat{y},j}\right\rangle \tag{C.50}$$

$$= \left\langle \frac{1}{N^2}\sum_k^N \hat{C}_{\hat{x},k}\hat{C}^*_{\hat{y},k}\hat{C}^*_{\hat{x},k}\hat{C}_{\hat{y},k}\right\rangle + \left\langle \frac{1}{N^2}\sum_k^N\sum_{j\neq k}^N \hat{C}_{\hat{x},k}\hat{C}^*_{\hat{y},k}\hat{C}^*_{\hat{x},j}\hat{C}_{\hat{y},j}\right\rangle \tag{C.51}$$

$$= \frac{1}{N^2}\sum_k^N\Big\langle \hat{C}_{\hat{x},k}\hat{C}^*_{\hat{y},k}\hat{C}^*_{\hat{x},k}\hat{C}_{\hat{y},k}\Big\rangle + \frac{1}{N^2}\sum_k^N\sum_{j\neq k}^N\Big\langle \hat{C}_{\hat{x},k}\hat{C}^*_{\hat{y},k}\Big\rangle\Big\langle \hat{C}^*_{\hat{x},j}\hat{C}_{\hat{y},j}\Big\rangle \tag{C.52}$$

$$= \frac{1}{N}\Big\langle \hat{C}_{\hat{x},k}\hat{C}^*_{\hat{y},k}\hat{C}_{\hat{x},k}\hat{C}^*_{\hat{y},k}\Big\rangle + \frac{1}{N^2}N\overline{\textsc{Csd}}[\hat{x},\hat{y};N](N-1)\overline{\textsc{Csd}}[\hat{x},\hat{y};N]^* \tag{C.53}$$

Now moving the average-squared term back

$$\textsc{Var}\Big[\widehat{\textsc{Csd}}[\hat{x},\hat{y};N]\Big] = \frac{1}{N}\Big\langle \hat{C}_{\hat{x},k}\hat{C}^*_{\hat{y},k}\hat{C}^*_{\hat{x},k}\hat{C}_{\hat{y},k}\Big\rangle - \frac{1}{N}\Big|\overline{\textsc{Csd}}[\hat{x},\hat{y};N]\Big|^2 \tag{C.54}$$

$$= \Bigg(\frac{|H_{\hat{x}}|^2\,|H_{\hat{y}}|^2}{N}\Big\langle (\hat{s}_k+\hat{n}_{\hat{x},k})(\hat{s}^*_k+\hat{n}^*_{\hat{y},k})(\hat{s}^*_k+\hat{n}^*_{\hat{x},k})(\hat{s}_k+\hat{n}_{\hat{y},k})\Big\rangle \tag{C.55}$$

$$- \frac{1}{N}\Big|\overline{\textsc{Csd}}[\hat{x},\hat{y};N]\Big|^2\Bigg)$$

$$= \Bigg(\frac{|H_{\hat{x}}|^2\,|H_{\hat{y}}|^2}{N}\Big\langle |\hat{s}_k|^4 + 2\,|\hat{s}_k|^2\,|\hat{n}_{\hat{x},k}|^2 + 2\,|\hat{s}_k|^2\,|\hat{n}_{\hat{y},k}|^2 + |\hat{n}_{\hat{x},k}|^2\,|\hat{n}_{\hat{y},k}|^2\Big\rangle \tag{C.56}$$

$$- \frac{1}{N}\Big|\overline{\textsc{Csd}}[\hat{x},\hat{y};N]\Big|^2\Bigg)$$

$$= \frac{|H_{\hat{x}}|^2\,|H_{\hat{y}}|^2}{N}(2s^4 + s^2n^2_{\hat{x}} + s^2n^2_{\hat{y}} + n^2_{\hat{x}}n^2_{\hat{y}}) - \frac{|H_{\hat{x}}|^2\,|H_{\hat{y}}|^2}{N}(s^4) \tag{C.57}$$

$$= \frac{|H_{\hat{x}}|^2\,|H_{\hat{y}}|^2}{N}(s^2+n^2_{\hat{x}})(s^2+n^2_{\hat{y}}) \tag{C.58}$$

$$\textsc{Var}\Big[\widehat{\textsc{Csd}}[\hat{x},\hat{y};N]\Big] = \frac{\overline{\textsc{Psd}}[\hat{x};N]\overline{\textsc{Psd}}[\hat{y};N]}{N} \tag{C.59}$$

Which is the expected result.

Now a couple of definitions

$$\widehat{\mathrm{COH}}[\hat{x},\hat{y};N] = \frac{\left|\widehat{\mathrm{CSD}}[\hat{x},\hat{y};N]\right|}{\sqrt{\widehat{\mathrm{PSD}}[\hat{x};N]\cdot\widehat{\mathrm{PSD}}[\hat{y};N]}} \tag{C.60}$$

$$\overline{\mathrm{COH}}[\hat{x},\hat{y};N] = \frac{\left|\overline{\mathrm{CSD}}[\hat{x},\hat{y};N]\right|}{\sqrt{\overline{\mathrm{PSD}}[\hat{x};N]\cdot\overline{\mathrm{PSD}}[\hat{y};N]}} \approx \overline{\mathrm{COH}}[\hat{x},\hat{y};N] \tag{C.61}$$

The under-lined coherence represents the "perfect" coherence, which the usual estimator doesn't quite measure. There is a bias between that perfect expectation and the usual coherence estimate that is explored later.

And a reminder of the definition of a two-point transfer estimator.

$$\widehat{\mathrm{XFER}}[\hat{y}\Rightarrow\hat{x};N] = \frac{\widehat{\mathrm{CSD}}[\hat{x},\hat{y};N]}{\widehat{\mathrm{PSD}}[\hat{y};N]} \tag{C.62}$$

One thing to check is whether higher-moments of the transfer-function estimator bias the result due to the random variable in the denominator.

$$\overline{\mathrm{XFER}}[\hat{y}\Rightarrow\hat{x};N] = \left\langle \frac{\widehat{\mathrm{CSD}}[\hat{x},\hat{y};N]}{\widehat{\mathrm{PSD}}[\hat{y};N]} \right\rangle \tag{C.63}$$

$$= \left\langle \frac{\widehat{\mathrm{CSD}}[\hat{x},\hat{y};N]}{\overline{\mathrm{PSD}}[\hat{y};N]} \sum_{j=0}^{\infty}\left(1-\frac{\widehat{\mathrm{PSD}}[\hat{y};N]}{\overline{\mathrm{PSD}}[\hat{y};N]}\right)^{j} \right\rangle \tag{C.64}$$

$$\text{to second order} \tag{C.65}$$

$$= \frac{\overline{\mathrm{CSD}}[\hat{x},\hat{y};N]}{\overline{\mathrm{PSD}}[\hat{y};N]} + \left\langle \frac{\widehat{\mathrm{CSD}}[\hat{x},\hat{y};N]}{\overline{\mathrm{PSD}}[\hat{y};N]}\left(1-\frac{\widehat{\mathrm{PSD}}[\hat{y};N]}{\overline{\mathrm{PSD}}[\hat{y};N]}\right) \right\rangle \tag{C.66}$$

$$= \frac{\overline{\mathrm{CSD}}[\hat{x},\hat{y};N]}{\overline{\mathrm{PSD}}[\hat{y};N]}\left(1+\left\langle \frac{\widehat{\mathrm{CSD}}[\hat{x},\hat{y};N]}{\overline{\mathrm{CSD}}[\hat{x},\hat{y};N]}\left(1-\frac{\widehat{\mathrm{PSD}}[\hat{y};N]}{\overline{\mathrm{PSD}}[\hat{y};N]}\right) \right\rangle\right) \tag{C.67}$$

$$= \frac{\overline{\mathrm{CSD}}[\hat{x},\hat{y};N]}{\overline{\mathrm{PSD}}[\hat{y};N]}\left(2 - \left\langle \frac{\widehat{\mathrm{CSD}}[\hat{x},\hat{y};N]\widehat{\mathrm{PSD}}[\hat{y};N]}{\overline{\mathrm{CSD}}[\hat{x},\hat{y};N]\overline{\mathrm{PSD}}[\hat{y};N]} \right\rangle\right) \tag{C.68}$$

$$= \frac{\overline{\mathrm{CSD}}[\hat{x},\hat{y};N]}{\overline{\mathrm{PSD}}[\hat{y};N]}\left(2 - \frac{\langle \hat{x}\hat{y}^*\hat{y}\hat{y}^*\rangle}{\langle \hat{x}\hat{y}^*\rangle\langle \hat{y}\hat{y}^*\rangle}\right) \tag{C.69}$$

no combinatoric factors, the expectation value is 1

$$\overline{\mathrm{XFER}}[\hat{y}\Rightarrow\hat{x};N] = \frac{H_{\hat{x}}}{H_{\hat{y}}\left(1+\frac{n_{\hat{y}}^2}{s^2}\right)} \tag{C.70}$$

This indicates that, to first order, the 2-point transfer function is statistically unbiased. The terms in the denominator show that if there is excess noise-power in the lock-in channel, the power-spectrum estimator will see it and will bias the result *lower* in a systematic fashion.

C.3 Variance of the 2-point transfer function

The calculation is easier to express if the variance of the ratio between the estimator and the expectation value is taken.

$$\mathrm{VAR}\left[\frac{\widehat{\mathrm{XFER}}[\hat{y}\Rightarrow\hat{x};N]}{\overline{\mathrm{XFER}}[\hat{y}\Rightarrow\hat{x};N]}\right] = \frac{\overline{\mathrm{PSD}}[\hat{y};N]^2}{\left|\overline{\mathrm{CSD}}[\hat{x},\hat{y};N]\right|^2}\left\langle \frac{\left|\widehat{\mathrm{CSD}}[\hat{x},\hat{y};N]\right|^2}{\left|\widehat{\mathrm{PSD}}[\hat{y};N]\right|^2}\right\rangle - 1 \tag{C.71}$$

Taylor-expand in $\left|\widehat{\mathrm{PSD}}[\hat{y};N]\right|^2$

$$= \frac{\overline{\mathrm{PSD}}[\hat{y};N]^2}{\left|\overline{\mathrm{CSD}}[\hat{x},\hat{y};N]\right|^2}\left\langle \frac{\left|\widehat{\mathrm{CSD}}[\hat{x},\hat{y};N]\right|^2}{\left\langle\left|\widehat{\mathrm{PSD}}[\hat{y};N]\right|^2\right\rangle}\sum_{j=0}^{\infty}\left(1 - \frac{\left|\widehat{\mathrm{PSD}}[\hat{y};N]\right|^2}{\left\langle\left|\widehat{\mathrm{PSD}}[\hat{y};N]\right|^2\right\rangle}\right)^j\right\rangle - 1 \tag{C.72}$$

to first order

$$\approx \frac{\left\langle\left|\widehat{\mathrm{CSD}}[\hat{x},\hat{y};N]\right|^2\right\rangle}{\left|\overline{\mathrm{CSD}}[\hat{x},\hat{y};N]\right|^2}\cdot\frac{\overline{\mathrm{PSD}}[\hat{y};N]^2}{\left\langle\left|\widehat{\mathrm{PSD}}[\hat{y};N]\right|^2\right\rangle} - 1 \tag{C.73}$$

$$= \frac{\left\langle \left| \widehat{\mathrm{CSD}}[\hat{x},\hat{y};N] \right|^2 \right\rangle}{\left| \overline{\mathrm{CSD}}[\hat{x},\hat{y};N] \right|^2} \cdot \frac{\overline{\mathrm{PSD}}[\hat{y};N]^2}{\mathrm{VAR}\left[\widehat{\mathrm{PSD}}[\hat{y};N]\right] + \overline{\mathrm{PSD}}[\hat{y};N]^2} - 1 \quad \text{(C.74)}$$

$$= \frac{\left\langle \left| \widehat{\mathrm{CSD}}[\hat{x},\hat{y};N] \right|^2 \right\rangle}{\left| \overline{\mathrm{CSD}}[\hat{x},\hat{y};N] \right|^2} \cdot \frac{\overline{\mathrm{PSD}}[\hat{y};N]^2}{(\frac{1}{N}+1)\overline{\mathrm{PSD}}[\hat{y};N]^2} - 1 \quad \text{(C.75)}$$

$$= \frac{N\left\langle \left| \widehat{\mathrm{CSD}}[\hat{x},\hat{y};N] \right|^2 \right\rangle}{(N+1)\left| \overline{\mathrm{CSD}}[\hat{x},\hat{y};N] \right|^2} - \frac{N+1}{N+1} \quad \text{(C.76)}$$

$$= \frac{N\left(\left\langle \left| \widehat{\mathrm{CSD}}[\hat{x},\hat{y};N] \right|^2 \right\rangle - \left| \overline{\mathrm{CSD}}[\hat{x},\hat{y};N] \right|^2 \right)}{(N+1)\left| \overline{\mathrm{CSD}}[\hat{x},\hat{y};N] \right|^2} - \frac{1}{N+1} \quad \text{(C.77)}$$

$$= \frac{N \cdot \mathrm{VAR}\left[\widehat{\mathrm{CSD}}[\hat{x},\hat{y};N]\right]}{(N+1)\left| \overline{\mathrm{CSD}}[\hat{x},\hat{y};N] \right|^2} - \frac{1}{N+1} \quad \text{(C.78)}$$

$$= \frac{1}{N+1}\left(\frac{\overline{\mathrm{PSD}}[\hat{x};N]\overline{\mathrm{PSD}}[\hat{y};N]}{\left| \overline{\mathrm{CSD}}[\hat{x},\hat{y};N] \right|^2} - 1 \right) \quad \text{(C.79)}$$

$$\mathrm{VAR}\left[\frac{\widehat{\mathrm{XFER}}[\hat{y} \Rightarrow \hat{x};N]}{\overline{\mathrm{XFER}}[\hat{y} \Rightarrow \hat{x};N]} \right] = \frac{1}{N+1}\left(\frac{1}{\overline{\mathrm{COH}}[\hat{x},\hat{y};N]^2} - 1 \right) \quad \text{(C.80)}$$

C.4 Variance of the 3-point transfer function

The calculation of the 3-point transfer function leaves it equivalent to a ratio of two 2-point transfers.

$$\widehat{\mathrm{XFER}}[\hat{x}:\hat{y}\Rightarrow\hat{z}] = \frac{\widehat{\mathrm{CSD}}[\hat{y},\hat{x}]}{\widehat{\mathrm{CSD}}[\hat{z},\hat{x}]} = \frac{\widehat{\mathrm{CSD}}[\hat{y},\hat{x}]}{\widehat{\mathrm{CSD}}[\hat{x},\hat{x}]}\frac{\widehat{\mathrm{CSD}}[\hat{x},\hat{x}]}{\widehat{\mathrm{CSD}}[\hat{z},\hat{x}]} \quad \text{(C.81)}$$

$$= \frac{\widehat{\mathrm{XFER}}[\hat{x}\Rightarrow\hat{y}]}{\widehat{\mathrm{XFER}}[\hat{x}\Rightarrow\hat{z}]} \quad \text{(C.82)}$$

This is interesting as the 2-point transfers can be biased if there is excess noise in $\hat{y}$ or $\hat{z}$, but the three-point is not. In any case, the reduction allows linear error propagation to estimate the variance of this estimate. Again ratios are taken to simplify the calculation and

eventually represent the noise in SNR.

$$\textsc{Var}\left[\frac{\widehat{\textsc{XFER}}[\hat{x}:\hat{y}\Rightarrow\hat{z}]}{\overline{\textsc{XFER}}[\hat{x}:\hat{y}\Rightarrow\hat{z}]}\right] = \textsc{Var}\left[\frac{\widehat{\textsc{XFER}}[\hat{x}\Rightarrow\hat{y}]}{\overline{\textsc{XFER}}[\hat{x}\Rightarrow\hat{y}]}\frac{\overline{\textsc{XFER}}[\hat{x}\Rightarrow\hat{z}]}{\widehat{\textsc{XFER}}[\hat{x}\Rightarrow\hat{z}]}\right] \tag{C.83}$$

$$= \left(\textsc{Var}\left[\frac{\widehat{\textsc{XFER}}[\hat{x}\Rightarrow\hat{y}]}{\overline{\textsc{XFER}}[\hat{x}\Rightarrow\hat{y}]}\right] + \textsc{Var}\left[\frac{\overline{\textsc{XFER}}[\hat{x}\Rightarrow\hat{z}]}{\widehat{\textsc{XFER}}[\hat{x}\Rightarrow\hat{z}]}\right]\right. \tag{C.84}$$

$$\left. - 2\mathfrak{Re}\left\{\textsc{Cov}\left[\frac{\widehat{\textsc{XFER}}[\hat{x}\Rightarrow\hat{y}]}{\overline{\textsc{XFER}}[\hat{x}\Rightarrow\hat{y}]}, \frac{\overline{\textsc{XFER}}[\hat{x}\Rightarrow\hat{z}]}{\widehat{\textsc{XFER}}[\hat{x}\Rightarrow\hat{z}]}\right]\right\}\right) \tag{C.85}$$

Dropping covariance and expanding variance of reciprocal

$$\leq \textsc{Var}\left[\frac{\widehat{\textsc{XFER}}[\hat{x}\Rightarrow\hat{y}]}{\overline{\textsc{XFER}}[\hat{x}\Rightarrow\hat{y}]}\right] + \left(\textsc{Var}\left[\frac{\widehat{\textsc{XFER}}[\hat{x}\Rightarrow\hat{z}]}{\overline{\textsc{XFER}}[\hat{x}\Rightarrow\hat{z}]}\right]^{-1} - 1\right)^{-1} \tag{C.86}$$

so the SNR has a lower estimate given.

$$\textsc{Snr}\left[\widehat{\textsc{XFER}}[\hat{x}:\hat{y}\Rightarrow\hat{z}]\right] \geq \left(\frac{1}{\textsc{Snr}\left[\widehat{\textsc{XFER}}[\hat{x}\Rightarrow\hat{y}]\right]^2} + \frac{1}{\left(\textsc{Snr}\left[\widehat{\textsc{XFER}}[\hat{x}\Rightarrow\hat{z}]\right] - 1\right)^2}\right)^{-\frac{1}{2}} \tag{C.87}$$

This SNR is the formula used for the three-point tranfer functions in this document

C.5 Biasing Corrections for Coherence

There is an issue with the coherence estimator in that the "perfect" coherence estimate can only be approximated by the biased estimator. This affects the estimates of the $\widehat{\textsc{XFER}}[\hat{y}\Rightarrow\hat{x}]$ snr.

$$\overline{\underline{\textsc{Coh}}}[\hat{x},\hat{y};N] \approx \overline{\textsc{Coh}}[\hat{x},\hat{y};N] \tag{C.88}$$

From the statistics of the CSD and PSD's, the bias can be derived to be

$$\overline{\text{Coh}}[\hat{x},\hat{y};N] = \overline{\underline{\text{Coh}}}[\hat{x},\hat{y};N]\left(1+\frac{1-\overline{\underline{\text{Coh}}}[\hat{x},\hat{y};N]}{N}\right) \tag{C.89}$$

This means that the usual Coherence estimator is actually not appropriate to use when the coherence is small. It is better to use the less-biased *squeezed*-coherence estimator derived by solving the previous equation,

$$\widehat{\underline{\text{Coh}}}[\hat{x},\hat{y};N] \approx \frac{1}{2}\left((N+1)-\sqrt{(N+1)^2-4N\cdot\widehat{\text{Coh}}[\hat{x},\hat{y};N]}\right) \tag{C.90}$$

this seems like a strange statistic to use, but it can be seen to work in the low and high coherence limits

Low measured coherence limit:

$$\overline{\underline{\text{Coh}}}[\hat{x},\hat{y};N] \approx \frac{1}{2}\left((N+1)-\sqrt{(N+1)^2}\right) = 0 \tag{C.91}$$

High measured coherence limit

$$\overline{\underline{\text{Coh}}}[\hat{x},\hat{y};N] \approx \frac{1}{2}\left((N+1)-\sqrt{(N+1)^2-4N}\right) \tag{C.92}$$

$$\approx \frac{1}{2}\left((N+1)-\sqrt{(N-1)^2}\right) = 1 \tag{C.93}$$

This indicates that the SNR of the two-point transfer-functions should be estimated as

$$\text{Snr}\left[\widehat{\text{Xfer}}[\hat{y}\Rightarrow\hat{x};N]\right] \approx \text{Var}\left[\frac{\widehat{\text{Xfer}}[\hat{y}\Rightarrow\hat{x};N]}{\overline{\text{Xfer}}[\hat{y}\Rightarrow\hat{x};N]}\right]^{-\frac{1}{2}} \tag{C.94}$$

$$\approx \sqrt{\frac{(N+1)\widehat{\underline{\text{Coh}}}[\hat{x},\hat{y};N]^2}{1-\widehat{\underline{\text{Coh}}}[\hat{x},\hat{y};N]^2}} \tag{C.95}$$

The three-point should use this formula substituted into eq. (C.87) on page 256.

Appendix D

AM/PM-BASIS FOR SINGLE-CARRIER OPTICAL TRANSFER

The amplitude and phase modulation basis for the interferometer starts from a representation of the light field:

$$A_{\text{beam}}(t) = A_{\text{src}}\left(1 + |\gamma_{\text{AM}}|\frac{\cos(2\pi F_{\text{mod}}t + \phi_{\text{AM}})}{2}\right) \cdot \exp\left(2\pi \text{i} F_{\text{c}}t + \text{i}|\gamma_{\text{PM}}|\frac{\cos(2\pi F_{\text{mod}} + \phi_{\text{PM}})}{2}\right) \tag{D.1}$$

where

$$\phi_{\text{AM}} = \arg(\gamma_{\text{AM}}) \tag{D.2}$$

$$\phi_{\text{PM}} = \arg(\gamma_{\text{PM}}) \tag{D.3}$$

We can see if this method of simplifying gives the correct power modulation in the small γ_{AM}, γ_{PM} regime (no $2F_{\text{mod}}$ factors).

$$P_{\text{beam}} = |A_{\text{beam}}(t)|^2 \tag{D.4}$$

$$= |A_{\text{src}}|^2 \left|1 + |\gamma_{\text{AM}}|\frac{\cos(2\pi F_{\text{mod}}t + \phi_{\text{AM}})}{2}\right|^2 \left|e^{2\pi \text{i} F_{\text{c}}t + \text{i}|\gamma_{\text{PM}}|\frac{\cos(2\pi F_{\text{mod}} + \phi_{\text{PM}})}{2}}\right|^2 \tag{D.5}$$

$$= |A_{\text{src}}|^2 \left(1 + |\gamma_{\text{AM}}|\cos(2\pi F_{\text{mod}}t + \phi_{\text{AM}}) + \mathcal{O}({\gamma_{\text{AM}}}^2)\right) \tag{D.6}$$

So the convention is to use *complex* γ modulation indices, where the phase of that complex number represents the phasing of the modulation itself. If a modulator were to have its drive cable extended to delay the drive by 90 deg ("lose" the phase), then the modulation index picks up $-\text{i}$ of phase as well.

splitting up the cos terms through the ϕ terms gives

$$A_{\text{beam}}(t) = A_{\text{src}}\left(1 + \mathfrak{Re}\{\gamma_{\text{AM}}\}\,\frac{\cos(2\pi F_{\text{mod}}t)}{2} - \mathfrak{Im}\{\gamma_{\text{AM}}\}\,\frac{\sin(2\pi F_{\text{mod}}t)}{2}\right) \cdot \exp\left(2\pi \mathrm{i} F_{\text{c}}t + \mathrm{i}\mathfrak{Re}\{\gamma_{\text{PM}}\}\,\frac{\cos(2\pi F_{\text{mod}}t)}{2} - \mathrm{i}\mathfrak{Im}\{\gamma_{\text{PM}}\}\,\frac{\sin(2\pi F_{\text{mod}}t)}{2}\right) \quad \text{(D.7)}$$

Now using exponential trigonometrics identities to split up the factors:

$$\cos(x) = \frac{e^{\mathrm{i}x} + e^{-\mathrm{i}x}}{2} \quad \text{(D.8)}$$

$$\sin(x) = \frac{e^{\mathrm{i}x} - e^{-\mathrm{i}x}}{2\mathrm{i}} = -\mathrm{i}\frac{e^{\mathrm{i}x} - e^{-\mathrm{i}x}}{2} \quad \text{(D.9)}$$

Allows the expansion

$$A_{\text{beam}}(t) = A_{\text{src}} \left(\begin{array}{r} 1 + (\mathfrak{Re}\{\gamma_{\text{AM}}\} + \mathrm{i}\mathfrak{Im}\{\gamma_{\text{AM}}\})\dfrac{e^{2\pi \mathrm{i} F_{\text{mod}}t}}{4} \\ + (\mathfrak{Re}\{\gamma_{\text{AM}}\} - \mathrm{i}\mathfrak{Im}\{\gamma_{\text{AM}}\})\dfrac{e^{-2\pi \mathrm{i} F_{\text{mod}}t}}{4} \end{array} \right) \cdot \exp\left(\begin{array}{r} 2\pi \mathrm{i} F_{\text{c}}t + \mathrm{i}(\mathfrak{Re}\{\gamma_{\text{PM}}\} + \mathrm{i}\mathfrak{Im}\{\gamma_{\text{PM}}\})\dfrac{e^{2\pi \mathrm{i} F_{\text{mod}}t}}{4} \\ + \mathrm{i}(\mathfrak{Re}\{\gamma_{\text{PM}}\} - \mathrm{i}\mathfrak{Im}\{\gamma_{\text{PM}}\})\dfrac{e^{-2\pi \mathrm{i} F_{\text{mod}}t}}{4} \end{array} \right) \quad \text{(D.10)}$$

Since all $\mathfrak{Im}\{\cdot\}$ terms have an imaginary coefficient, this can be simplified

$$A_{\text{beam}}(t) = A_{\text{src}}\left(1 + \frac{\gamma_{\text{AM}}}{4}e^{2\pi \mathrm{i} F_{\text{mod}}t} + \frac{\gamma^*_{\text{AM}}}{4}e^{-2\pi \mathrm{i} F_{\text{mod}}t}\right) \cdot \exp\left(2\pi \mathrm{i} F_{\text{c}}t + \mathrm{i}\frac{\gamma_{\text{PM}}}{4}e^{2\pi \mathrm{i} F_{\text{mod}}t} + \mathrm{i}\frac{\gamma^*_{\text{PM}}}{4}e^{-2\pi \mathrm{i} F_{\text{mod}}t}\right) \quad \text{(D.11)}$$

Now, assuming $\gamma_{\text{PM}} \ll 1$ the γ_{PM} terms may be expanded out of the exponentials and

then assuming $\gamma_{\mathrm{AM}} \ll 1$ allows cross terms to be dropped to give:

$$A_{\mathrm{beam}}(t) = A_{\mathrm{src}}\left(1 + \left(\frac{\gamma_{\mathrm{AM}}}{4} + \mathrm{i}\frac{\gamma_{\mathrm{PM}}}{4}\right)e^{2\pi \mathrm{i} F_{\mathrm{mod}} t} + \left(\frac{\gamma^*_{\mathrm{AM}}}{4} + \mathrm{i}\frac{\gamma^*_{\mathrm{PM}}}{4}\right)e^{-2\pi \mathrm{i} F_{\mathrm{mod}} t}\right) e^{2\pi \mathrm{i} F_{\mathrm{c}} t} \tag{D.12}$$

The power measured should appear the same in the small modulation limit

$$P_{\mathrm{beam}} = |A_{\mathrm{src}}|^2 \left|1 + \left(\frac{\gamma_{\mathrm{AM}}}{4} + \mathrm{i}\frac{\gamma_{\mathrm{PM}}}{4}\right)e^{2\pi \mathrm{i} F_{\mathrm{mod}} t} + \left(\frac{\gamma^*_{\mathrm{AM}}}{4} + \mathrm{i}\frac{\gamma^*_{\mathrm{PM}}}{4}\right)e^{-2\pi \mathrm{i} F_{\mathrm{mod}} t}\right|^2 \tag{D.13}$$

$\downarrow$ dropping small cross-terms

$$\begin{aligned} &= |A_{\mathrm{src}}|^2 \Bigg(1 + \left(\frac{\gamma_{\mathrm{AM}}}{4} + \mathrm{i}\frac{\gamma_{\mathrm{PM}}}{4}\right)e^{2\pi \mathrm{i} F_{\mathrm{mod}} t} + \left(\frac{\gamma^*_{\mathrm{AM}}}{4} + \mathrm{i}\frac{\gamma^*_{\mathrm{PM}}}{4}\right)e^{-2\pi \mathrm{i} F_{\mathrm{mod}} t} \\ &\qquad + \left(\frac{\gamma_{\mathrm{AM}}}{4} + \mathrm{i}\frac{\gamma_{\mathrm{PM}}}{4}\right)^* e^{-2\pi \mathrm{i} F_{\mathrm{mod}} t} + \left(\frac{\gamma^*_{\mathrm{AM}}}{4} + \mathrm{i}\frac{\gamma^*_{\mathrm{PM}}}{4}\right)^* e^{2\pi \mathrm{i} F_{\mathrm{mod}} t}\Bigg) \end{aligned} \tag{D.14}$$

$$\begin{aligned} &= |A_{\mathrm{src}}|^2 \Bigg(1 + \left(\frac{\gamma_{\mathrm{AM}}}{4} + \mathrm{i}\frac{\gamma_{\mathrm{PM}}}{4}\right)e^{2\pi \mathrm{i} F_{\mathrm{mod}} t} + \left(\frac{\gamma^*_{\mathrm{AM}}}{4} + \mathrm{i}\frac{\gamma^*_{\mathrm{PM}}}{4}\right)e^{-2\pi \mathrm{i} F_{\mathrm{mod}} t} \\ &\qquad + \left(\frac{\gamma^*_{\mathrm{AM}}}{4} - \mathrm{i}\frac{\gamma^*_{\mathrm{PM}}}{4}\right)e^{-2\pi \mathrm{i} F_{\mathrm{mod}} t} + \left(\frac{\gamma_{\mathrm{AM}}}{4} - \mathrm{i}\frac{\gamma_{\mathrm{PM}}}{4}\right)e^{2\pi \mathrm{i} F_{\mathrm{mod}} t}\Bigg) \end{aligned} \tag{D.15}$$

$$= |A_{\mathrm{src}}|^2 \left(1 + \frac{\gamma_{\mathrm{AM}}}{2} e^{2\pi \mathrm{i} F_{\mathrm{mod}} t} + \frac{\gamma^*_{\mathrm{AM}}}{2} e^{-2\pi \mathrm{i} F_{\mathrm{mod}} t}\right) \tag{D.16}$$

$$= |A_{\mathrm{src}}|^2 \Big(1 + \mathfrak{Re}\{\gamma_{\mathrm{AM}}\} \cos(2\pi \mathrm{i} F_{\mathrm{mod}} t) + \mathfrak{Im}\{\gamma_{\mathrm{AM}}\} \sin(2\pi \mathrm{i} F_{\mathrm{mod}} t)\Big) \tag{D.17}$$

$$= |A_{\mathrm{src}}|^2 \Big(1 + |\gamma_{\mathrm{AM}}| \cos(2\pi \mathrm{i} F_{\mathrm{mod}} t + \phi_{\mathrm{AM}})\Big) \tag{D.18}$$

Which is the correct answer as given from the full form above

D.1 Transformation Rules

Starting from a beam with some amount of AM and PM at a frequency, The transformation of γ_{AM} γ_{PM} as the optical field passes through the optical transfer-function may be derived. Call the transfer function $H(F)$ as a function of frequency.

Now the beam field should be represented in frequency-domain, which is easy since the time-domain representation is reduced to terms linear in $e^{2\pi \mathrm{i} F t}$.

$$\widetilde{A}_{\mathrm{beam}}(F) = A_{\mathrm{src}}\Bigg(\delta[F - F_{\mathrm{c}}] + \Big(\frac{\gamma_{\mathrm{AM}}}{4} + \mathrm{i}\frac{\gamma_{\mathrm{PM}}}{4}\Big)\delta[F - (F_{\mathrm{c}} + F_{\mathrm{mod}})] + \Big(\frac{\gamma^*_{\mathrm{AM}}}{4} + \mathrm{i}\frac{\gamma^*_{\mathrm{PM}}}{4}\Big)\delta[F - (F_{\mathrm{c}} - F_{\mathrm{mod}})]\Bigg) \tag{D.19}$$

So the transformation through the interferometer transforms linearly

$$\widetilde{A}_{\mathrm{out}}(F) = H(F)\widetilde{A}_{\mathrm{in}}(F) \tag{D.20}$$

$$\widetilde{A}_{\mathrm{out}}(F) = H(F)\widetilde{A}_{\mathrm{in}}(F) \tag{D.21}$$

$$= H(F)\frac{A_{\mathrm{srcin}}}{4}\Bigg(4\delta[F - F_{\mathrm{c}}] + (\gamma_{\mathrm{AMin}} + \mathrm{i}\gamma_{\mathrm{PMin}})\delta[F - (F_{\mathrm{c}} + F_{\mathrm{mod}})] + (\gamma^*_{\mathrm{AMin}} + \mathrm{i}\gamma^*_{\mathrm{PMin}})\delta[F - (F_{\mathrm{c}} - F_{\mathrm{mod}})]\Bigg) \tag{D.22}$$

$$= \frac{A_{\mathrm{srcin}}}{4}\Bigg(4H(F_{\mathrm{c}})\delta[F - F_{\mathrm{c}}] + H(F_{\mathrm{c}} + F_{\mathrm{mod}})(\gamma_{\mathrm{AMin}} + \mathrm{i}\gamma_{\mathrm{PMin}})\delta[F - (F_{\mathrm{c}} + F_{\mathrm{mod}})] + H(F_{\mathrm{c}} - F_{\mathrm{mod}})(\gamma^*_{\mathrm{AMin}} + \mathrm{i}\gamma^*_{\mathrm{PMin}})\delta[F - (F_{\mathrm{c}} - F_{\mathrm{mod}})]\Bigg) \tag{D.23}$$

$$= \frac{A_{\mathrm{srcin}}H(F_{\mathrm{c}})}{4}\Bigg(4\delta[F - F_{\mathrm{c}}] + \frac{H(F_{\mathrm{c}} + F_{\mathrm{mod}})}{H(F_{\mathrm{c}})}(\gamma_{\mathrm{AMin}} + \mathrm{i}\gamma_{\mathrm{PMin}})\delta[F - (F_{\mathrm{c}} + F_{\mathrm{mod}})] + \frac{H(F_{\mathrm{c}} - F_{\mathrm{mod}})}{H(F_{\mathrm{c}})}(\gamma^*_{\mathrm{AMin}} + \mathrm{i}\gamma^*_{\mathrm{PMin}})\delta[F - (F_{\mathrm{c}} - F_{\mathrm{mod}})]\Bigg) \tag{D.24}$$

$$\widetilde{A}_{\mathrm{out}}(F) = \frac{A_{\mathrm{srcout}}}{4}\Bigg(4\delta[F - F_{\mathrm{c}}] + (\gamma_{\mathrm{AMout}} + \mathrm{i}\gamma_{\mathrm{PMout}})\delta[F - (F_{\mathrm{c}} + F_{\mathrm{mod}})] + (\gamma^*_{\mathrm{AMout}} + \mathrm{i}\gamma^*_{\mathrm{PMout}})\delta[F - (F_{\mathrm{c}} - F_{\mathrm{mod}})]\Bigg) \tag{D.25}$$

Equating the last two lines in the basis' generated by each delta-function generates a set of relations:

$$A_{\mathrm{srcout}} = H(F_{\mathrm{c}})A_{\mathrm{srcin}} \tag{D.26}$$

$$(\gamma_{\mathrm{AMout}} + \mathrm{i}\gamma_{\mathrm{PMout}}) = \frac{H(F_{\mathrm{c}} + F_{\mathrm{mod}})}{H(F_{\mathrm{c}})}(\gamma_{\mathrm{AMin}} + \mathrm{i}\gamma_{\mathrm{PMin}}) \tag{D.27}$$

$$(\gamma^*_{\mathrm{AMout}} + \mathrm{i}\gamma^*_{\mathrm{PMout}}) = \frac{H(F_{\mathrm{c}} - F_{\mathrm{mod}})}{H(F_{\mathrm{c}})}(\gamma^*_{\mathrm{AMin}} + \mathrm{i}\gamma^*_{\mathrm{PMin}}) \tag{D.28}$$

The last one can be transformed then to be

$$(\gamma_{\mathrm{AMout}} - \mathrm{i}\gamma_{\mathrm{PMout}}) = \frac{h^*(F_{\mathrm{c}} - F_{\mathrm{mod}})}{h^*(F_{\mathrm{c}})}(\gamma_{\mathrm{AMin}} - \mathrm{i}\gamma_{\mathrm{PMin}}) \tag{D.29}$$

now to help in simplifying the rest

$$H_+ = \frac{H(F_{\mathrm{c}} + F_{\mathrm{mod}})}{H(F_{\mathrm{c}})} \tag{D.30}$$

$$H_- = \frac{h^*(F_{\mathrm{c}} - F_{\mathrm{mod}})}{h^*(F_{\mathrm{c}})} \tag{D.31}$$

$$\begin{bmatrix} 1 & \mathrm{i} \\ 1 & -\mathrm{i} \end{bmatrix}\begin{bmatrix} \gamma_{\mathrm{AMout}} \\ \gamma_{\mathrm{PMout}} \end{bmatrix} = \begin{bmatrix} H_+ & 0 \\ 0 & H_- \end{bmatrix}\begin{bmatrix} 1 & \mathrm{i} \\ 1 & -\mathrm{i} \end{bmatrix}\begin{bmatrix} \gamma_{\mathrm{AMin}} \\ \gamma_{\mathrm{PMin}} \end{bmatrix} \tag{D.32}$$

solved to be

$$\begin{bmatrix} \gamma_{\mathrm{AMout}} \\ \gamma_{\mathrm{PMout}} \end{bmatrix} = \begin{bmatrix} 1 & \mathrm{i} \\ 1 & -\mathrm{i} \end{bmatrix}^{-1}\begin{bmatrix} H_+ & 0 \\ 0 & H_- \end{bmatrix}\begin{bmatrix} 1 & \mathrm{i} \\ 1 & -\mathrm{i} \end{bmatrix}\begin{bmatrix} \gamma_{\mathrm{AMin}} \\ \gamma_{\mathrm{PMin}} \end{bmatrix} \tag{D.33}$$

and reduced to the final form

$$\begin{bmatrix}\gamma_{\mathrm{AMout}}\\ \gamma_{\mathrm{PMout}}\end{bmatrix} = \frac{1}{2}\begin{bmatrix} H_+ + H_- & \mathrm{i}(H_+ - H_-)\\ \mathrm{i}(H_- - H_+) & H_+ + H_-\end{bmatrix}\begin{bmatrix}\gamma_{\mathrm{AMin}}\\ \gamma_{\mathrm{PMin}}\end{bmatrix} \tag{D.34}$$

and finally to simplify the notation further

$$H_{\mathrm{amp}}(F_{\mathrm{c}}) = \frac{A_{\mathrm{srcout}}}{A_{\mathrm{srcin}}} = H(F_{\mathrm{c}}) \tag{D.35}$$

$$H_{\mathrm{even}}(F_{\mathrm{c}}, F_{\mathrm{mod}}) = \frac{H_+ + H_-}{2} = \frac{H(F_{\mathrm{c}} + F_{\mathrm{mod}})}{2H(F_{\mathrm{c}})} + \frac{h^*(F_{\mathrm{c}} - F_{\mathrm{mod}})}{2h^*(F_{\mathrm{c}})} \tag{D.36}$$

$$H_{\mathrm{odd}}(F_{\mathrm{c}}, F_{\mathrm{mod}}) = \mathrm{i}\frac{H_+ - H_-}{2} = \frac{\mathrm{i}H(F_{\mathrm{c}} + F_{\mathrm{mod}})}{2H(F_{\mathrm{c}})} - \frac{\mathrm{i}h^*(F_{\mathrm{c}} - F_{\mathrm{mod}})}{2h^*(F_{\mathrm{c}})} \tag{D.37}$$

$$\begin{bmatrix}\gamma_{\mathrm{AMout}}\\ \gamma_{\mathrm{PMout}}\end{bmatrix} = \begin{bmatrix} H_{\mathrm{even}} & H_{\mathrm{odd}}\\ -H_{\mathrm{odd}} & H_{\mathrm{even}}\end{bmatrix}\begin{bmatrix}\gamma_{\mathrm{AMin}}\\ \gamma_{\mathrm{PMin}}\end{bmatrix} \tag{D.38}$$

so now the even component preserves AM-to-AM and the odd component will cause PM-to-AM and vice-versa.

D.2 Port-amplitude Units (root-watts)

The γ modulation indices are unitless, effectively representing the relative size of the sidebands with respect to the carrier. An alternate useful characterization is in modulation power, with units of field strength most conveniently "root watts" or "root photons". Instead of the even and odd transfer functions, these units must also carry around the amplitude adjustment. The coefficients are:

$$A_{\mathrm{AM}}(F_{\mathrm{c}}, F_{\mathrm{mod}}) = A_{\mathrm{src}}\gamma_{\mathrm{AM}} \tag{D.39}$$

$$A_{\mathrm{PM}}(F_{\mathrm{c}}, F_{\mathrm{mod}}) = A_{\mathrm{src}}\gamma_{\mathrm{PM}} \tag{D.40}$$

$$t_{\text{even}}(F_{\text{c}}, F_{\text{mod}}) = H_{\text{amp}}(F_{\text{c}}, F_{\text{mod}}) H_{\text{even}}(F_{\text{c}}, F_{\text{mod}}) \tag{D.41}$$

$$= \frac{1}{2}\left(H(F_{\text{c}} + F_{\text{mod}}) + \frac{H(F_{\text{c}})}{h^*(F_{\text{c}})} h^*(F_{\text{c}} - F_{\text{mod}}) \right) \tag{D.42}$$

$$t_{\text{odd}}(F_{\text{c}}, F_{\text{mod}}) = H_{\text{amp}}(F_{\text{c}}, F_{\text{mod}}) H_{\text{odd}}(F_{\text{c}}, F_{\text{mod}}) \tag{D.43}$$

$$= \frac{\text{i}}{2}\left(H(F_{\text{c}} + F_{\text{mod}}) - \frac{H(F_{\text{c}})}{h^*(F_{\text{c}})} h^*(F_{\text{c}} - F_{\text{mod}}) \right) \tag{D.44}$$

Transforming as

$$\begin{bmatrix} A_{\text{AMout}} \\ A_{\text{PMout}} \end{bmatrix} = \begin{bmatrix} t_{\text{even}} & t_{\text{odd}} \\ -t_{\text{odd}} & t_{\text{even}} \end{bmatrix} \begin{bmatrix} A_{\text{AMin}} \\ A_{\text{PMin}} \end{bmatrix} \tag{D.45}$$

Power units have a strong advantage in that one can compare them to shot noise $\frac{\hbar\omega}{2}$ amplitude to determine the sensitivity detecting amplitude-modulation. These derivations are then useful to cross-reference to other detectors or points of reference in the optical system.

D.3 Example transfer functions through the cavity (Schnupp Asymmetry

ok now if we can use cavity models to predict $H(F)$ then we can model how the AM and PM propagate. for the input into the cavity, there is a transfer function (not derived here yet)

$$H_{\text{cavity}}(F) = \frac{t_{\text{prm}}}{1 - r_{\text{prm}} r_{\text{ifo}} e^{\text{i}\left(\frac{2\pi F}{F_{\text{FSR}}} + \Phi_{\text{HOM}}\right)}} \tag{D.46}$$

where

$$r_{\rm prm} = \sqrt{1 - T_{\rm prm}} \tag{D.47}$$

$$t_{\rm prm} = \sqrt{T_{\rm prm}} \tag{D.48}$$

$$r_{\rm ifo} = \sqrt{1 - \underbrace{T_{\rm scatter} - T_{\rm defect} - \sin^2(2\pi F L_\delta/c + \phi_\delta)}_{\text{collecting terms: } T_{\rm mich}}} \tag{D.49}$$

and the term coupling out of the interferometer from the inside of the cavity is (ignoring contrast defect as it is inherently multi-mode):

$$H_{\rm cavAS}(F) = \sin(2\pi F L_\delta/c) e^{2\pi {\rm i} F L_{\rm cmn}/c} \tag{D.50}$$

so the table to PR-Michelson AS-transfer function is $H_{\rm ifo} = H_{\rm cavity}(F) \cdot H_{\rm cavAS}(F)$ Now by convention, the principle resonant mode (approximately the 00 mode) is set to have $\Phi_{\rm HOM} = 0$ as the CARM loop sets $F_{\rm c}$ such that $0 = \frac{2\pi F}{F_{\rm FSR}} + \phi_{\rm 00mode}$. In this case it is easiest to measure all of the other phase-shifts relative to the resonant mode and so assume the resonant mode has 0-phasing (even though in general it doesn't). Now what are the cross-couplings for the resonant mode.

$$H_{\rm ifo}(F_{\rm c}) = \frac{t_{\rm prm}}{1 - r_{\rm prm} r_{\rm ifo}} \sin(2\pi F_{\rm c} L_\delta/c) e^{2\pi {\rm i} F_{\rm c} L_{\rm cmn}/c} \tag{D.51}$$

$$H_{\rm ifo}(F_{\rm c} + F_{\rm mod}) = \frac{t_{\rm prm}}{1 - r_{\rm prm} r_{\rm ifo} e^{{\rm i}\left(\frac{2\pi F_{\rm mod}}{F_{\rm FSR}}\right)}} \sin(2\pi (F_{\rm c} + F_{\rm mod}) L_\delta/c) e^{2\pi {\rm i} (F_{\rm c} + F_{\rm mod}) L_{\rm cmn}/c} \tag{D.52}$$

and because the interferometer is locked at some phase-offset for a given carrier frequency and unknown DARM-offset, we can use the convention

$$\phi_\delta = 2\pi \frac{F_{\rm c} L_\delta}{c} \tag{D.53}$$

and the sum angle formula will be important to derive the even and odd cases due to the change in cancellations between them

$$\sin(2\pi(F_{\mathrm{c}}+F_{\mathrm{mod}})L_\delta/c) = \sin(2\pi F_{\mathrm{c}}L_\delta/c)\cos(2\pi F_{\mathrm{mod}}L_\delta/c) + \cos(2\pi F_{\mathrm{c}}L_\delta/c)\sin(2\pi F_{\mathrm{mod}}L_\delta/c) \tag{D.54}$$

$$\sin(2\pi(F_{\mathrm{c}}-F_{\mathrm{mod}})L_\delta/c) = \sin(2\pi F_{\mathrm{c}}L_\delta/c)\cos(2\pi F_{\mathrm{mod}}L_\delta/c) - \cos(2\pi F_{\mathrm{c}}L_\delta/c)\sin(2\pi F_{\mathrm{mod}}L_\delta/c) \tag{D.55}$$

so

$$H_{\mathrm{ifo:amp}} = \sin(\phi_\delta)\frac{t_{\mathrm{prm}}}{1-r_{\mathrm{prm}}r_{\mathrm{ifo}}}e^{2\pi \mathrm{i}F_{\mathrm{c}}L_{\mathrm{cmn}}/c} \tag{D.56}$$

$$H_{\mathrm{ifo:even}}(F_{\mathrm{c}},F_{\mathrm{mod}}) = \cos(2\pi F_{\mathrm{mod}}L_\delta/c)\frac{1-r_{\mathrm{prm}}r_{\mathrm{ifo}}}{1-r_{\mathrm{prm}}r_{\mathrm{ifo}}e^{2\pi \mathrm{i}F_{\mathrm{mod}}/F_{\mathrm{FSR}}}}e^{2\pi \mathrm{i}F_{\mathrm{mod}}L_{\mathrm{cmn}}/c} \tag{D.57}$$

$$H_{\mathrm{ifo:odd}}(F_{\mathrm{c}},F_{\mathrm{mod}}) = \left(\frac{\sin(2\pi F_{\mathrm{mod}}L_\delta/c)}{\tan(\phi_\delta)}\right)\frac{1-r_{\mathrm{prm}}r_{\mathrm{ifo}}}{1-r_{\mathrm{prm}}r_{\mathrm{ifo}}e^{2\pi \mathrm{i}\frac{F_{\mathrm{mod}}}{F_{\mathrm{FSR}}}}}e^{2\pi \mathrm{i}F_{\mathrm{mod}}L_{\mathrm{cmn}}/c} \tag{D.58}$$

The H_{odd} term with sin in it is the coupling we are used to for the PM to AM conversion due to the Schnupp asymmetry along with the cavity-pole suppression

D.4 Higher-Order-Mode transfer functions

In this notation, the only change to make to determine the even and odd couplings for higher-order-modes is to now take non-zero Φ_{HOM} contributions. Additionally, a coupling term for the (small) creation of HOM's from the input beam-shape to the interferometer

beam-shape is included as B_{HOM}.

$$H_{\mathrm{HOM}}(F_{\mathrm{c}}) = \frac{B_{\mathrm{HOM}} t_{\mathrm{prm}} \sin(\phi_\delta)}{1 - r_{\mathrm{prm}} r_{\mathrm{ifo}} e^{\mathrm{i}\Phi_{\mathrm{HOM}}}} e^{2\pi \mathrm{i} F_{\mathrm{c}} L_{\mathrm{cmn}}/c} \tag{D.59}$$

$$H_{\mathrm{HOM}}(F_{\mathrm{c}} + F_{\mathrm{mod}}) = \frac{B_{\mathrm{HOM}} t_{\mathrm{prm}} \sin(2\pi(F_{\mathrm{c}} + F_{\mathrm{mod}}) L_\delta/c + \phi_\delta)}{1 - r_{\mathrm{prm}} r_{\mathrm{ifo}} e^{\mathrm{i}\left(\frac{2\pi F_{\mathrm{mod}}}{F_{\mathrm{FSR}}} + \Phi_{\mathrm{HOM}}\right)}} e^{2\pi \mathrm{i}(F_{\mathrm{c}} + F_{\mathrm{mod}}) L_{\mathrm{cmn}}/c} \tag{D.60}$$

where for conciseness these variables are defined:

$$H_{\mathrm{HOM:amp}} = B_{\mathrm{HOM}} \frac{t_{\mathrm{prm}}}{X(0\mathrm{Hz}, \Phi_{\mathrm{HOM}})} \sin(2\pi F_{\mathrm{c}} L_\delta/c) \tag{D.61}$$

$$\begin{aligned} H_{\mathrm{HOM:even}}(F_{\mathrm{c}}, F_{\mathrm{mod}}) &= \\ &= \frac{1}{2}\left((u+v)\frac{X(0\mathrm{Hz}, \Phi_{\mathrm{HOM}})}{X(F_{\mathrm{mod}}, \Phi_{\mathrm{HOM}})} + (u-v)\frac{X(0\mathrm{Hz}, -\Phi_{\mathrm{HOM}})}{X(F_{\mathrm{mod}}, -\Phi_{\mathrm{HOM}})}\right) e^{2\pi \mathrm{i} F_{\mathrm{mod}} L_{\mathrm{cmn}}/c} \end{aligned} \tag{D.62}$$

$$\begin{aligned} H_{\mathrm{HOM:odd}}(F_{\mathrm{c}}, F_{\mathrm{mod}}) &= \\ &= \frac{\mathrm{i}}{2}\left((u+v)\frac{X(0\mathrm{Hz}, \Phi_{\mathrm{HOM}})}{X(F_{\mathrm{mod}}, \Phi_{\mathrm{HOM}})} - (u-v)\frac{X(0\mathrm{Hz}, -\Phi_{\mathrm{HOM}})}{X(F_{\mathrm{mod}}, -\Phi_{\mathrm{HOM}})}\right) e^{2\pi \mathrm{i} F_{\mathrm{mod}} L_{\mathrm{cmn}}/c} \end{aligned} \tag{D.63}$$

$$X(F, \Phi_{\mathrm{HOM}}) = 1 - r_{\mathrm{prm}} r_{\mathrm{ifo}} e^{\mathrm{i}(2\pi F/F_{\mathrm{FSR}} + \Phi_{\mathrm{HOM}})} \tag{D.64}$$

$$u = \cos(2\pi F_{\mathrm{mod}} L_\delta/c) \tag{D.65}$$

$$v = \frac{\sin(2\pi F_{\mathrm{mod}} L_\delta/c)}{\tan(\phi_\delta)} \tag{D.66}$$

So the even and odd terms will pick up some extreme behavior now when $\frac{2\pi F_{\mathrm{mod}}}{F_{\mathrm{FSR}}} \approx \Phi_{\mathrm{HOM}}$. because the expression is not possible to simplify to the intuitive level that the principle mode can be. This complexity is characteristic of detuned cavities.

References

[1] A. Bandyopadhyay and J. Rai. Geometrical Representation of Angular Momentum Coherence and Squeezing. *eprint arXiv:quant-ph/0012083*, December 2000.

[2] Raphael Bousso. The holographic principle. *Rev. Mod. Phys.*, 74:825–874, Aug 2002.

[3] Carlton M. Caves. Quantum-mechanical noise in an interferometer. *Phys. Rev. D*, 23:1693–1708, Apr 1981.

[4] Carlton M. Caves and Bonny L. Schumaker. New formalism for two-photon quantum optics. i. quadrature phases and squeezed states. *Phys. Rev. A*, 31:3068–3092, May 1985.

[5] 1942 Gardiner, C. W. (Crispin W.). *Quantum noise : a handbook of Markovian and non-Markovian quantum stochastic methods with applications to quantum optics*. Springer series in synergetics,. Springer, Berlin ; New York, array edition, 2000.

[6] Y. S. Kim. *Phase space picture of quantum mechanics : group theoretical approach*. World Scientific lecture notes in physics ;. World Scientific, Singapore ; Teaneck, NJ, 1991.

[7] O. Kwon and C. J. Hogan. Interferometric Tests of Planckian Quantum Geometry Models. *ArXiv e-prints*, October 2014.

[8] 1944 Orszag, Miguel. *Quantum optics : including noise reduction, trapped ions, quantum trajectories, and decoherence*. Advanced texts in physics. Springer, Berlin ; New York, 2000.

[9] V. V. (Valentin Vladimirovich) Petrov. *Limit theorems of probability theory : sequences of independent random variables*. Oxford studies in probability. Clarendon Press ; Oxford University Press, Oxford : New York, 1994.

[10] Luca Pezzè, Philipp Hyllus, and Augusto Smerzi. Phase-sensitivity bounds for two-mode interferometers. *Phys. Rev. A*, 91:032103, Mar 2015.

[11] E. Rubiola. Tutorial on the double balanced mixer. *ArXiv Physics e-prints*, August 2006.

[12] Bonny L. Schumaker and Carlton M. Caves. New formalism for two-photon quantum optics. ii. mathematical foundation and compact notation. *Phys. Rev. A*, 31:3093–3111, May 1985.

[13] J. Sperling and W. Vogel. Dirac's Quantum Phase Problem. *ArXiv e-prints*, July 2009.

[14] Bernard Yurke, Samuel L. McCall, and John R. Klauder. Su(2) and su(1,1) interferometers. *Phys. Rev. A*, 33:4033–4054, Jun 1986.